OPTIMISATION OF COMPOSITIONS AND HEAT TREATMENTS OF PT-BASED SUPERALLOYS

Mxolisi Brendon Shongwe

A dissertation submitted to the Faculty of Engineering and the Built Environment, University of the Witwatersrand, in fulfilment of the requirements for the degree of Master of Science in Engineering

JOHANNESBURG, 2008

DECLARATION

I, Mxolisi Brendon Shongwe, declare that this dissertation is my own work except where otherwise acknowledges. It is submitted for the degree of Master of Science in Engineering at the University of the Witwatersrand, Johannesburg. It is not been submitted previously at this, or any other university for any degree or examination.

_____ _____

SIGNATURE DATE

ABSTRACT

This study investigated the optimisation of compositions and heat treatment of Pt-based Pt-Al-Cr-Ru superalloys. Initially, six alloys of different compositions were selected using an optimum composition from previous research as a starting point. These alloys were analysed in both the as-cast and heat treated conditions. The heat treatment comprised two stages, first at 1500°C for 18 hours and quenched in water, followed by 1100°C for 120 hours and then air cooled. Microstructural characterisation was carried out in an HR FEI Nova NanoSEM in BSE mode, also using EDX, and XRD. The as-cast alloys had (Pt) dendrites with a eutectic/eutectoid of (Pt) + ~Pt_3Al, with tetragonal ~Pt_3Al precipitated in the dendrites. All heat treated alloys had precipitates of tetragonal ~Pt_3Al in a (Pt) matrix. The volume fraction of the precipitates varied, and the maximum proportion was 30%. To increase the volume fraction, more samples were made with 11 at.% Al. All of the 78 at.% Pt alloys had more ~Pt_3Al precipitates than the 80 at.% Pt alloys, and the Pt_{80}:Al_{11}:Ru_5:Cr_4 alloy had no discernable precipitates. The microstructure was similar to the first batch of samples and Pt_{78}:Al_{11}:Ru_5:Cr_6 had the highest precipitate volume fraction.

The hardness of the alloys was also studied in both conditions. Cracking and slip modes around the hardness indentations were studied to evaluate the toughness. In both conditions, most of the alloys had high hardnesses and exhibited wavy slip, with no cracking from the indentation corners. Pt_{78}:Al_{11}:Ru_5:Cr_6 was the promising alloy because it had the best microstructure (highest proportion of precipitates), a high Al content for oxidation resistance and a reasonable low Pt content for both reduction in price and density.

DEDICATION

I would like to dedicate this work to God and my parents: Edgar Shongwe and Anna Shongwe, for everything and being the best parents in the world, which God perfected before the foundations of the earth. I love you!!.

ACKNOWLEDGEMENTS

I would like to thank the following people and organisations, without which the work would not have been possible:

- My supervisors, Prof. L.A. Cornish and Dr. R. Süss for their continued support. Especially Prof. Cornish, for her commitment in both my personal and professional progress which has allowed me to give her continued trust and confidence, that has been revealed by her regular and structured basis for my evaluation in the research project.

- The financial assistance of the Platinum Development Initiative (PDI) and the South African Department of Science and Technology, DST/NRF Centre of Excellence in Strong Materials (CoE-SM) and the Mellon Foundation are gratefully acknowledged.

- The Microscopy and Microanalysis Unit at the University of the Witwatersrand.

- Edson Mahuma for manufacturing and sectioning of samples.

- Lizelle Glaner for hours of invaluable work at the HR-SEM, Mintek.

- Mintek for granting me this opportunity and for permission to publish the results.

- Finally but not least, thanks to all my family and friends who helped me in many, treasured ways. I will never forget the love and support from every one of you.

TABLE OF CONTENTS

LIST OF FIGURES

LIST OF TABLES

CHAPTER ONE

INTRODUCTION AND BACKGROUND

One definition of a superalloy is: “an alloy developed for elevated temperature service, usually based on group VIII elements, where relatively severe mechanical stressing is encountered, and where high surface stability is frequently required” [1987Sim]. The most widely used and sophisticated superalloys are the nickel-based alloys; about 70 % of the weight of a modern jet turbine engine consists of nickel-based superalloys. These superalloys exhibit high yield stresses and also excellent resistance to environmental attack at high temperatures [1987Sim].

Superalloy development in the United States began in the 1930s, prompted by the need for more heat-resistant materials in aircraft engine turbochargers. It has been paced, since the early 1940s, by the increasing demands of advancing gas turbine technology. For purposes of classification, three main groups of superalloys are identified, namely: cobalt-based, nickel-based, and iron-based. The nickel-iron-based alloys are considered as a special group within the nickel-based class. Chromium-based alloys are not generally regarded as superalloys. The range of applications for which superalloys are used has expanded to many other areas and now includes land-based gas turbines, rocket engines, chemical and petroleum plants. Superalloys are particularly well suited for these demanding applications because of their ability to retain most of their strength even after long exposure times above 650°C. Their versatility stems from the fact that they combine this high strength with good low-temperature ductility and excellent surface stability [1972Sim].

Developments in alloying and processing techniques have increased the maximum temperatures at which superalloys can be used to about 1000°C, which represents about 90% of their melting temperature [1987Sim]. However, the melting temperatures and oxidation resistances of these alloys ultimately limit the maximum temperature attainable [1987Sim, [1999Cle]. The demand for materials capable of attaining even higher operating temperatures is increasing since increased operating temperatures imply:

- Greater thrust-to-mass ratios
- Improved fuel efficiency
- Reduction of noise levels

- Reduced pollution.

Thermal barrier coatings are currently being investigated in the hope of achieving significant improvements in the operating temperatures of these alloys [1998Gow]. However, coating technology is complicated and expensive, and also considered to be 'high risk' because of flaw sensitivity [1987Sim, 1994Gob]. The maximum operating temperature, even of a coated alloy, is therefore affected by the temperature capabilities of the base alloy.

The search for improved superalloys continues with possibly more resources and techniques than that for any other alloy type. Despite many years of work on superalloys, there are still developments which are expected to be achieved [1987Sim]. Although nickel-based superalloys will probably continue to form the basis of jet engines for many years to come, there is an argument for examining a completely new system with the potential for operation in the ultra-high temperature regime. Higher melting point alloys have the additional advantage of microstructural stability and hence improved creep resistance, since the diffusion rates of high melting point elements are generally extremely slow [1974Avn].

To meet the demands of increased strength, particularly for thermal fatigue resistance for turbine blades and vanes, the superalloy technologist has evolved methods of directional solidification or controlled grain growth whereby all crystals are aligned along the length of the component, thus eliminating weakening transverse boundaries. The superalloy technologist has even gone a giant step further to produce single crystal components. A major barrier to the increase in use temperature of alloy systems for engines is oxidation and hot corrosion. Corrosion has become a more difficult problem to overcome than strength and ductility. Many current alloys are coated for use at high service temperature [1972Sim, 1999Car1].

Alloys based on intermetallic compounds such as NiAl, TiAl and RuAl have received considerable attention in recent years, because the ordered structure of intermetallic compounds imparts remarkable high temperature strength [1997Wil]. However, most intermetallic compounds are inherently brittle at room temperature, and the development of useful alloys is limited by this brittleness [1997Wil]. Refractory metals such as Mo, Ta and W have also been considered, but these alloys have limited high temperature oxidation resistance, and also limited creep resistance because of their more open body centred cubic (b.c.c) crystal

structure [1987Sim]. Ceramics and composite materials are also the focus of considerable research, but their poor room-temperature toughness, low resistance to thermal shock and poor oxidation resistance remain problematic [1993Raj].

An alternative approach is the development of alloys based on the platinum group metals [1996Yam]. The PGMs (Ru, Ir, Rh, Os, Pd and Pt) generally have high melting temperatures, and environmental resistance superior to that of the refractory alloys. Additionally, certain PGMs such as Rh, Pd, Ir and Pt have f.c.c. crystal structures, which may allow analogous alloys to the nickel-based superalloys to be developed. Scientists at the National Institute for Materials Science (NIMS, formerly NRIM) in Japan have achieved promising results for Ir- and Rh-based alloys [1996Yam]. Alloys with strengths of up to 200 MPa at 1800°C have been produced.

Experimental Pt-based alloys have been studied at Mintek. It was found that successful Ni-based superalloy analogues could be manufactured with alloys of the approximate composition Pt_{82}:Al_{14}:X_4 where X was Cr, Ti and Ru [200Hil1, 2001Hil2]. The best properties were exhibited by the Pt-Al-Cr and Pt-Al-Ru alloys, although the precipitate volume fraction was not as high as in the Ni-based superalloys. A quaternary was targeted from a combination of these alloys [2001 Hil2, 2002Cor]. Chromium stabilized the cubic $L1_2$ ~Pt_3Al precipitate, and Ru gave solid-solution strengthening to the (Pt) matrix. Experimentation gave Pt_{84}:Al_{11}:Ru_2:Cr_3 as the best composition with a reasonable proportion of precipitates and good properties, including hardness. The volume fraction of ~Pt_3Al was estimated, using image analysis, to be approximately 25 – 30%. The highest hardness was found in the alloy without primary ~Pt_3Al. There was no clear relationship between the hardness and the composition or microstructure.

Since the precipitate volume fraction was not as high as in the Ni-based super alloys, it still needs improvement. Thus, this work is an attempt to increase the ~Pt_3Al volume fraction in Pt-Al-Ru-Cr alloys, by varying compositions and heat treatments. This dissertation therefore summarises the results of the various compositions investigated. Chapter 2 and 3 cover the literature review and experimental work. The results and discussion are given in Chapters 4 and 5. Conclusions and recommendations are also given.

CHAPTER TWO

LITERATURE SURVEY

Superalloys based on platinum-group metals are being developed for high-temperature applications. These alloys have two-phase microstructures comprising either ordered precipitates in a matrix analogous to the nickel-based superalloys or a fine dispersion of oxide particles in a matrix analogous to oxide-dispersion-strengthened nickel-based alloys.

The aim of this literature survey is to give a review on the developments and progress made in the development of platinum-group metal superalloys for high and ultra-high temperature use and as well as their properties and morphology, with more attention given to the Pt-based superalloys. The review will first highlight the history of superalloys, nickel-based superalloys, earlier work done on the development of a new generation of materials to succeed the nickel-based superalloys, followed by the latest work done in this field using collaborative studies being undertaken by Mintek and a number of alloy development centres.

2.1 The Development and History of Superalloys

2.1.2 Nickel-Based Superalloys

Nickel-based alloys are the most complex, widely used, and perhaps the most fascinating of the superalloys [1987Sim]. Their combination of high-temperature strength and oxidation resistance renders them unparalleled for service as structural high-temperature materials. These alloys contain up to 14 elemental alloying constituents, as well as additions of trace elements [1992Bro]. The chemical compositions of these alloys are selected to produce the desired structure and properties for a specific application [1990Lee]. Material strength, surface stability, density and thermal conductivity are just some of the properties which are controlled by the alloy composition [1990Lee].

The NBSA development has been extensively reviewed by Sims *et al.* [1987Sim, 1972Sim]. Vacuum melting in the 1950s allowed for very fine control of the chemical composition of NBSAs and reduction in contamination and in turn led to a revolution in processing

techniques such as directional solidification of alloys and single crystal superalloys. Single-crystal superalloys (SC superalloys) are formed as a single crystal using a modified version of the directional solidification technique, so there are no grain boundaries in the material. The mechanical properties of most other alloys depend on the presence of grain boundaries, but at high temperatures, they would participate in creep and must be replaced by other mechanisms. In many such alloys, islands of an ordered intermetallic phase sit in a matrix of disordered phase, all with the same crystalline lattice. This approximates the dislocation-pinning behaviour of grain boundaries, without introducing any amorphous solid into the structure. In NBSAs creep resistance is dependent on slowing the speed of dislocations within the crystal structure. The γ' phase (Ni_3Al) presents a barrier to dislocations and the γ' phase size can be precisely controlled by careful precipitation hardening heat treatments [1987Sim].

The nickel-based alloys use strengthening mechanisms such as solid solution and precipitation strengthening. Solid solutioned strengthened alloys, such as Hastelloy X, are used in applications requiring only modest strength. In the most demanding applications, such as hot sections of gas turbine engines, precipitation strengthened alloys are required. Most nickel-based alloys contain 10-20% Cr, up to 8% Al and Ti, 5-10% Co, and small amounts of B, Zr, and C. Other common additions are Mo, W, Ta, Hf, and Nb [1995Eri, 1999Car2, 1996Eri]. In broad terms, the elemental additions in Ni-based superalloys can be categorized as being [1987Sim]:

i) The γ formers (elements that tend to partition to the γ matrix)
ii) The γ' formers (elements that partition to the γ' precipitate)
iii) Carbide formers, and
iv) Elements that segregate to the grain boundaries.

Elements which are considered γ formers are Group V, VI, and VII elements such as Co, Cr, Mo, W, and Fe. The atomic diameters of these alloys are only 3-13% different from Ni (the primary matrix element). The γ' formers come from group III, IV, and V elements and include Al, Ti, Nb, Ta, and Hf. The atomic diameters of these elements differ from Ni by 6-18%. The main carbide formers are Cr, Mo, W, Nb, Ta and Ti. The primary grain boundary elements are B, C, and Zr. Their atomic diameters are 21-27% different from Ni [1995Eri, 1984Gia, 1996Eri].

2.1.3 Applications

The dominance of superalloys is reflected in the fact that they currently comprise over 50% of the weight of advanced aircraft engines. The widespread use of superalloys in turbine engines, coupled with the fact that the thermodynamic efficiency of turbine engines is increased with increasing turbine inlet temperatures, provides the motivation for increasing the maximum-use temperature of superalloys. In fact, during the past 30 years turbine airfoil temperature capability has increased on average by about 15°C per year. Two major factors which have made this increase possible are [1994Nab, 2001Fis2]:

1) Advanced processing techniques, which improved alloy cleanliness (thus improving reliability) and/or the production of tailored microstructures such as directionally solidified or single-crystal material.
2) Alloy development resulting in higher-use-temperature materials primarily through the additions of refractory elements such as Re, W, Ta and Mo.

About 60% of the use-temperature increases have occurred due to advanced cooling concepts; 40% have resulted from material improvements. State-of-the-art turbine blade surface temperatures are near 1,150°C; the most severe combinations of stress and temperature correspond to an average bulk metal temperature approaching 1,000°C [1994Nab].

Although superalloys retain significant strength to temperatures near 980^{o}C, they tend to be susceptible to environmental attack because of the presence of reactive alloying elements (which provide their high-temperature strength). Surface attack includes oxidation, hot corrosion and thermal fatigue. In the most demanding applications, such as turbine blade and vanes, superalloys are coated to improve environmental resistance [1994Nab, 2001Fis2].

2.1.4 Processing of Superalloys

The material and casting technique improvements that have taken place during the last 50 years have enabled superalloys to be used first as equiaxed castings in the 1940s, then as directionally solidified (DS) materials during the 1960s, and finally as single crystals (SC) in

the 1970s. The advancement in each casting technique has resulted in higher use temperatures [1972Sim, 1968 Pie, 1970Ver].

SC castings were a spin-off from the technological advances made in the DS casting processes. SC castings are produced in a similar fashion to DS by selecting a single grain, via a grain selector. During solidification, this single grain grows to encompass the entire part. Single crystals obtain their outstanding strength through the elimination of grain boundaries that are present in both equiaxed and directionally solidified materials. In addition, the elimination of grain boundary strengtheners such as C, B, Si, and Zr raises the single crystal's melting point. By increasing the alloy's melting point, the homogenization heat-treat temperature can be increased without fear of incipient melting, thus allowing for more complete solutioning of the γ' and thereby increasing alloy strength and maximum use temperature [1970Ver, 1999Car2, 1995Eri, 1996Eri]. The single crystal nickel-based superalloys contain a high volume fraction of strengthening LI_2 ordered Ni_3Al-based γ' phase particles homogeneously distributed in the γ matrix as near cubical precipitates (Figure 2.1) [1999Car1].

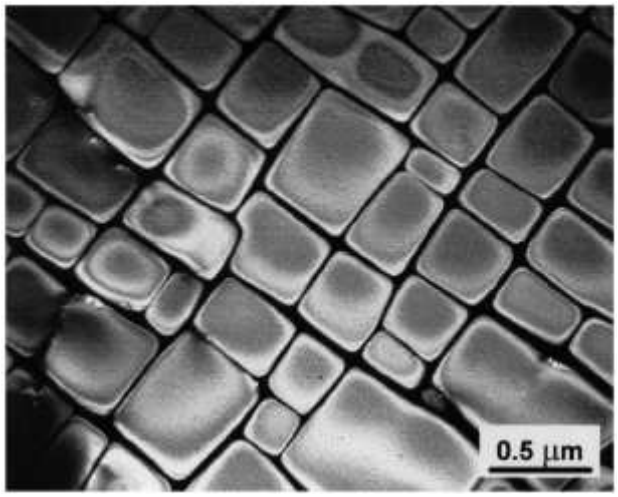

Figure 2.1. Two-phased γ - γ' microstructure in fully annealed heat-treated AM3 first generation single crystal superalloy [1999Car1].

2.2 The Search for a New Generation of Materials

The attributes that make intermetallic compounds desirable materials for high-temperature structural applications have been widely reported [1995Wes]. Intermetallics have properties such as good diffusional creep resistance, high-temperature strength, high melting points, good oxidation resistance and low densities for performance in service regimes which the

nickel-based superalloys cannot meet. Unfortunately, their almost-universal low tolerance to defects makes them unsuitable for application in critical components. Engineering design and alloy development therefore have to address the competing requirements for high-temperature strength and ambient-temperature toughness. This has led to the interest in multi-phase systems which bring together these apparently contradictory attributes. Three such approaches are currently under investigation [2000Wol].

In the first instance, the success of the Ni-based superalloys leads one to seek succeeding generations of high-temperature alloys that make use of the principles of a high volume fraction of finely-dispersed, coherent precipitates within a ductile matrix. Analogous γ/γ' systems with much higher melting points, based on $L1_2$ precipitates (ordered f.c.c) in a f.c.c matrix (the matrix usually has the higher melting point) are limited in number. Some of the platinum group metals are almost unique among the high-melting point metals in that they have f.c.c structures. Moreover, they have environmental resistance that enables them to be considered for high-temperature use. Systems based on iridium (Ir), rhodium (Rh) and platinum (Pt) have attracted attention that has led to the suggestion that they form a class of alloys to be named 'refractory alloys' by Yamabe-Mitarai, Maruko, Yokokawa and Harada [1997Yam]. (This terminology is something of a misnomer insofar as refractory metals are normally associated with strong affinities for oxygen, whereas most of the platinum metals are relatively noble in this respect [2000Wol].)

Secondly, analogous precipitation-strengthened systems have similarly been proposed for the b.c.c metals, in this case with an ordered b.c.c structure contained within a ductile b.c.c matrix (or β/β'). Among the most oxidation-resistant materials are ferritic alloys based on iron-chromium-aluminium (Fe-Cr-Al), typically with compositions around 20 wt.% Cr and 5 wt.% Al (balance Fe). Various attempts at alloying have been made to induce the precipitation of coherent precipitates in these systems, and one such study examined alloying with ruthenium (Ru) to enhance not only the strength, but also the oxidation and corrosion resistance of these alloys [1999Ngw].

Thirdly, there are the so-called *in situ* composite microstructures, which exploit 'ductile phase toughening'. Methods to produce ductile phase toughening stem from the recognition that 'ductile' secondary phases contribute not only towards deflecting crack propagation in

the usual way, but also to strengthening (by acting as obstacles to dislocation motion at the phase interfaces). In particular, eutectic systems lend themselves to exploitation of inherently compatible phases in a finely divided mixture, and are natural candidates for structural intermetallic composites [1996Wol, 1999Hil].

The following sections will give more focus on research work that has been done on the platinum-based superalloys, as they are of interest for the investigation at hand. A limited discussion will be given on topics such as PGM-based refractory superalloys, oxide-dispersion-strengthened (ODS) platinum-based alloys, and a review of these materials is considered relevant for comparison purposes, as research work involved in these materials also concerns improving the properties and microstructure.

2.2.1 PGM-Based Refractory Superalloys

The first work undertaken on PGM-based superalloys was on Rh- and Ir-based alloys [1996Yam]. The rationale was that these elements not only have the f.c.c structure, which could permit a similar microstructure to the NBSAs, but also have higher melting points than the NBSAs – 1960°C and 2443°C for Rh and Ir, respectively. Additionally, the alloys based on Rh and Ir have superior environmental resistance compared with the refractory alloys. Workers at the National Institute for Materials Science (NIMS) in Japan have achieved promising results for both Ir- and Rh-based alloys [1998Yam]. Two-phase microstructures were obtained similar to the NBSAs and strengths reaching a maximum of 200MPa at 1800°C were obtained [1996Yam]. The high potential application temperatures of these alloys gave rise to the name “refractory superalloys” [1996Yam].

Pure Ir, and binary Ir-X alloys with nominal compositions between 12 and 18 at.% X (where X = Ti, V, Zr, Nb, Hf, or Ta) as well as binary alloys of Rh-15 at.% X (where X = Ti, Nb, and Ta) were produced by arc-melting in an argon atmosphere. Characterisation included scanning and transmission electron microscopy and X-ray diffraction. Microscopy revealed $L1_2$ precipitates in an f.c.c matrix [1997Yam]. When the alloys were heat treated at 1500°C, cuboid $L1_2$ precipitates were seen in Ir–Nb, Ir-Zr alloys exhibited platelike precipitates, and the Ir-V alloy had irregular precipitates [1998Yam].

Compression tests were undertaken in air at an ambient temperature of 1200°C and under argon at 1500°C and 1800°C, in order to determine the 0.2% proof stresses. The results are shown in Figure 2.2 with flow stresses of CMSX-10 and Mar-M247 (third generation NBSAs), as well as a tungsten alloy for comparison. The results indicated that binary Ir-Zr performed better than a highly alloyed NBSA above ~1000°C [1998Yam]. The good compression tests results, especially from such simple alloys with low precipitate densities, indicate the great potential these alloys have for ultra-high temperature applications.

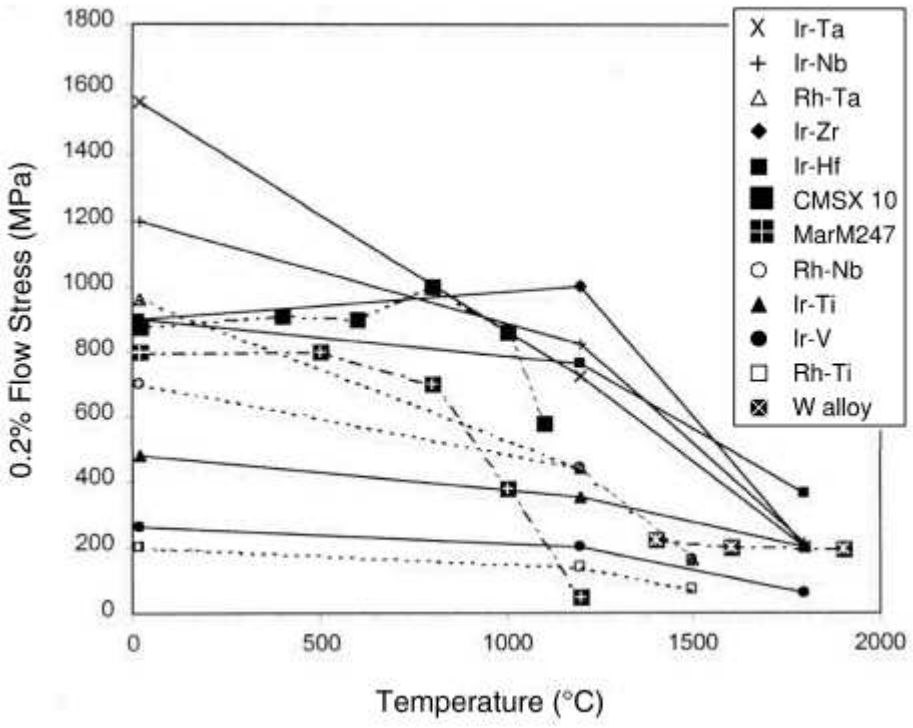

Figure 2.2. Effect of temperature on 0.2% flow stress during compression testing of as-cast Ir- and Rh-based alloys with 15% secondary elements, together with Ni-based and W-based alloys [1998Yam].

For a number of reasons, development studies on Ir-based superalloys have been extended to examine effects of alloying with Ni-based superalloys ("cross alloying") [2000Yu1, 2000Yu2]. Although attractive mechanically, the simple Ir binary systems have a number of drawbacks: high density, restricted room-temperature ductility, relatively poor high-temperature oxidation resistance (Ir forms volatile oxides above 1196°C), and, most significantly, the limited physical supply of Ir globally. Only ~4 tonnes of Ir are produced annually to meet the already high demand by a variety of industrial applications. World (Ir

and Rh) resources would be unable to sustain a major new bulk application, and these alloys must inevitably find use in only the most performance critical and speciality applications.

On the other hand, platinum enjoys relative abundance and excellent environmental resistance although it has a more modest melting point (1772°C) than Ir, a Pt solid solution can be equilibrated with an $L1_2$ phase in a number of different systems [2000Wol].

Nevertheless, even though the Ir-based superalloys have some drawbacks as mentioned above, further research work has been done to eliminate some of these problems. Subsequent work involved the reduction of density and/or cost without diminishing the properties. The density was reduced by substituting some iridium in Ir_{85}:Nb_{15} with Ni, Mo, Ta, and W [2000Gu]. The best alloy was Ir_{75}:Nb_{15}:Ni_{10} (at.%), although it still had a high density compared with NBSAs and its compressive ductility was ~5% at ambient temperature [1999Gu1]. Ir-based alloys had higher strength than the Rh-based alloys, but also higher density and lower ductility [1999Gu2]. Alloys of composition $(Ir,Rh)_{75}$:Nb_{15}:Ni_{10} (at.%) were manufactured, characterized, and subjected to compression testing. All exhibited $L1_2$ precipitates and had melting temperatures above 1900°C. They had high specific strength up to 1200°C, although this decreased at higher temperatures. The best alloy, where the Ir:Rh ratio was 3:1, outperformed Ir-, Co-, and Ta- based alloys [2002Gu]. Work is ongoing to further improve the alloys.

2.2.2 Oxide-Dispersion-Strengthened Platinum-Based Alloys

If the application temperatures of up to 95% of the melting temperatures of the platinum matrix and/or severe corrosion resistance are prerequisites, Oxide-Dispersion-Strengthened (ODS) platinum-based alloys may outperform precipitation-strengthened platinum-based superalloys. In these alloys, small amounts of stable oxide particles are finely distributed throughout the alloy matrix. The creep and stress-rupture strengths at temperatures of 0.8-0.9 T_m are greatly increased due to reduced dislocation mobility and stabilization of the grain-boundary structure, even for long exposure times [1973Joh, 1988Joh].

Most ODS platinum-based alloys are produced by complicated and expensive powder metallurgy (P/M) processes. However, disadvantageous mechanical properties have prevented

the broader application of these alloys. The P/M ODS platinum-based alloys often obtain their high strength only at the price of poor ductility (i.e. these materials are brittle and tend to form cracks in high-temperature service) [2000Völ]. Furthermore, these ODS materials experience processing problems, especially in welding. The fusion welding process results in a considerable decrease in strength in the welding zone down to that of the matrix phase.

In order to overcome the disadvantages of the P/M ODS alloys, Pt DPH (dispersion-hardened) materials were developed recently by W.C. Heraeus GmbH & Co. in cooperation with the University of Applied Sciences Jena [2001Fis1]. The Pt DPH alloy has oxide particles, which are visible in the TEM images (Figure 2.3), and inhibit grain boundary mobility. Therefore, Pt DPH shows excellent grain-boundary stability and remains fine-grained at high annealing temperatures. Several oxide particle fractions are observed in Pt DPH, one with sizes ranging from tenths of a micron to a few microns. Energy-dispersive X-ray measurements in the transmission electron microscope indicate that the particles consist of ZrO_2-Y_2O_3 mixed oxides. Surprisingly, although most of the oxide particles are rather coarse, these particles are responsible for the substantial strengthening effect observed in the DPH materials. Furthermore, DPH materials show much better ductility than ODS platinum-based produced by P/M [2000Völ]. The Pt DPH materials have already proven themselves in the laboratory and in industrial applications [2002Fis, 2001Fis2].

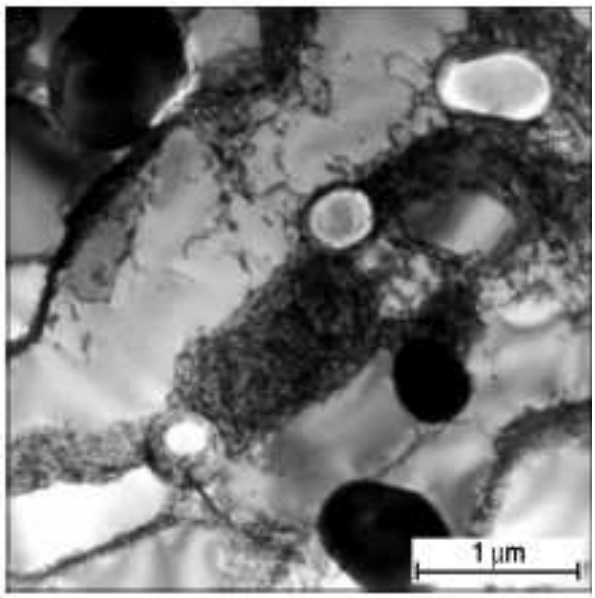

Figure 2.3. Bright-field TEM image of the Pt DPH alloy, showing dislocation networks around coarse particles composed of zirconium and yttrium oxide. The alloy was loaded with 3.5 MPa in tension for 5 h at 1600°C [2001Fis1].

2.2.3 Platinum-Based Superalloys

2.2.3.1 Introduction

The development of platinum-based superalloys is still in its infancy, and there is potential for high strength by conventional alloying and ODS. In order for them to be used in jet engines, the innovative designs will be required to take advantage of the excellent properties of platinum-based alloys, while avoiding the problems of high density and cost. The Ir-based alloys show very high strength, but they do not have the oxidation resistance of the PGMs due to high alloying [1996Yam].
Platinum-based alloys have already been successfully applied in the aerospace and glass industries [1990Lup, 1988Wha]. For these applications, exceptional chemical stability, oxidation resistance, high melting points, ductility, thermal-shock resistance, and electrical or thermal conductivity counterbalance the exceptionally high price of platinum.

Pure platinum has relatively low mechanical strength, therefore platinum is usually alloyed with up to ~20% rhodium or up to about ~30% iridium. Platinum alloys with more than 20% rhodium or iridium are very difficult to process, and alloys with iridium contents of more than 20% tend to embrittle when exposed to intermediate temperatures. Pure platinum and common solid-solution platinum-rhodium alloys are highly oxidation resistant, even at temperatures above 1000°C. Platinum alloys show small weight losses after long exposure to high temperatures due to evaporation of the alloying element iridium. ODS platinum-based alloys are used for the most demanding applications at temperatures of up to 92% of the melting temperature of the platinum matrix [2001Fis1, 1988Wha, 1990Lup].

2.2.3.2 Development: Properties and Microstructure

Following the success of the two-phase structures in iridium- and rhodium-based refractory superalloys, a two-phase microstructure in platinum-based alloys was attempted [2000Wol]. Since platinum has the same structure as nickel and a similar chemistry, a Pt-based superalloy analogous to NBSAs was considered possible, but with a higher melting point (since the melting points are 1769°C for platinum, compared with 1455°C for nickel) and improved oxidation resistance [1996Yam, 1997Yam, 1998Yam].

A platinum-based solid solution was selected for the matrix phase [2000Wol, 2000Hil1]. An ordered precipitate was preferred for the main precipitate because it should provide the same good properties as the NBSAs [2001Hil1]. A screening was conducted of the Pt binary phases based on these criteria:

- High phase stability
- High melting point
- Oxidation resistance
- High thermal conductivity, and
- Low thermal expansion and (if possible) low density.

The selected candidate systems were those with Al, Nb, Ta, and Ti [2001Hil1]. A survey of Rh, Ni and Ru was also conducted for the solid-solution strengthener. Ternary systems from these elements were examined, and if intermetallic phases other than the $L1_2$ phase formed between the two other elemental additions in the targeted range, the system was excluded. The first systems tried were Pt-Al-Ni, Pt-Al-Ru, Pt-Al-Cr, Pt-Al-Ti, Pt-Al-Re, Pt-Ti-Ru, Pt-Ti-Re, Pt-Ta-Ru, Pt-Ta-Re, and Pt-Nb-Ru. Alloys based on Pt-Al were found to be the only alloys worth considering, because of their oxidation resistance [2000Hil2]. Thus, systems based on the Pt-Al-X ternaries received the most attention at Mintek [2002Hil]. Simple ternary alloys have been tested in compression at temperatures up to 1350°C, Figure 2.4, and found to outperform their conventional Ni-based counterparts (these, of course, are limited by their melting point at these extremes of temperature) [2001Hil5]. Static oxidation trials show considerable efficacy of the aluminium in providing a protective adherent scale on the Pt-Al-based alloys [2000Hil1]. In this regard, the Pt-based systems have also proved to be capable of withstanding greater extremes of temperature than their base metal counterparts, as shown in Figure 2.5.

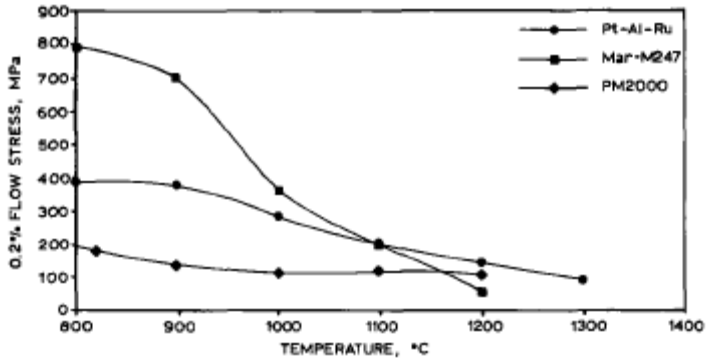

Figure 2.4. High-temperature compression strength of Pt-Al-Ru γ/γ′ alloy compared to Mar-M247 (a Ni-based superalloy) and tensile strength of PM2000 (an Fe-based superalloy) [2001Hil5].

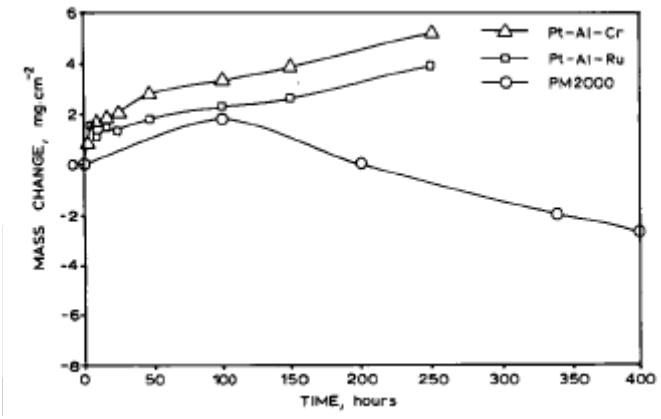

Figure 2.5. Isothermal oxidation behavior of Pt-Al-Cr and Pt-Al-Ru γ/γ′ alloys at 1350°C compared to PM2000 (an Fe-based superalloy) at 1300°C, showing that Pt alloys exhibit ideal para-linear behaviour, unlike mass loss shown by PM2000 [2000Hil1].

Most of the refractory additions to platinum debilitate its environmental resistance, leading to severe internal oxidation. In this respect, the Pt-Al system holds great promise, having a considerable history as a protective coating on Ni-based superalloys [1996Nat]. Platinum aluminides represent some of the most adherent, oxidation- and hot corrosion-resistant phases identified to date. Studies on the Pt-Al system have shown that as little as 2 wt% of Al in Pt is sufficient to establish a thin protective oxide coating at temperatures up 1450°C [1976Fel]. However, Mintek's work has shown that more Al is needed [2001Süs].

The microstructure of a (Pt)-Pt_3Al alloy, developed by solutionising and ageing, is shown in Figure 2.6. Among its principal features are strongly oriented cuboid precipitates, typically present in a bimodal size distribution. The microstructure is similar to (Ni)-Ni_3Al alloys [1980Wee], and the distinctive cuboid geometry is an indication of low mismatch strain and a high degree of coherency. The existence of a low-temperature variant of the Pt_3Al γ′ phase manifested by a lath or twinned microstructure. This is problematic because microstructural stability and dimensional tolerances could be compromised during service [2000Wol]. The Pt_3Al phase has been shown to have greater strength in compression than Ir_3Nb at temperatures up to about 1000°C [1980Wee, 1999Yam], but the disordered platinum solid solution lacks the high critical resolved shear stress (CRSS) of Ir.

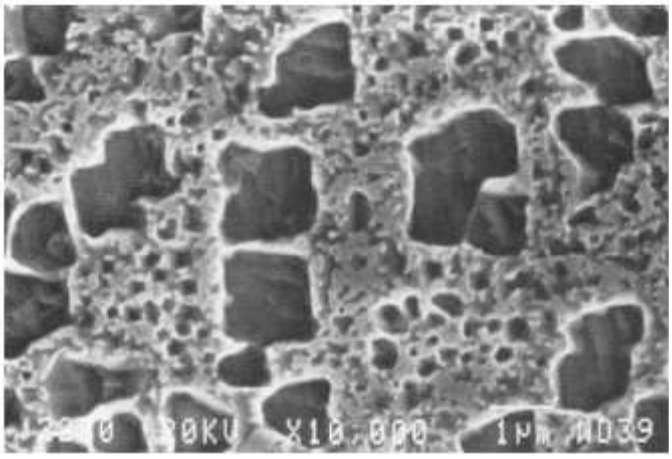

Figure 2.6. Cuboid Pt_3Al precipitates in $Pt_{88}Al_{12}$, which has been solutioned and aged at 1350°C, showing evidence of a sub-micron secondary precipitates [2000Wol].

Although the flow stress of Pt_3Al decreases with increasing temperature, it still is greater at high temperature than that of Ni_3Al (γ') and Ir_3Nb [1999Yam]. However, in the Pt-Al-X systems, the cubic $L1_2$ Pt_3Al phase that exists at high temperatures [2000Hil2] transforms to $D0'_c$ (U_3Si structure) at lower temperatures. In the Pt-Al binary, the cubic $L1_2$–Pt_3Al is stable at room temperature only when the composition of this phase lies on the Al–rich side of stoichiometry, which is out of the f.c.c/Pt_3Al two–phase region. There are two versions of the Pt-Al phase diagram. According to Massalski [1990Mas], there are two phases of Pt_3Al, and the $L1_2$ form which coexists with (Pt) at high temperatures, transforms to a tetragonal structure at about 1280°C. Conversely, Mishima *et al.* [1986Mis] reported three Pt_3Al phases and stated the consecutive transformations of $\gamma' \Rightarrow \gamma'_1 \Rightarrow \gamma'_2$ ($L1_2 \Rightarrow$ DOc $\Rightarrow$DO′c) were martensitic and occurred at 340°C and 130°C.

In a study by Douglas, Neethling, Santamarta, Schryvers and Cornish [2006Dou1] on the ordering behaviour of Pt_3Al, the precipitates were found to consist of plates that are twins and have a specific orientation relationship in respect to the matrix. Each plate contained a high density of thin platelets lying perpendicular to the c-direction (Figure 2.7). The precipitates were expected to crystallise in the DO′c unit cell. However, the experimental results showed that a different ordered structure, based on the modification of the DO′c unit cell occurred instead (Figure 2.8).

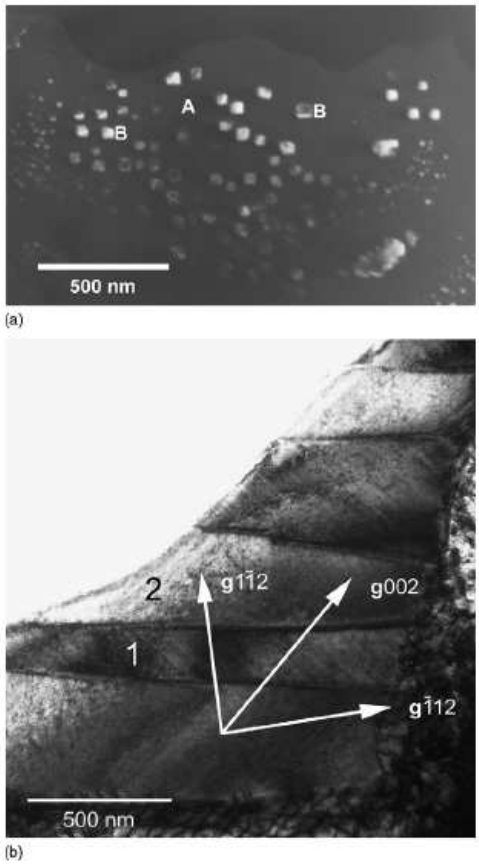

Figure 2.7. (a) Dark-field TEM micrograph showing γ′ precipitates (bright) embedded in the matrix (dark), b) Bright-field TEM micrograph of γ′ precipitate containing stacked plates (e.g. 1 and 2); g vectors are labelled relative to the precipitate diffraction pattern.

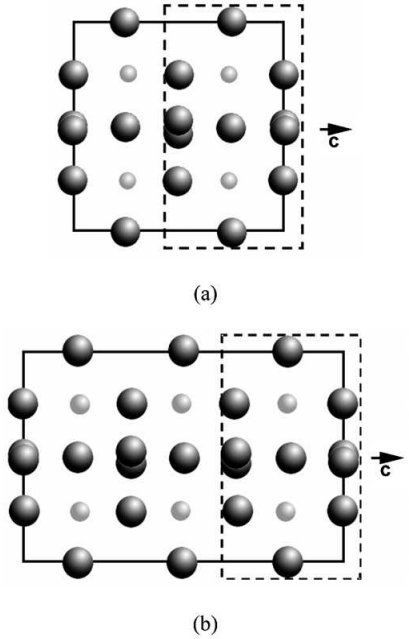

Figure 2.8. (a) Unit cell of the DO'_c structure, B = [110]. (b) Unit cell of modified DO'_c unit cell, B = [110] [2006Dou1].

Since good properties exist with the $\gamma + \gamma'$ structure in the NBSAs, the system was used regardless of the disadvantage of two Pt_3Al forms, but a ternary element that would stabilise the higher-temperature, preferred structure of the Pt_3Al precipitate was needed. The next screening consisted of verifying the two-phase microstructure, measuring room temperature hardness, and testing the oxidation properties against the ODS iron-based alloy PM2000. High-temperature compression testing was also done using Mar-M247 as a benchmark. All of the alloys had good mechanical properties but the best environmental properties were exhibited by alloys with Ti, Cr, and Ru additions. Partial isothermal sections at 1350°C in the Pt-rich corner were derived for the Pt-Al-Cr [2001Hil2], Pt-Al-Ru [2001Big], and Pt-Al-Ti [2001Hil2] systems. Figure 2.9 shows the stress-rupture curves. The Pt_{86}:Al_{10}:Cr_4 (at.%) alloy possesses the highest strength and the shallowest slope of the stress-rupture curve. Furthermore, the measurements on Pt_{86}:Al_{10}:Cr_4 showed the least amount of scatter around the stress-rupture curve. The Pt_{86}:Al_{10}:Ru_4 has a slightly lower stress rupture strength than Pt_{86}:Al_{10}:Cr_4 (at.%) at the investigated stress levels [2001Hil2].

In another study by Hill *et al*. [2001Hil3] on the effects of some ternary alloying additions (Ti, Cr, Ru, Ta and Ir) on the phase relations and properties of two-phase (Pt)/~Pt_3Al alloys, the crystal structure and morphology of the ~Pt_3Al phase were examined. The compressive strengths and melting temperatures of the alloys were also determined. It was found that Ti, Cr and Ta partitioned to ~Pt_3Al and stabilised the $L1_2$ form. The ~Pt_3Al phase in these alloys had cuboid morphologies and a small lattice misfit with the matrix (about -0.7%). The tetragonal DO'_c form of ~Pt_3Al was observed in the alloys containing Ru and Ir. The compressive strengths of the alloys were found to depend on the proportion of ~Pt_3Al in the microstructures, higher strengths being recorded for alloys containing larger proportions of ~Pt_3Al.

Transmission electron microscopy was used to study the microstructure of the alloys Pt_{86}:Al_{10}:X_4, where X was Ti, Cr, Ru, Ta, or Ir [2001Hil3]. The precipitates were mostly cuboid (Figure 2.10). However, although the mechanical properties were encouraging as compared to the benchmark materials, the volume fraction of the precipitates was only about 30%, instead of the ~70-80% [1987Sim] value for NBSAs. The misfits were mostly low and indicated that the structures were likely to be stable at high temperatures, without coarsening and loss of properties. Although heat treatments can improve the volume fractions, more alloy additions

were tried before concentrating on the heat treatment. However, trials on the quaternary alloy did show that heat treatment at 1450°C improved the precipitate volume fraction [2001Hil3].

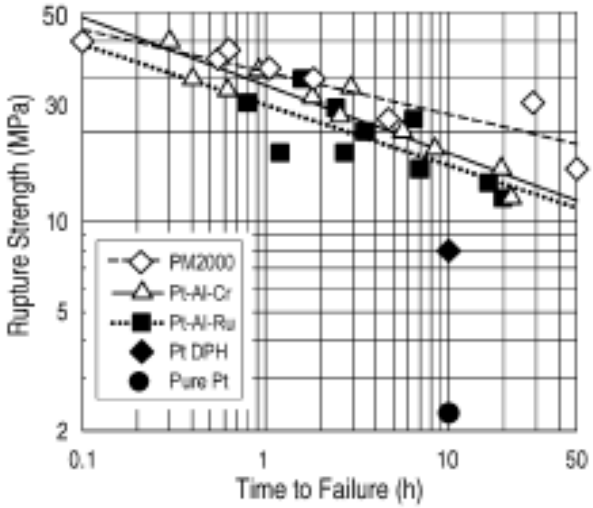

Figure 2.9. Stress-rupture curves of 86Pt-10Al-4Cr, 86Pt-10Al-4Ru (at.%), and PM2000 at 1300°C, compared with 10 h stress-rupture strength of dispersion-hardened Pt and pure Pt at 1300^{0}C [2001Hil2].

Figure 2.10. Dark-field transmission electron microscopy (TEM) image of 86Pt-10Al-4Ti (at.%), showing the cuboidal nature of the Pt_3Al precipitates [2001Hil3].

Since Pt-Al-Cr and Pt-Al-Ru were the best alloys from the ternary alloy trials [2003Hil3], quaternary alloys were made comprising both ternary additions. Chromium stabilized the cubic $L1_2$ Pt_3Al precipitate, and Ru gave solid-solution strengthening to the (Pt) matrix. Different

compositions were tried, shown in Table 2.1. The samples were heat treated at 1350°C for 96 hours. The microstructure was examined using an SEM and, where possible, the phases were analysed using electron dispersive X-ray spectroscopy (EDS). Cornish *et al.* [2002Cor] found that three of the alloys were single-phase ~Pt_3Al, while three had two-phase microstructures. Two of these had large areas of ~Pt_3Al, together with a mixture of (Pt) and ~Pt_3Al (Figure 2.11 (a)). The third (Pt_{84}:Al_{11}:Ru_2:Cr_3) was composed entirely of a fine two-phase mixture, which is the desired microstructure (Figure 2.11 (b)). The EDS analyses of the overall and phase compositions are given in Table 2.1, although the phases were too small to analyse accuratetly. The hardness are shown in Table 2.2. They also found that the alloys were reasonably ductile, although some of the hardness indentations exhibited some small cracks on the edges.

Table 2.1. Compositions of the Pt-Al-Ru-Cr alloys after heat treatment 1350°C for 96 hours [2002Cor].

Alloy Composition	Phase	Phase composition (at.%)			
		Pt	Al	Cr	Ru
Pt_{78}:$Al_{15.5}$:Ru_2:$Cr_{4.5}$	(Pt)	79.7 ± 0.5	8.4 ± 0.5	5.5 ± 0.5	6.5 ± 0.5
	~Pt_3Al	75.2 ± 0.3	20.5 ± 0.4	0.8 ± 0.2	3.5 ± 0.4
	(Pt)/ ~Pt_3Al	79.3 ± 0.5	10.6 ± 0.6	4..5 ± 0.4	5.6 ± 0.7
$Pt_{81.5}$:$Al_{11.5}$:$Ru_{2.5}$:$Cr_{4.5}$	~Pt_3Al	76.0 ± 0.1	20.9 ± 0.4	0.3 ± 0.3	2.8 ± 0.2
	(Pt)/ ~Pt_3Al	81.2 ± 0.5	11.6 ± 0.1	2.7 ± 0.3	4.5 ± 0.3
Pt_{84}:Al_{11}:Ru_2:Cr_3	(Pt)/ ~Pt_3Al	83.5 ± 1.3	11.3 ± 0.6	2.4 ± 0.5	2.8 ± 0.4

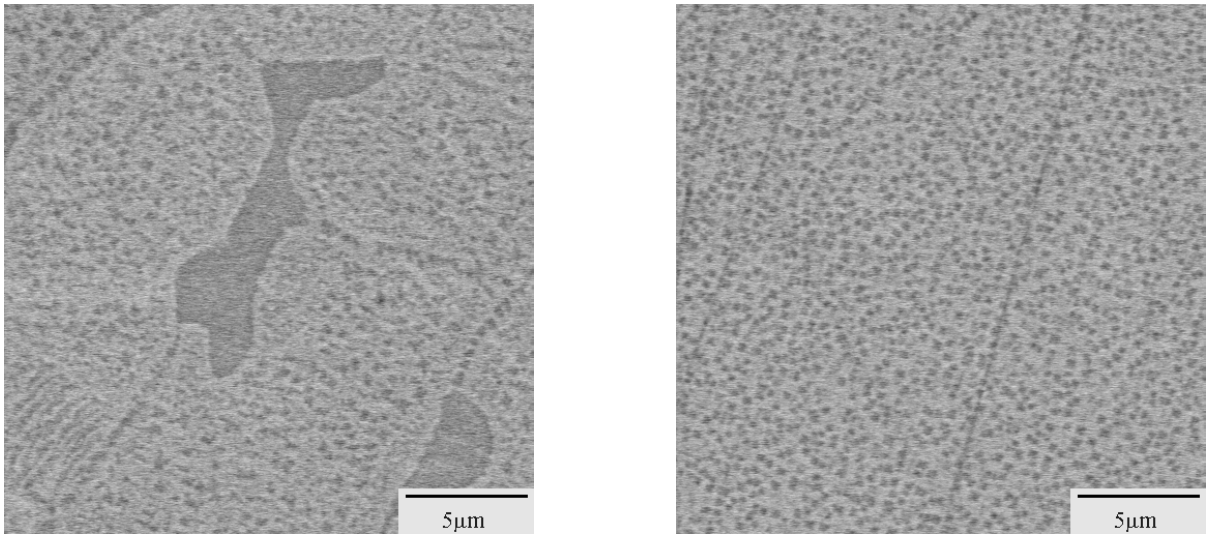

a) $Pt_{81.5}$:$Al_{11.5}$:$Ru_{2.5}$:$Cr_{4.5}$ **b) Pt_{84}:Al_{11}:Ru_2:Cr_3**

Figure 2.11. SEM micrographs, in back-scattered electron (BSE) mode, of the two types of two-phase alloys; a) with primary ~Pt_3Al (dark contrast) in a fine matrix of (Pt) (light) and ~Pt_3Al; b) Fine matrix of (Pt) and ~Pt_3Al [2002Cor].

Table 2.2. Vickers hardness of the two-phase quaternary alloys, using a 10 kg load [2002Cor].

Alloy Designation	Hardness (HV_{10})
Pt_{78}:$Al_{15.5}$:Ru_2:$Cr_{4.5}$	428 ± 11
$Pt_{81.5}$:$Al_{11.5}$:$Ru_{2.5}$:$Cr_{4.5}$	453 ± 16
Pt_{84}:Al_{11}:Ru_2:Cr_3	472 ± 14

Table 2.3. Compositions of the Pt-Al-Ru-Cr alloys after heat treatment 1350°C for 96 hours [2002Cor].

Alloy Composition	Phase	Phase composition (at.%)			
		Pt	Al	Cr	Ru
Pt_{85}:Al_{11}:Ru_2:Cr_2	~Pt_3Al	76.6 ± 0.4	21.8 ± 0.2	0.0 ± 0.0	1.6 ± 0.3
	(Pt)/ ~Pt_3Al	85.3 ± 0.3	10.1 ± 0.7	2.2 ± 0.1	2.4 ± 0.3
Pt_{84}:$Al_{11.5}$:Ru_2:$Cr_{2.5}$	~Pt_3Al	76.0 ± 0.5	22.2 ± 0.2	0.4 ± 0.4	1.4 ± 0.3
	(Pt)/ ~Pt_3Al	84.9 ± 0.6	10.1 ± 1.4	2.3 ± 1.1	2.7 ± 0.9
Pt_{83}:Al_{11}:$Ru_{2.5}$:$Cr_{3.5}$	~Pt_3Al	76.1 ± 0.8	21.4 ± 0.6	0.6 ± 0.6	1.9 ± 0.2
	(Pt)/ ~Pt_3Al	84.9 ± 0.4	9.5 ± 0.2	2.4 ± 0.3	3.2 ± 0.3
$Pt_{80.5}$:$Al1_{2.5}$:$Ru_{2.5}$:$Cr_{4.5}$	~Pt_3Al	75.9 ± 0.7	20.6 ± 0.6	0.8 ± 0.4	2.7 ± 0.4
	(Pt)/ ~Pt_3Al	81.6 ± 1.0	9.2 ± 1.2	3.9 ± 1.5	5.3 ± 0.7
$Pt_{81.5}$:$Al_{11.5}$:$Ru_{2.5}$:$Cr_{4.5}$	~Pt_3Al	76.3 ± 0.3	20.6 ± 0.1	0.5 ± 0.1	2.6 ± 0.2
	(Pt)/ ~Pt_3Al	83.0 ± 0.8	9.2 ± 0.4	3.1 ± 0.1	4.7 ± 0.4

Cornish, Hohls, Hill, Prins, Süss and Compton [2002Cor] produced more alloys to ascertain if the volume fraction of the ~Pt_3Al precipitates could be increased. Table 2.3 shows the EDS results that were found after heat treatment for 96 hours at 1350°C in argon. They found that only the Pt_{85}:Al_{11}:Ru_2:Cr_3 alloys had a clearly resolvable fine two-phase micorstructure, but there were also small areas of primary ~Pt_3Al. The hardness of the alloys are given in Table 2.4, and ranged from 417 to 430 HV_{10}. The alloys showed good ductility, with no cracking around the indentations. In an attempt to improve the microstructure of the second batch of alloys, a second heat treatment was conducted for 96 hours at 1350°C in air. For all but one of the alloys, there was no improvement. However, alloy $Pt_{81.5}$:$Al_{11.5}$:$Ru_{2.5}$:$Cr_{4.5}$ showed a clear, fine two-phase microstructure, possibly due to the change in its overall composition. There was no primary ~Pt_3Al in evidence, so the overall composition is that of the two-phase mixture. Since the overall composition changed, the sample was redesignated as Pt_{85}:Al_7:Ru_3:Cr_3. Figure 2.12 shows the microstructure of this alloy after the first and second heat treatments. The hardnesses were re-measured and are given in Table 2.5, and ranged from 396 to 415 HV_{10}. All samples were within the errors compared to the first anneal with

the exception of $Pt_{81.5}$:$Al_{11.5}$:$Ru_{2.5}$:$Cr_{4.5}$ which was slightly lower. Cornish *et al.* [2002Cor] concluded that it is possible to produce a fine two-phase γ/γ' structure in the Pt-Al-Ru-Cr system, with precipitates of similar shape to those in the nickel-based superalloys. The composition of Pt_{84}:Al_{11}:Ru_2:Cr_3 was found to be the optimum composition because it had no primary phase.

In another study by Cornish, Fischer and Völkl [2003Cor], heat treatments were conducted on the quaternary alloys at 1150°C, 1250°C, 1350°C, and 1450°C for 96 h to verify that the microstructure could be optimized. The highest temperature was the best for optimizing the fineness of the microstructure, which was so fine that it was difficult to distinguish the two phases, although X-ray diffraction proved the existence of the ~Pt_3Al phase [2003Cor].

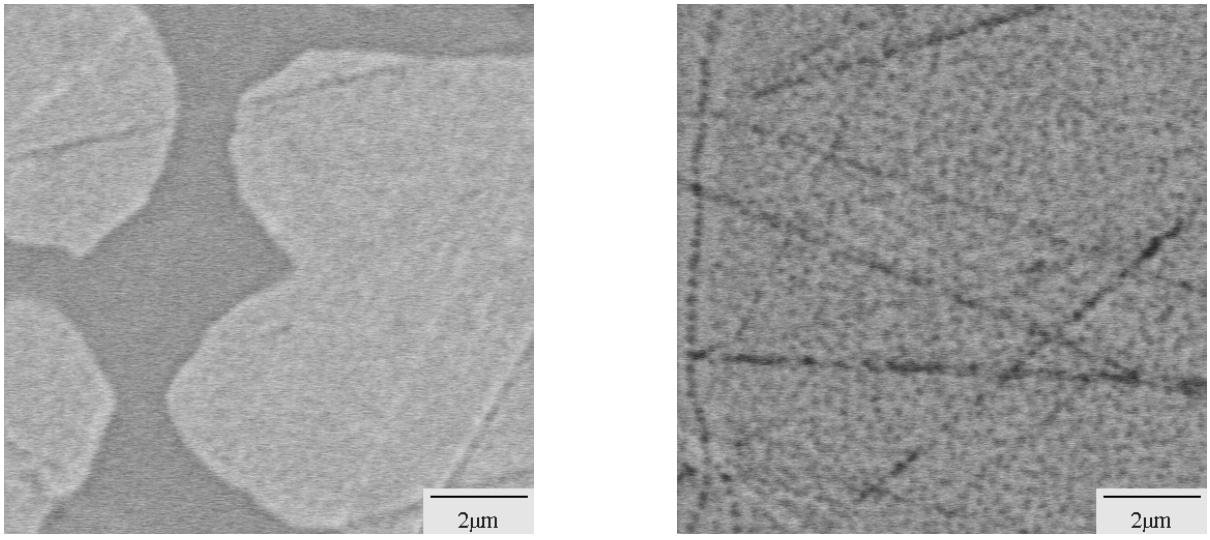

(a) First heat treatment $Pt_{81.5}$:$Al_{11.5}$:$Ru_{2.5}$:$Cr_{4.5}$

(b) Second heat treatment Pt_{85}:Al_7:Ru_3:Cr_5

Figure 2.12. SEM BSE micrographs of alloy $Pt_{81.5}Al_{11.5}Ru_{2.5}Cr_{4.5}$, a) (Pt) dendrites (light) with a (Pt) + ~Pt_3Al eutectic (dark) and b) ~Pt_3Al precipitates (dark) in a (Pt) matrix (light) [2002Cor].

Table 2.4. Vickers hardness of heat treated second batch of quaternary alloys, using a 10 kg load [2002Cor].

Alloy Designation	Hardness (HV10)
Pt_{85}:Al_{11}:Ru_2:Cr_2	430 ± 5
Pt_{84}:$Al_{11.5}$:Ru_2:$Cr_{2.5}$	425 ± 21
Pt_{83}:Al_{11}:$Ru_{2.5}$:$Cr_{3.5}$	421 ± 12
$Pt_{80.5}$:$Al1_{2.5}$:$Ru_{2.5}$:$Cr_{4.5}$	419 ± 22
$Pt_{81.5}$:$Al_{11.5}$:$Ru_{2.5}$:$Cr_{4.5}$	423 ± 10
$Pt_{79.5}$:$Al_{10.5}$:$Ru_{4.5}$:$Cr_{5.5}$	417 ± 8

Table 2.5. Vickers hardness of the second batch of quaternary alloys after the second heat treatement, using a 10 kg load [2002Cor].

Alloy Designation	Hardness (HV10)
Pt_{85}:Al_{11}:Ru_2:Cr_2	403 ± 20
Pt_{84}:$Al_{11.5}$:Ru_2:$Cr_{2.5}$	403 ± 14
Pt_{83}:Al_{11}:$Ru_{2.5}$:$Cr_{3.5}$	405 ± 8
$Pt_{80.5}$:$Al1_{2.5}$:$Ru_{2.5}$:$Cr_{4.5}$	414 ± 9
$Pt_{81.5}$:$Al_{11.5}$:$Ru_{2.5}$:$Cr_{4.5}$	396 ± 6
$Pt_{79.5}$:$Al_{10.5}$:$Ru_{4.5}$:$Cr_{5.5}$	415 ± 10

The effects of other additions are also being assessed. It must be noted that commercial NBSAs have at least 14 components, while the Pt-based alloys are based only on the quaternary Pt-Al-Cr-Ru. The Pt-Al-Co system was studied [2003Cho, 2004Cho], and Co additions were made to the quaternary alloy. The results show that Co does not appear to have any increased hardening effect, although there was no attempt to optimize the heat treatments [2003Cor]. Similarly, nickel was also purposely left out of the list of the ternary additions, because its lower melting point may lower the melting point range of the alloy. Subsequently, because nickel has such a good solid-solution strengthening effect on Pt [2001Zha], it was added to the quaternary alloy in varying amounts from 5 at.% to 50 at.%. The hardness increased with the nickel content but not as much as expected, and surprisingly, the melting points also increased [2003Cor].

Additionally, Pt-Rh-Zr alloys [2000Fai1, 2000Fai2] have been studied, although the microstructure needs optimizing. Pt-Rh-Hf alloys [2001Fai] have also been characterized and tested. Two-phase structures based on alloys of two composition ranges containing precipitates based on Rh_3Hf and γ' (~$Pt_{80}Hf_{20}$) have been studied, and mechanical properties are also very promising, although the oxidation properties were not good.

2.2.3.3 Development of Pt-Based Superalloys with Ni Additions

Work has also been done at the Universities of Jena and Bayreuth, Germany. In the investigations by Vorberg, Wenderoth, Fischer, Glatzel and R. Völkl [2004Vor, 2005Wen], alloys with $Pt_{75\text{-}81}$:$Al_{10\text{-}13}$:$Cr_{3\text{-}6}$:Ni_6, showed similar two–phase microstructures to the Pt–Al–Cr–Ru alloy and lattice misfits similar to conventional NBSAs. In a two–phase structure with cuboid and $L1_2$–ordered ~Pt_3Al precipitates of about 300nm size were generated by controlled cooling after homogenization heat treatment, Vorberg *et al.* [2004Vor] reported a ~Pt_3Al volume fraction of about 50% in an alloy with Pt_{76}:Al_{12}:Cr_6:Ni_6. The ~Pt_3Al

morphology varied between spherical and cuboid. The aluminum and nickel contents in the Pt–Al–Cr–Ni quaternary system were optimised to ensure a high ~Pt_3Al volume fraction and cuboid ~Pt_3Al morphology. Chromium increased the ~Pt_3Al volume fraction and decreased the absolute value of the lattice misfit between (Pt) and ~Pt_3Al. Partitioning of chromium to the (Pt) matrix in Pt–Al based alloys was found by several researchers [2001Hil2, 2005Wen]. The Goldsmith radius of chromium (0.125nm) is smaller than that of Pt (0.138nm) and aluminium (0.144nm). Therefore, increasing chromium content should more strongly decrease the lattice parameter of the matrix rather than that of the ~Pt_3Al phase, and hence decrease the absolute value of the lattice misfit. A similar influence on the misfit by adding nickel (atomic radius 0.124nm) to Pt–Al–Cr–Ni alloys was also found previously [2005Hül].

Vorberg *et al.* [2004Vor] also found that dendritic as-cast structures of $Pt_{78.5}$:$Al_{12.5}$:Cr_3:Ni_6, Pt_{82}:Al_{12}:Ni_6 and Pt_{76}:Al_{12}:Cr_6:Ni_6 could be homogenised by heat treatment at 1500 to 1510°C. Formation of ~Pt_3Al precipitates was almost completetly suppresed in $Pt_{78.5}$:$Al_{12.5}$:Cr_3:Ni_6 after homogenization for 12 hours at 1500°C and subsequent water quenching. Air cooling led to a homogenous distribution of ~Pt_3Al particles with 200nm average edge lengths and a volume fraction of 30%. The same alloy showed coarse particles after furnace cooling from 1500°C. The entire γ' volume fraction was 34%. Controlled air cooling after solution heat treatment was found sufficient to provoke a microstrcuture similar to nickel-based superalloys [2004Vor] and the same results were obtained previously by Vorberg *et al.* [2009Völ].

Völkl, Yamabe-Mitarai, Huang and Harada [2005Völ] also investigated the Pt-Al-Sc system. Heat treatment of samples for 48 hours at 1300°C followed by furnace cooling was found sufficient to homogenize dendritic segregation. In another set of samples heat treated at 1300°C for 96 hours in argon filled with quartz tubes, both the γ and γ' phases coarsened. Völkl *et al.* [2005Völ] concluded that to achieve fine γ' particles the samples had to be heat treated for 48 hours at 1300°C followed by water quenching [2005Völ].

Hüller, Wenderoth, Vorberg, Fischer, Glatzel and Völkl [2005Hül] investigated Pt-Al-Cr-Ni alloys with constant contents of 11 at.% Al and 3 at.% Cr. Nickel was added in various amounts as a potential solid solution strengthener, to lower density and price. Metallographic preparation was carried out by embedding samples in phenolic resin with carbon filler,

ground, and polished with diamond paste down to 1 µm grain size. Finally, the samples were electrolytically etched for 20 seconds with 5 V direct current in 5 % aqueous solution of potassium cyanide (KCN). Pt_{79}:Al_{11}:Cr_3:Ni_7 showed a very promising microstructure with a homogenous distribution of $L1_2$-ordered Pt_3Al precipitates of 200 - 500 nm and 23% volume fraction. The lattice misfit after aging for 120 hours at 1000°C was about -0.1%, i.e. in the same range as in commercial Ni-based superalloys.

Based on these results, studies were carried out by Wenderoth, Cornish, Süss, Vorberg, Fischer and Glatzel [2005Wen], to optimise the γ′ volume fraction and morphology by both higher Al content and higher solution heat treatment temperatures. Pt-based alloys with 14 at.% Al and 3 at.% Cr, and varying Ni contents were prepared. A two-step heat treatment was carried out. Samples were homogenised for 12 hours at 1500°C and quenched in water, followed by a precipitation heat treatment for 12 hours at 1000°C, also followed by water quenching. After quenching, evenly distributed γ′ particles of about 200nm were found in the γ matrix (Figure 2.13). The fine precipitates were apparently formed by secondary precipitation during cooling from the heat treatment at 1500°C. Subsequent aging at 1000°C for 120 hours led to different morphologies (Figure 2.14). In Pt_{79}:Al_{14}:Cr_3:Ni_4 and Pt_{77}:Al_{14}:Cr_3:Ni_6, a precipitate volume fraction of 30% was found, whereas in Pt_{75}:Al_{14}:Cr_3:Ni_8, 33% was detected. Even though the γ′ volume fractions in the alloys were comparable, the precipitate morphologies were quite different. Alloy Pt_{79}:Al_{14}:Cr_3:Ni_4 showed irregular shaped precipitates, whereas in alloy Pt_{77}:Al_{14}:Cr_3:Ni_6, cuboid and uniformly oriented γ′ precipitates were found. In contrast, Pt_{75}:Al_{14}:Cr_3:Ni_8, had mainly spherical precipitates (Figure 2.15). They found that the average precipitate sizes were larger than in Pt-Al-Cr-Ni alloys with 11 at.% [2005Hül], which showed maximum size of 100 - 500 nm after aging.

From this study, Wenderoth *et al*. [2005Wen] concluded that:

- Ni additions decreased the absolute lattice misfit in Pt-Al-Cr-Ni, in agreement with the results of Hüller *et al.* [2005Hül]
- Alloying Pt-Al based alloys with both Cr and Ni stabilised the $L1_2$ structure of Pt_3Al
- Interdendritic γ/γ′eutectics could be removed by solution heat treatments for 12 hours at 1500°C. Ageing for 12 hours at 1000°C led to a homogeneous distribution of the precipitates. Pt_{77}:Al_{13}:Cr_3:Ni_7 showed cuboid Pt_3Al precipitates with 520nm average

size, and a microstructure very close to that of conventional Ni-based superalloys [2005Wen].

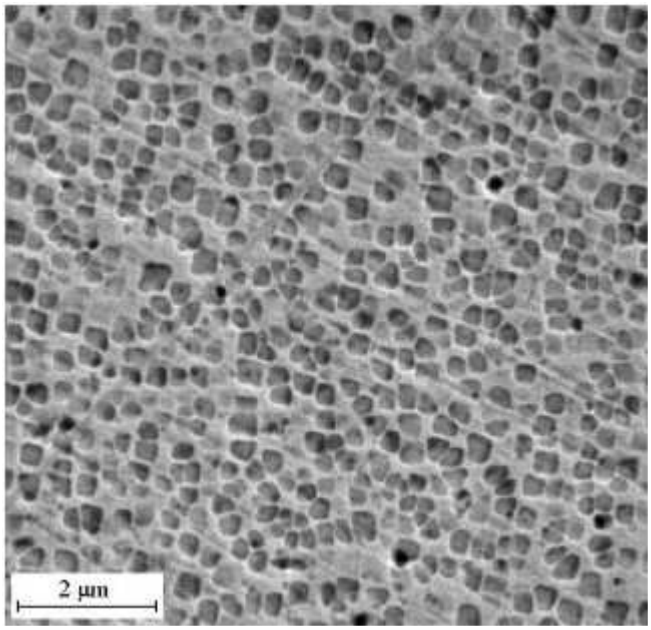

Figure 2.13. Secondary electron SEM micrograph of Pt_{77}:Al_{14}:Cr_3:Ni_6, after homogenisation for 12 h at 1500°C [2005Wen], showing ~Pt_3Al precipitates (dark) in a (Pt) matrix (light).

Further work has been done by Wenderoth, Völkl, Vorberg, Yamabe-Mitarai, Harada and Glatzel [2007Wen] on Pt-Al-Cr-Ni alloy with additions of 2 at.% Mo, Re, Ru and W. After the homogenisation heat treatment and air cooling, all alloys show a bimodal distribution of γ′ precipitates (Figure 2.16). Mo, Re, and W additions were found to increase strength above 1000°C, whereas Ru was found to have no beneficial effect on strength. W was found to increase the γ′ volume fraction most effectively. However, the oxidation resistance was worsened dramatically by W additions and Re-containing alloys showed the best resistance against γ′ growth and coarsening during long-term ageing [2007Wen].

2.2.3.4 The Pt-based Superalloys with Ir and Nb additions

The quaternary Ir–Nb–Pt–Al system has been studied by [2003Hua, 2004Hua1, 2004Hua2, 2005Hua]. An f.c.c/$L1_2$ two–phase structure exists in both Pt–Al and Ir–Nb binary systems and the lattice parameters of $L1_2$ phases (~Ir_3Nb and ~Pt_3Al) are similar. The solubility of Nb in the $L1_2$ – ~Pt_3Al phase could not be obtained directly in the Pt_{86}:Al_{10}:Nb_4 ternary alloy because of the small size of the phases. Nb and Ta have similar atomic radii to Al and similar

electronic structure (being in the same group in the periodic table), which should give similar solubility characteristics. The solubility of Ta in Pt_3Al was 5 at.%; accordingly, a similar solubility was expected for Nb. No phase transformation was detected [2004Hua2, 2005Hua], which indicated that the $L1_2$–Pt_3Al structure was stabilized to room temperature in the Ir–Nb–Pt–Al system, which was attributed to Nb.

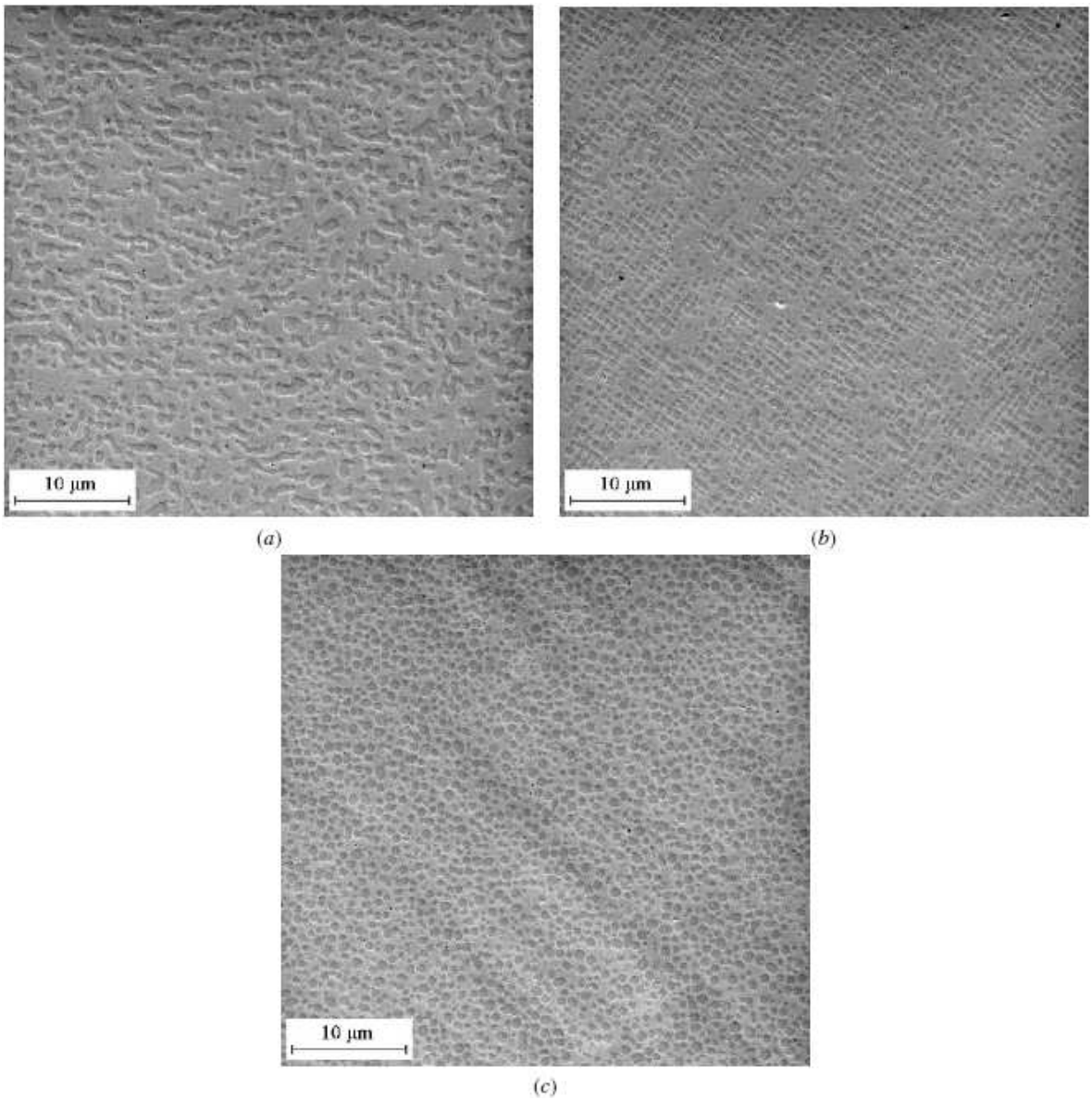

Figure 2.14. Secondary electron SEM micrographs (a) Pt_{79}:Al_{14}:Cr_3:Ni_4, (b) Pt_{77}:Al_{14}:Cr_3:Ni_6, (c) Pt_{75}:Al_{14}:Cr_3:Ni_8, after heat treatment for 12 h at 1500°C and 120 h at 1000°C in Ar, showing two-phase microstructures with evenly distributed ~Pt_3Al precipitates (dark) in a (Pt) matrix (light) [2005Wen].

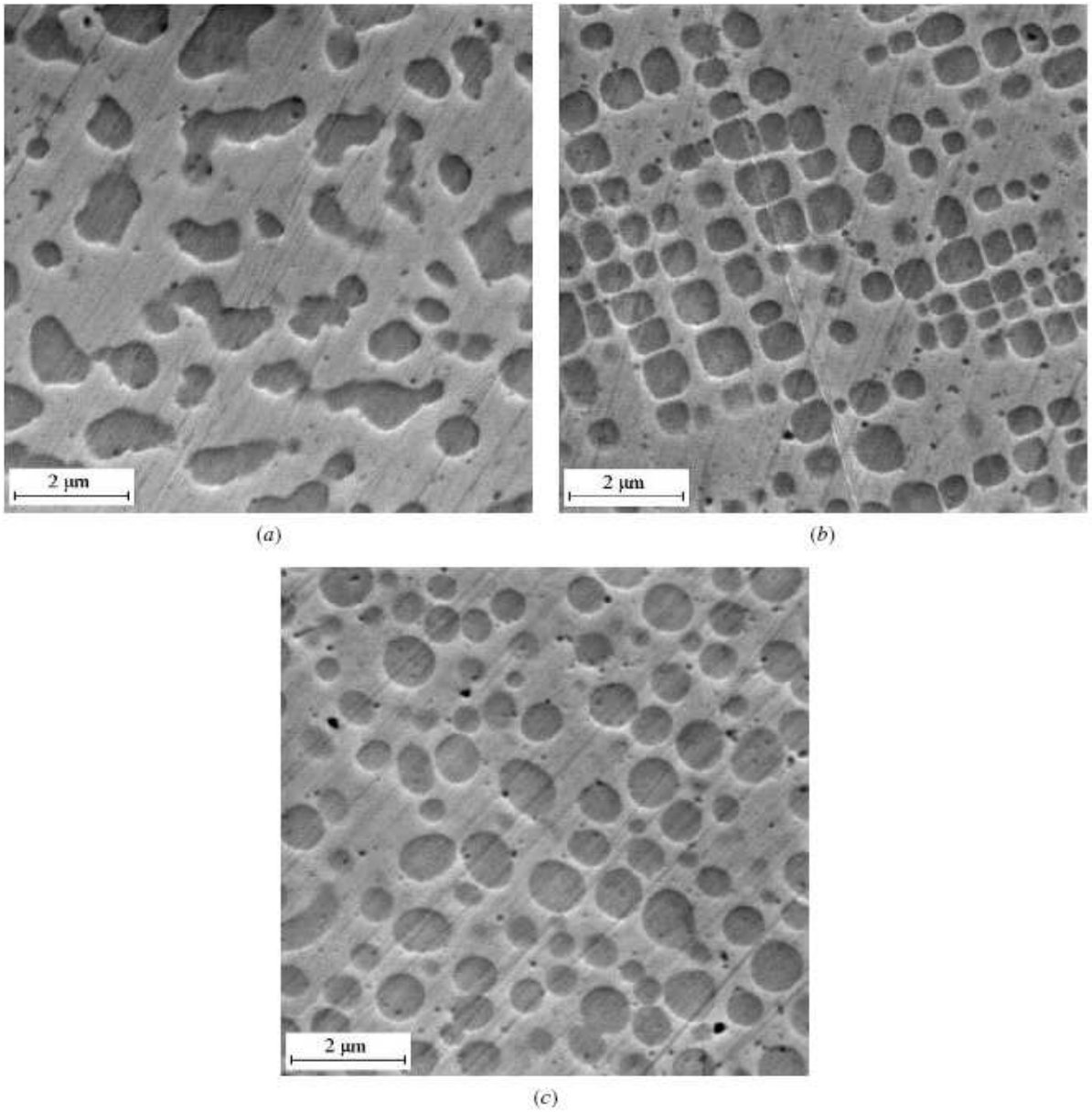

Figure 2.15. Secondary electron SEM micrographs of alloys annealed for 12 h at 1500°C and 120 h at 1000°C in Ar, showing ~Pt_3Al (dark) in (Pt) (light) two-phase microstructures (a) Pt_{79}:Al_{14}:Cr_3:Ni_4, (b) Pt_{77}:Al_{14}:Cr_3:Ni_6, and (c) Pt_{75}:Al_{14}:Cr_3:Ni_8 [2005Wen].

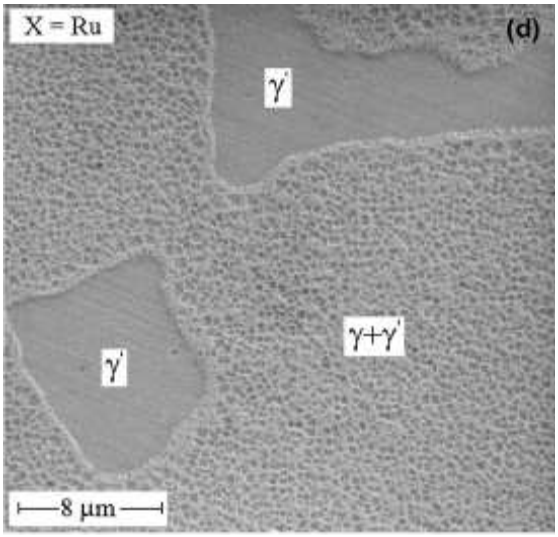

Figure 2.16. SEM SE micrograph of the γ/γ′ microstructure of Pt_{75}:Al_{12}:Cr_6:Ni_5:Ru_2 after homogenisation heat treatment, showing ~Pt_3Al (dark) and ~Pt_3Al precipitates in a (Pt) matrix [2007Wen].

2.2.3.5 Higher component Pt-Based Superalloys

Süss, Cornish, Douglas, Mwamba, Glaner, Chown and Williams [2006Süs] studied Pt_{79}:Al_{11}:Cr_3:Ru_2:Co_5 five-component and the Pt_{86}:Al_{11}:Cr_3:Ru_2 quaternary alloys. Samples were prepared and heat treated at 1350°C and 1400°C followed by cooling. Three different cooling methods were used in an attempt to achieve a high volume fraction of Pt_3Al precipitates: furnace cooling, air cooling and water quenching. The samples were then OPS-polished and examined using a High Resolution (HR) FEI Nova NanoSEM. Figures 2.17 and 2.18 show images of Pt_{79}:Al_{11}:Cr_3:Ru_2:Co_5 and Pt_{79}:Al_{11}:Cr_3:Ru_2:Co_5 after heat treatment at 1350°C and 1400°C, and cooling. Tables 2.6 and 2.7 summarize the observations that were made.

For the five-component alloy, Süss *et al.* [2006Süs] (Figures 2.17 and 2.18) to obtain a good volume fraction of precipitates less than 100 nm, air-cooling after annealing at 1400°C was the best. This agreed with the results from Bayreuth and Jena Universities [2004Vor]. A reasonable volume fraction of 100-200 nm precipitates was also obtained by furnace cooling from 1350°C. For the quaternary alloy, reasonable volume fractions of 100-200 nm particles were obtained after annealing and furnace or air cooling from 1350°C. Furnace cooling from both temperatures promoted the formation of ogdoadically-diced precipitates (like Maltese crosses) [1958Wes] in both alloys. This micorstructure gives less good properties [1987Sim]. Water quenching these alloys from either 1350°C or 1400°C yielded low volume fractions,

unless the precipitates were too small to be observed, and if this was the case, TEM was considered necessary for viewing of the precipitates. XRD confirmed the presence of (Pt) and ~Pt_3Al, without stating whether $L1_2$ or DO'_c - ~Pt_3Al was present.

Table 2.6. Comments regarding γ′ precipitate shape, size and volume fractions in annealed samples of Pt_{86}:Al_{11}:Cr_3:Ru_2 and Pt_{79}:Al_{11}:Cr_3:Ru_2:Co_5 at 1350°C [2006Süs].

	Alloy	
Cooling regime	***Pt_{79}:Al_{11}:Cr_3:Ru_2:Co_5***	***Pt_{86}:Al_{11}:Cr_3:Ru_2***
Furnace cooled	150-200 nm precipitates regular distribution decent vol. %	Bimodal distribution: Small cuboidal: <50 nm Octoadically-diced: ~250-300 nm decent vol. %
Air cooled	~150 nm precipitates regular distribution	Mixed size distribution: 110-200 nm (average ~150 nm) decent vol. %
Water quenched	~50 nm precipitates Very low vol. %	50-100 nm Low vol. %

Table 2.7. Comments regarding γ′ precipitate shape, size and volume fractions in annealed samples of Pt_{86}:Al_{11}:Cr_3:Ru_2 and Pt_{79}:Al_{11}:Cr_3:Ru_2:Co_5 at 1400°C [2006Süs].

	Alloy	
Cooling regime	***Pt_{79}:Al_{11}:Cr_3:Ru_2:Co_5***	***Pt_{86}:Al_{11}:Cr_3:Ru_2***
Furnace cooled	Bimodal distribution: cuboidal: <100 nm - 300 nm Octoadically diced: ~1 μm	300-350 nm precipitates Few ogdoadically diced
Air cooled	50-100 nm High vol. %	50-100 nm Very very small vol. %
Water quenched	~50 nm precipitates Very low vol. %	50-100 nm Very low vol. %

Cooling regime	***Pt_{79}:Al_{11}:Cr_3:Ru_2:Co_5***	***Pt_{86}:Al_{11}:Cr_3:Ru_2***
Furnace cooled	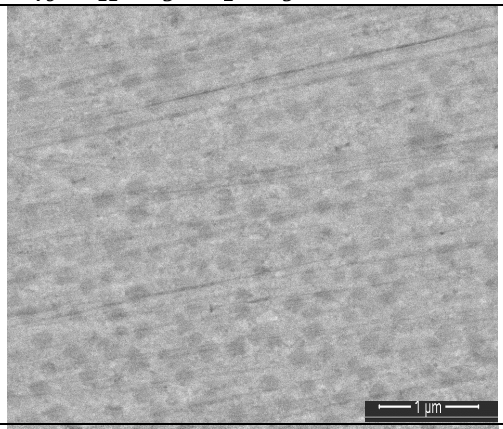	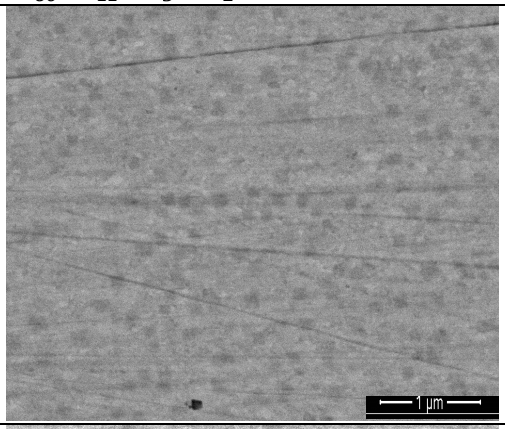
Air cooled	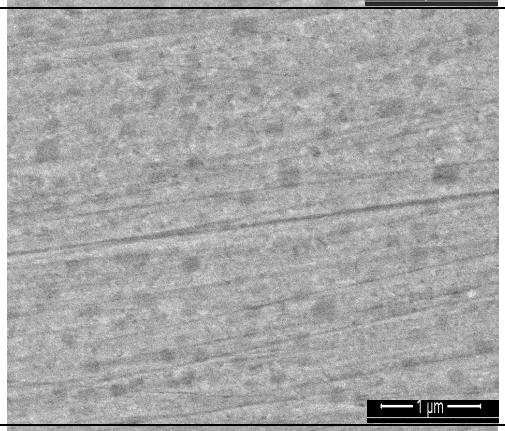	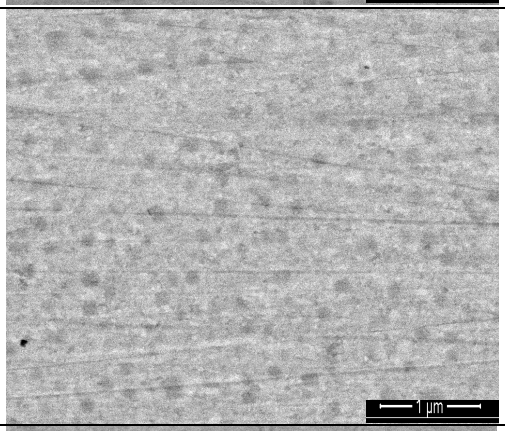
Water quenched	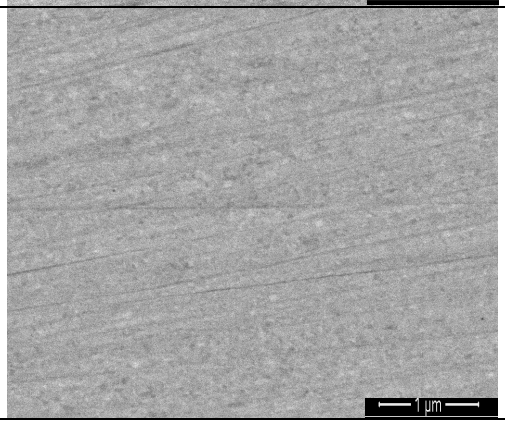	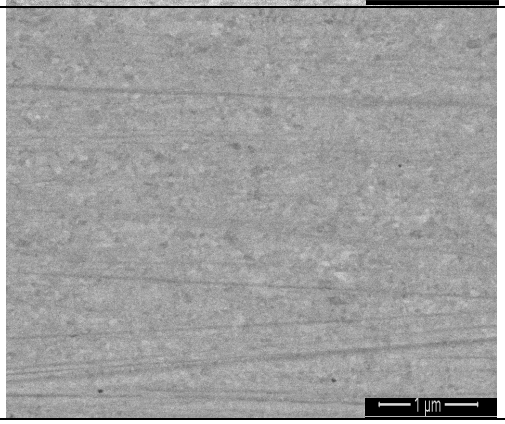

Figure 2.17. BSE HR-SEM images of Pt_{86}:Al_{11}:Cr_3:Ru_2 and Pt_{79}:Al_{11}:Cr_3:Ru_2:Co_5 after heat treatment at 1350°C with different cooling rates [2006Süs], showing ~Pt_3Al precipitates (dark) in a (Pt) matrix (light).

Cooling regime	$Pt_{79}:Al_{11}:Cr_3:Ru_2:Co_5$	$Pt_{86}:Al_{11}:Cr_3:Ru_2$
Furnace cooled	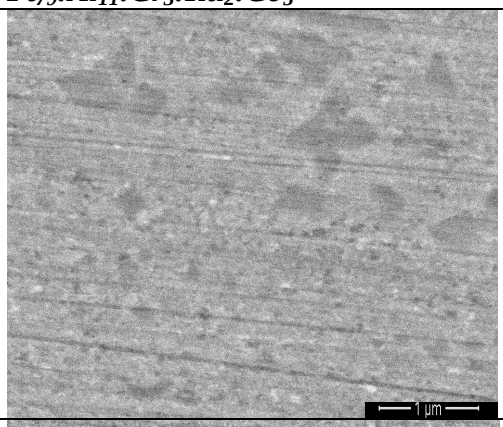	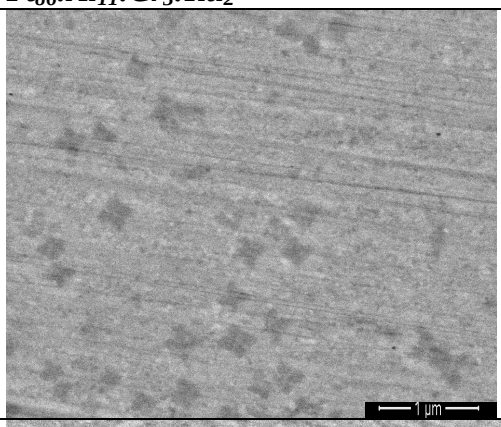
Air cooled	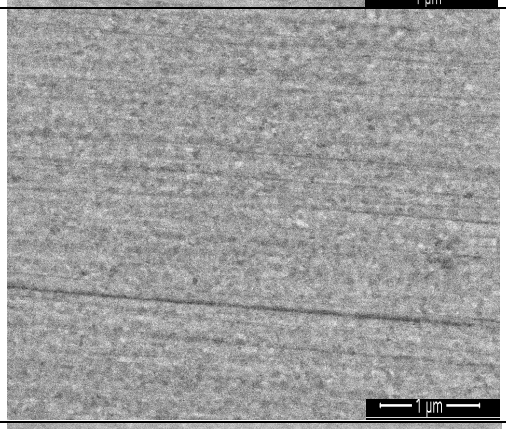	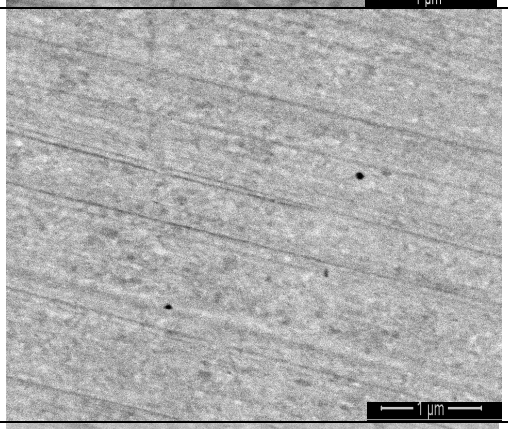
Water quenched	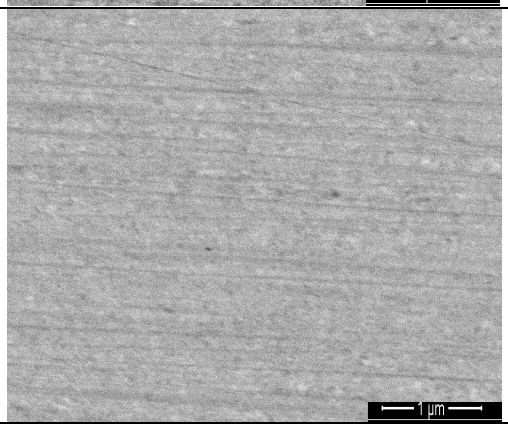	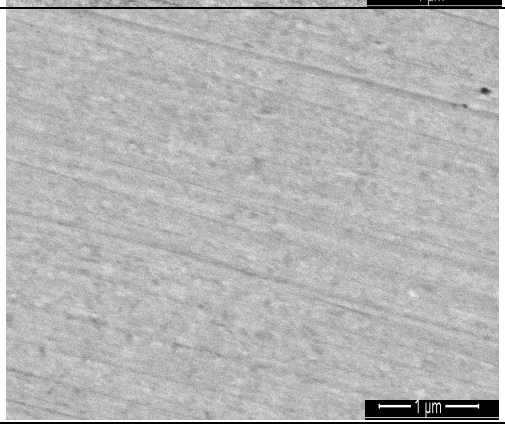

Figure 2.18. BSE HR-SEM images of $Pt_{86}:Al_{11}:Cr_3:Ru_2$ and $Pt_{79}:Al_{11}:Cr_3:Ru_2:Co_5$ after heat treatment at 1400°C with different cooling rates [2006Süs], showing ~Pt_3Al precipitates (dark) in a (Pt) matrix (light).

The most recent work on the platinum-based superalloys was carried out at Mintek by Marekwa, Cornish and Süss [2007Mar], on the $Pt_{81.5}$:$Al_{11.2}$:$Ru_{2.5}$:Cr_3:$B_{0.3,}$ Pt_{78}:$Al_{15.2}$:Ru_2:$Cr_{4.5}$:$B_{0.3}$ and Pt_{80}:$Al_{13.7}$:Ru_3:Cr_3:$B_{0.3}$ alloys. The work was aimed at assessing the influence of boron additions on the microstructures in the as-cast and heat treated conditions. Samples were manufactured, then cut in half. One half was analysed in the as-cast condition and the other half heat treated at 1500°C then quenched in water, followed by heat treating at 1100°C for 120 hours then air-cooled. The samples were then OPS-polished and examined using a High Resolution (HR) FEI Nova NanoSEM equipped with an EDX system. XRD was also carried out and confirmed the presence of γ (Pt) and γ′ Pt_3Al phases in all alloys for both conditions.

The results are shown in Figures 2.19 to 2.24 [2007Mar], and all as-cst samples consisted of light (Pt) dendrites with an interdendritic eutectic of (Pt) + ~Pt_3Al. Lighter regions were also observed in the dendrites. $Pt_{81.5}$:$Al_{11.2}$:$Ru_{2.5}$:Cr_3:$B_{0.3}$ and Pt_{80}:$Al_{13.7}$:Ru_3:Cr_3:$B_{0.3}$ had precipitates within the dendrites. All heat treated samples contained ~Pt_3Al precipitates in a matrix of (Pt) (Figures 2.22 to 2.24), and the microstructures only differed in the precipitate proportions. Pt_{78}:$Al_{15.2}$:Ru_2:$Cr_{4.5}$:$B_{0.3}$ had the highest proportion of precipitates followed by $Pt_{81.5}$:$Al_{11.2}$:$Ru_{2.5}$:Cr_3:$B_{0.3}$ and Pt_{80}:$Al_{13.7}$:Ru_3:Cr_3:$B_{0.3}$ had the least. ~Pt_3Al precipitated on the grain boundaries for Pt_{78}:$Al_{15.2}$:Ru_2:$Cr_{4.5}$:$B_{0.3}$. The precipitates were rounded in shape.

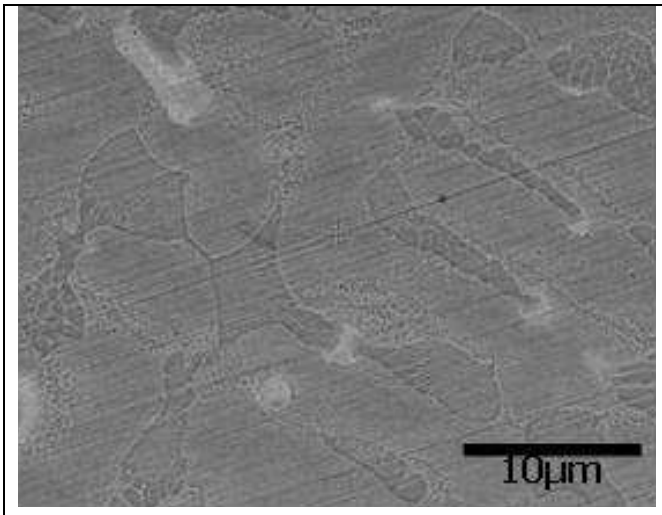

Figure 2.19. HR-SEM-BSE image of $Pt_{81.5}$:$Al_{11.2}$:$Ru_{2.5}$:Cr_3:$B_{0.3}$ in the as-cast condition, showing (Pt) dendrites (medium light) with ~Pt_3Al precipitates and lighter stained regions, and interdendritic eutectic of (Pt) + ~Pt_3Al (dark) [2007Mar].

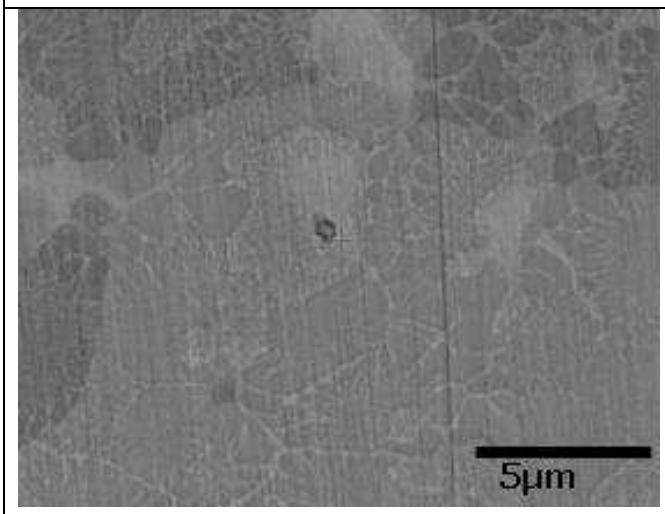

Figure 2.20. HR-SEM-BSE image of Pt_{78}:$Al_{15.2}$:Ru_2:$Cr_{4.5}$:$B_{0.3}$ in the as-cast condition, showing coarsened ((Pt) + ~Pt_3Al) (dark) and discrete (Pt) phase (medium light) [2007Mar].

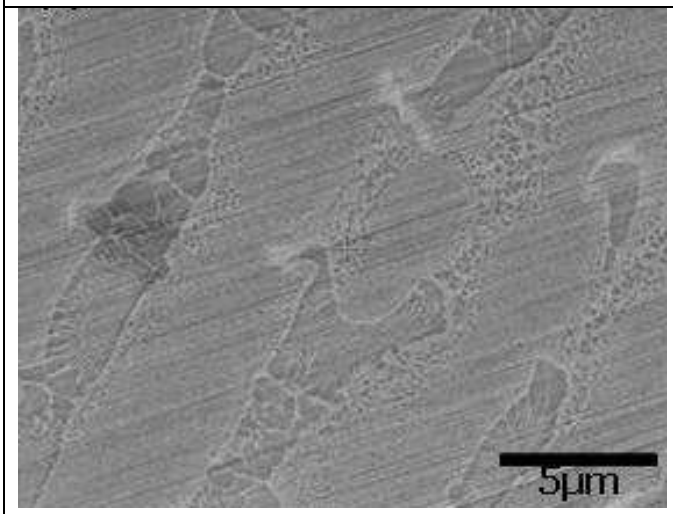

Figure 2.21. HR-SEM-BSE image of Pt_{80}:$Al_{13.7}$:Ru_3:Cr_3:$B_{0.3}$ in the as-cast condition, showing (Pt) dendrites (medium light) with ~Pt_3Al precipitates and a eutectic of (Pt) + ~Pt_3Al (dark) [2007Mar].

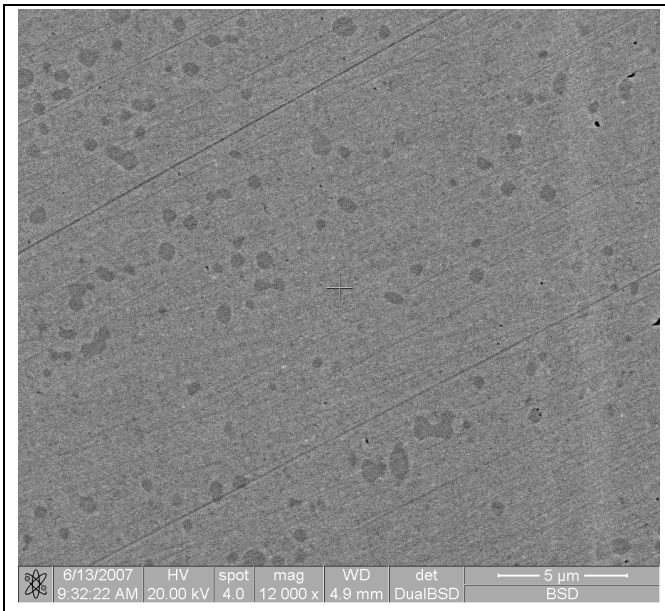

Figure 2.22. HR-SEM-BSE image of $Pt_{81.5}:Al_{11.2}:Ru_{2.5}:Cr_3:B_{0.3}$ heat treated at 1500°C and quenched in water followed by heat treating at 1100°C for 120 hours then air-cooled, showing fewer and coarse ~Pt_3Al precipitates (dark) in a (Pt) matrix (light) [2007Mar].

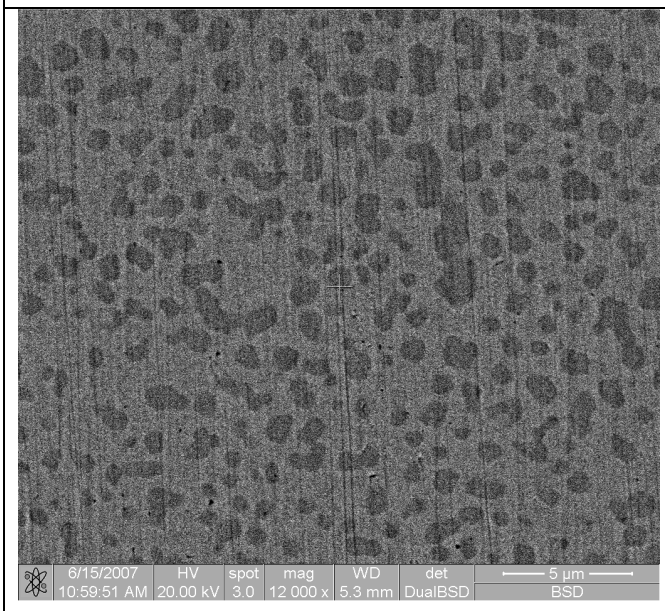

Figure 2.23. HR-SEM-BSE image of $Pt_{78}:Al_{15.2}:Ru_2:Cr_{4.5}:B_{0.3}$ heat treated at 1500°C and quenched in water followed by heat treating at 1100°C for 120 hours then air-cooled, showing ~Pt_3Al precipitates (dark) in a (Pt) matrix (light) [2007Mar].

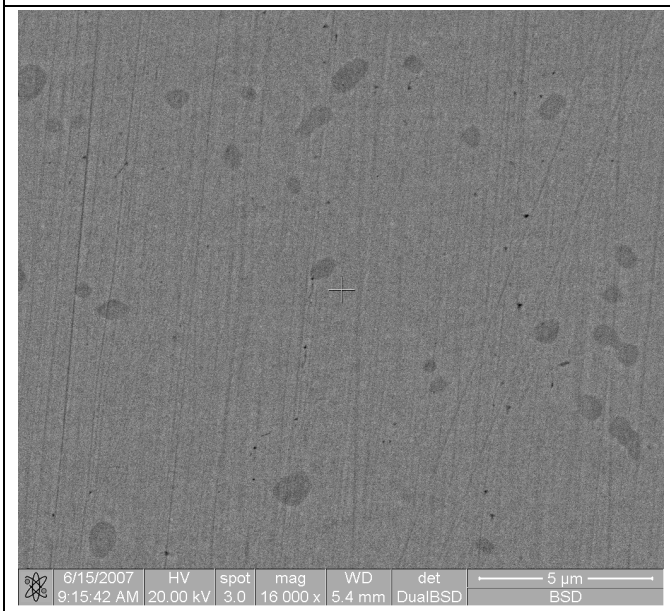

Figure 2.24. HR-SEM-BSE image of $Pt_{80}:Al_{13.7}:Ru_3:Cr_3:B_{0.3}$ heat treated at 1500°C and quenched in water followed by heat treating at 1100°C for 120 hours then air-cooled, showing very few and coarse ~Pt_3Al precipitates (dark) in a (Pt) matrix (light) [2007Mar].

2.2.3.6 Rationale of this Investigation

Alloys based on platinum-group metals, namely, Pt, Ir, and Rh, have exhibited two phase structures that are analogous to nickel-based superalloys. The results so far are very promising, in that good mechanical properties have been attained at higher temperatures than is possible with NBSAs. Additionally, the misfit between the precipitates and the matrix indicates that the selected microstructures should be very stable and not coarsen too much at high temperatures. However, Cornish *et al.* [2007Cor] found that binary Pt_3Al precipitates coarsened, and so required alloying additions to stabilise the precipitates. Thus, although the research is still at a very early stage, the results are very promising [2003Cor]. The work at Mintek has shown the potential of the Pt-based superalloys for high temperature applications, and current work is concentrating on Pt-Al-Cr-Ru quaternary alloys, which is the alloy of interest for this investigation. Increased research efforts in this area are warranted, since thorough characterizations of platinum alloys will assist future development for current and future application needs [2001Hil5].

From an economical point of view, cost can be significantly discounted when it is appreciated that precious metals invariably re-enter the secondary market by means of recycling, and the real cost is only the interest lost due to holding the metal plus the recycling cost. Perhaps two more serious constraints worth factoring in are: (1) the limited physical supply of certain platinum group metals (notably Ir and Rh), which limits their use in large-scale bulk applications, and (2) the necessity of possible new processing techniques [2000Wol]. The major disadvantages of the Pt-based superalloys are higher price and density than NBSAs. Although much heavier, the Pt–based alloys have the advantage of higher temperature application which is important for improved efficiency of turbine engines, greater thrust, fuel efficiency, and reduced pollution. Secondly, the Pt-based superalloys have good mechanical properties and high temperature oxidation resistance [2001Süs1, 2006Mal]. Considering these two points, the Pt-based superalloys could be useful, especially if turbine jet engines could be redesigned to accommodate denser materials. Other additions are being considered in order to decrease both the density and the cost of the alloys. Process metallurgy has lagged behind alloy development, and high-volume component production of these high-melting point compounds has to improve before it becomes an industrial reality [2000Wol].

CHAPTER THREE

EXPERIMENTAL PROCEDURE

3.1 Manufacture

Alloy buttons of mass 2g were prepared from pellets and chunks of the respective elements. The purity of the Pt, Al, Cr and Ru was at least 99.9 %. The combined elements were melted in an arc-furnace in an Ar atmosphere on a water-cooled copper hearth. Before each button melt took place, a button of Ti was melted, which acted as an O_2 scavenger. Each button was turned over and re-melted at least two times to ensure thorough mixing of the elements. The alloys were named according to their nominal compositions in atomic percent. The as-cast alloy buttons were cut into two halves using a STRUERS automatic cutting machine with an Accutom® cutting wheel.

3.2 Sample Annealing

The other halves were homogenized in air in a Lenton muffle furnace at 1500°C for 18 hours and quenched in water, followed by a heat treating at 1100°C for 120 hours then air cooled.

3.3 Metallographic Preparation

Both halves of each sample were prepared for metallographic examination. Samples were mounted and ground to 1200 grit on SiC paper. The samples were then polished using diamond impregnated clothes of 3µm down to 1µm followed by an oxide polishing (OP-S) system. In the OP-S system, polishing is achieved through a combination of chemical treatment (the solution has a pH of 8) and gentle abrasive action, and it allows selective polishing of the softer phases and makes subsequent etching of the sample superfluous.

3.4 Sample Characterisation

3.4.1 Scanning Electron Microscopy (SEM) – Microstructure

The microstructures of the alloys were initially examined in a JEOL 840 SEM operated at 20kV, then an FEI Nova NanoSEM with an operating voltage of normally 20kV and a working distance of approximately 6mm for imaging. All micrographs were taken in

backscattered electron (BSE) mode, so that phases with lower average atomic numbers could be identified by their darker contrasts than those with a higher average atomic number. Table 3.1 shows the atomic numbers of the elements and major phases in the high Pt-content Pt-Al-Cr-Ru quaternary alloys of this study. The precipitate volume fractions were derived from counting the precipitates that were on the nodes of 10 grid placements, since the contrast of the phases was not sufficient for image analysis.

All the compositions reported are in atomic percent (at.%), and were obtained in the FEI Nova Nano HR-SEM by energy dispersive X-ray spectroscopy (EDS) where each analysis took 100 seconds. The analyses quoted are the average of at least four determinations on different areas. The error in the compositions was typically in the first decimal place. Where the error was greater, it was probably due to the electron beam scattering into a neighbouring phase.

Table 3.1. Atomic numbers of the elements and major phases in the Pt-Al-Cr-Ru quaternary alloys studied.

Element/Phase	Atomic Number
Al	13
Cr	24
Ru	44
Pt	78
(Pt)	78
Pt_3Al	62

3.4.2 X–ray Diffraction

X-ray diffraction (XRD) was used to confirm the phases identified. The spectra were obtained on a Philips PW 1710 diffractometer. A Cu-Kα source with a tube current and voltage of 20mA and 40kV respectively was employed, and the sample was rotated through a 2θ angular range from 10° to 100°. The step size was $0.020°.s^{-1}$ with intensity collected for 1s per step. Spectra analysis was done using X′Pert HighScore Philips Software. Phases were identified by comparison with the ICDD database [2003Xpe]. The reference stick pattern, peak list and lattice parameters for each of the pure phases are shown in Appendix B.

3.5 Mechanical Tests

Hardness measurements on both as-cast and heat treated samples were carried out on a Vickers hard tester using a 10kg load. The analyses quoted are the average of at least five determinations on different areas. Photographs of the hardness indentions were taken using an optical microscope to obtain a qualitative evaluation of the alloys' toughness and where possible, slipping modes.

3.5.1 Correlation Between Hardness and Yield Strength

Hardness covers several properties: resistance to deformation, and is an indication of resistance to abrasion. However, hardness number is not really a true property of the material and is an empirical value that should be seen in conjunction with the experimental methods and hardness scale used. A correlation may be established between hardness and some other material property such as yield strength. The yield strength may be estimated based on hardness test results, which are much simpler to obtain. This correlation depends upon specific test data and cannot be extrapolated to include other materials not tested. The yield strength of the material can be approximated as [1962McL, URLHar]:

$$\sigma_y = C \times HV \qquad 1$$

Where:

σ_y = yield strength (MPa).

C = constant determined by geometrical factors usually ranging between 2 and 4.
HV = Vickers hardness number (MPa).

The Vickers hardness number from experimental results is normally in kg/mm^2 and 1 kg/mm^2 = 9.807 MPa. Taking into account geometrical factors, Equation 1, becomes:

For HV $\leq$ 175 MPa: $\sigma_y = 3.55 \times HV$ 2

For HV > 175 MPa.: $\sigma_y = 3.38 \times HV$ 3

CHAPTER FOUR

RESULTS

4.1. First Batch of Samples

Initially, microstructural analysis of the first batch of as-cast samples were carried out in a JEOL 840 SEM, but the resolution was not sufficient to discern the finest particles. When the High Resolution (HR) FEI Nova NanoSEM became available, it was used for all samples.

Mass losses after melting were monitored, and were found to be within acceptable limits, of less than 2 %, and only one alloy showing a mass loss greater than 1 % (Table 4.1). The Pt_{78}:$Al_{15.5}$:Ru_2:$Cr_{4.5}$ showed the highest mass loss during melting (1.5 %), and comparisons of EDX measurents confirmed this, since the Al was less than planned in all cases where there was mass loss.

Table 4.1. Actual mass of samples before and after melting and % weight loss.

Alloy	Unmelted (g)	Melted (g)	% Weight Loss
Pt_{78}:$Al_{15.5}$:Ru_2:$Cr_{4.5}$	2.0006	1.9708	1.5
Pt_{80}:Al_{14}:Ru_3:Cr_3	2.0001	1.9858	0.7
Pt_{81}:$Al_{11.5}$:$Ru_{2.5}$:$Cr_{4.5}$	1.9998	1.9859	0.7
Pt_{82}:Al_{12}:Ru_2:Cr_4	2.0006	1.9895	0.6
Pt_{84}:Al_{11}:Ru_2:Cr_3	1.9999	1.9827	0.9
Pt_{85}:Al_7:Ru_3:Cr_5	2.0006	1.9847	0.8

4.1.1 As-cast Alloys: Microstructural Characterisation

4.1.1.1. Nominal Pt_{78}:$Al_{15.5}$:Ru_2:$Cr_{4.5}$

HR-SEM-BSE images in the as-cast condition are shown in Figure 4.1, taken at different areas of the alloy. Figure 4.1 (a) shows that the alloy has different areas that differ in contrast, due to different grain orientation. Some scratches can be seen on the microstructure, sample preparation was improved by carrying out polishing for longer times but still showed many scratches. However, this was still not removing the earlier damage. Both the edge and centre consisted of the (Pt) phase with a eutectic-like mixture of (Pt) + ~Pt_3Al (Figures 4.1 (b) and

(c)). Fine ~Pt_3Al precipitates can be seen in the outside of the dendrites (Figure 4.1 (c)). The proportion of the dendrites was 54 ± 10% of the microstructure. The average dendrites arm spacing was about 9.2 ± 1.5 µm.

The phase compositions are shown in Table 4.2. A decrease in Al was observed, due to losses by evaporation during melting. Ru and Cr had limited solubility in the ((Pt) + ~Pt_3Al) eutectic, and partitioned almost exclusively to (Pt). The composition of the dendrite edges with larger precipitates was close to the overall alloy composition, and there was slightly lower solubility of Ru and Cr compared to the dendrites centres with smaller precipitates. The standard deviation was well below 1 % for all the phases. The apparent lighter phase in the dendrites was too small for reliable EDX analysis.

Table 4. 2. EDX Phase compositions of nominal Pt_{78}:$Al_{15.5}$:Ru_2:$Cr_{4.5}$ in the as-cast condition.

Phase description	Al	Ru	Cr	Pt	Phase
Overall	11.5 ± 0.7	1.7 ± 0.8	4.1 ± 0.5	82.7 ± 0.6	-
Eutectic (Dark)	19.5 ± 0.4	0.7 ± 0.0	2.2 ± 0.2	77.6 ± 0.3	(Pt) + ~Pt_3Al
Dendrites (Light)	9.6 ± 0.7	1.7 ± 0.2	5.4 ± 0.3	83.3 ± 0.4	(Pt) + ~Pt_3Al
Dendrites + Visible precipitates	12.6 ± 0.5	1.1 ± 0.3	4.5 ± 0.6	81.8 ± 0.8	(Pt) + ~Pt_3Al

Although the microstructure was more difficult to discern than the other alloys, the XRD spectrum (Figure 4.5) confirmed the presence of ~Pt_3Al and (Pt). Both forms of ~Pt_3Al (the tetragonal and cubic) were checked in XRD. Figures 4.2 to 4.4 show the experimental spectrum of the sample with the database lines [2003Xpe] for each of the phases. Peak shifting was observed relative to the pattern lines of the pure phases. The (Pt) peaks shifted to the right. Tetragonal DO'_c - ~Pt_3Al had peaks shifting in both directions (left and right) relative to pure DO'_c - ~Pt_3Al. This is allowed since the structure is tetragonal. $L1_2$ - ~Pt_3Al also apparently had shifting in both directions relative to pure $L1_2$ - ~Pt_3Al lines, which is not possible for a cubic phase which can only change its spacings in the same direction. The highest intensity peak at about $2\theta = 46°$ shows that the peak is a probable combination of the (Pt) and DO'_c - ~Pt_3Al lines. The second highest intensity peak ($2\theta = 39°$) is also probably a combination of the (Pt) and DO'_c - ~Pt_3Al lines to give a higher intensity. The third highest intensity peak ($2\theta = 81°$) shows similar behaviour. All peaks could be matched without

including the $L1_2$ - ~Pt_3Al. Thus, it is unlikely that $L1_2$ - ~Pt_3Al is present in the sample. Table 4.3 contains the identified peaks together with the d-spacings.

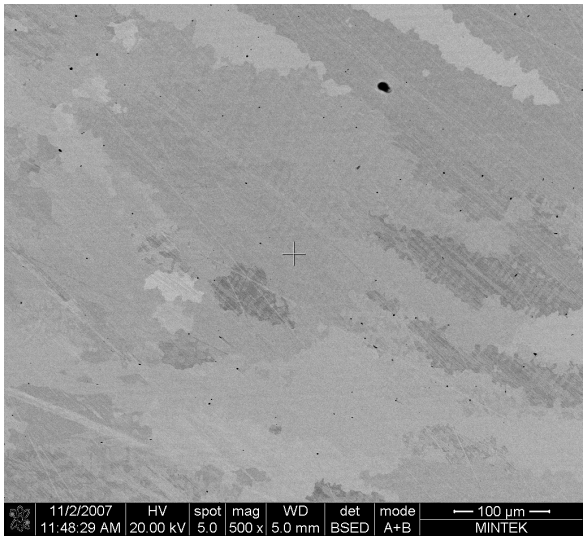

(a)

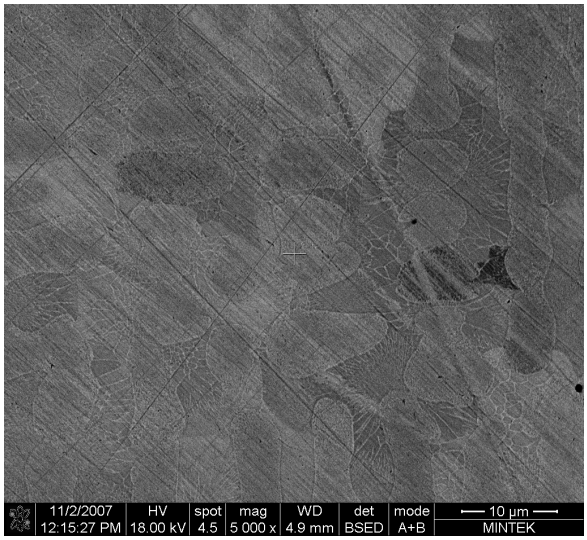

(b)

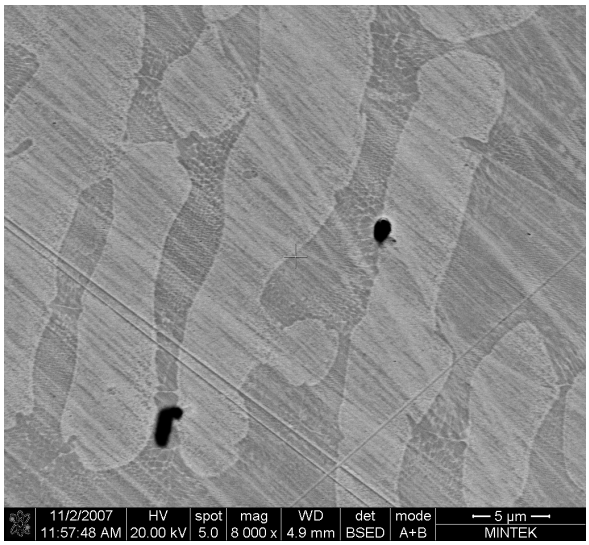

(c)

Figure 4.1. HR-SEM-BSE image of nominal Pt_{78}:$Al_{15.5}$:Ru_2:$Cr_{4.5}$, as-cast condition, showing different orientations of grains (a), and (b) and (c) taken from the edge and centre showing (Pt) dendrites (light) with fine ~Pt_3Al precipitates and a eutectic of (Pt) + ~Pt_3Al (dark).

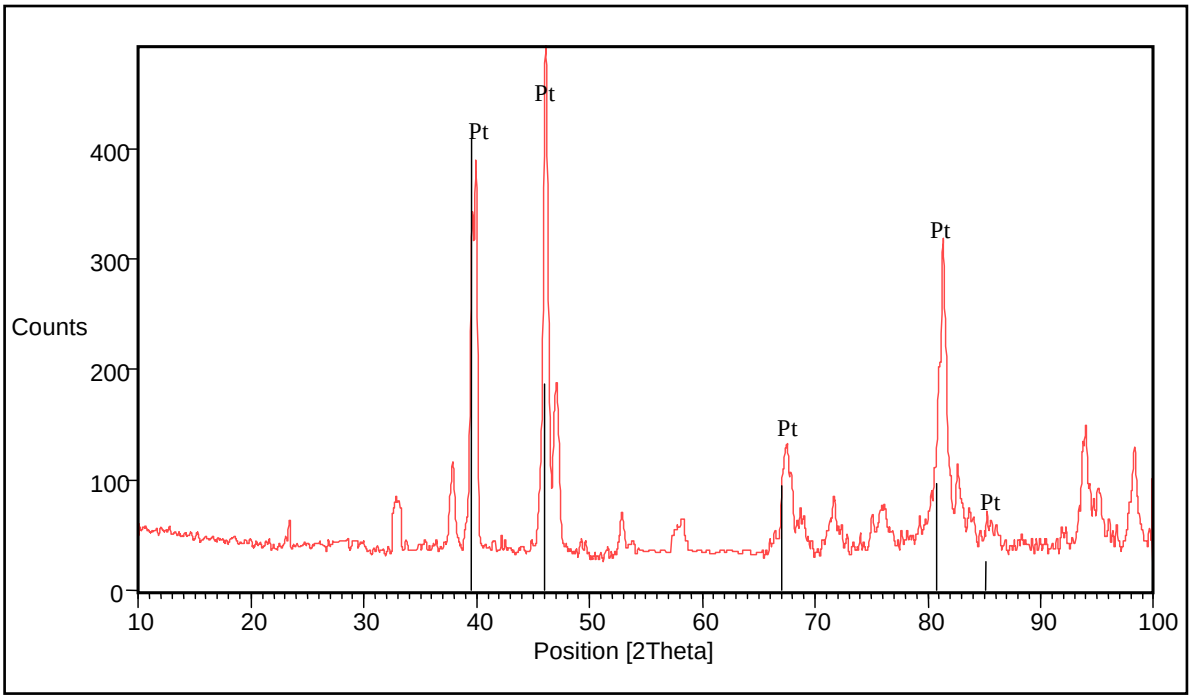

Figure 4.2. XRD Pattern of nominal $Pt_{78}:Al_{15.5}:Ru_2:Cr_{4.5}$ in the as-cast condition, showing identified Pt peaks.

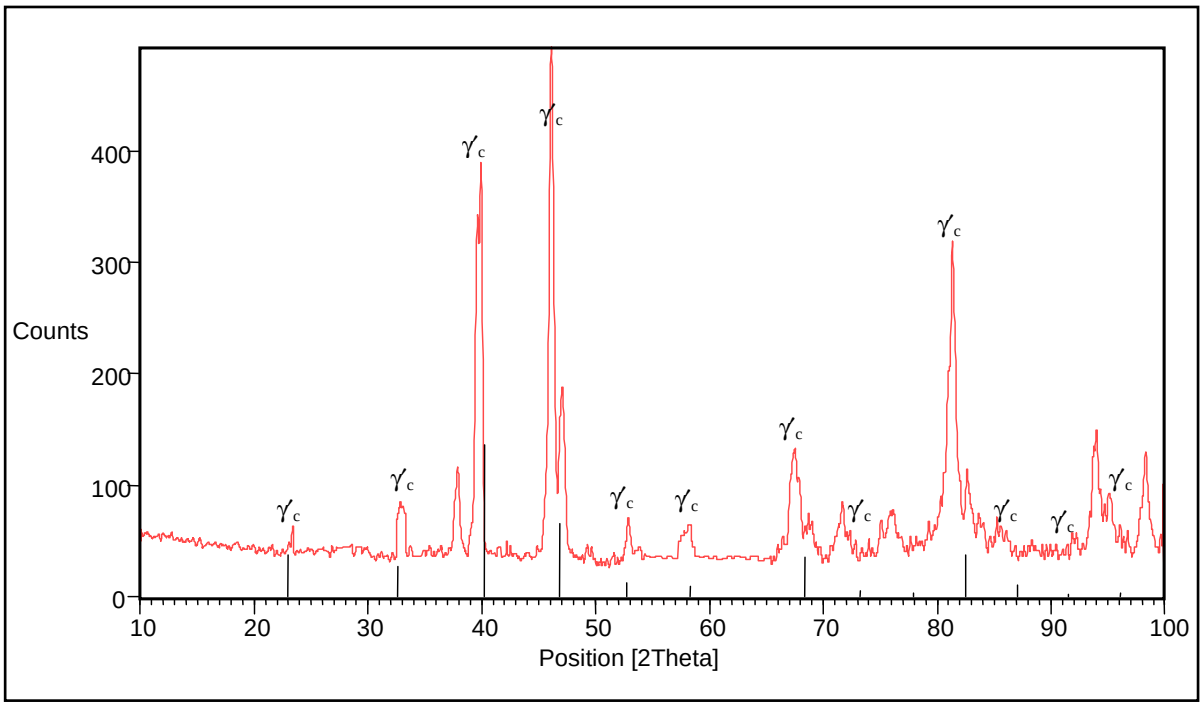

Figure 4.3. XRD Pattern of nominal $Pt_{78}:Al_{15.5}:Ru_2:Cr_{4.5}$ in the as-cast condition, showing apparent $L1_2$ – ~Pt_3Al peaks.

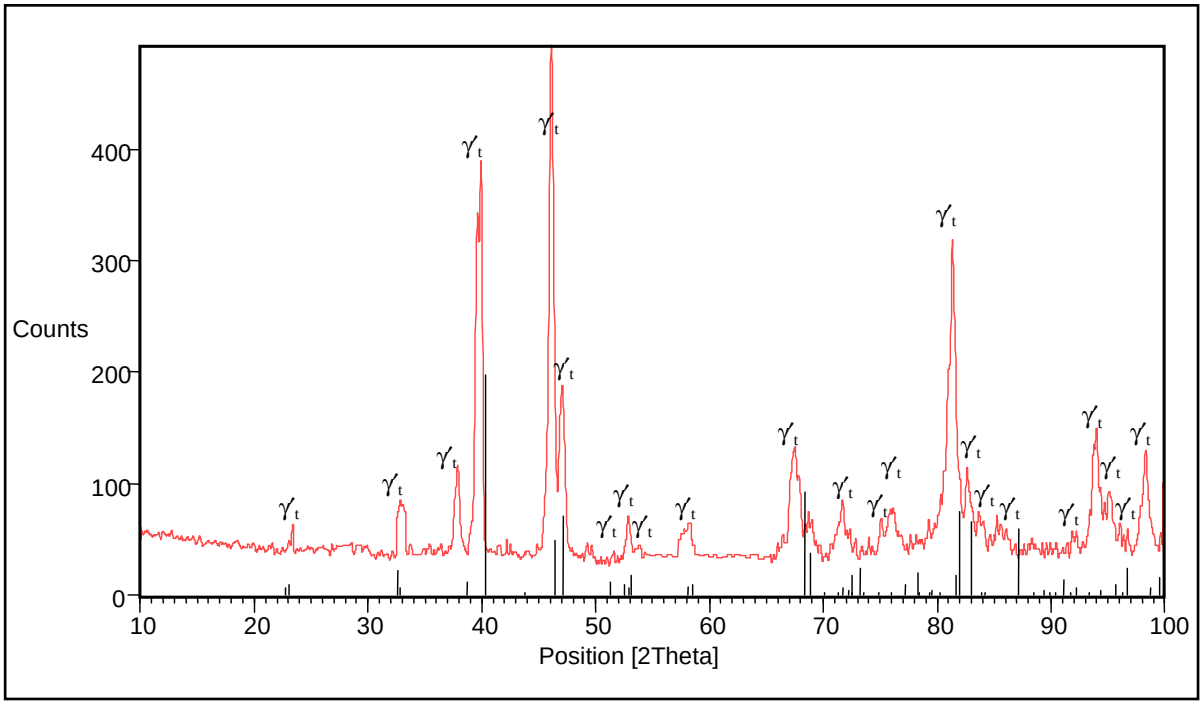

Figure 4.4. XRD Pattern of nominal Pt_{78}:$Al_{15.5}$:Ru_2:$Cr_{4.5}$ in the as-cast condition, showing identified DO'_c – ~Pt_3Al peaks.

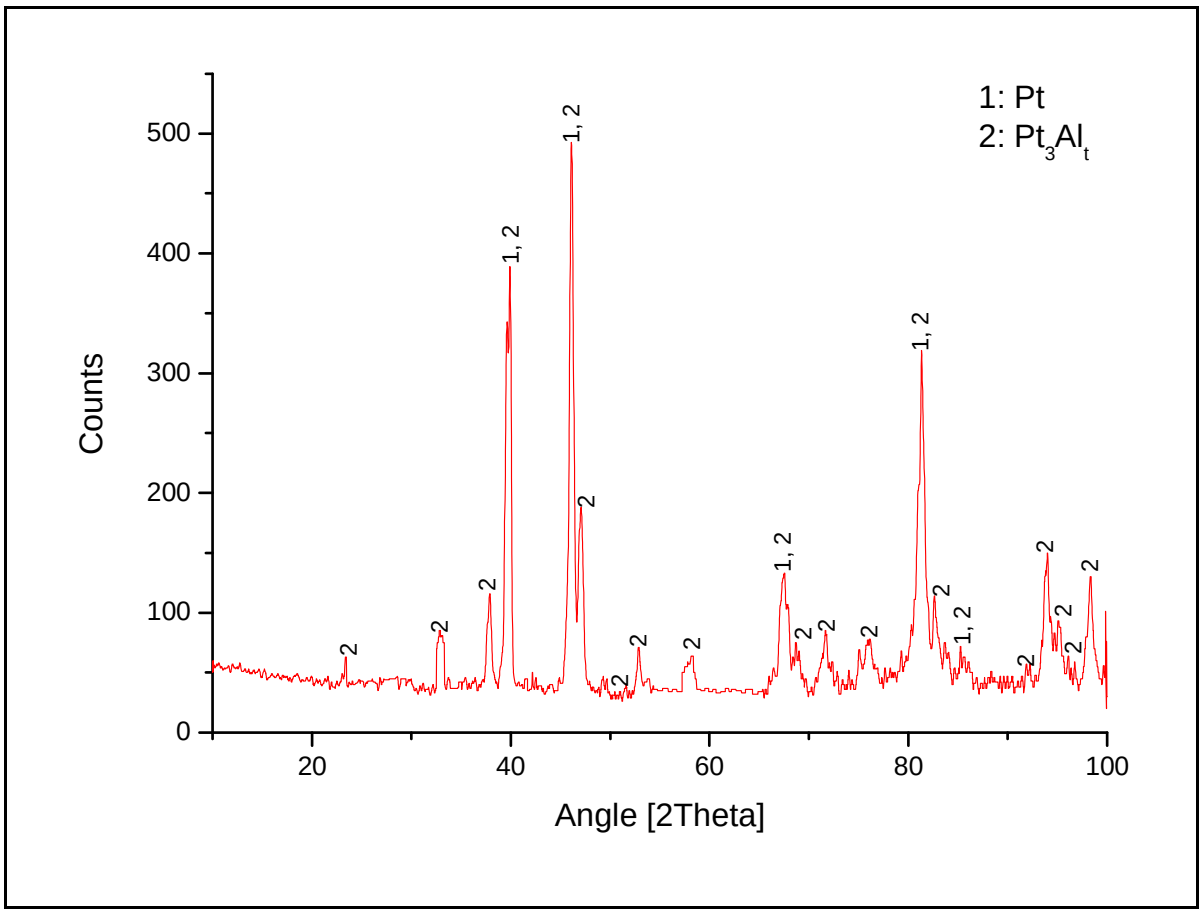

Figure 4.5. XRD pattern of nominal Pt_{78}:$Al_{15.5}$:Ru_2:$Cr_{4.5}$ in the as-cast condition, showing all identified phases.

Table 4.3. XRD peaks for Pt_{78}:$Al_{15.5}$:Ru_2:$Cr_{4.5}$ in the as-cast condition.

Position 2θ(°)	Height (counts)	Full-Width Half-Maximum 2θ(°)	d-spacing (Å)	Relative Intensity (%)	Phase (s)
22.7637	221.66	0.1771	3.90652	19.86	γ'_t
32.6699	41.93	0.3936	2.74109	9.37	γ'_t
33.1902	42.81	0.2362	2.6993	9.57	γ'_t
37.0803	11.15	0.2362	2.42457	2.19	-
37.9137	75.5	0.2362	2.37317	16.87	γ'_t
39.5926	296.97	0.3149	2.27632	66.36	γ'_t
39.9671	335.38	0.2165	2.25585	74.95	(Pt), γ'_t
42.9418	9.26	0.9446	2.10622	2.71	-
46.0696	447.49	0.4133	1.97024	100	(Pt), γ'_t
47.1001	152.88	0.2362	1.92951	34.16	γ'_t
48.8406	30.53	0.5510	1.86475	8.92	-
52.8734	37.85	0.3149	1.73163	8.46	γ'_t
58.2522	28.77	0.4723	1.5839	6.43	γ'_t
67.3246	76.01	0.7872	1.39084	16.99	(Pt), γ'_t
71.6905	47.64	0.3149	1.31649	10.64	γ'_t
72.4499	59.88	0.2755	1.30456	11.75	-
75.0744	29.04	0.3149	1.26533	6.49	γ'_t
76.0081	34.98	0.4723	1.2521	7.82	γ'_t
81.3334	257.53	0.2165	1.18304	57.55	(Pt), γ'_t
82.6381	57.95	0.3149	1.16764	12.95	γ'_t
85.6362	15.97	0.9446	1.13428	3.57	(Pt), γ'_t
93.9751	102.95	0.3936	1.05434	23.01	γ'_t
95.1791	42.85	0.3149	1.04416	9.58	γ'_t
98.3252	84.63	0.384	1.01815	18.91	γ'_t

4.1.1.2 Nominal Pt_{80}:Al_{14}:Ru_3:Cr_3

HR-SEM-BSE images of the centre and edge microstructure are shown in Figure 4.6 and both consisted of (Pt) dendrites with a (Pt) + ~Pt_3Al eutectic. Discerning of the microstructure was relatively difficult; hence a high magnification was used. Fine ~Pt_3Al precipitates were seen in the edges of the dendrites. Similarities of the edge and centre microstructures confirmed homogeneity of the sample. The dendrites were the major phase with an arm spacing of 4.5 ± 1.3 µm and a proportion of 92 ± 5% of the microstructure.

The phase compositions are shown in Table 4.4 and the overall composition was close to the targeted composition. Ru and Cr had limited solubility in the eutectic ((Pt) + ~Pt_3Al), and partitioned preferentially to (Pt). The composition of the edges of dendrites with larger precipitates was close to the overall alloy composition. The standard deviation of the measurements varied, with the highest error in the dendrite edges with precipitates, which is due to electron beam scattering into the surrounding areas. Note that even the eutectic areas are too small to analyse acurately.

Table 4.4. EDX Phase compositions of nominal Pt_{80}:Al_{14}:Ru_3:Cr_3 in the as-cast condition.

Phase description	Al	Ru	Cr	Pt	Phase
Overall	12.7 ± 0.5	2.1 ± 0.8	2.8 ± 0.8	82.4 ± 1.2	-
Eutectic (Dark)	19.2 ± 0.7	0.7 ± 0.6	1.6 ± 0.6	78.5 ± 0.3	(Pt) + ~Pt_3Al
Dendrites (Light)	10.6 ± 0.8	3.2 ± 0.9	3.8 ± 0.5	82.4 ± 1.2	(Pt) + ~Pt_3Al
Dendrites + Visible precipitates	14.5 ± 1.6	1.7 ± 0.3	1.9 ± 0.6	81.9 ± 1.9	(Pt) + ~Pt_3Al

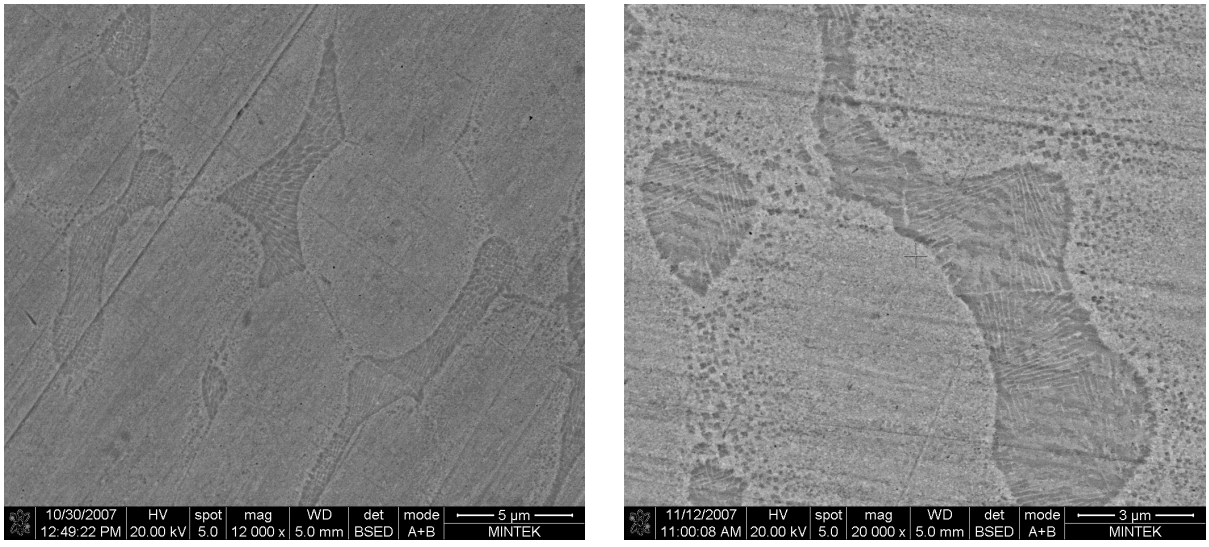

(a) **(b)**

Figure 4.6. HR-SEM-BSE image of nominal Pt_{80}:Al_{14}:Ru_3:Cr_3, as-cast condition, taken from the (a) edge and (b) centre showing (Pt) dendrites (light) with fine ~Pt_3Al precipitates and a eutectic of (Pt) + ~Pt_3Al (dark).

The XRD spectrum (Figure 4.10) confirmed that the alloy contained ~Pt_3Al and (Pt). Figures 4.7 to 4.9 show peak shifts of the individual phases which were similar to those of Pt_{78}:$Al_{15.5}$:Ru_2:$Cr_{4.5}$. It was observed that the three highest intensity peaks at about 2θ = 39°, 48° and 82°, were a possible combination of the (Pt) and DO'_c - ~Pt_3Al lines, with $L1_2$ - ~Pt_3Al excluded. A shift in both directions of the apparent $L1_2$ - ~Pt_3Al phase peaks relative to the pure phase lines was observed, showing that the $L1_2$ - ~Pt_3Al phase could not be

present as a third phase in the sample. All peaks can be matched without the $L1_2$ - ~Pt_3Al phase, thus showing its likely absence. Figure 4.10 shows the experimental XRD spectrum labelled for all of the identified phases and some minor peaks were unidentified. Table 4.5 shows the identified peaks together with the d-spacings.

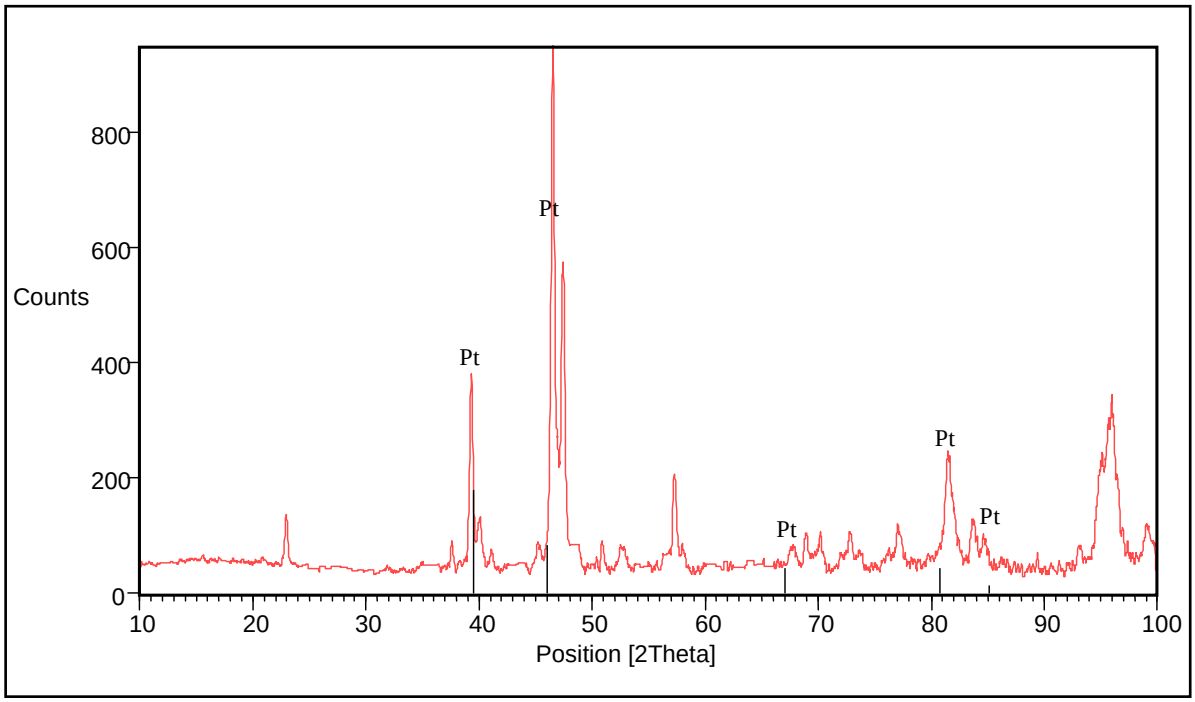

Figure 4.7. XRD Pattern of nominal Pt_{80}:Al_{14}:Ru_3:Cr_3 in the as-cast condition, showing identified Pt peaks.

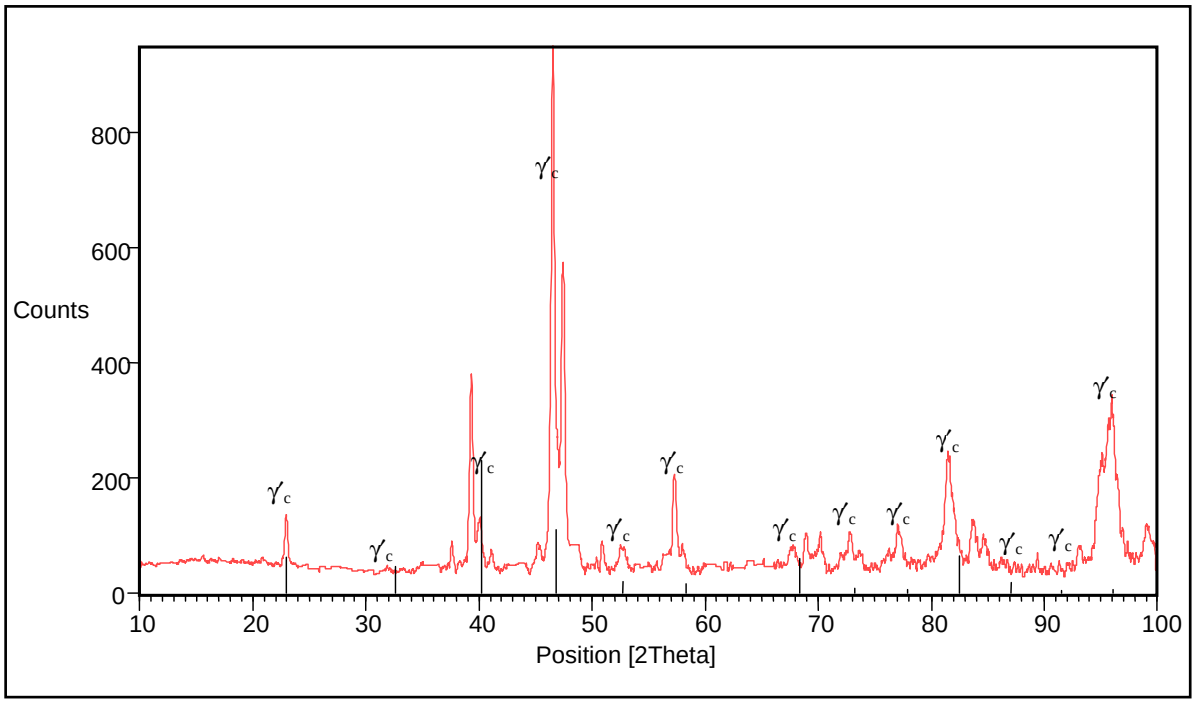

Figure 4.8. XRD Pattern of nominal Pt_{80}:Al_{14}:Ru_3:Cr_3 in the as-cast condition, showing apparent $L1_2$ – ~Pt_3Al peaks.

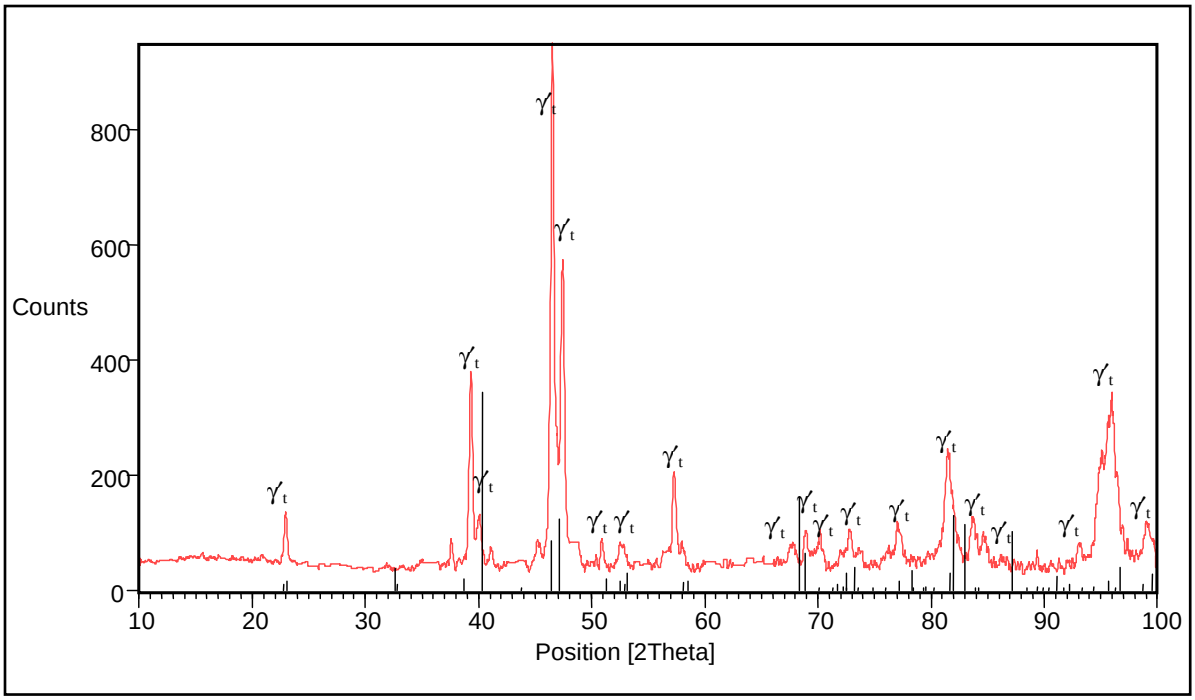

Figure 4.9. XRD Pattern of nominal Pt_{80}:Al_{14}:Ru_3:Cr_3 in the as-cast condition, showing identified DO'_c – ~Pt_3Al peaks.

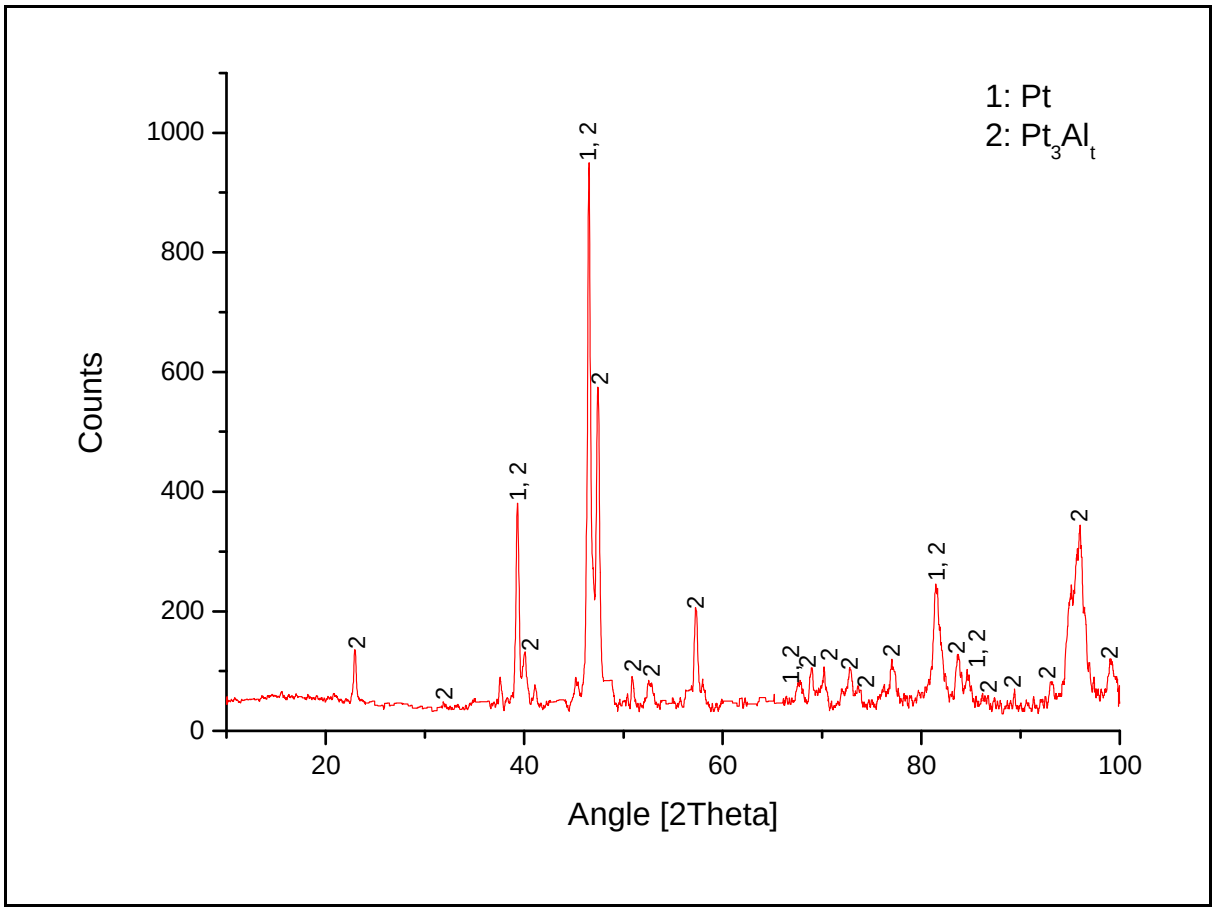

Figure 4.10. XRD pattern of nominal Pt_{80}:Al_{14}:Ru_3:Cr_3 in the as-cast condition, showing all identified phases.

Table 4.5. XRD peaks for Pt_{80}:Al_{14}:Ru_3:Cr_3 in the as-cast condition.

Position 2θ(°)	Height (counts)	Full-Width Half-Maximum 2θ(°)	d-spacing (Å)	Relative Intensity (%)	Phase (s)
22.9807	83.81	0.2558	3.87010	9.21	γ'_t
37.5749	45.12	0.2362	2.39378	4.96	γ'_t
38.2413	26.12	0.2755	2.35359	6.28	-
39.3335	338.36	0.2362	2.29072	37.18	γ'_t
40.1184	85	0.2165	2.24769	9.34	(Pt), γ'_t
41.1189	33.22	0.3149	2.19528	3.65	γ'_t
42.5835	19.84	0.3149	2.12311	4.77	-
45.1810	39.04	0.3149	2.00691	9.39	-
45.2500	41.71	0.3936	2.00400	4.58	(Pt), γ'_t
46.5369	910.14	0.2558	1.95154	100	γ'_t
47.5332	449.11	0.3346	1.91294	49.34	γ'_t
48.7105	44.42	0.4723	1.86942	4.88	γ'_t
50.8578	46.32	0.1771	1.79542	5.09	γ'_t
52.6804	36.64	0.6298	1.73752	4.03	γ'_t
57.3180	161.59	0.3542	1.60747	17.75	γ'_t
67.4997	28.13	0.7085	1.38766	8.09	(Pt), γ'_t
67.6696	28.37	0.2362	1.38458	8.29	-
68.9951	60.96	0.3542	1.36119	6.7	γ'_t
70.1865	58.64	0.2362	1.34097	6.44	γ'_t
72.8118	63.46	0.3542	1.29896	6.97	γ'_t
73.7249	26.66	0.4723	1.28512	2.93	γ'_t
77.0300	66.25	0.3149	1.23802	7.28	γ'_t
81.4197	181.29	0.3149	1.18200	19.92	(Pt), γ'_t
83.6671	74.39	0.551	1.15588	8.17	γ'_t
84.6808	43.93	0.3936	1.14462	4.83	(Pt), γ'_t
85.8743	12.87	0.6298	1.13174	2.53	γ'_t
91.2757	20.31	0.3936	1.07833	3.98	γ'_t
92.6516	30.96	0.1920	1.06501	6.07	γ'_t
94.4752	167.75	0.1680	1.04920	32.91	γ'_t
95.4493	69.52	0.1200	1.04106	13.64	γ'_t
95.9983	58.97	0.3149	1.03741	11.57	γ'_t
98.8659	75.04	0.2880	1.01402	14.72	γ'_t

4.1.1.3 Nominal $Pt_{81.5}$:$Al_{11.5}$:$Ru_{2.5}$:$Cr_{4.5}$

HR-SEM-BSE images are shown in Figure 4.11, taken at the centre and edge of the sample. Black spots in the microstructure were porosity. The average dendrite arm spacing was about 8.0 ± 1.1 µm with a proportion of 80 ± 8% of the microstructure. Both centre and edge microstructure (Figures 4.11 (a) and (b)) consisted of (Pt) dendrites with fine ~Pt_3Al precipitates and an interdendritic eutectic (Pt) + ~Pt_3Al. All dendrites had precipitates, but they were more noticeable at the edges, because they were larger. The structure of the eutectic-like regions were very fine.

The phase compositions are shown in Table 4.6. Ru and Cr had extremely limited solubility in the ((Pt) + ~Pt_3Al) eutectic, and partitioned almost exclusively to (Pt). The dendrites edges with precipitates were close to the overall alloy composition. A slightly lower solubility of Ru and Cr were noticed, compared to the dendrite centres with smaller precipitates. The standard deviation was below 1 at.% for most of the elements, except for the (Pt) phase with a standard deviation of 1.3 at.% for Al, most likely due to the precipitates. Inaccuracy would have been caused by the finess of the microstructure.

Table 4.6. EDX Phase compositions of nominal $Pt_{81.5}$:$Al_{11.5}$:$Ru_{2.5}$:$Cr_{4.5}$ in the as-cast condition.

Phase description	Al	Ru	Cr	Pt	Phase
Overall	11.7 ± 0.3	1.7 ± 0.2	3.9 ± 0.2	82.7 ± 0.3	-
Eutectic (Dark)	20.2 ± 0.7	0.7 ± 0.3	1.4 ± 0.2	77.7 ± 0.6	(Pt) + ~Pt_3Al
Dendrites (Light)	8.0 ± 1.3	2.5 ± 0.3	5.0 ± 0.4	84.5 ± 0.7	(Pt) + ~Pt_3Al
Dendrites + Visible precipitates	13.0 ± 0.8	1.2 ± 0.2	3.1 ± 0.2	82.7 ± 0.6	(Pt) + ~Pt_3Al

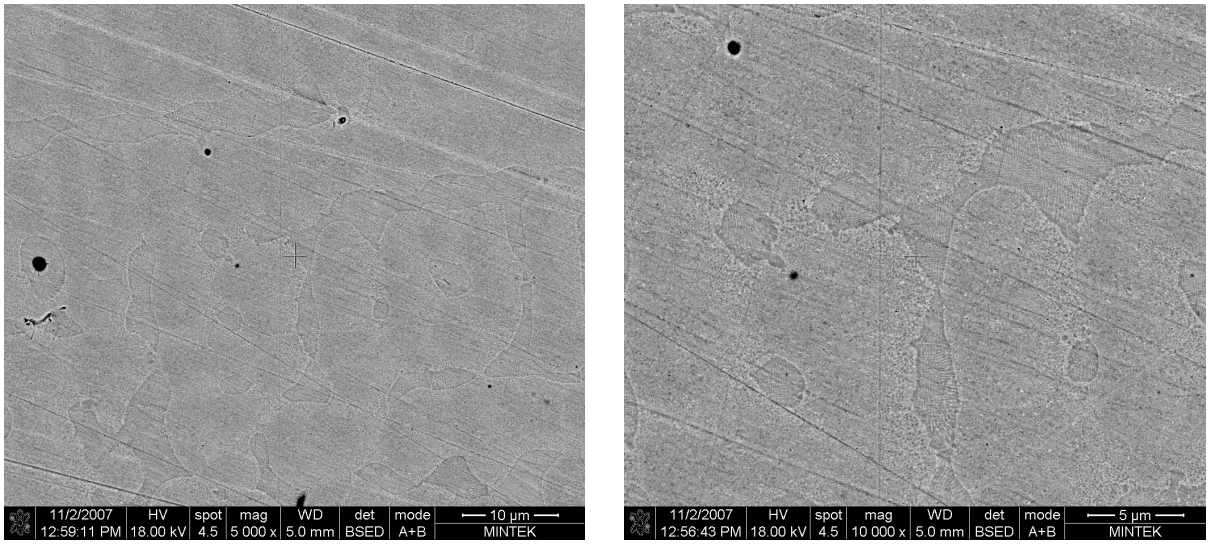

(a) **(b)**

Figure 4.11. HR-SEM-BSE image of nominal $Pt_{81.5}$:$Al_{11.5}$:$Ru_{2.5}$:$Cr_{4.5}$, as-cast condition, taken from the (a) edge and (b) centre showing (Pt) dendrites (light) with fine ~Pt_3Al precipitates and a eutectic of (Pt) + ~Pt_3Al (dark).

Shown in Figures 4.12 to 4.14 is the experimental XRD spectrum of the sample together with the lines for each of the three expected phases. Peak shifting of the phases was observed, with similar behaviour to Pt_{78}:$Al_{15.5}$:Ru_2:$Cr_{4.5}$ and Pt_{80}:Al_{14}:Ru_3:Cr_3. The reasons summarised below give explanations why the ~Pt_3Al structure is present in the alloy:

- Three of the highest intensity peaks (at about 2θ = 39°, 48° and 68°), were a combination of (Pt) and DO'_c - ~Pt_3Al lines.

- The apparent $L1_2$ - ~Pt_3Al phase peaks have a shift in both directions relative to the pure phase lines, in contrary to the shift expected to be in one direction for a cubic phase.

- All peaks can be matched without the $L1_2$ - ~Pt_3Al phase.

Figure 4.15 shows the experimental XRD spectrum labelled for all of the identified peaks, and Table 4.7 shows the identified peaks together with their d-spacings.

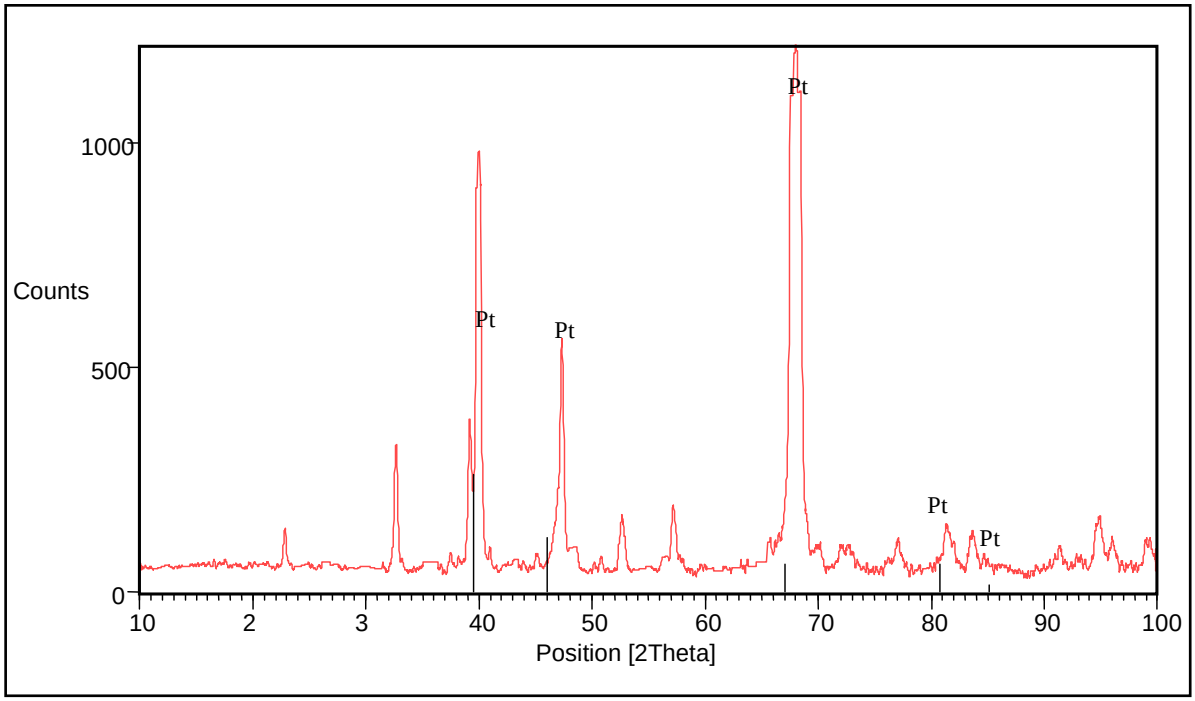

Figure 4.12. XRD Pattern of nominal $Pt_{81.5}$:$Al_{11.5}$:$Ru_{2.5}$:$Cr_{4.5}$ in the as-cast condition, showing identified Pt peaks.

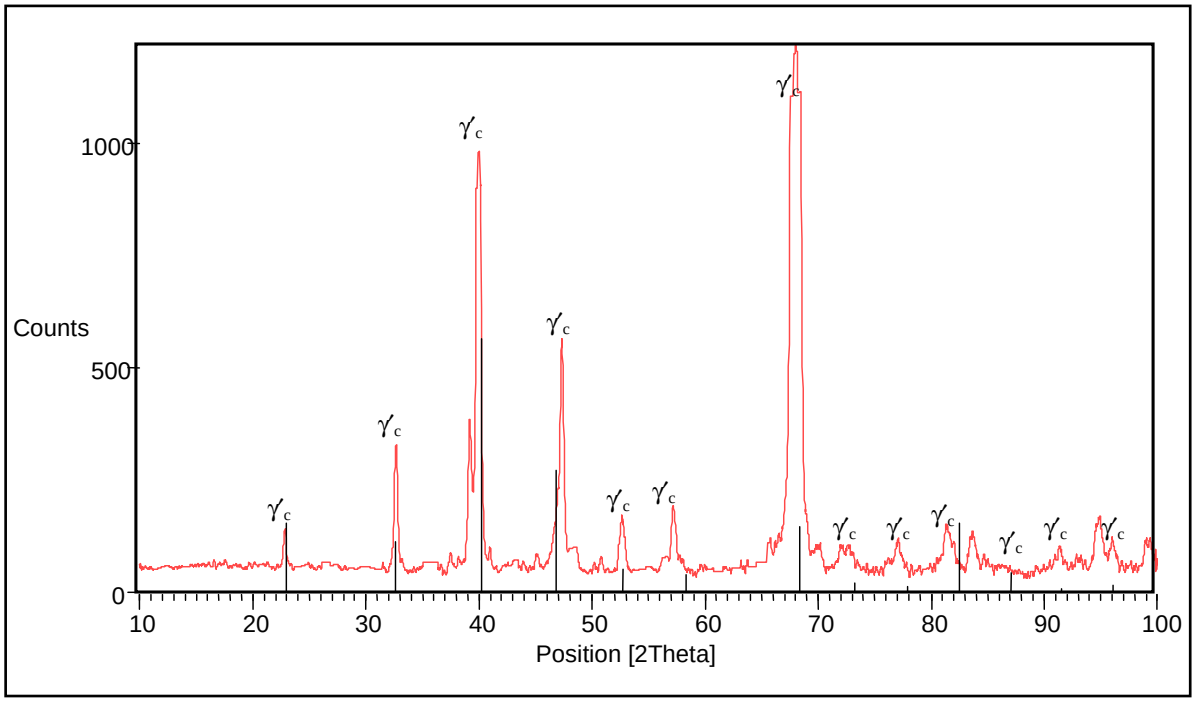

Figure 4.13. XRD Pattern of nominal $Pt_{81.5}$:$Al_{11.5}$:$Ru_{2.5}$:$Cr_{4.5}$ in the as-cast condition, showing apparent $L1_2$ – ~Pt_3Al peaks.

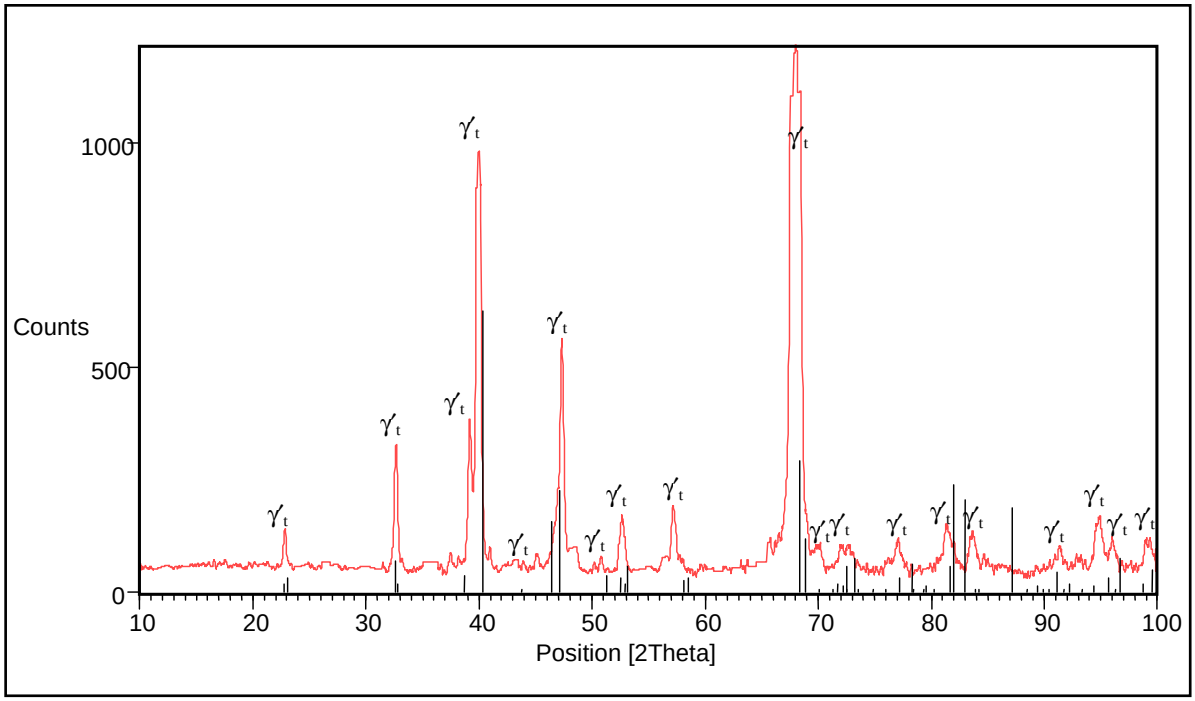

Figure 4.14. XRD Pattern of nominal $Pt_{81.5}$:$Al_{11.5}$:$Ru_{2.5}$:$Cr_{4.5}$ in the as-cast condition, showing identified DO'_c – ~Pt_3Al peaks.

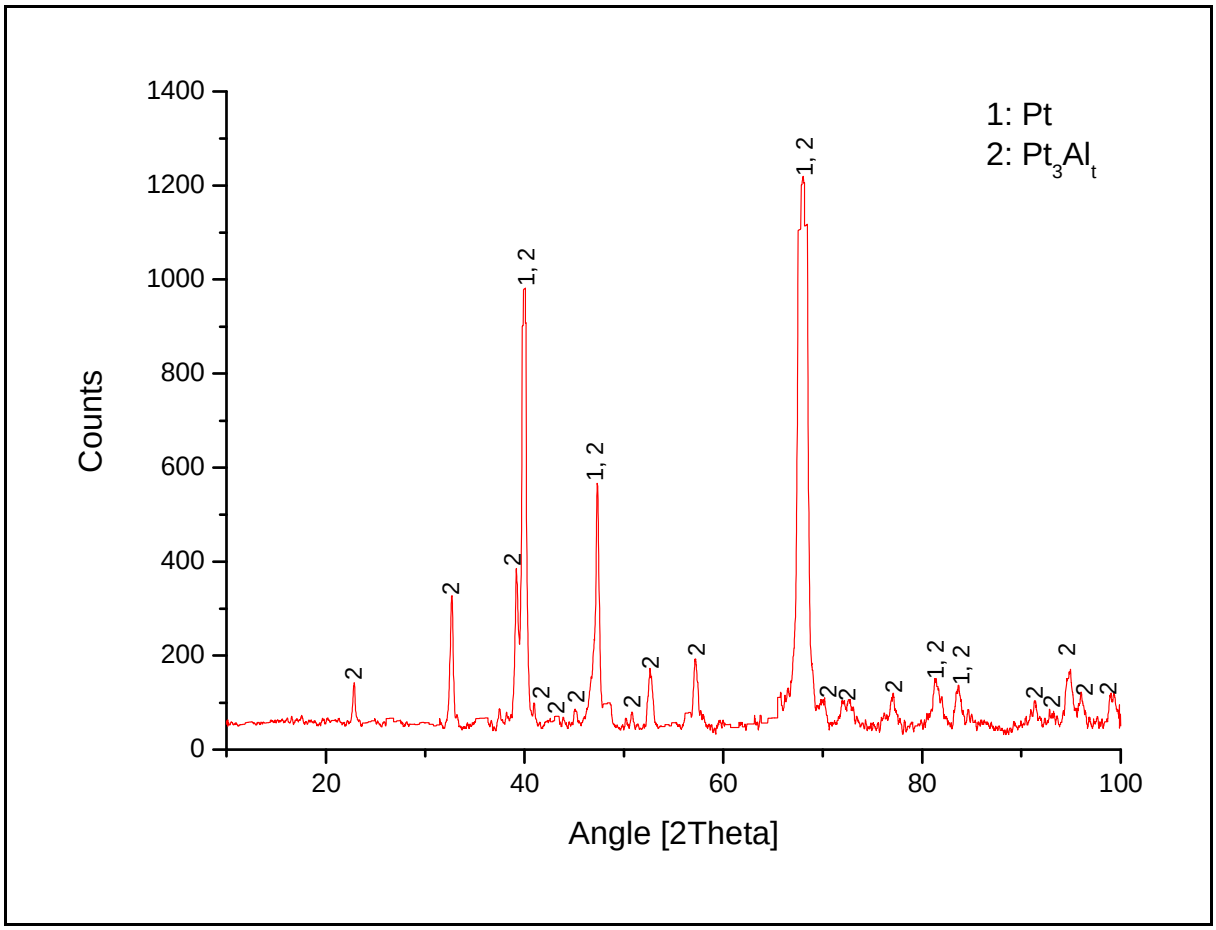

Figure 4.15. XRD pattern of nominal $Pt_{81.5}$:$Al_{11.5}$:$Ru_{2.5}$:$Cr_{4.5}$ in the as-cast condition, showing all identified phases.

Table 4.7. XRD peaks for $Pt_{81.5}$:$Al_{11.5}$:$Ru_{2.5}$:$Cr_{4.5}$ in the as-cast condition.

Position 2θ(°)	Height (counts)	Full-Width Half-Maximum 2θ(°)	d-spacing (Å)	Relative Intensity (%)	Phase (s)
22.8816	80.49	0.2558	3.88665	6.95	γ'_t
26.6548	12.69	0.9446	3.34441	1.1	γ'_t
32.6962	272.95	0.3149	2.73894	23.56	γ'_t
37.4468	37.42	0.2362	2.40168	3.23	γ'_t
38.2275	44.71	0.2362	2.35441	7.33	-
39.1576	337.18	0.1771	2.3006	29.11	γ'_t
39.7742	855.22	0.072	2.26447	73.83	γ'_t
40.1444	852.51	0.0787	2.24629	73.6	(Pt), γ'_t
40.9891	50.16	0.2362	2.20193	4.33	γ'_t
42.9728	19.05	0.9446	2.10477	1.64	γ'_t
45.1139	38.45	0.3149	2.00973	3.32	γ'_t
47.6024	54.44	0.3936	1.87333	4.7	γ'_t
47.7403	514.83	0.2362	1.92028	44.45	(Pt), γ'_t
47.7994	74.50	0.1968	1.90290	5.14	-
50.8109	32.06	0.2362	1.79697	2.77	γ'_t
52.6046	119.17	0.2362	1.73984	10.29	γ'_t
57.6429	72.62	0.1674	1.57428	9.72	-
57.2092	141.26	0.3149	1.61027	12.2	γ'_t
65.6655	54.21	0.3149	1.4219	4.68	γ'_t
67.5212	1050.52	0.096	1.38612	90.7	γ'_t
68.0006	1158.29	0.2362	1.37865	100	(Pt), γ'_t
68.4545	1065.2	0.1181	1.37061	91.96	γ'_t
70.1548	47.6	0.551	1.3415	4.11	γ'_t
72.0084	45.15	0.3149	1.31146	3.9	γ'_t
77.0284	66.3	0.3149	1.23804	5.72	γ'_t
81.1782	70.95	0.3542	1.18491	6.13	(Pt), γ'_t
83.6177	71.94	0.551	1.15644	6.21	(Pt), γ'_t
84.2575	33.34	0.3936	1.14928	4.46	-
91.3303	51.31	0.3149	1.07783	4.43	γ'_t
93.0316	19.44	0.7872	1.06253	1.68	γ'_t
94.9143	113.82	0.3149	1.04637	9.83	γ'_t
96.0525	61.28	0.3149	1.03697	5.29	γ'_t
98.9313	61.06	0.288	1.01353	5.27	γ'_t

4.1.1.4. Nominal $Pt_{82}:Al_{12}:Ru_2:Cr_4$

HR-SEM-BSE images are shown in Figure 4.16, taken at different areas of the alloy. Both the centre and edge consisted of (Pt) dendrites with ~Pt_3Al precipitates and a eutectic of (Pt) + ~Pt_3Al (Figures 16 (a) and (c)), confirming homogeneity of the sample. The eutectic had a very fine structure, probably originating from both the binary eutectic and eutectoid reactions. The average dendrites arm spacing was 9.5 ± 2.3 µm. The dendrites proportion was 76 ± 8% of the microstructure.

The phase compositions are shown in Table 4.8. The composition of the dendrite edges with more precipitates was close to the overall alloy composition. Similar to the other samples, Ru and Cr had limited solubility in the ((Pt) + ~Pt_3Al) eutectic, and partitioned almost exclusively to (Pt). A slightly lower solubility of Ru and Cr at the edges of the dendrites with precipitates was noticed, compared to the inner dendrites with fewer precipitates.

Table 4.8. EDX Phase compositions of nominal $Pt_{82}:Al_{12}:Ru_2:Cr_4$ in the as-cast condition.

Phase description	Al	Ru	Cr	Pt	Phase
Overall	11.2 ± 0.4	1.8 ± 0.3	3.5 ± 0.4	83.5 ± 0.6	-
Eutectic (Dark)	18.3 ± 0.1	0.6 ± 0.2	1.4 ± 0.3	79.7 ± 0.2	(Pt) + ~Pt_3Al
Dendrites (Light)	10.4 ± 0.7	1.8 ± 0.1	2.5 ± 0.3	85.3 ± 0.8	(Pt) + ~Pt_3Al
Dendrites + Visible precipitates	12.1 ± 0.3	1.1 ± 0.4	2.0 ± 0.2	84.8 ± 0.5	(Pt) + ~Pt_3Al

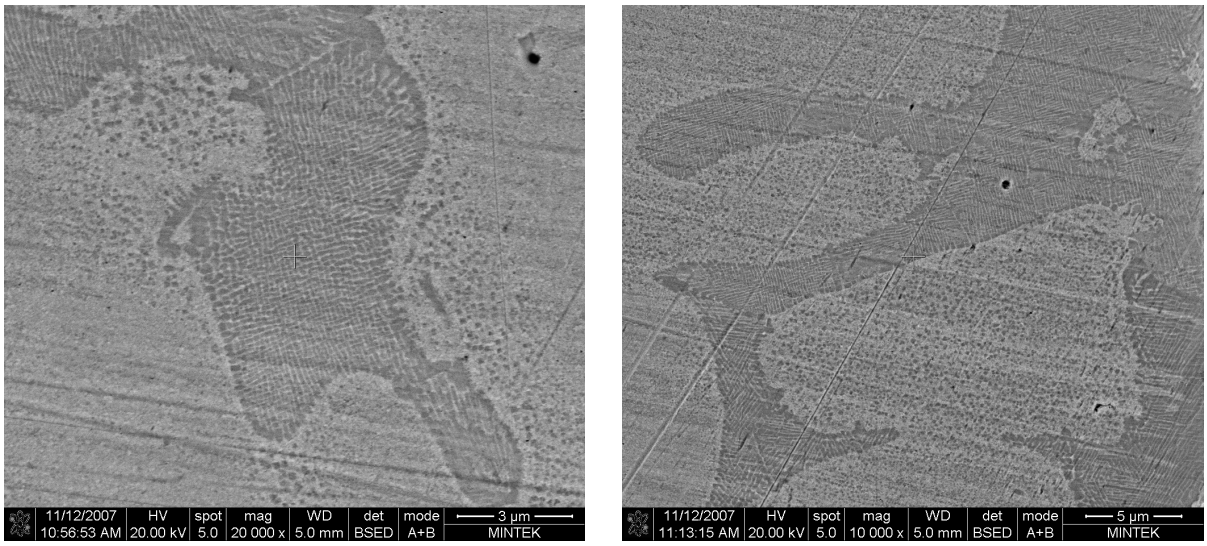

(c) **(d)**

Figure 4.16. HR-SEM-BSE image of nominal $Pt_{82}:Al_{12}:Ru_2:Cr_4$, as-cast condition, (a) taken from the centre and (b) edge showing (Pt) dendrites (light) with ~Pt_3Al precipitates (dark) and a eutectic of (Pt) + ~Pt_3Al.

The XRD spectrum showed that the alloy contained ~Pt_3Al and (Pt) (Figure 4.20). Peak shifting of the individual phases relative to the pure phase lines was observed (Figures 4.17 to 4.19), similar to the alloys described previously. There was a shift in both directions of the apparent $L1_2$ - ~Pt_3Al phase peaks relative to the pure phase lines, indicating that the $L1_2$ - ~Pt_3Al phase is probably not present, since for a cubic phase the shift can only be in one direction. The highest intensity peaks (at about 2θ = 40°, 47° and 68°) showed similar behaviour to the high intensity peaks for $Pt_{78}:Al_{15.5}:Ru_2:Cr_{4.5}$, $Pt_{80}:Al_{14}:Ru_3:Cr_3$ and $Pt_{81.5}:Al_{11.5}:Ru_{2.5}:Cr_{4.5}$. Figure 4.20 shows the experimental XRD spectrum labelled for all of the identified phases. Table 4.9 shows the identified peaks together with their d-spacings.

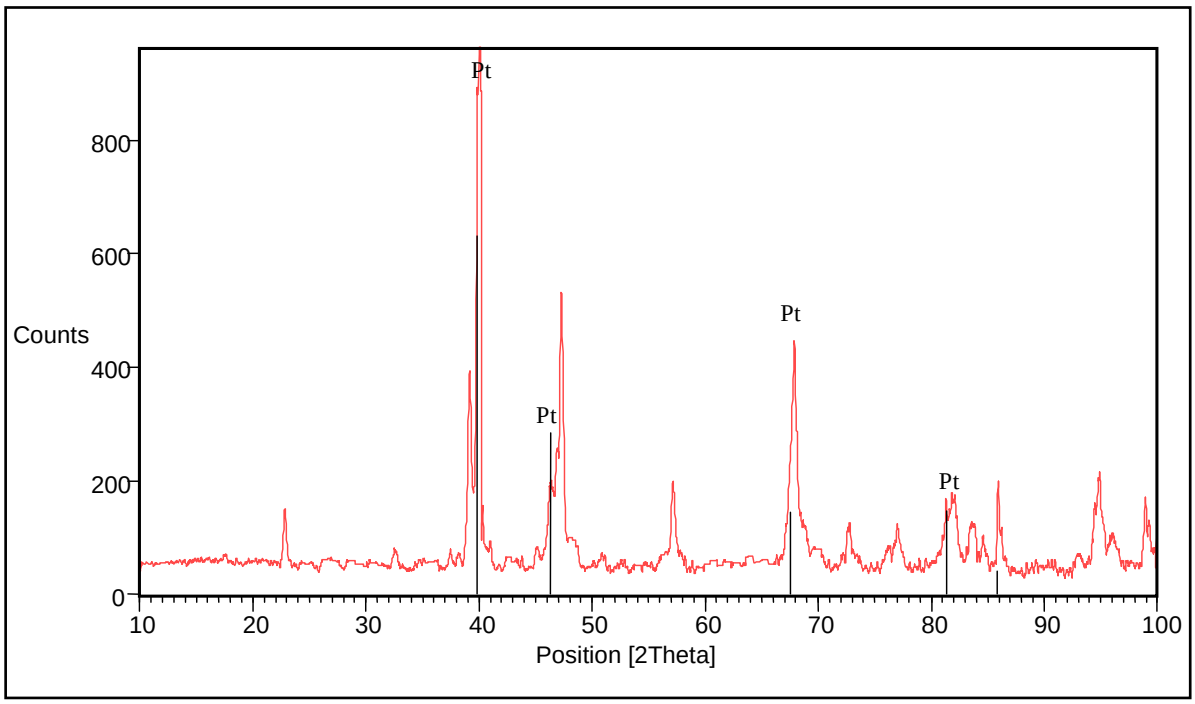

Figure 4.17. XRD Pattern of nominal $Pt_{82}:Al_{12}:Ru_2:Cr_4$ in the as-cast condition, showing identified Pt peaks.

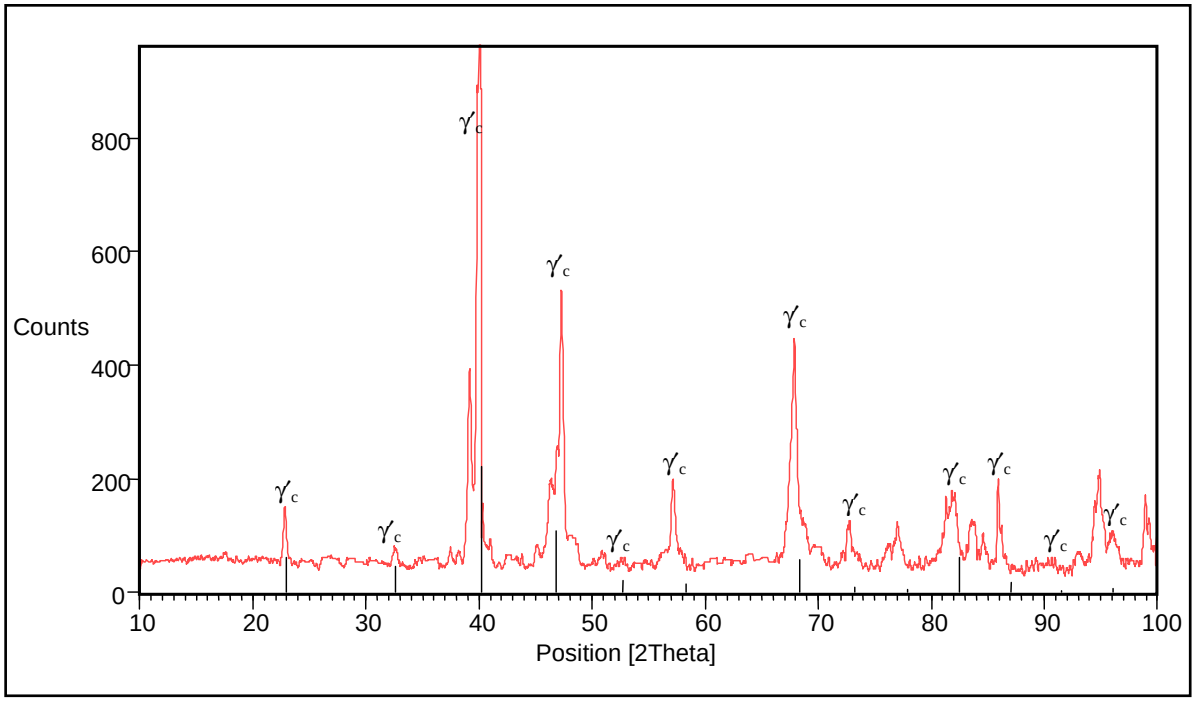

Figure 4.18. XRD Pattern of nominal Pt_{82}:Al_{12}:Ru_2:Cr_4 in the as-cast condition, showing apparent $L1_2$ – ~Pt_3Al peaks.

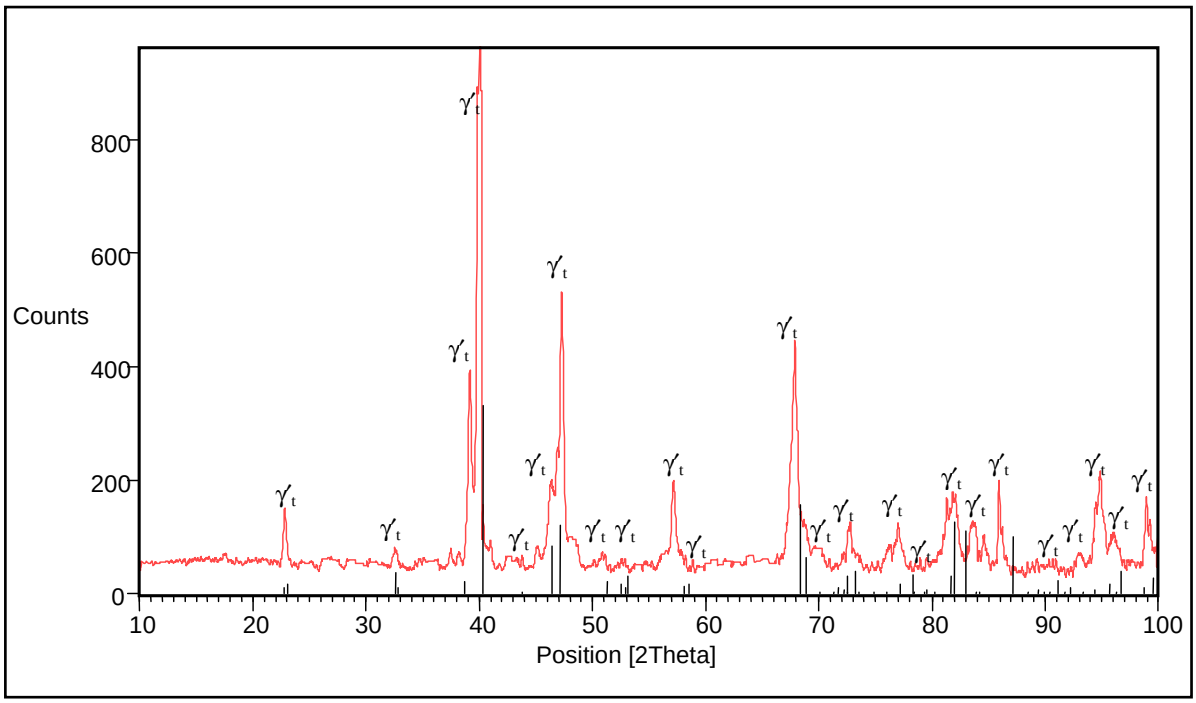

Figure 4.19. XRD Pattern of nominal Pt_{82}:Al_{12}:Ru_2:Cr_4 in the as-cast condition, showing identified DO'_c – ~Pt_3Al peaks.

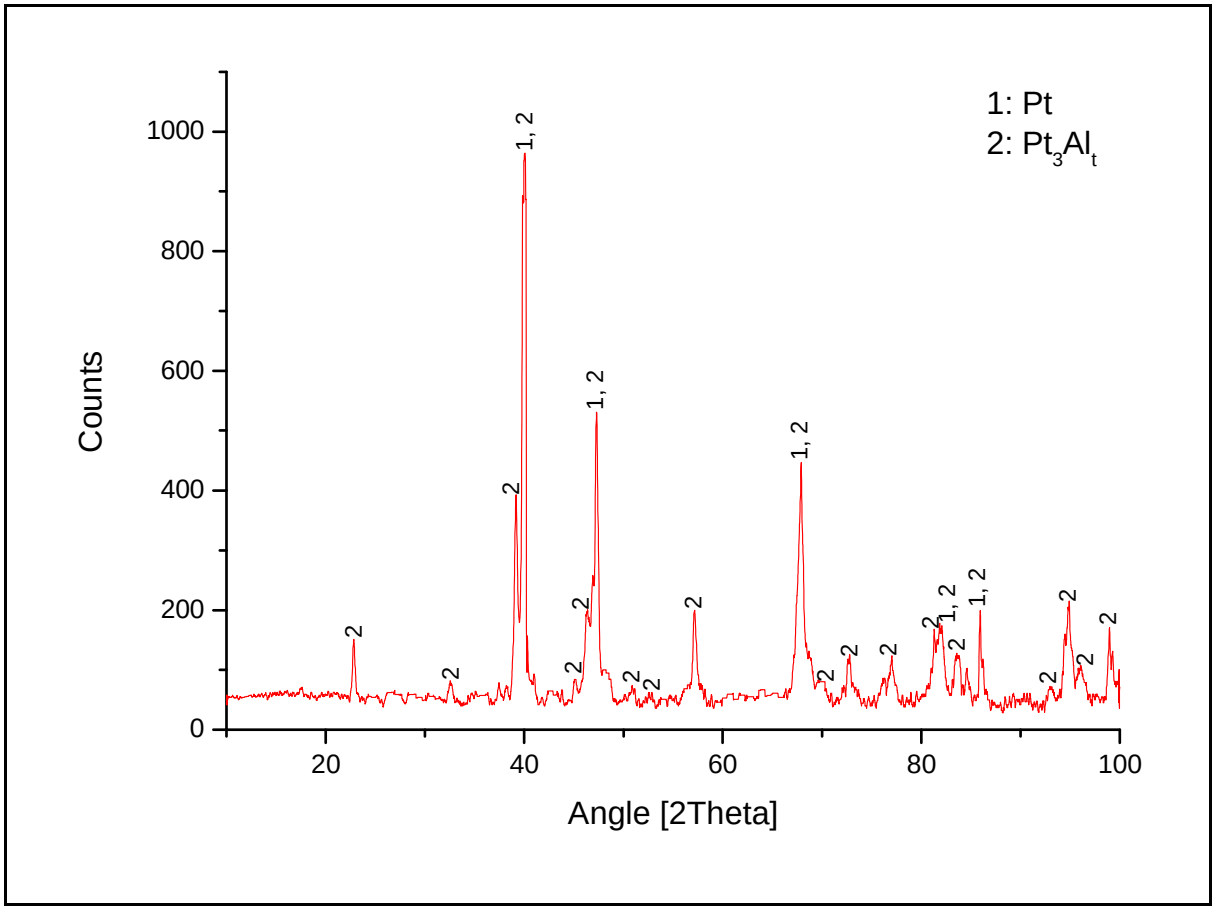

Figure 4.20. XRD pattern of nominal Pt_{82}:Al_{12}:Ru_2:Cr_4 in the as-cast condition, showing all identified phases.

Table 4.9. XRD peaks for Pt_{82}:Al_{12}:Ru_2:Cr_4 in the as-cast condition.

Position 2θ(°)	Height (counts)	Full-Width Half-Maximum 2θ(°)	d-spacing (Å)	Relative Intensity (%)	Phase (s)
22.8154	96.77	0.2362	3.89778	11.59	γ'_t
26.7925	14.37	0.9446	3.32754	1.72	γ'_t
32.6144	30.63	0.3936	2.74562	3.67	γ'_t
37.4518	29.32	0.2362	2.40136	3.51	-
39.8563	835.31	0.072	2.25999	100	γ'_t
40.1866	831.19	0.1378	2.24403	99.51	(Pt), γ'_t
41.0163	45.89	0.2362	2.20054	5.49	γ'_t
42.9269	16.18	0.9446	2.10692	1.94	γ'_t
43.3687	73.11	0.1968	2.08647	6.72	-
45.181	39.04	0.3149	2.00691	4.67	γ'_t
46.2302	140.04	0.2755	1.96377	16.77	γ'_t
47.3068	482.31	0.2558	1.92156	57.74	γ'_t
48.4595	48.98	0.4723	1.87852	5.86	(Pt), γ'_t
51.0355	19.62	0.551	1.78959	2.35	γ'_t
52.7527	13.68	0.6298	1.73531	1.64	γ'_t
57.0432	124.21	0.1968	1.61456	14.87	γ'_t
67.8847	383.13	0.1574	1.38072	45.87	(Pt), γ'_t
70.1334	29.05	0.6298	1.34186	3.48	γ'_t
72.684	67.02	0.3149	1.30093	8.02	γ'_t
77.0178	69.91	0.3149	1.23818	8.37	γ'_t
81.2996	113.3	0.144	1.18247	13.56	γ'_t
81.9699	116.38	0.4723	1.17546	13.93	(Pt), γ'_t
83.8106	74.23	0.2362	1.15427	8.89	γ'_t
84.5823	53.89	0.2362	1.1457	6.45	γ'_t
85.9366	155.87	0.1771	1.13108	18.66	(Pt), γ'_t
92.9611	33.47	0.551	1.06315	4.01	γ'_t
94.8785	174.47	0.2362	1.04667	20.89	γ'_t
96.0784	63.91	0.4723	1.03676	7.65	γ'_t
98.94	133.39	0.168	1.01346	15.97	γ'_t

4.1.1.5. Nominal $Pt_{84}:Al_{11}:Ru_2:Cr_3$

HR-SEM-BSE images of both the edge and centre microstructure are shown in Figures 4.21 and both consisted of (Pt) dendrites with a (Pt) + ~Pt_3Al eutectic, showing homogeneity. Fine ~Pt_3Al precipitates were also observed throughout the dendrites, but were larger at the edges (Figure 4.21 (b) and (c)), which ranged from about 50 nm to 250 nm. The dendrites proportion was 85 ± 10% and average arm spacing of 10.3 ± 1.5 µm. A lighter apparent third phase was also seen which was most likely a preparation artefact.

The phase compositions are shown in Table 4.10, and the overall composition was close to the targeted composition. Ru and Cr had very limited solubility in the ((Pt) + ~Pt_3Al) eutectic, and partitioned almost exclusively to (Pt). The solubility of Ru and Cr in the dendrites with precipitates was low, compared to the dendrites where the precipitates could be less easily seen.

Table 4.10. EDX Phase compositions of nominal $Pt_{84}:Al_{11}:Ru_2:Cr_3$ in the as-cast condition.

Phase description	Al	Ru	Cr	Pt	Phase
Overall	10.0 ± 0.5	1.6 ± 0.6	2.7 ± 0.2	85.9 ± 0.8	-
Eutectic (Dark)	17.9 ± 0.4	0.7 ± 0.5	1.2 ± 0.1	80.2 ± 0.6	(Pt) + ~Pt_3Al
Dendrites (Light)	9.1 ± 0.5	1.4 ± 0.3	2.4 ± 0.1	87.1 ± 0.9	(Pt) + ~Pt_3Al
Dendrites + Visible precipitates	14.2 ± 0.2	0.8 ± 0.7	1.6 ± 0.4	83.4 ± 0.5	(Pt) + ~Pt_3Al

The XRD spectrum confirmed the presence of DO′$_c$ - ~Pt_3Al and (Pt). The apparent $L1_2$ - ~Pt_3Al peaks had shifts in both directions relative to the pure phase lines (Figure 4.23), contrary to the shift expected in one direction. Three of the high intensity peaks (at about 2θ = 40°, 47° and 68°), show similar behaviour to that observed with the high intensity peaks for $Pt_{78}:Al_{15.5}:Ru_2:Cr_{4.5}$, $Pt_{80}:Al_{14}:Ru_3:Cr_3$, $Pt_{81.5}:Al_{11.5}:Ru_{2.5}:Cr_{4.5}$. All reasonable peaks on the XRD spectrum were matched without $L1_2$ - ~Pt_3Al included (Figure 4.25), showing that $L1_2$ - ~Pt_3Al was not present. Table 4.11 shows the identified peaks together with their d-spacings.

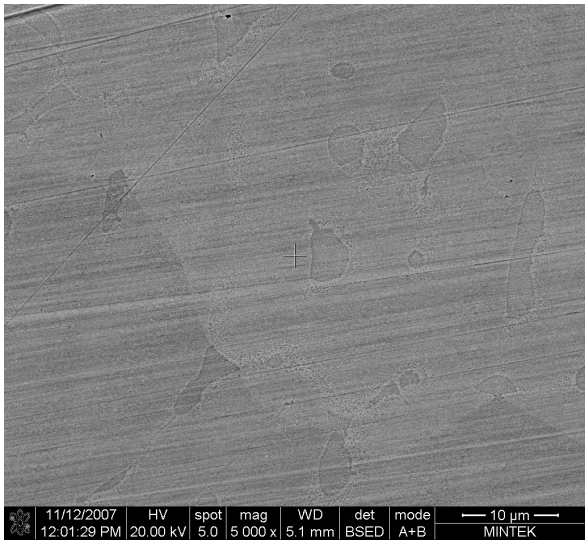

(a)

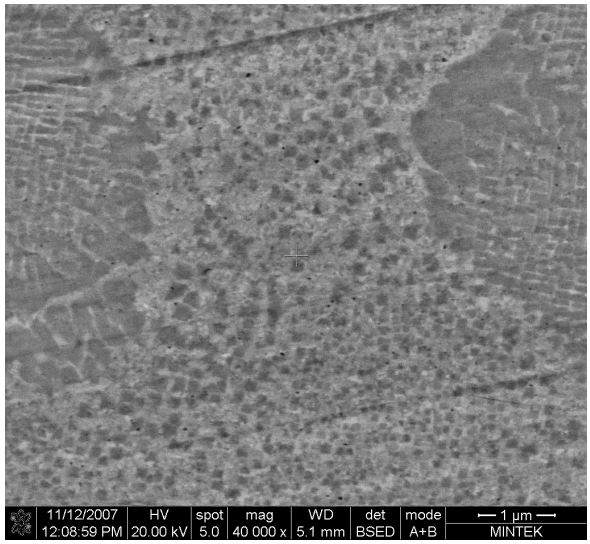

(b)

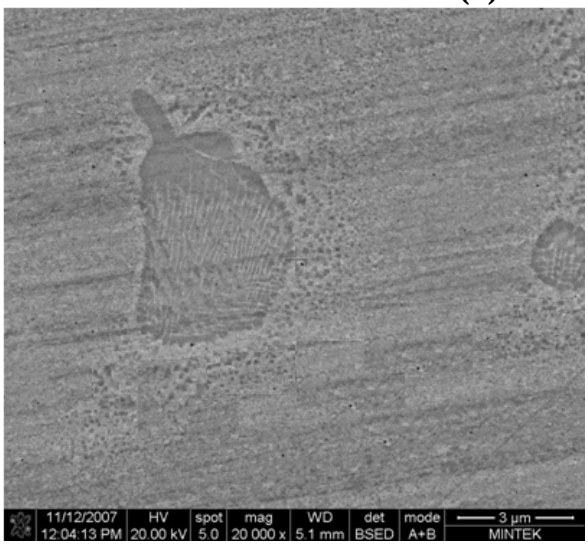

(c)

Figure 4.21. HR-SEM-BSE image of nominal Pt_{84}:Al_{11}:Ru_2:Cr_3, as-cast condition, taken from the centre (a-b) and (c) edge of the sample, showing (Pt) dendrites (light) with ~Pt_3Al precipitates and a eutectic of (Pt) + ~Pt_3Al.

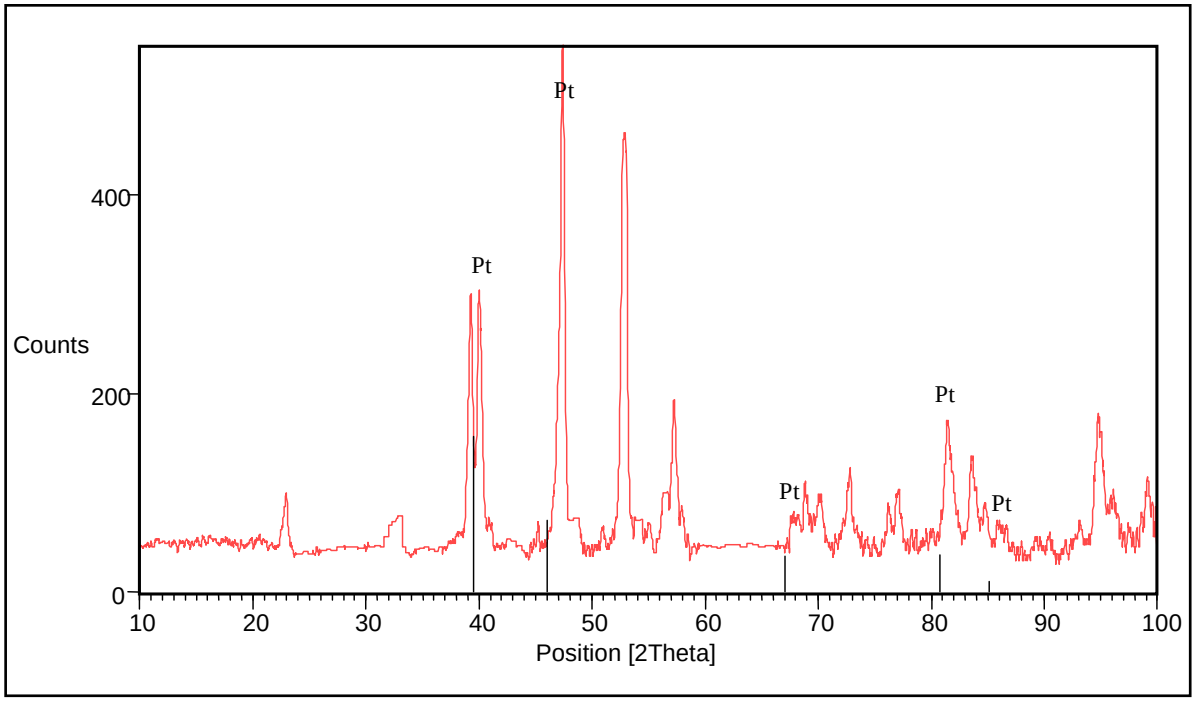

Figure 4.22. XRD Pattern of nominal Pt_{84}:Al_{11}:Ru_2:Cr_3 in the as-cast condition, showing identified Pt peaks.

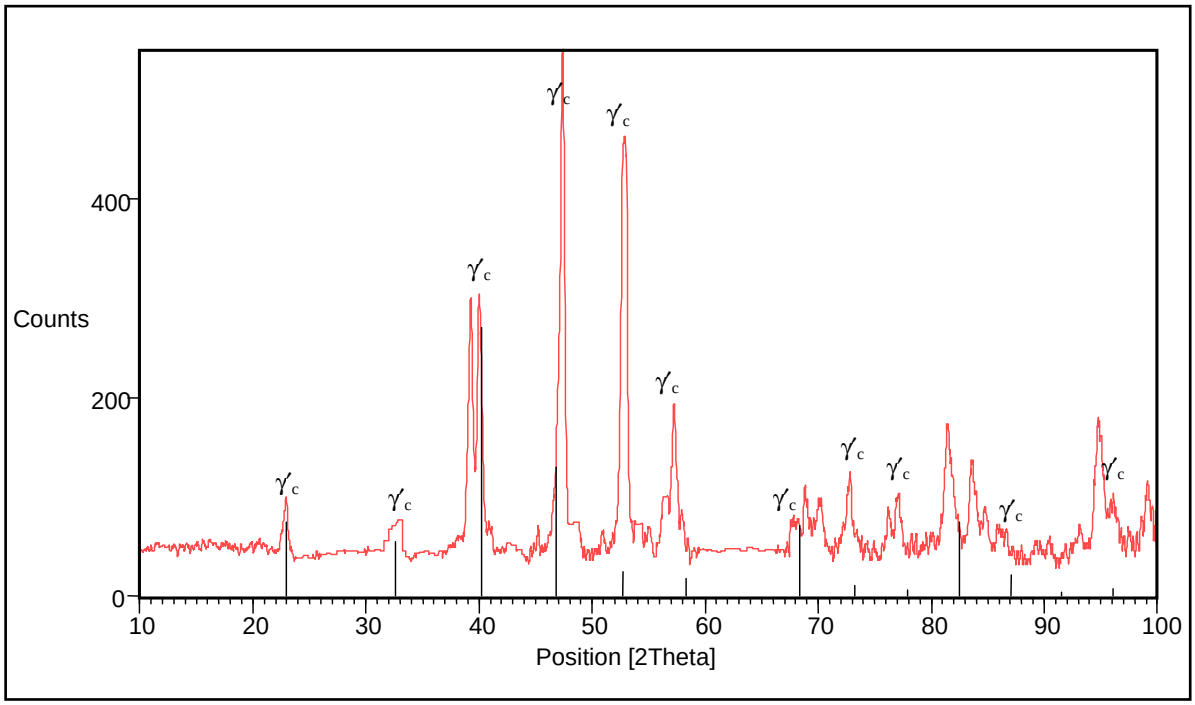

Figure 4.23. XRD Pattern of nominal Pt_{84}:Al_{11}:Ru_2:Cr_3 in the as-cast condition, showing apparent $L1_2$ – ~Pt_3Al peaks.

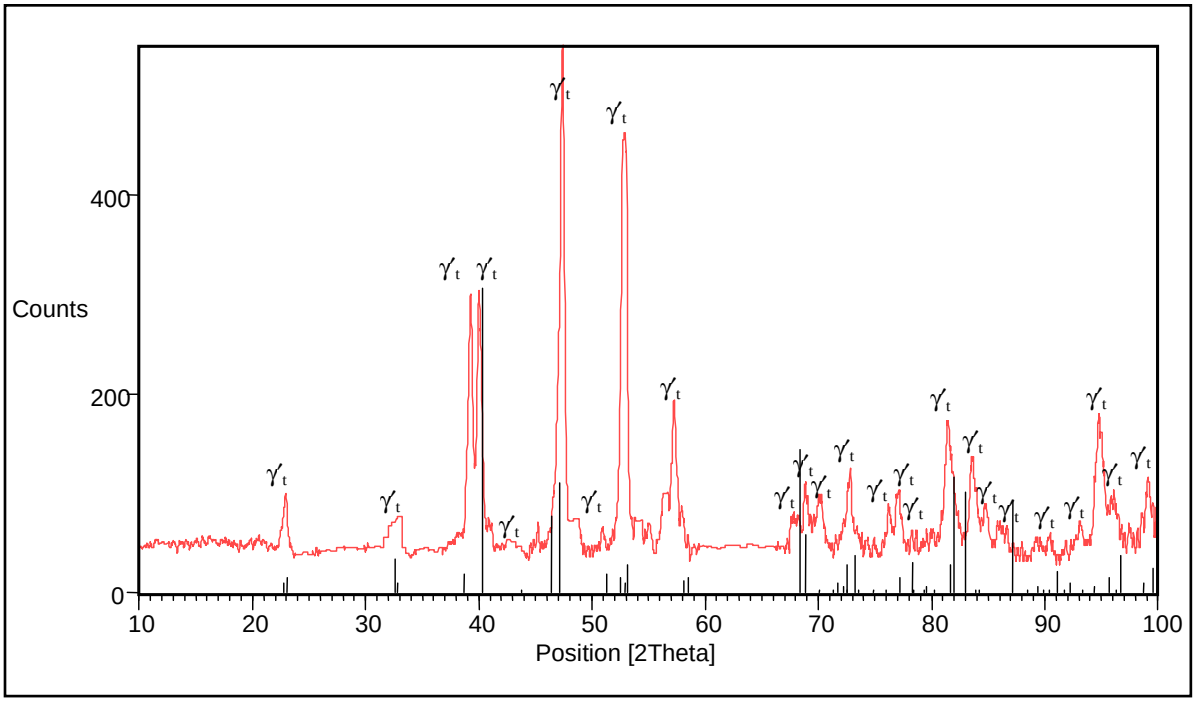

Figure 4.24. XRD Pattern of nominal Pt_{84}:Al_{11}:Ru_2:Cr_3 in the as-cast condition, showing identified DO'_c – ~Pt_3Al peaks.

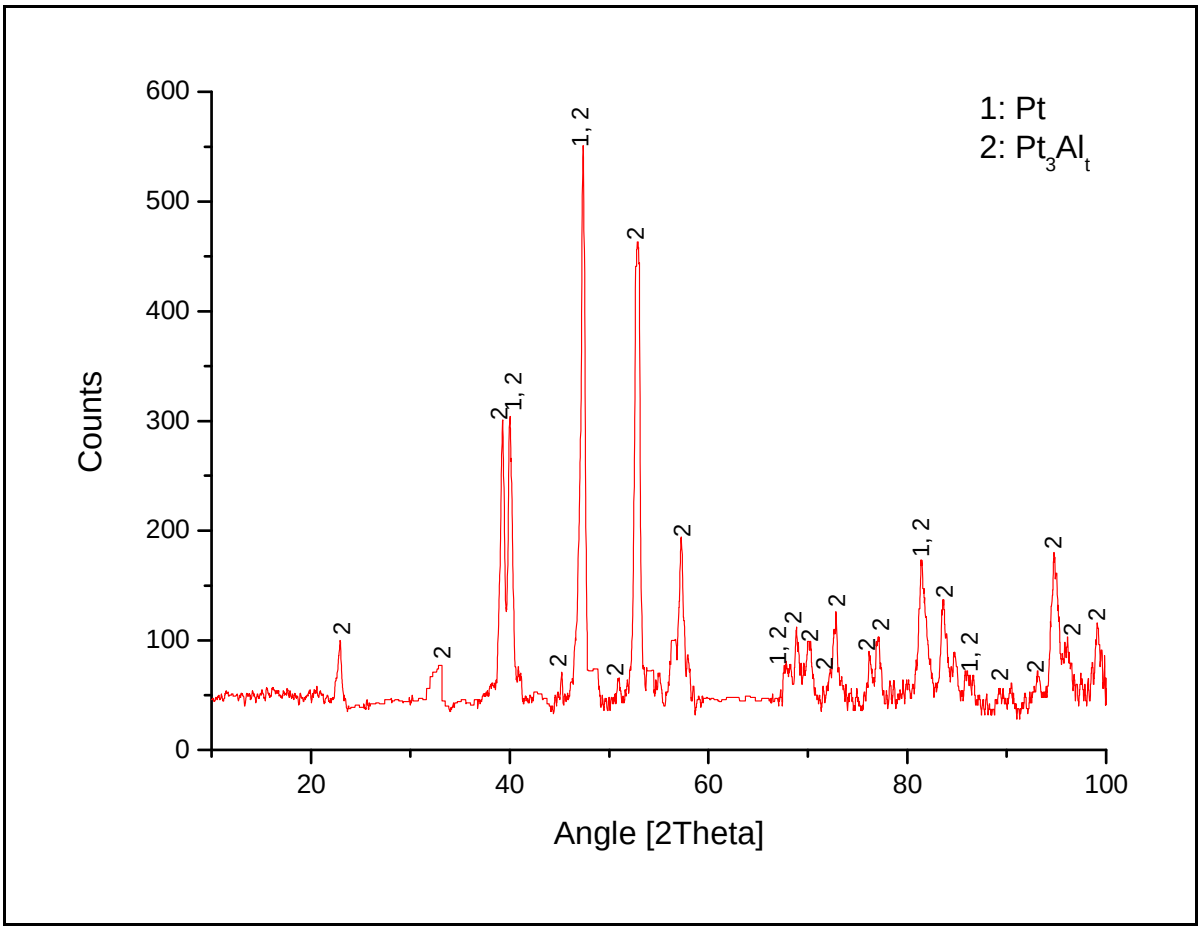

Figure 4.25. XRD pattern of nominal Pt_{84}:Al_{11}:Ru_2:Cr_3 in the as-cast condition, showing all identified phases.

Table 4.11. XRD peaks for Pt_{84}:Al_{11}:Ru_2:Cr_3 in the as-cast condition.

Position 2θ(°)	Height (counts)	Full-Width Half-Maximum 2θ(°)	d-spacing (Å)	Relative Intensity (%)	Phase (s)
22.9598	58.02	0.3149	3.87359	11.45	γ'_t
32.6379	33.6	0.9446	2.7437	6.63	γ'_t
39.3087	244.4	0.3149	2.2921	48.24	γ'_t
39.9816	244.43	0.1771	2.25506	48.24	(Pt), γ'_t
40.1324	24.21	0.1200	2.25066	4.38	-
45.0789	13.38	0.4723	2.01121	2.64	γ'_t
47.4100	506.68	0.2165	1.91762	100	(Pt), γ'_t
48.8406	30.53	0.551	1.86475	6.03	γ'_t
52.6967	390.35	0.1968	1.73702	77.04	γ'_t
53.0583	390.58	0.096	1.7246	77.09	γ'_t
56.3475	53.76	0.4723	1.63283	10.61	γ'_t
56.9511	72.76	0.4800	1.61562	4.31	-
57.3053	143.39	0.2165	1.6078	28.3	γ'_t
67.877	28.75	0.4723	1.38086	5.67	(Pt), γ'_t
68.8677	59.27	0.3149	1.36339	11.7	γ'_t
70.1423	48.94	0.4723	1.34171	9.66	γ'_t
72.7714	72.62	0.3936	1.29958	14.33	γ'_t
76.2303	41.64	0.2362	1.249	8.22	γ'_t
77.0036	54.02	0.3936	1.23837	10.66	γ'_t
81.3928	111.28	0.3936	1.18233	21.96	γ'_t
81.2549	58.21	0.6720	1.18300	5.53	-
83.6341	72.91	0.3542	1.15625	14.39	(Pt), γ'_t
84.6808	43.93	0.3936	1.14462	4.83	(Pt), γ'_t
89.2924	15.42	0.4723	1.09706	3.04	γ'_t
92.8041	21.38	0.5760	1.06366	4.25	-
93.1203	30.98	0.4723	1.06176	6.11	γ'_t
94.8489	130.28	0.3936	1.04692	25.71	γ'_t
96.1375	55.4	0.4723	1.03628	10.93	γ'_t
99.0951	74.48	0.384	1.01229	14.7	γ'_t

4.1.1.6. Nominal $Pt_{85}:Al_7:Ru_3:Cr_5$

HR-SEM-BSE images of both the edge and centre microstructure are shown in Figure 4.26, and discerning the microstructure was difficult, hence a higher magnification was used to view the microstructure. Both edge and centre consisted of (Pt) dendrites with fine ~Pt_3Al precipitates within and a eutectic of (Pt) + ~Pt_3Al. The dendrites were the major phase, 84 ± 7%, with an average arm spacing of 6.1 ± 1.3 µm.

The phase compositions are shown in Table 4.12, with Ru and Cr having limited solubility in the eutectic and partitioned preferentially to the (Pt) phase. A slightly lower solubility of Ru and Cr were measured, compared to the dendrites without the precipitates.

Table 4.12. EDX Phase compositions of nominal $Pt_{85}:Al_7:Ru_3:Cr_5$ in the as-cast condition.

Phase description	Al	Ru	Cr	Pt	Phase
Overall	6.1 ± 0.4	0.9 ± 0.3	3.5 ± 0.4	89.5 ± 0.6	-
Eutectic (Dark)	13.7 ± 0.1	0.6 ± 0.2	1.4 ± 0.3	84.3 ± 0.2	(Pt) + ~Pt_3Al
Dendrites (Light)	2.9 ± 0.3	1.8 ± 0.4	4.9 ± 0.2	90.4 ± 0.5	(Pt) + ~Pt_3Al
Dendrites + Visible precipitates	7.6 ± 0.7	0.8 ± 0.1	2.5 ± 0.3	89.1 ± 0.8	(Pt) + ~Pt_3Al

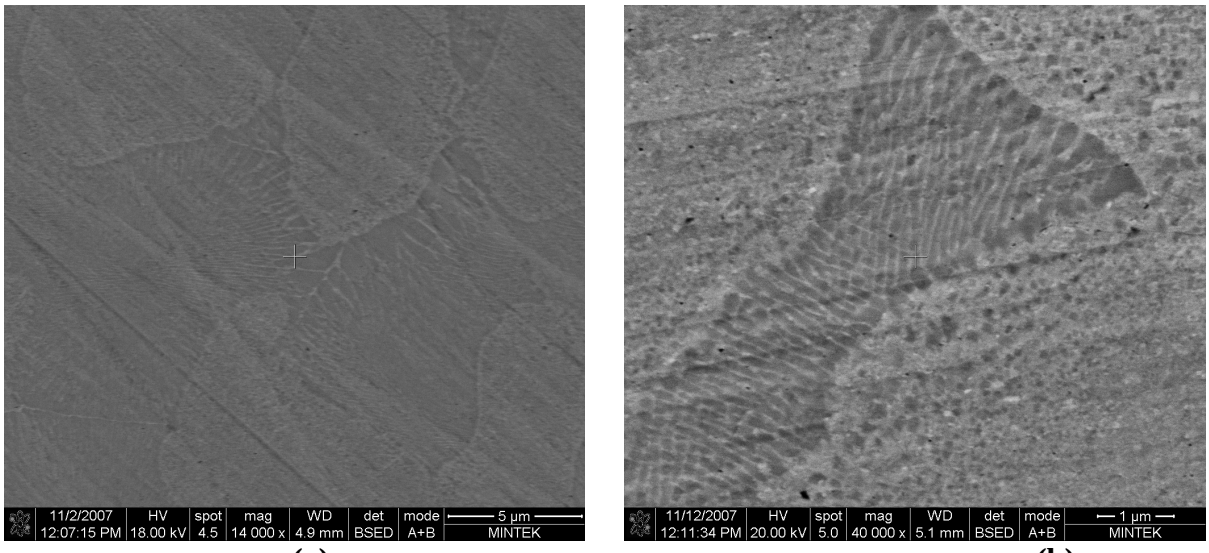

(a) **(b)**

Figure 4.26. HR-SEM-BSE image of nominal $Pt_{85}:Al_7:Ru_3:Cr_5$, as-cast condition, taken from the edge showing (Pt) dendrites (light) with fine ~Pt_3Al precipitates and a eutectic of (Pt) + ~Pt_3Al (dark).

As with the rest of the alloys, it was uncertain if both DO'_c - Pt_3Al and $L1_2$ - ~Pt_3Al were present in the alloy. The following observations were made:

- The shift for a cubic phase can only be in one direction. However, the apparent $L1_2$ - ~Pt_3Al had shifts in both directions (Figure 4.28).
- The peaks of DO'_c - Pt_3Al agree well (Figure 4.29).
- The highest intensity peaks (at about 2θ = 40°, 47° and 68°) were shown to be a combination of the DO'_c - Pt_3Al and (Pt) lines.
- All reasonable peaks on the XRD spectrum were matched without $L1_2$ - ~Pt_3Al.

The above four reasons show that $L1_2$ - ~Pt_3Al was not present. Figure 4.30 shows the experimental XRD spectrum labelled for all the identified phases. Table 4.13 shows the identified peaks together with their d-spacings.

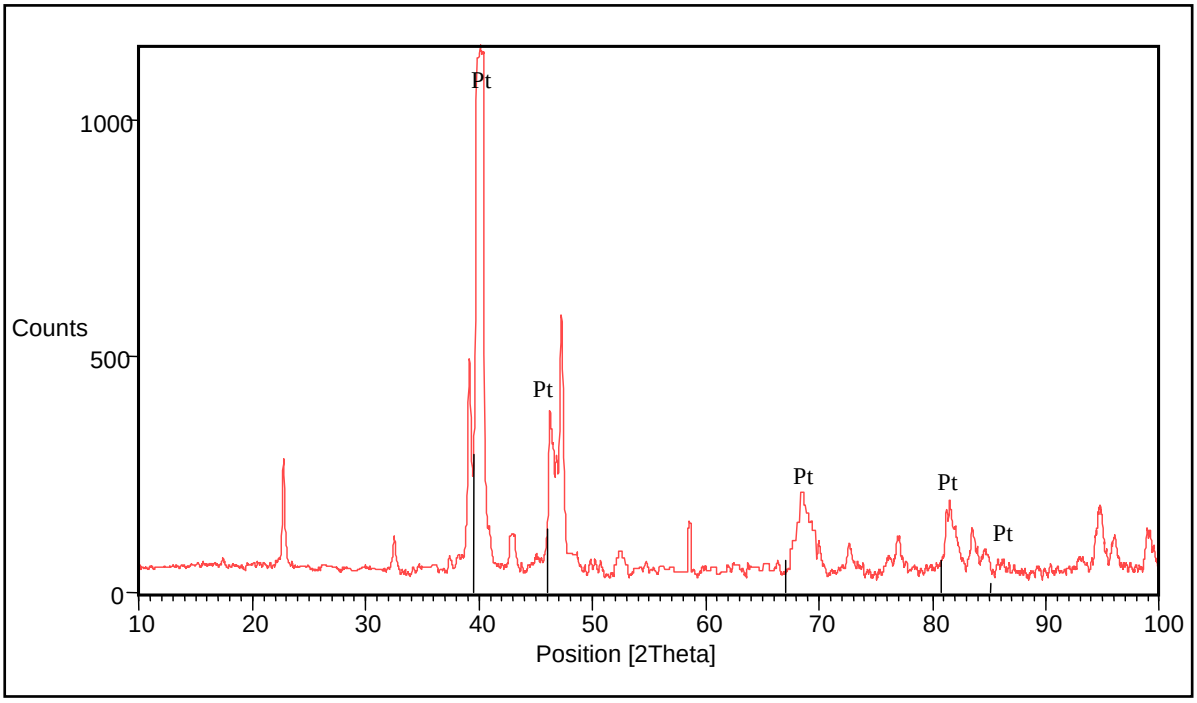

Figure 4.27. XRD Pattern of nominal Pt_{85}:Al_7:Ru_3:Cr_5 in the as-cast condition, showing identified Pt peaks.

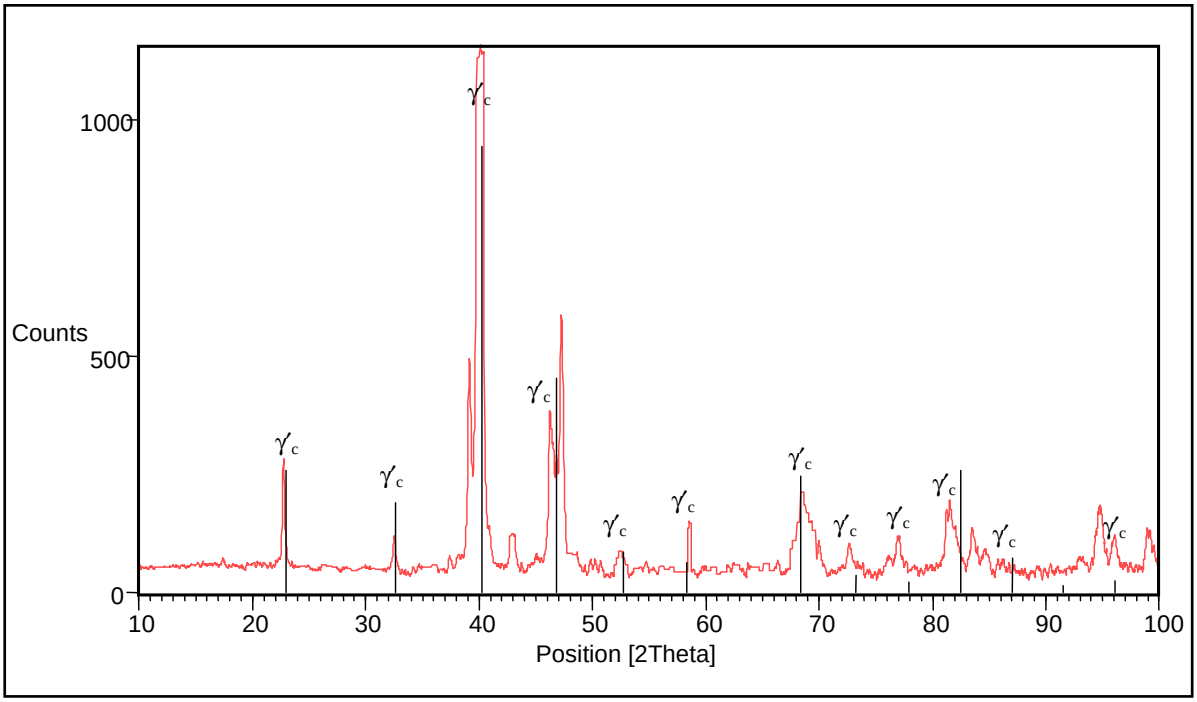

Figure 4.28. XRD Pattern of nominal Pt_{85}:Al_7:Ru_3:Cr_5 in the as-cast condition, showing apparent $L1_2$ – ~Pt_3Al peaks.

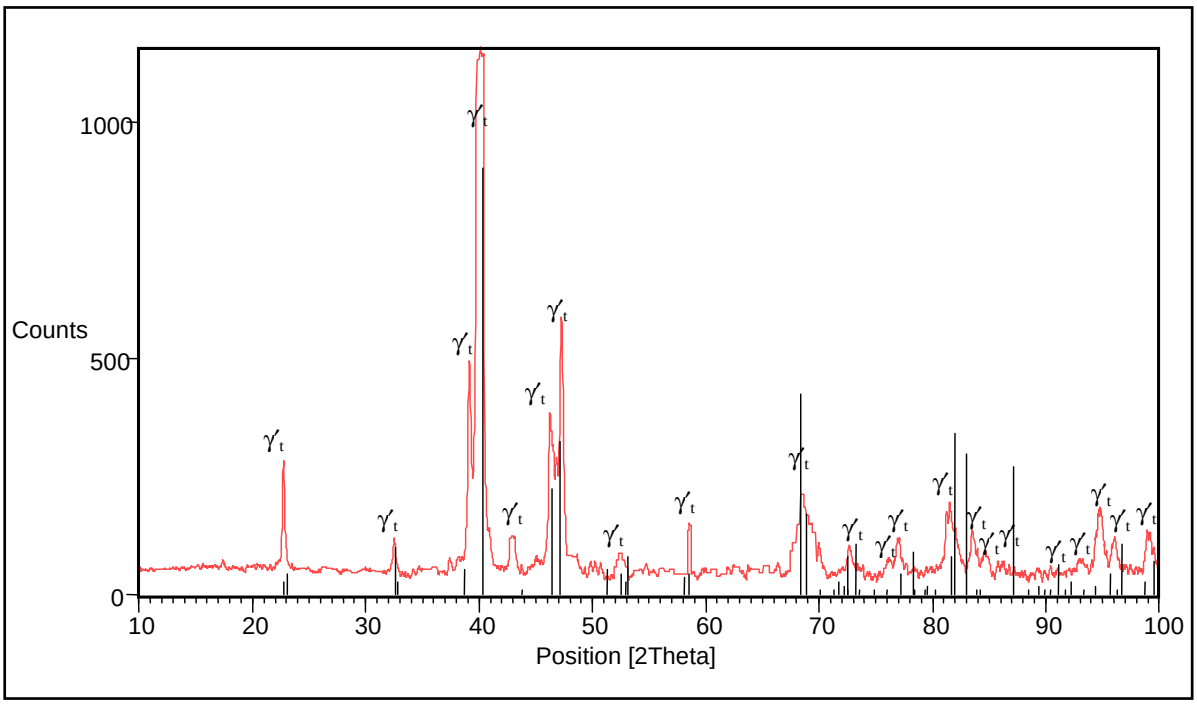

Figure 4.29. XRD Pattern of nominal Pt_{85}:Al_7:Ru_3:Cr_5 in the as-cast condition, showing identified DO'_c – ~Pt_3Al peaks.

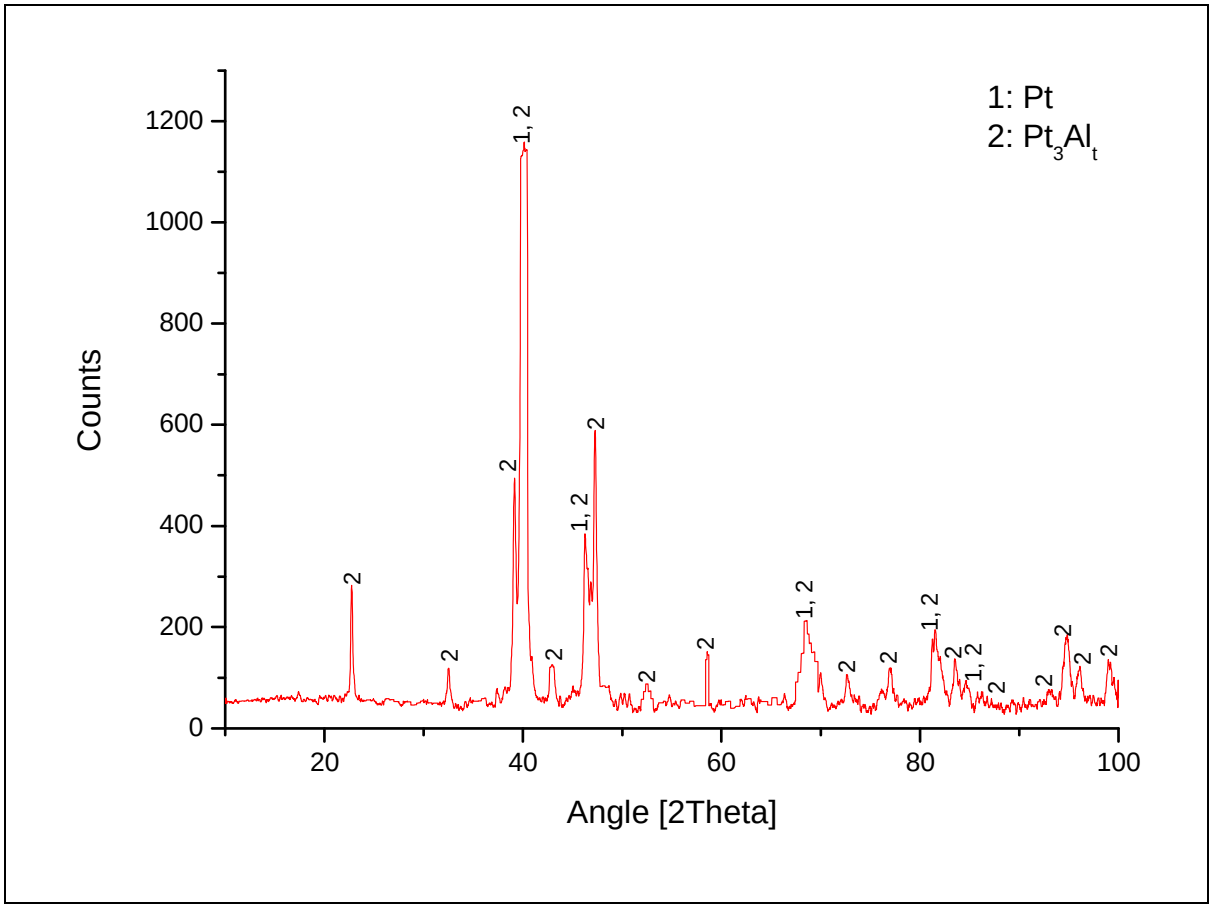

Figure 4.30. XRD pattern of nominal Pt_{85}:Al_7:Ru_3:Cr_5 in the as-cast condition, showing all identified phases.

Table 4.13. XRD peaks for Pt_{84}:Al_{11}:Ru_2:Cr_3 in the as-cast condition.

Position 2θ(°)	Height (counts)	Full-Width Half-Maximum 2θ(°)	d-spacing (Å)	Relative Intensity (%)	Phase (s)
22.7637	221.66	0.1771	3.90652	19.86	γ'_t
32.5079	74.19	0.1771	2.75438	6.65	γ'_t
37.4213	27.98	0.2362	2.40325	2.51	-
39.1127	431.14	0.2558	2.30313	38.64	γ'_t
39.7769	1070.99	0.1181	2.2662	95.98	γ'_t
40.4358	1115.87	0.072	2.22893	100	(Pt), γ'_t
42.806	75.49	0.551	2.11259	6.77	γ'_t
45.2802	30.86	0.3936	2.00316	4.53	-
46.2565	318.16	0.1771	1.96272	28.51	(Pt), γ'_t
47.2516	524.16	0.2755	1.92368	46.97	γ'_t
50.7506	23.29	0.2362	1.79896	2.09	γ'_t
50.8876	47.71	0.2362	1.79444	8.95	-
52.4518	46.94	0.7872	1.74455	4.21	γ'_t
58.4854	92.37	0.1181	1.57814	8.28	γ'_t
66.3958	19.67	0.2362	1.40802	1.76	γ'_t
68.4684	146.23	0.3149	1.37037	13.1	(Pt), γ'_t
72.6633	61.04	0.3936	1.30125	5.47	γ'_t
76.1197	33.16	0.551	1.25054	2.97	γ'_t
76.9908	72.47	0.3936	1.23855	6.49	γ'_t
81.2113	125.17	0.1771	1.18451	11.22	γ'_t
83.5484	88.32	0.3149	1.15722	7.91	(Pt), γ'_t
84.7545	40.11	0.4723	1.14381	3.59	(Pt), γ'_t
85.8022	24.86	0.2755	1.13251	2.23	γ'_t
93.1089	27.07	0.6298	1.06186	2.43	γ'_t
94.8829	128.68	0.3542	1.04663	11.53	γ'_t
96.0745	74.19	0.4723	1.03679	6.65	γ'_t
98.9098	79.06	0.48	1.01369	7.09	γ'_t

4.1.2 Heat Treated Alloys: Microstructural Characterisation

4.1.2.1 Nominal $Pt_{78}:Al1_{5.5}:Ru_2:Cr_{4.5}$

An HR-SEM-BSE image is given in Figure 4.31, showing a microstructure with very fine ~Pt_3Al precipitates in a (Pt) matrix, which were very difficult to discern due to scratches. The sample appeared fairly homogeneous as the whole surface showed the same microstructure.

The overall composition is shown in Table 4.14, and was different from the as-cast composition. The scratches and fineness of the microstructure prevented further analysis.

Table 4.14. EDX overall composition of nominal $Pt_{78}:Al_{15.5}:Ru_2:Cr_{4.5}$ in the heat treated condition.

Phase description	Al	Ru	Cr	Pt	Phase
Overall	9.8 ± 0.7	1.5 ± 0.3	3.8 ± 0.8	84.9 ± 0.5	-

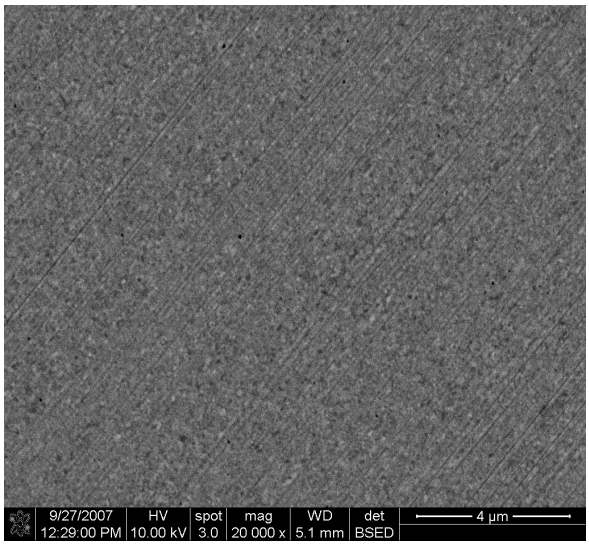

Figure 4.31. HR-SEM-BSE image of nominal $Pt_{78}:Al_{15.5}:Ru_2:Cr_{4.5}$ after heat treatment, showing very fine ~Pt_3Al precipitates (dark) in a (Pt) matrix (light).

The XRD spectrum of the heat treated samples was different from the as-cast samples and had a high background. The (Pt) peaks shifted to the right relative to pure Pt lines (Figure 4.32). $L1_2$ - ~Pt_3Al had shifting in both directions relative to pure $L1_2$ - ~Pt_3Al lines, which is not possible for a cubic phase (Figure 4.33). The highest intensity peaks (at about 2θ = 46°, 81°) shows that the peaks are probable a combination of the (Pt) and all peaks are matched without the $L1_2$ - ~Pt_3Al phase included in the XRD spectrum, thus $L1_2$ - ~Pt_3Al is not

present. Figure 4.35 shows the experimental XRD spectrum labelled for all of the identified phases. Table 4.15 gives the identified peaks together with the d-spacings.

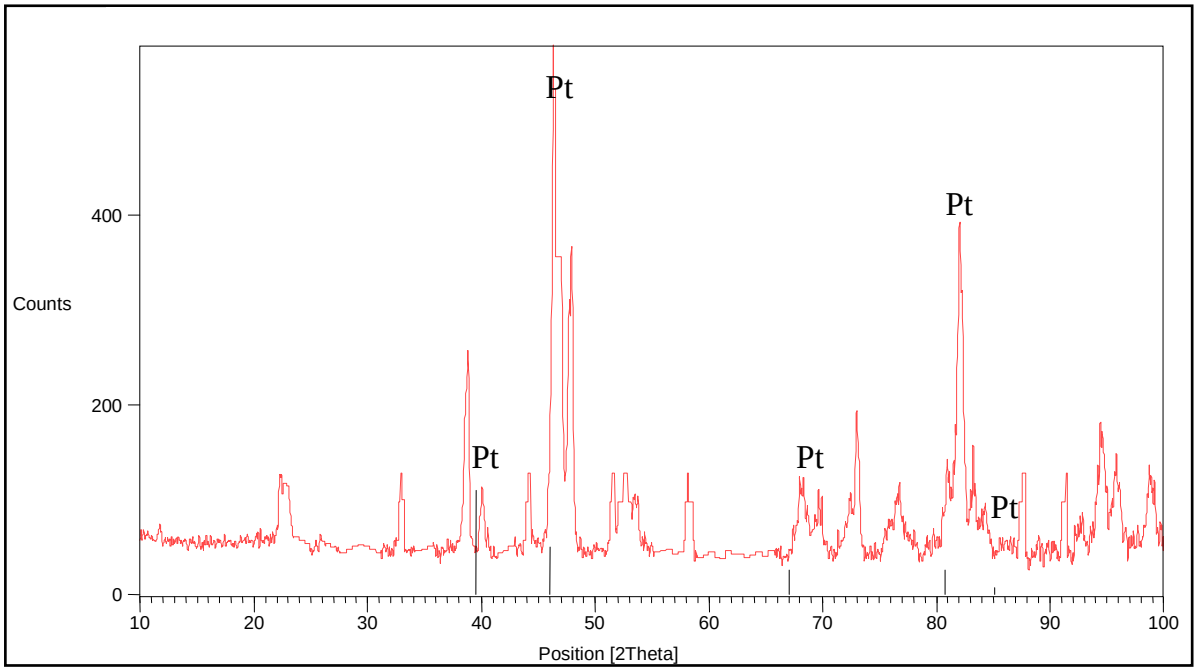

Figure 4.32. XRD Pattern of nominal Pt_{78}:$Al_{15.5}$:Ru_2:$Cr_{4.5}$ in the heat treated condition, showing identified Pt peaks.

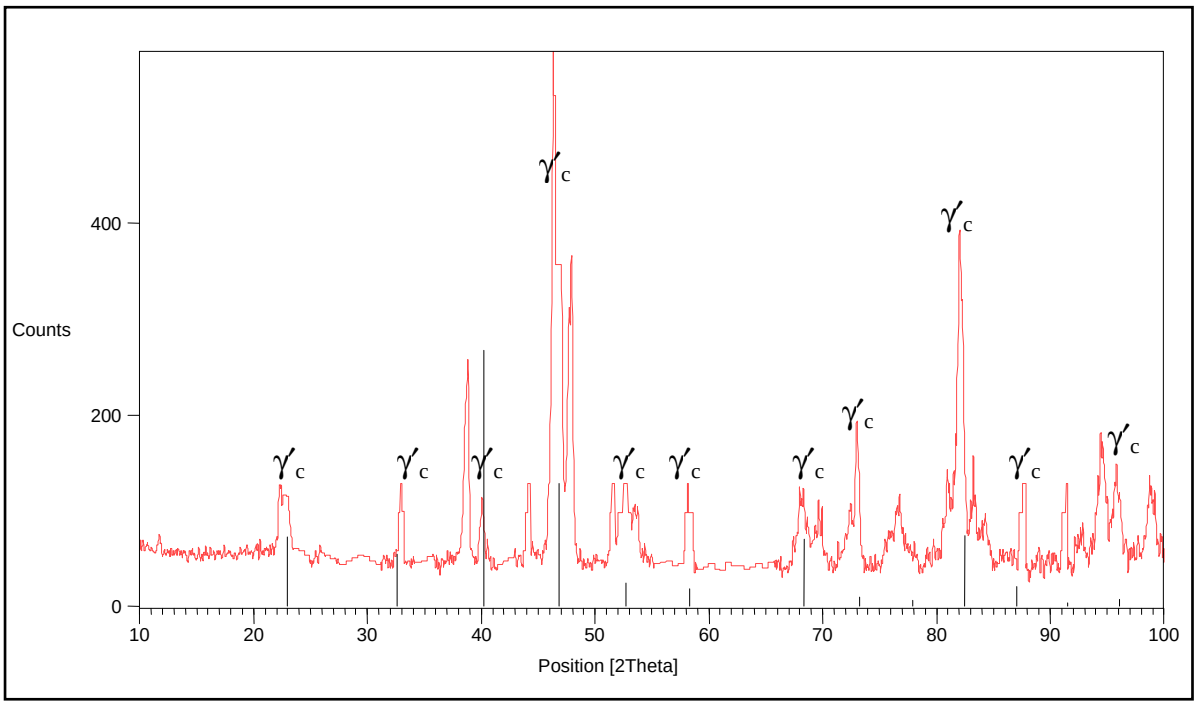

Figure 4.33. XRD Pattern of nominal Pt_{78}:$Al_{15.5}$:Ru_2:$Cr_{4.5}$ in the heat treated condition, showing apparent $L1_2$ – ~Pt_3Al peaks.

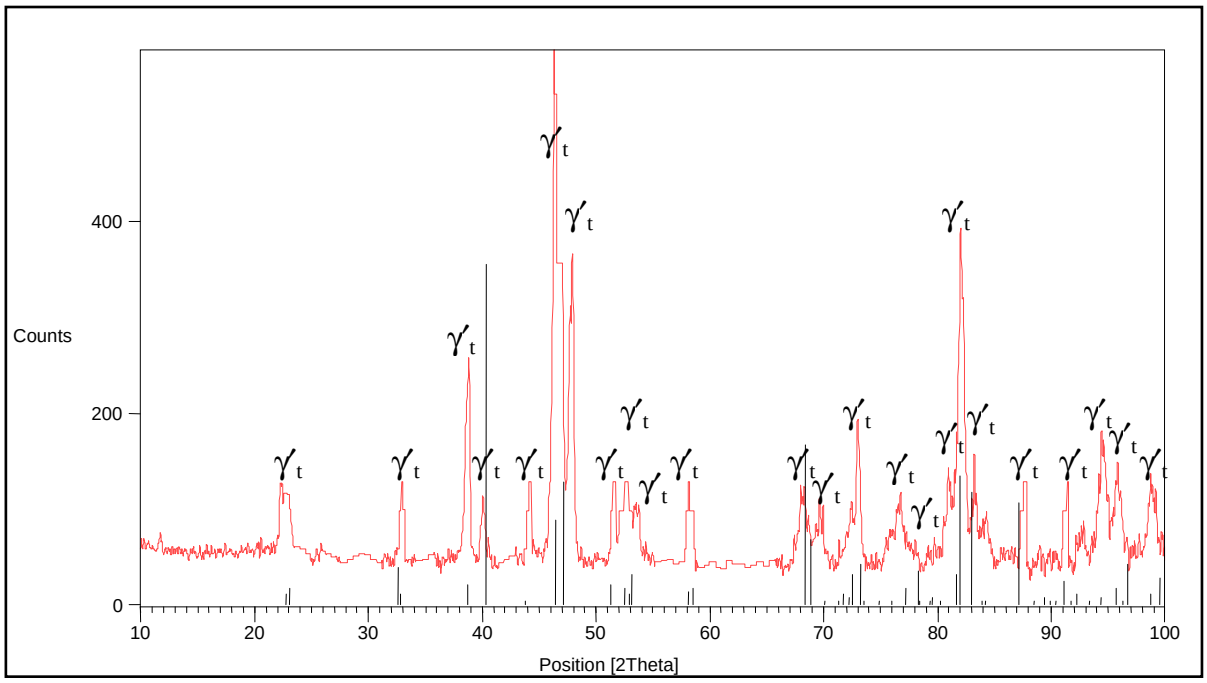

Figure 4.34. XRD Pattern of nominal Pt_{78}:$Al_{15.5}$:Ru_2:$Cr_{4.5}$ in the heat treated condition, showing identified DO'_c – ~Pt_3Al peaks.

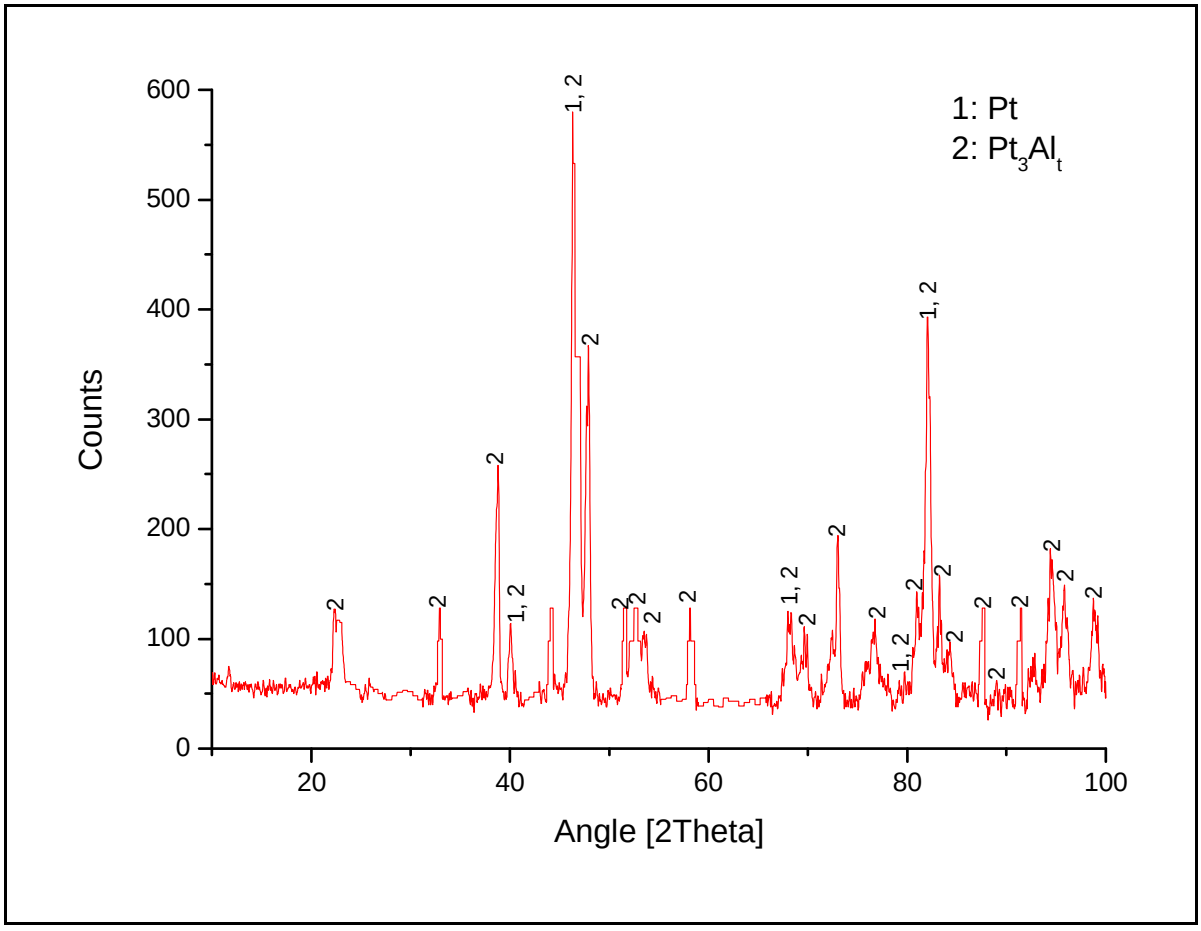

Figure 4.35. XRD pattern of nominal Pt_{78}:$Al_{15.5}$:Ru_2:$Cr_{4.5}$ in the heat treated condition, showing all identified phases.

Table 4.15. XRD peaks for Pt_{78}:$Al_{15.5}$:Ru_2:$Cr_{4.5}$ in the heat treated condition.

Position 2θ(°)	Height (counts)	Full-Width Half-Maximum 2θ(°)	d-spacing (Å)	Relative Intensity (%)	Phase (s)
22.8066	56.27	0.4723	3.89926	11.79	γ′t
26.7334	12.59	0.4723	3.74905	4.27	-
32.9473	82.31	0.3149	2.71864	17.24	γ′t
38.8085	205.15	0.1378	2.32048	42.97	(Pt), γ′t
40.0653	64.47	0.3936	2.25055	13.50	γ′t
44.3440	36.22	0.2362	2.04282	6.84	-
44.2385	77.86	0.2362	2.04745	16.31	γ′t
46.3687	477.44	0.1574	1.95823	100.00	γ′t
46.9892	299.26	0.1574	1.93381	62.68	γ′t
47.7327	258.11	0.2160	1.90383	54.06	(Pt), γ′t
47.9090	314.17	0.1968	1.89881	65.80	γ′t
51.6376	80.93	0.2362	1.77013	16.95	γ′t
52.6670	77.63	0.3149	1.73793	16.26	γ′t
53.5133	51.57	0.3936	1.71242	10.80	γ′t
58.1032	77.67	0.3149	1.58761	16.27	γ′t
69.9383	44.05	0.1440	1.34401	9.23	(Pt), γ′t
73.0010	135.82	0.1968	1.29606	28.45	γ′t
81.0199	75.07	0.2362	1.18682	15.72	(Pt), γ′t
82.0491	340.23	0.1920	1.17355	71.26	(Pt), γ′t
83.2671	88.87	0.2362	1.16041	18.61	γ′t
84.2032	37.90	0.4723	1.14988	7.94	γ′t
87.7179	86.65	0.2362	1.11265	18.15	γ′t
91.4482	87.56	0.1440	1.07586	18.34	γ′t
95.7896	60.01	0.3149	1.03912	12.57	γ′t
98.7958	63.54	0.2880	1.01456	13.31	γ′t

4.1.2.2 Nominal Pt_{80}:Al_{14}:Ru_3:Cr_3

An HR-SEM-BSE image of nominal Pt_{80}:Al_{14}:Ru_3:Cr_3 is shown in Figure 4.36. The microstructure was very difficult to discern due to the scratches, even under the HR-SEM and showed very fine ~Pt_3Al precipitates in a (Pt) matrix. The scratches and fineness of the microstructure prevented further compositional analysis. The overall composition is shown in Table 4.16, with Ru and Cr close to the targeted and as-cast compositions.

Table 4.16. EDX overall composition of nominal Pt_{80}:Al_{14}:Ru_3:Cr_3 in the heat treated condition.

Phase description	Al	Ru	Cr	Pt	Phase
Overall	8.6 ± 0.8	2.0 ± 0.6	2.4 ± 0.9	87.0 ± 0.7	-

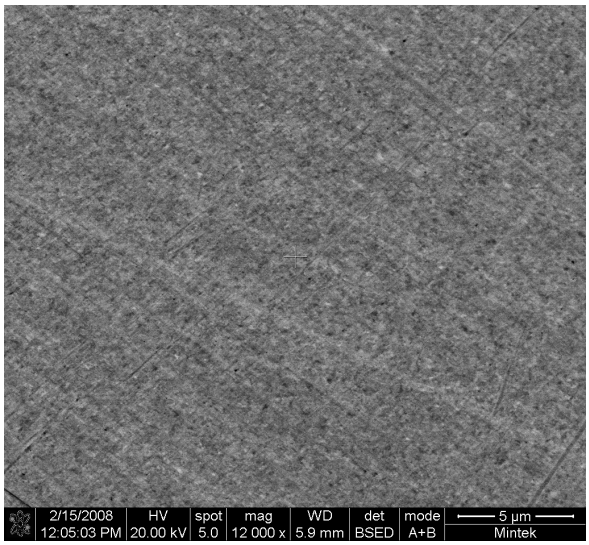

Figure 4.36. HR-SEM-BSE image of nominal Pt_{80}:Al_{14}:Ru_3:Cr_3 after heat treatment, showing very fine ~Pt_3Al precipitates (dark) in a (Pt) matrix (light) and a third lighter phase.

Similar to the first alloy, the same observations were made regarding $L1_2$ - ~Pt_3Al. All peaks were matched without $L1_2$ - ~Pt_3Al included. The peaks of DO'_c - ~Pt_3Al agree well with the XRD spectrum (Figure 4.39). Figure 4.40 shows the experimental XRD spectrum labelled for all of the identified phases. Table 4.17 shows the identified peaks together with their d-spacings.

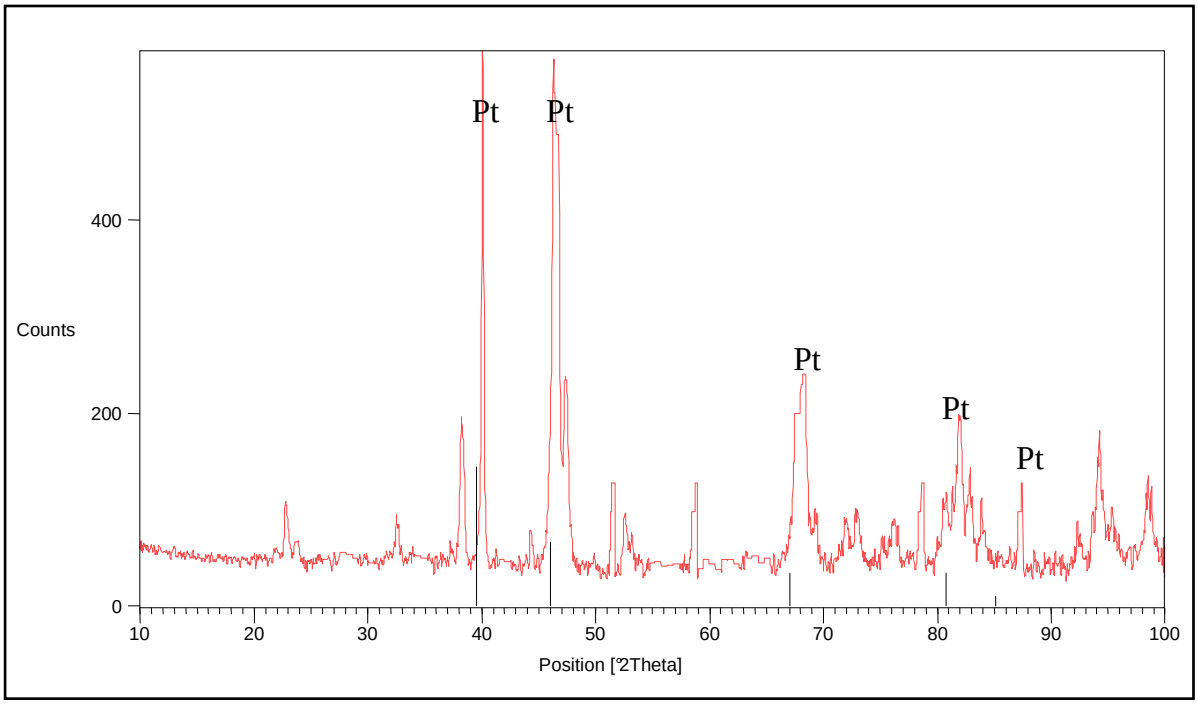

Figure 4.37. XRD Pattern of nominal Pt_{80}:Al_{14}:Ru_3:Cr_3 in the heat treated condition, showing identified Pt peaks.

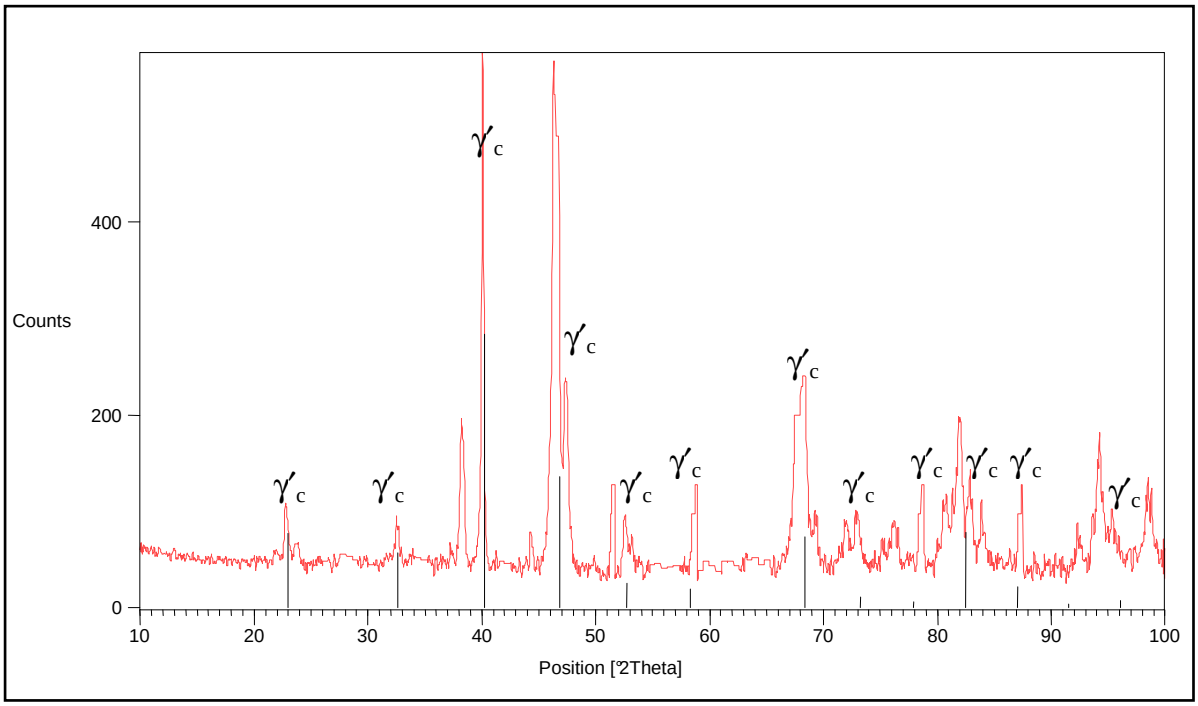

Figure 4.38. XRD Pattern of nominal Pt_{80}:Al_{14}:Ru_3:Cr_3 in the heat treated condition, showing apparent $L1_2$ – ~Pt_3Al peaks.

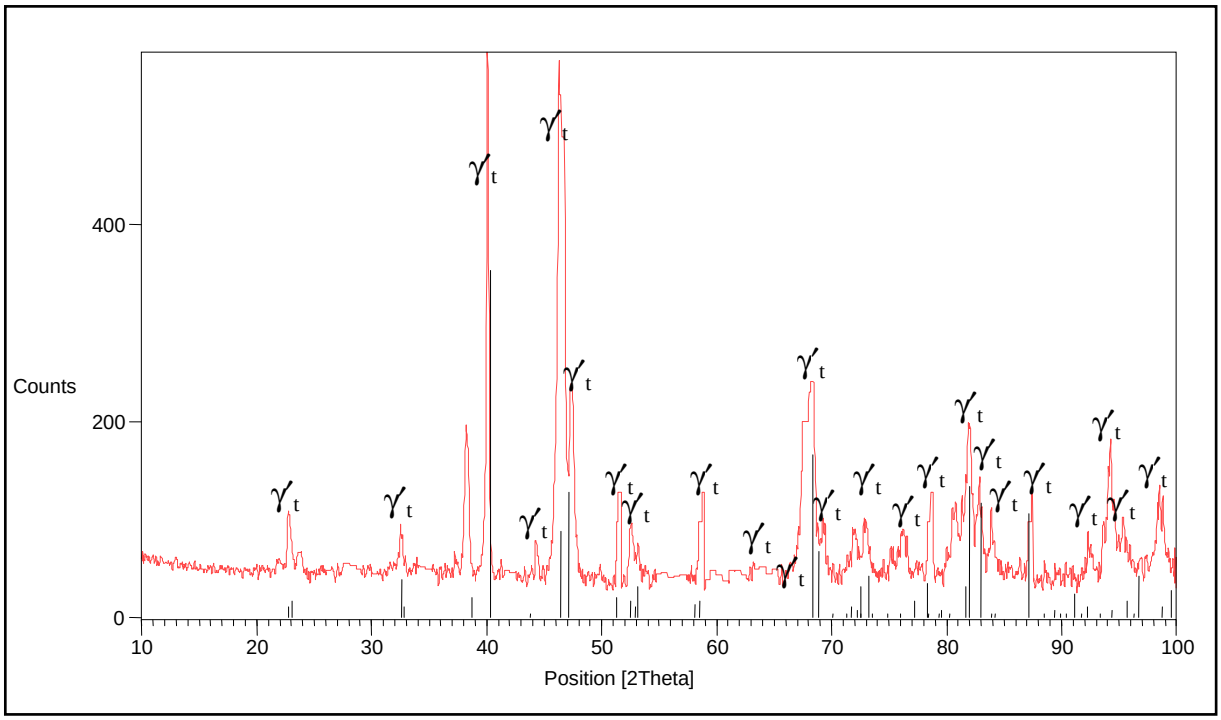

Figure 4.39. XRD Pattern of nominal Pt_{80}:Al_{14}:Ru_3:Cr_3 in the heat treated condition, showing identified DO'_c – ~Pt_3Al peaks.

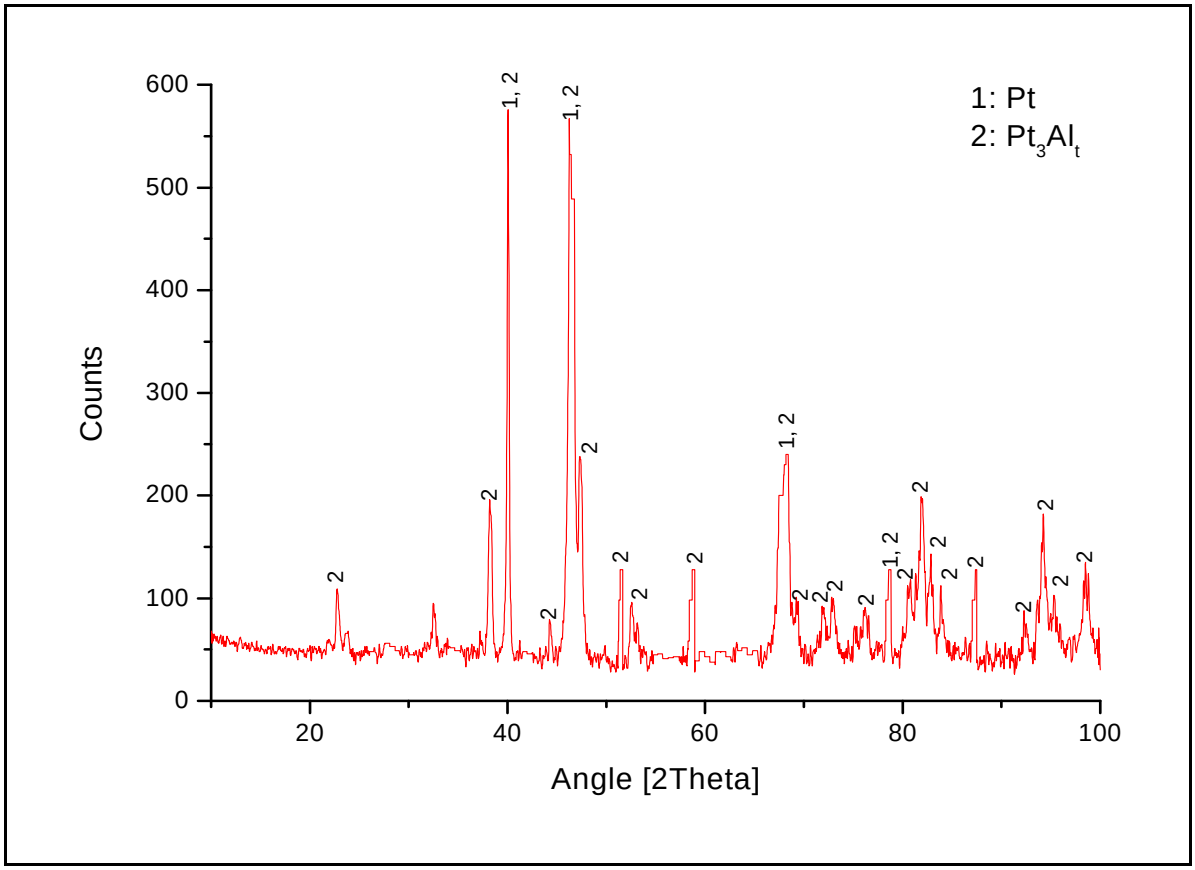

Figure 4.40. XRD pattern of nominal Pt_{80}:Al_{14}:Ru_3:Cr_3 in the heat treated condition, showing all identified phases.

Table 4.17. XRD peaks for Pt_{80}:Al_{14}:Ru_3:Cr_3 in the heat treated condition.

Position 2θ(°)	Height (counts)	Full-Width Half-Maximum 2θ(°)	d-spacing (Å)	Relative Intensity (%)	Phase (s)
22.7773	57.92	0.2755	3.90420	10.94	γ′t
26.7334	12.59	0.4723	3.74905	4.27	-
32.5604	39.45	0.2362	2.75006	7.45	γ′t
38.2275	144.71	0.2362	2.35441	27.33	γ′t
40.0588	529.57	0.1968	2.25089	100.00	(Pt), γ′t
44.3440	36.22	0.2362	2.04282	6.84	γ′t
46.3307	471.48	0.2362	1.95975	89.03	γ′t
46.7020	428.60	0.1574	1.94503	80.93	-
47.3530	183.14	0.1574	1.91980	34.58	(Pt), γ′t
49.7994	74.50	0.1908	1.90290	5.14	-
51.5550	93.06	0.1968	1.77277	17.57	γ′t
52.5746	54.74	0.3149	1.74077	10.34	γ′t
54.5736	45.88	0.3149	1.71064	6.14	-
58.8340	88.72	0.1968	1.56962	16.75	γ′t
67.5115	144.57	0.3149	1.38744	27.30	γ′t
68.3455	189.04	0.3149	1.37253	35.70	(Pt), γ′t
69.2870	45.67	0.2362	1.35616	8.62	γ′t
71.9780	39.46	0.3149	1.31194	7.45	γ′t
72.9404	45.85	0.3936	1.29699	8.66	γ′t
78.7153	83.85	0.2362	1.21568	15.83	γ′t
80.7007	49.17	0.3936	1.19071	9.29	γ′t
81.9667	141.15	0.3936	1.17550	26.65	(Pt), γ′t
82.8454	80.07	0.3936	1.16525	15.12	γ′t
83.8653	58.82	0.1680	1.15270	11.11	γ′t
87.4090	89.78	0.1440	1.11486	16.95	(Pt), γ′t
92.3848	26.94	0.3936	1.06827	5.09	γ′t
94.2003	101.21	0.3149	1.05241	19.11	γ′t
98.4625	59.62	0.2880	1.01710	11.26	γ′t

4.1.2.3 Nominal $Pt_{81.5}$:$Al_{11.5}$:$Ru_{2.5}$:$Cr_{4.5}$

HR-SEM-BSE images of both the centre and edge microstructure are shown in Figure 4.9, and both consisted of rounded ~Pt_3Al precipitates in a (Pt) matrix, confirming homogeneity of the sample. The precipitates were not aligned within the grains. The average precipitate size was 0.8 ± 0.4 µm with a volume fraction of 12 ± 6 % of the microstructure. Some ~Pt_3Al precipitated on grain boundaries.

The phase compositions are shown in Table 4.18. The overall composition varied from the targeted and as-cast composition. The ~Pt_3Al precipitates could not be measured accurately since they were far too small (much less than 3 µm beam spread expected), although the standard deviation was small, which is due to similar areas being measured. Thus, the analyses are very approximate. However, they were useful for accessing trends on the solubility of the elements in the (Pt) and ~Pt_3Al phase.

Table 4.18. EDX Phase compositions of nominal $Pt_{81.5}$:$Al_{11.5}$:$Ru_{2.5}$:$Cr_{4.5}$ in the heat treated condition.

Phase description	Al	Ru	Cr	Pt	Phase
Overall	8.6 ± 0.5	1.4 ± 0.1	3.8 ± 0.1	86.2 ± 0.5	-
Dark (Precipitates)	21.6 ± 0.3	0.5 ± 0.3	1.6 ± 0.1	76.3 ± 0.1	~Pt_3Al
Light (Matrix)	8.5 ± 0.5	1.2 ± 0.2	3.6 ± 0.2	86.7 ± 0.2	(Pt)

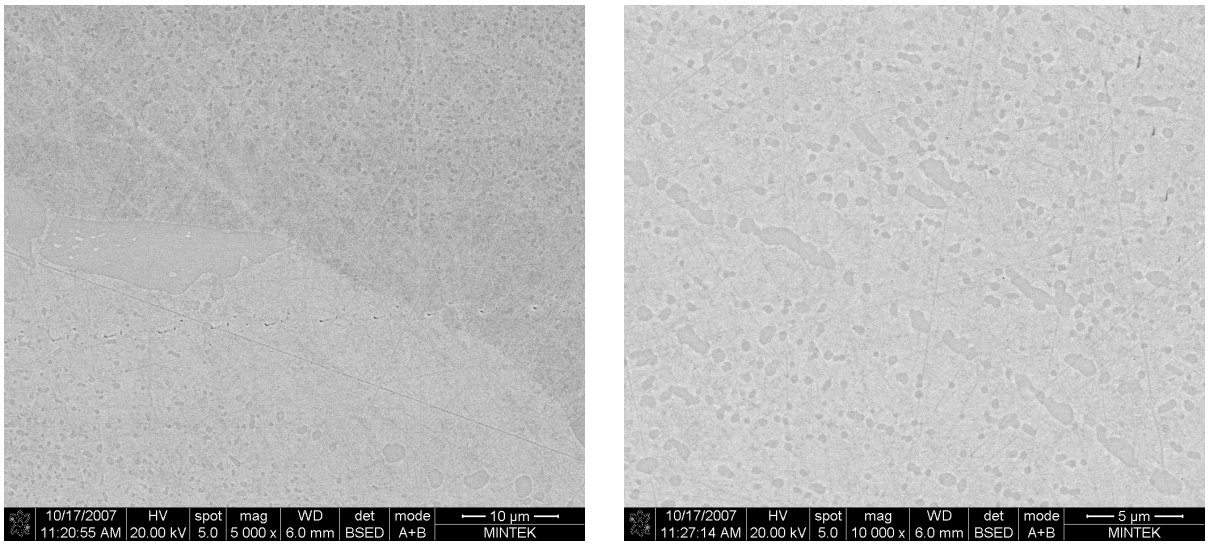

(a) **(b)**

Figure 4.41. HR-SEM-BSE image of nominal $Pt_{81.5}$:$Al_{11.5}$:$Ru_{2.5}$:$Cr_{4.5}$ after heat treatment, taken from the edge (a) and centre (b), showing ~Pt_3Al precipitates (dark) in a (Pt) matrix (light).

The apparent $L1_2$ - ~Pt_3Al had shifts in both directions relative to the pure phase lines (Figure 4.43), showing that it cannot be present. (Pt) and DO'_c - ~Pt_3Al agreed well and matched all peaks (Figures 4.42 to 4.44) and the high intensity peaks were a combination of both phases. Table 4.19 shows the identified peaks together with their d-spacings.

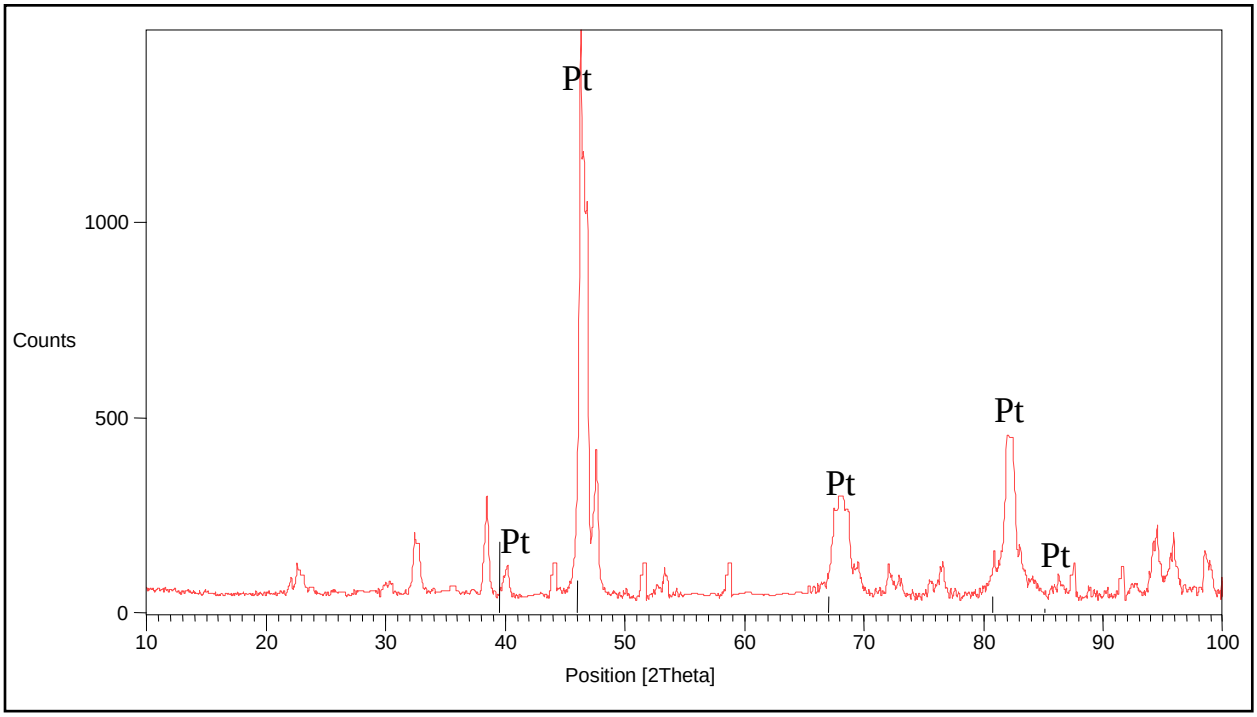

Figure 4.42. XRD Pattern of nominal $Pt_{81.5}$:$Al_{11.5}$:$Ru_{2.5}$:$Cr_{4.5}$ in the heat treated condition, showing identified Pt peaks.

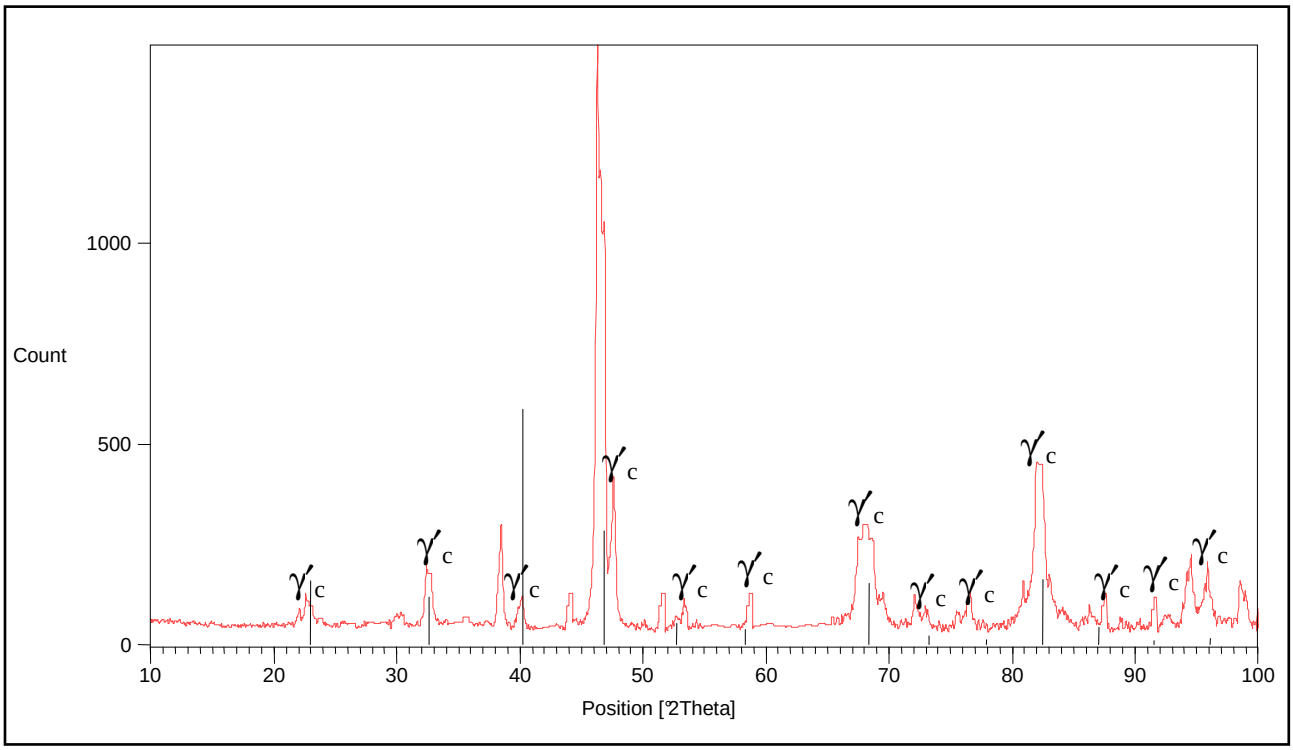

Figure 4.43. XRD Pattern of nominal $Pt_{81.5}$:$Al_{11.5}$:$Ru_{2.5}$:$Cr_{4.5}$ in the heat treated condition, showing apparent $L1_2$ – ~Pt_3Al peaks.

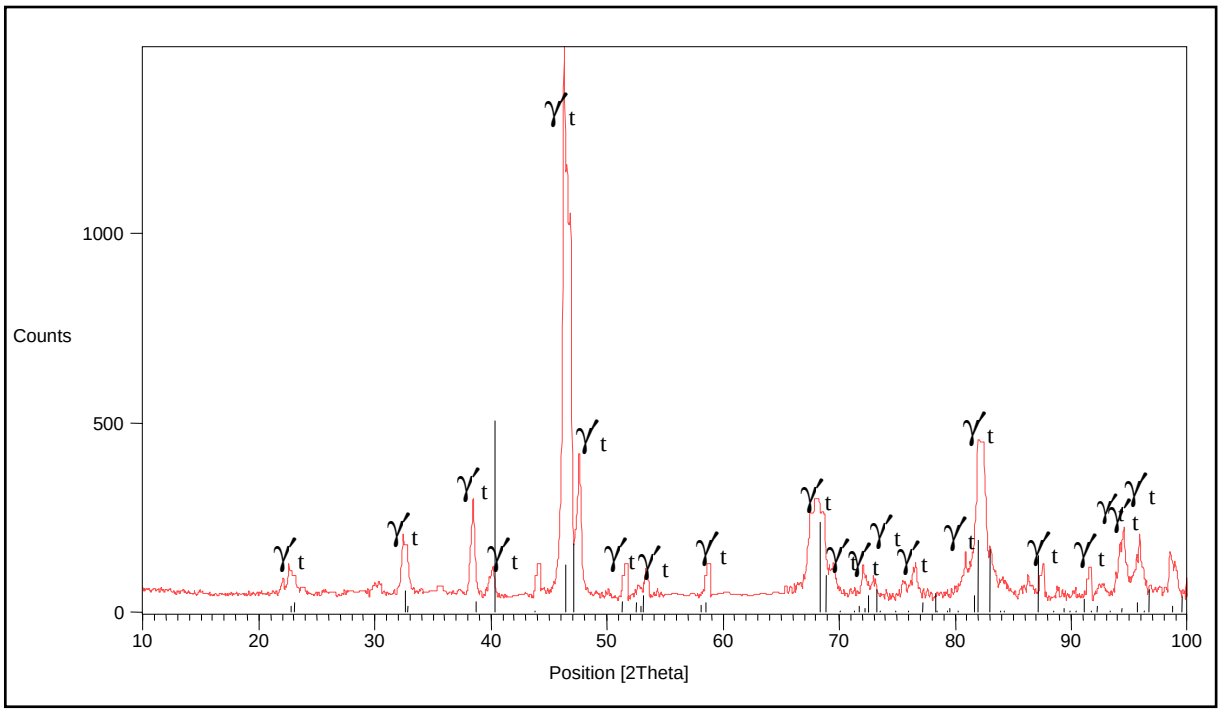

Figure 4.44. XRD Pattern of nominal $Pt_{81.5}$:$Al_{11.5}$:$Ru_{2.5}$:$Cr_{4.5}$ in the heat treated condition, showing identified DO'_c – ~Pt_3Al peaks.

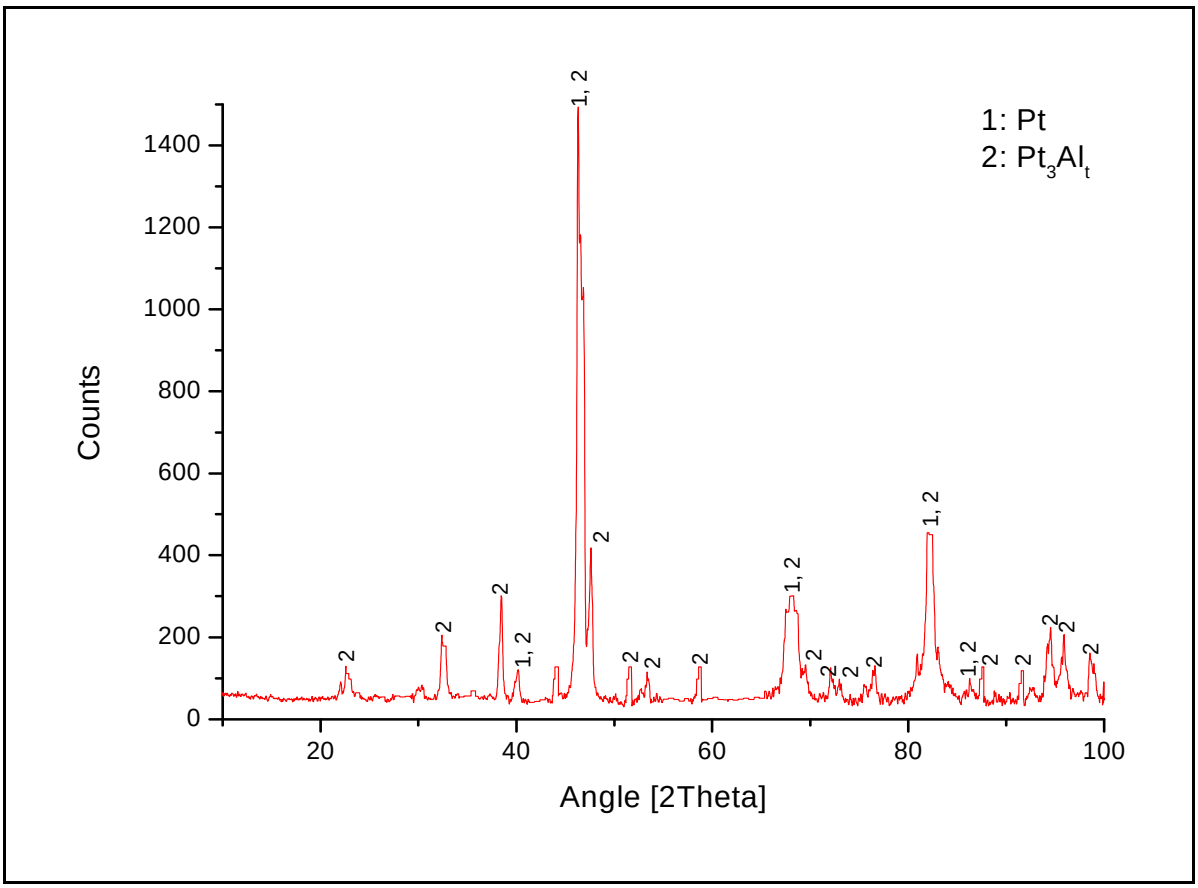

Figure 4.45. XRD pattern of nominal $Pt_{81.5}$:$Al_{11.5}$:$Ru_{2.5}$:$Cr_{4.5}$ in the heat treated condition, showing all identified phases.

Table 4.19. XRD peaks for $Pt_{81.5}$:$Al_{11.5}$:$Ru_{2.5}$:$Cr_{4.5}$ in the heat treated condition.

Position 2θ(°)	Height (counts)	Full-Width Half-Maximum 2θ(°)	d-spacing (Å)	Relative Intensity (%)	Phase (s)
22.0432	34.18	0.2362	4.03253	2.43	γ′t
22.6925	54.27	0.3149	3.91861	3.86	γ′t
32.4332	133.52	0.1968	2.76055	9.50	-
32.7586	120.72	0.2362	2.73387	8.59	γ′t
38.4615	248.76	0.1574	2.34062	17.70	-
40.1688	76.14	0.2165	2.24498	5.42	(Pt), γ′t
44.4778	77.46	0.2362	2.28805	12.63	-
44.1842	78.23	0.1181	2.04984	5.57	γ′t
46.3045	1405.09	0.1574	1.96079	100.00	(Pt), γ′t
46.8510	973.23	0.1181	1.93919	69.26	γ′t
47.6012	348.67	0.2755	1.91037	24.81	γ′t
51.6645	84.01	0.1181	1.76927	5.98	γ′t
53.4050	47.40	0.3936	1.71564	3.37	γ′t
58.7858	78.64	0.1181	1.57079	5.60	γ′t
67.4778	177.46	0.2362	1.38805	12.63	γ′t
68.6671	195.46	0.1574	1.36689	13.91	(Pt), γ′t
69.4509	63.90	0.3149	1.35336	4.55	γ′t
72.0823	72.57	0.1440	1.30922	5.16	γ′t
72.9896	38.56	0.3936	1.29624	2.74	γ′t
75.5812	37.72	0.2362	1.25810	2.68	γ′t
76.5252	70.97	0.3936	1.24492	5.05	γ′t
80.9122	81.40	0.1440	1.18715	5.79	γ′t
82.0155	358.53	0.2880	1.17395	25.52	γ′t
82.4845	322.43	0.3149	1.16943	22.95	(Pt), γ′t
87.6029	81.99	0.1920	1.11289	5.84	γ′t
91.6623	74.33	0.1968	1.07479	5.29	γ′t
92.6166	28.02	0.4723	1.06620	1.99	γ′t
94.2123	130.87	0.1920	1.05144	9.31	γ′t
94.5258	166.87	0.1920	1.04877	11.88	γ′t
95.9047	147.11	0.1680	1.03732	10.47	γ′t
98.5453	88.63	0.2400	1.01646	6.31	γ′t

4.1.2.4 Nominal $Pt_{82}:Al_{12}:Ru_2:Cr_4$

HR-SEM-BSE images of nominal $Pt_{82}:Al_{12}:Ru_2:Cr_4$ are shown in Figure 4.46. Figure 4.10 (a) shows the differing contrast due to different grain orientations and black spots are porosity. Cracks and pores filled with debris were also seen. One region (Figure 4.44 (b)) appeared to be lower (and so was easier to remove on preparation), with the surrounding regions being a two-phase mixture of (Pt) + ~Pt_3Al. Figure 4.44 (c) is representative of the sample microstructure with rounded ~Pt_3Al precipitates in a (Pt) matrix. The precipitates were randomly aligned, and some ~Pt_3Al precipitated on grain boundaries. The volume fraction of the precipitates was 10 ± 5 % with an average size of 0.9 ± 0.6 µm.

The phase compositions are shown in Table 4.20, but the phases were too small to analyse accurately. Aluminium was found to partition mostly to the ~Pt_3Al precipitates compared to the (Pt) phase. Ruthenium and Cr had an extremely limited solubility in the ~Pt_3Al precipitates and partitioned to the (Pt) phase.

Table 4.20. EDX Phase compositions of nominal $Pt_{82}:Al_{12}:Ru_2:Cr_4$ in the heat treated condition.

Phase description	Al	Ru	Cr	Pt	Phase
Overall	10.3 ± 0.3	0.9 ± 0.6	3.5 ± 0.4	85.3 ± 0.5	-
Dark (Precipitates)	20.7 ± 0.4	0.5 ± 0.2	1.9 ± 0.1	76.9 ± 0.4	~Pt_3Al
Light (Matrix)	6.2 ± 0.3	2.2 ± 0.1	4.6 ± 0.2	87.0 ± 0.5	(Pt)

Considering the high intensity peaks and peaks shift, Figures 4.47 to 4.49 show only the presence (Pt) and DO'_c - ~Pt_3Al (Figure 4.50). Table 4.21 shows the identified peaks together with their d-spacings.

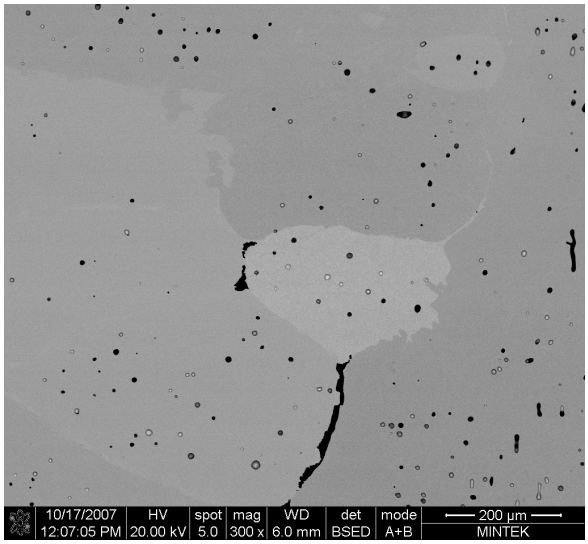

(a)

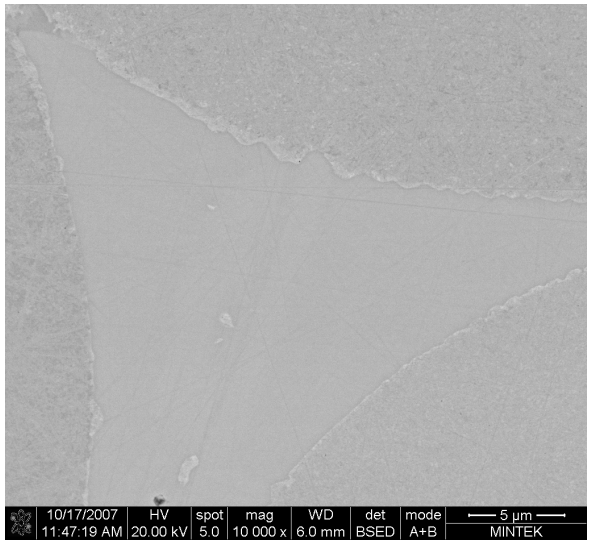

(b)

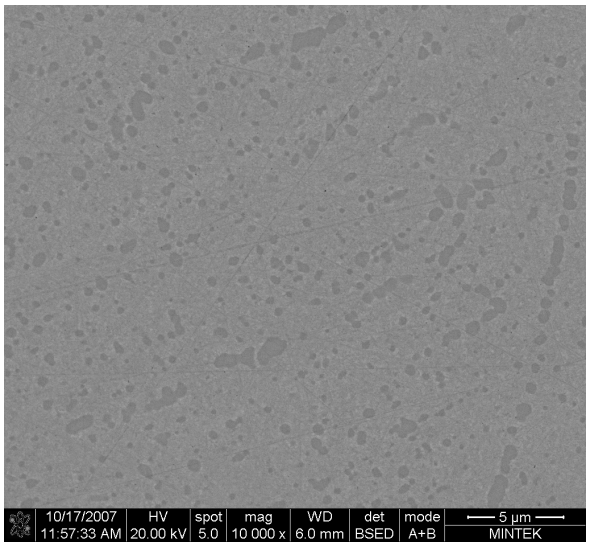

(c)

Figure 4.46. HR-SEM-BSE image of nominal Pt_{82}:Al_{12}:Ru_2:Cr_4 after heat treatment, showing the differing contrast, due to different grain orientations (a), and (b) and (c) taken from the centre and edge shows ~Pt_3Al precipitates in a (Pt) matrix (light).

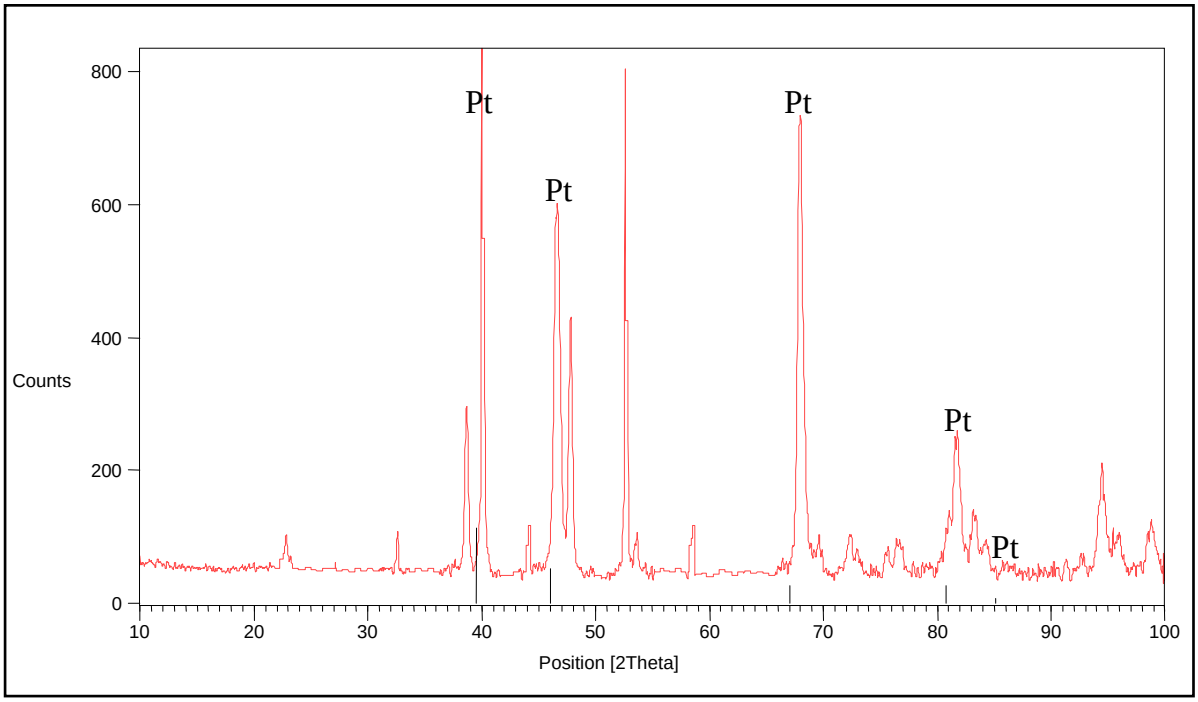

Figure 4.47. XRD Pattern of nominal Pt_{82}:Al_{12}:Ru_2:Cr_4 in the heat treated condition, showing identified Pt peaks.

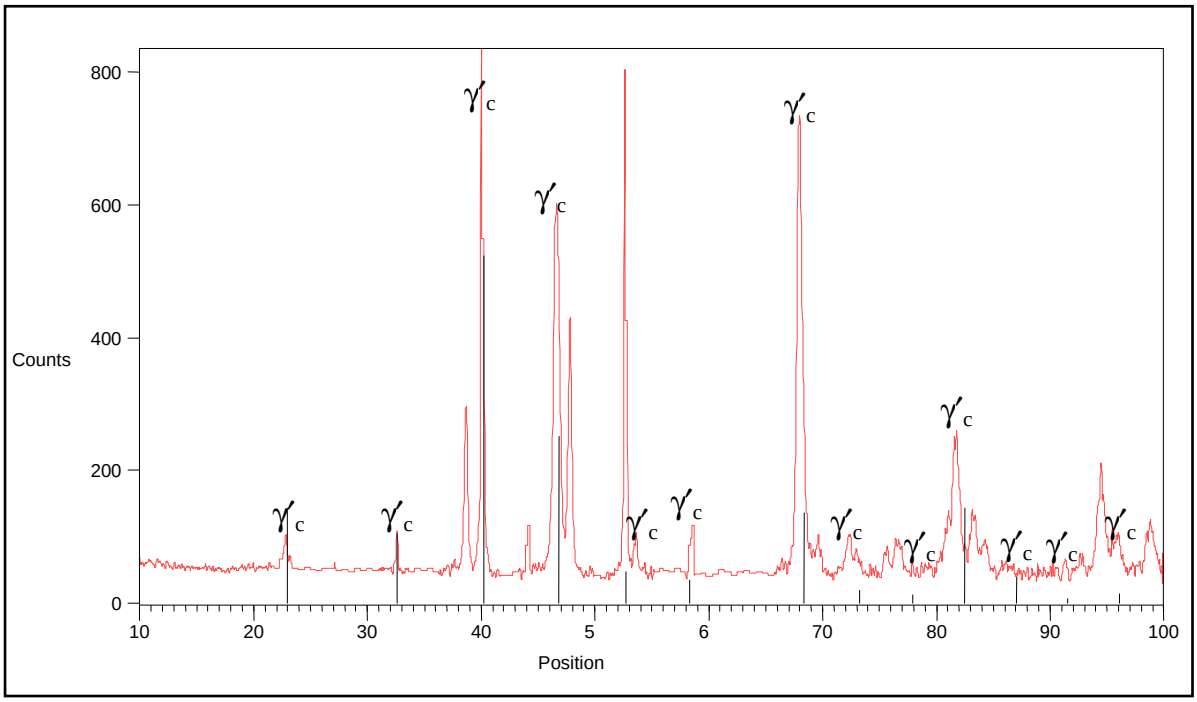

Figure 4.48. XRD Pattern of nominal Pt_{82}:Al_{12}:Ru_2:Cr_4 in the heat treated condition, showing apparent $L1_2$ – ~Pt_3Al peaks.

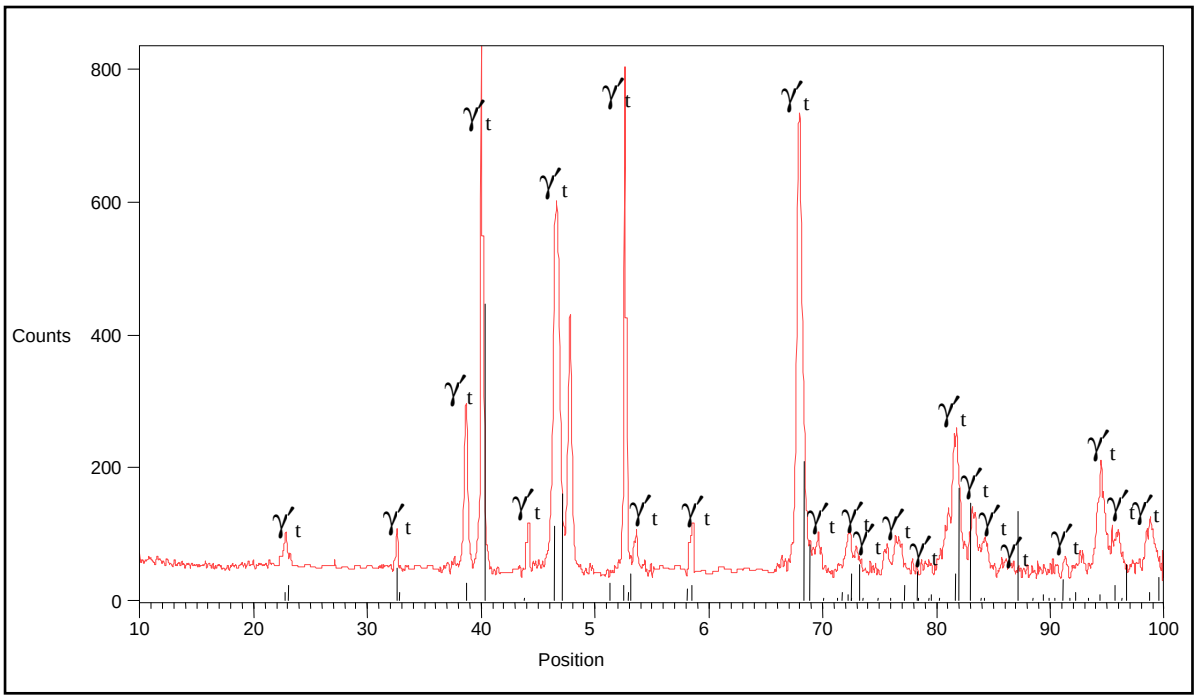

Figure 4.49. XRD Pattern of nominal Pt_{82}:Al_{12}:Ru_2:Cr_4 in the heat treated condition, showing identified DO'_c – ~Pt_3Al peaks.

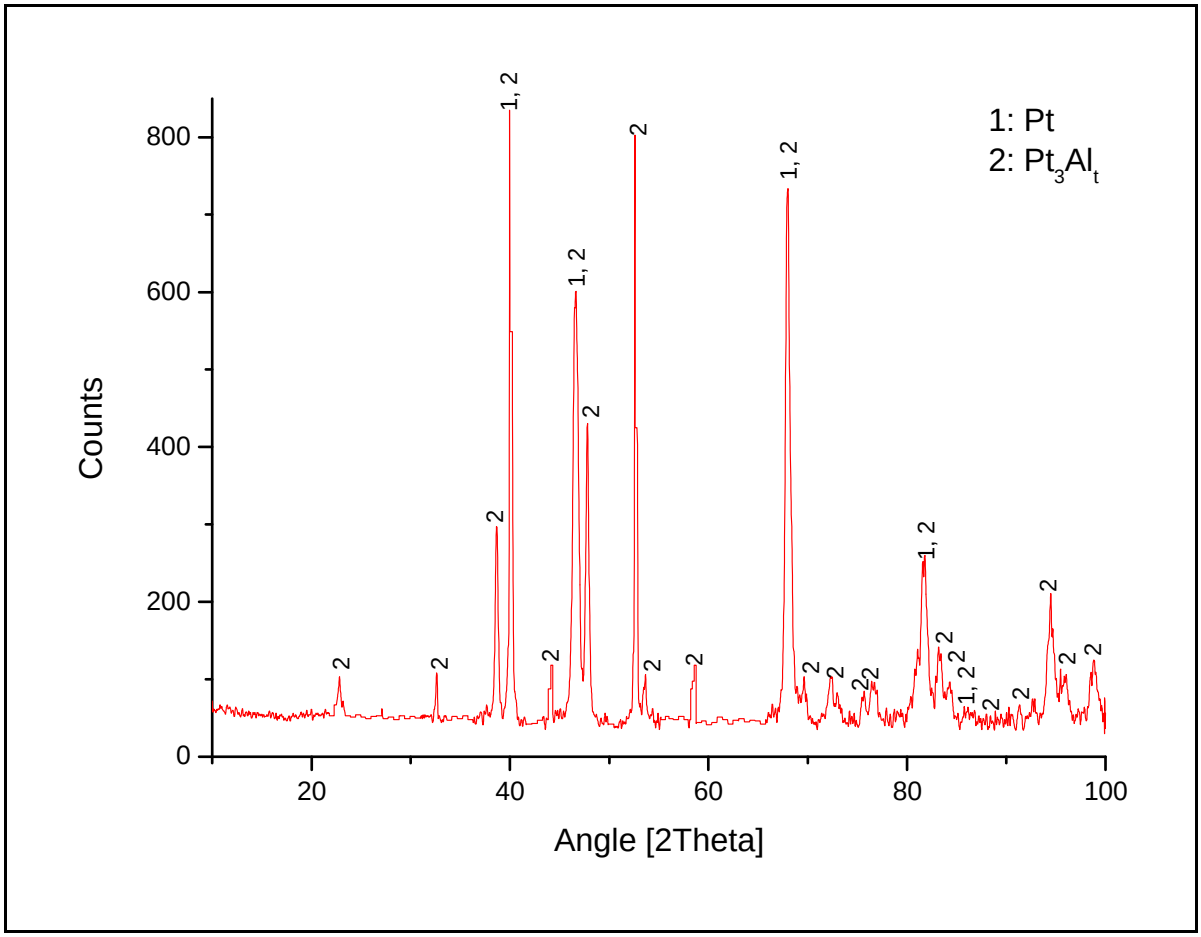

Figure 4.50. XRD pattern of nominal Pt_{82}:Al_{12}:Ru_2:Cr_4 in the heat treated condition, showing all identified phases.

Table 4.21. XRD peaks for Pt_{82}:Al_{12}:Ru_2:Cr_4 in the heat treated condition.

Position 2θ(°)	Height (counts)	Full-Width Half-Maximum 2θ(°)	d-spacing (Å)	Relative Intensity (%)	Phase (s)
22.8038	47.86	0.2362	3.89974	6.41	γ′t
32.6161	60.10	0.1771	2.74549	8.05	γ′t
38.2275	144.71	0.2362	2.35441	27.33	-
38.6680	244.48	0.3346	2.32859	32.73	γ′t
39.9865	746.89	0.0720	2.25293	100.00	(Pt), γ′t
40.2183	506.12	0.0787	2.24234	67.76	γ′t
44.1889	68.76	0.1574	2.04963	9.21	γ′t
46.4494	497.36	0.1378	1.95501	66.59	(Pt), γ′t
46.7857	465.44	0.3149	1.94174	62.32	γ′t
47.7994	374.50	0.1968	1.90290	50.14	γ′t
49.1064	13.92	0.3149	1.81039	4.19	-
52.5884	667.88	0.0720	1.73890	89.42	γ′t
52.7769	374.58	0.0984	1.73457	50.15	γ′t
53.5736	45.88	0.3149	1.71064	6.14	γ′t
58.6429	72.62	0.1574	1.57428	9.72	γ′t
62.9172	9.30	0.1378	1.47722	2.80	-
67.8449	548.71	0.1771	1.38143	73.47	γ′t
69.5993	36.44	0.3149	1.35084	4.88	(Pt), γ′t
72.3402	43.91	0.3936	1.30626	5.88	γ′t
75.6058	25.46	0.3936	1.25776	3.41	γ′t
81.7273	149.55	0.4723	1.17833	20.02	(Pt), γ′t
83.2580	62.84	0.3149	1.16052	8.41	γ′t
84.2575	33.34	0.3936	1.14928	4.46	(Pt), γ′t
91.3143	24.86	0.3936	1.07798	3.33	γ′t
92.4482	87.56	0.1440	1.07586	18.34	γ′t
92.6166	28.02	0.4723	1.06620	1.99	γ′t
95.7896	60.01	0.3149	1.03912	12.57	γ′t
94.2123	130.87	0.1920	1.05144	9.31	γ′t
98.7958	63.54	0.2880	1.01456	13.31	γ′t

4.1.2.5 Nominal Pt_{84}:Al_{11}:Ru_2:Cr_3

HR-SEM-BSE images of the centre and edge microstructure of nominal Pt_{84}:Al_{11}:Ru_2:Cr_3 are shown in Figures 4.51, and consisted of rounded ~Pt_3Al precipitates in a (Pt) matrix, confirming homogeneity of the sample. Subgrain boundaries were also seen. The volume fraction of the precipitates was 12 ± 5 % with an average size of 1.1 ± 0.3 µm and they were not aligned.

The phase compositions are shown in Table 4.22, although the phases were too small for accurate analysis. Ru and Cr were within 0.5 at.% the targeted composition. The ~Pt_3Al precipitates had a limited solubility of Ru and Cr and partitioned mostly to (Pt). The composition of the (Pt) phase was comparable to the overall composition.

Table 4.22. EDX Phase compositions of nominal Pt_{84}:Al_{11}:Ru_2:Cr_3 in the heat treated condition.

Phase description	Al	Ru	Cr	Pt	Phase
Overall	8.7 ± 0.2	1.8 ± 0.2	2.7 ± 0.4	86.8 ± 0.5	-
Dark (Precipitates)	22.1 ± 0.3	0.5 ± 0.3	1.3 ± 0.3	76.1 ± 0.5	~Pt_3Al
Light (Matrix)	7.2 ± 0.7	2.4 ± 0.2	2.7 ± 0.1	87.7 ± 0.9	(Pt)

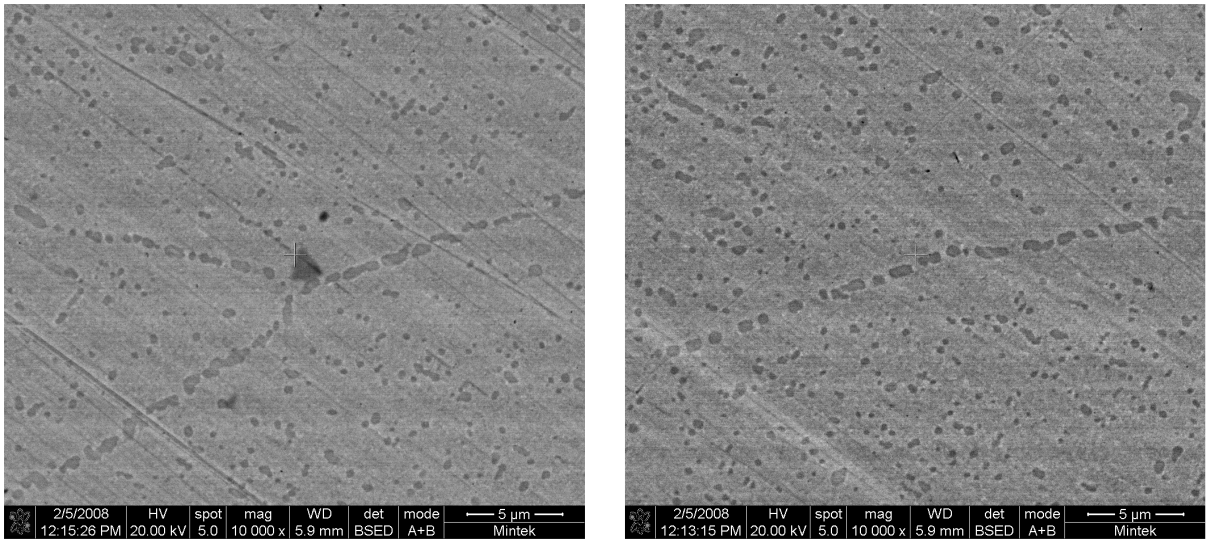

(a) **(b)**

Figure 4.51. HR-SEM-BSE image of nominal Pt_{84}:Al_{11}:Ru_2:Cr_3 after heat treatment, taken from the centre (a) and edge (b), shows ~Pt_3Al precipitates (dark) in a (Pt) matrix.

The (Pt) and DO'_c - ~Pt_3Al peaks were found to be in better agreement with the XRD spectrum compared to the apparent $L1_2$ - ~Pt_3Al phase (Figures 4.52 to 4.54). Table 4.23 shows the identified peaks together with their d-spacings.

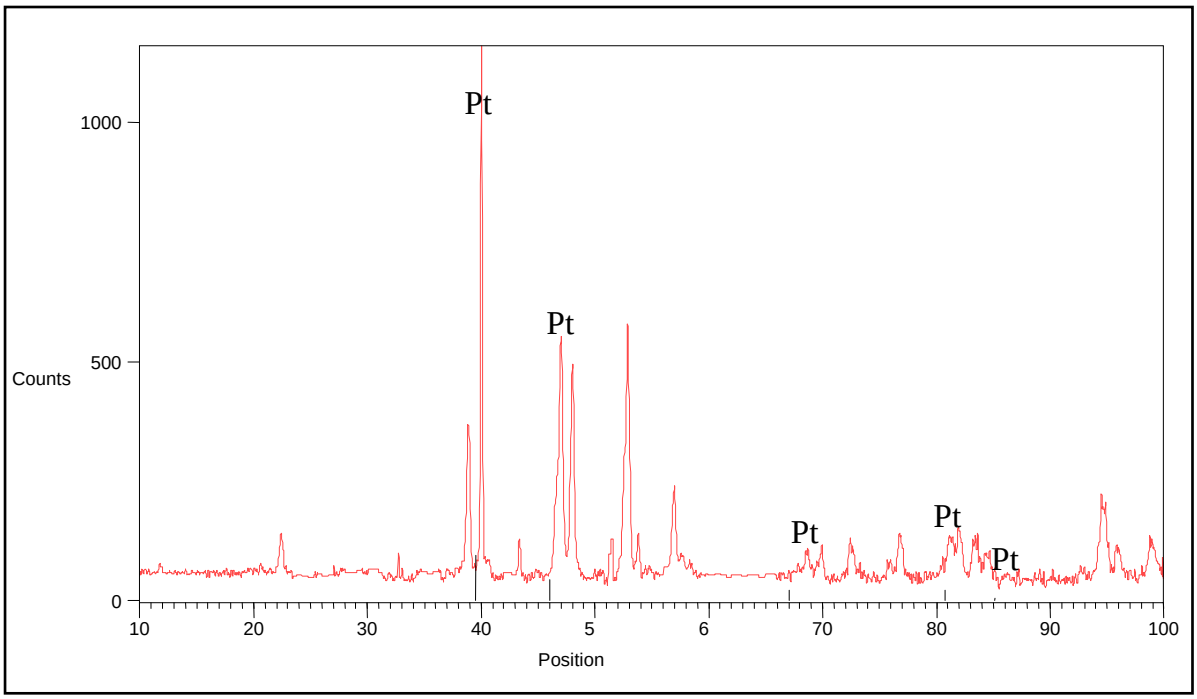

Figure 4.52. XRD Pattern of nominal Pt_{84}:Al_{11}:Ru_2:Cr_3 in the heat treated condition, showing identified Pt peaks.

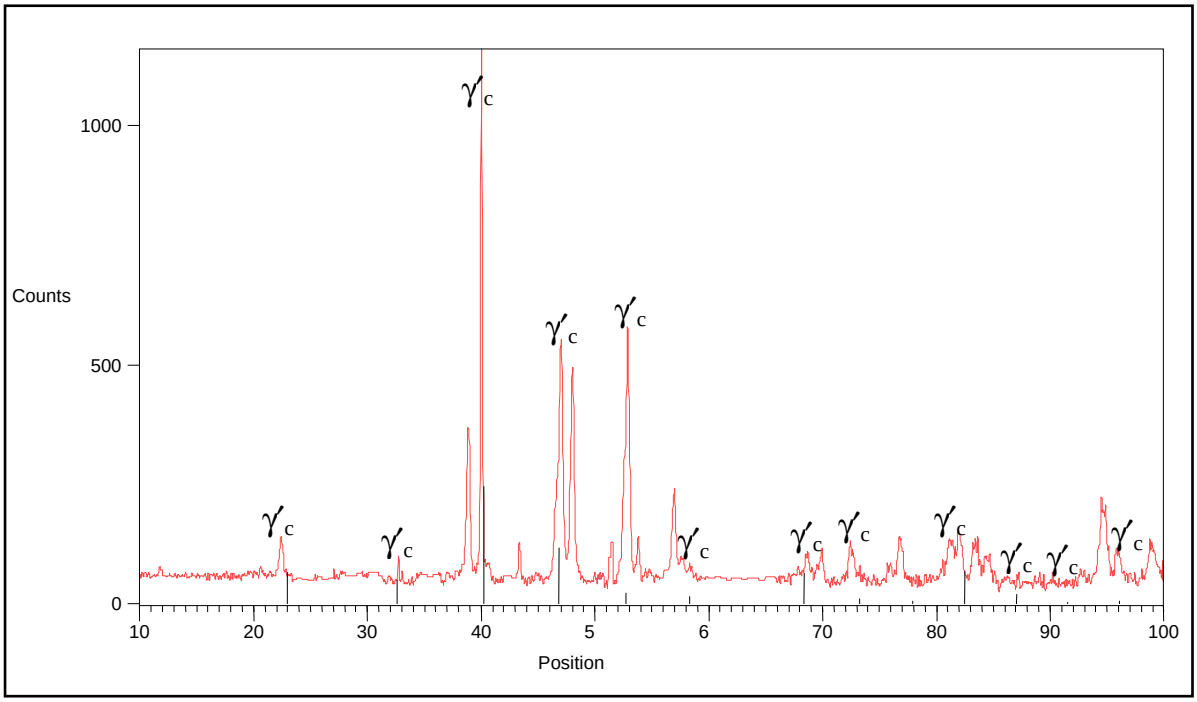

Figure 4.53. XRD Pattern of nominal Pt_{84}:Al_{11}:Ru_2:Cr_3 in the heat treated condition, showing apparent $L1_2$ – ~Pt_3Al peaks.

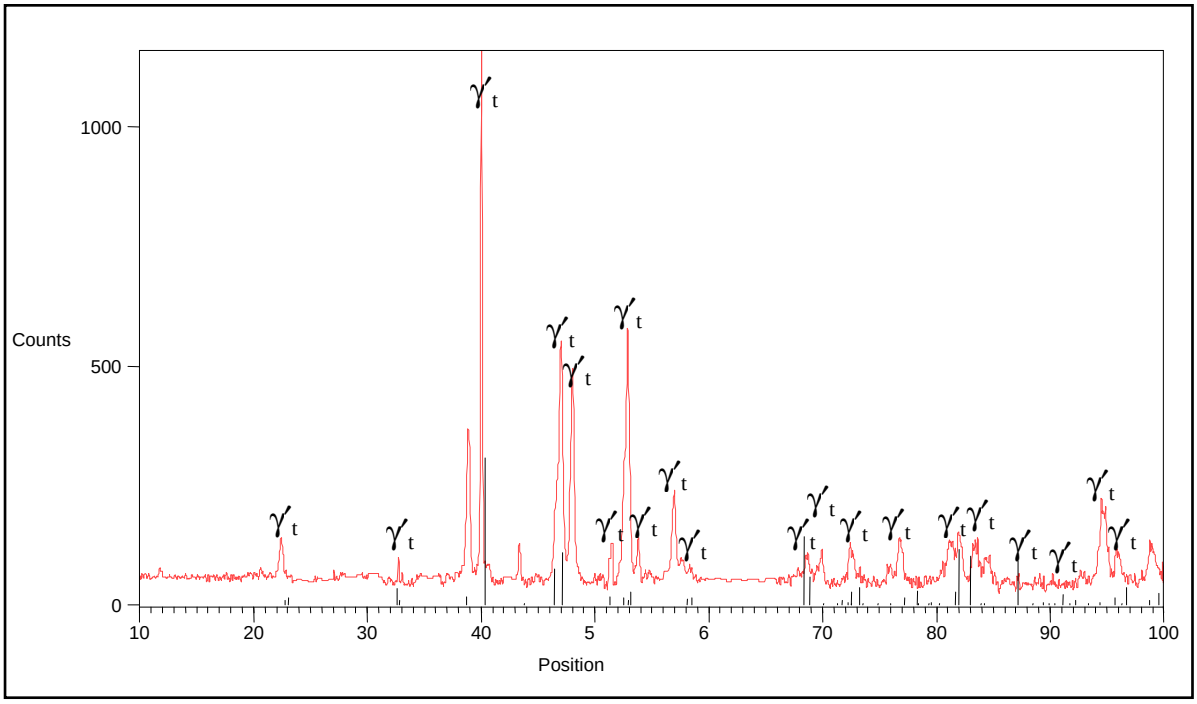

Figure 4.54. XRD Pattern of nominal Pt_{84}:Al_{11}:Ru_2:Cr_3 in the heat treated condition, showing identified DO'_c – ~Pt_3Al peaks.

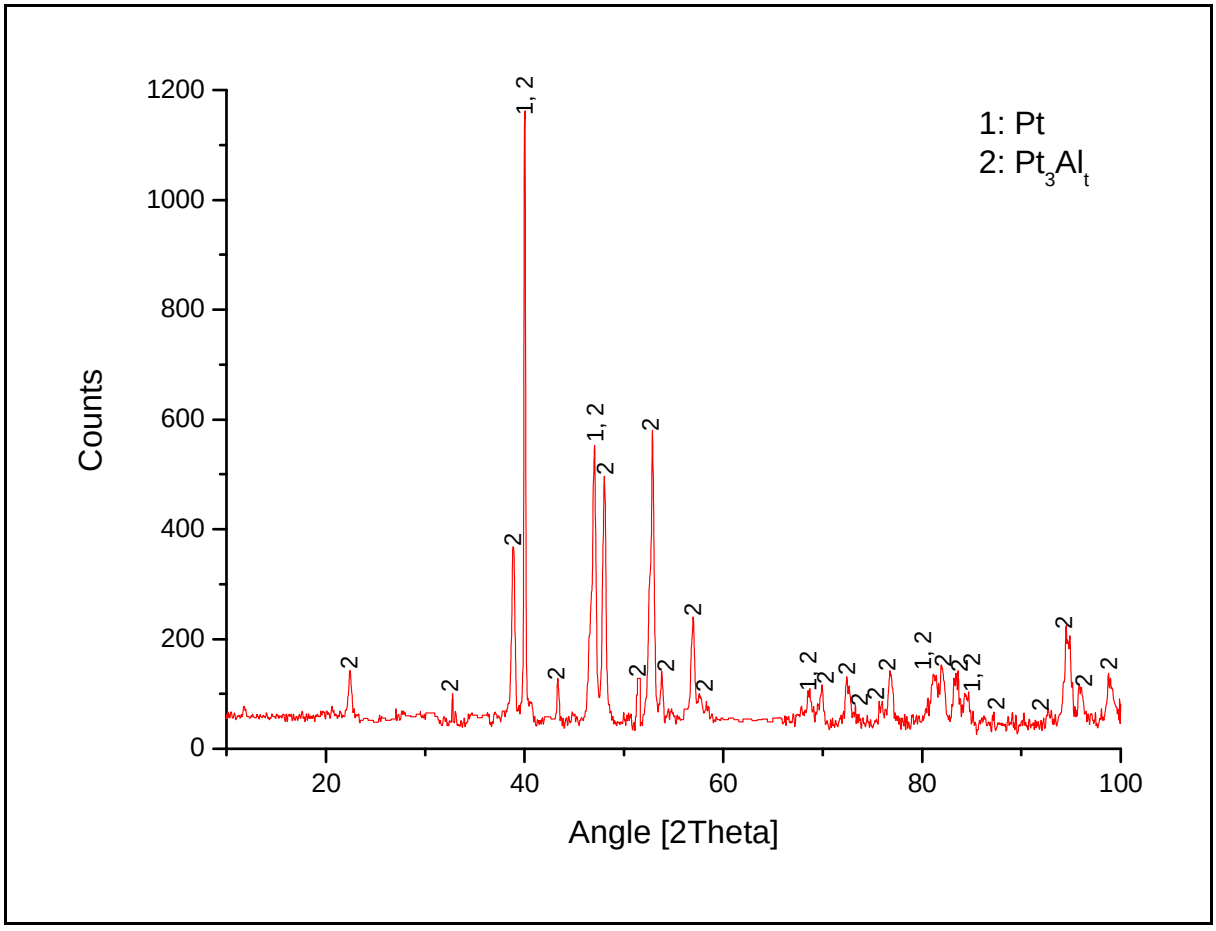

Figure 4.55. XRD pattern of nominal Pt_{84}:Al_{11}:Ru_2:Cr_3 in the as-cast condition, showing all identified phases.

Table 4.23. XRD peaks for Pt_{84}:Al_{11}:Ru_2:Cr_3 in the heat treated condition.

Position 2θ(°)	Height (counts)	Full-Width Half-Maximum 2θ(°)	d-spacing (Å)	Relative Intensity (%)	Phase (s)
22.4375	80.05	0.2362	3.96255	7.36	γ′t
32.7569	56.03	0.1181	2.73401	5.15	γ′t
38.8712	296.60	0.3149	2.31688	27.26	-
39.6336	298.98	0.3149	2.27406	44.95	γ′t
40.0149	1087.88	0.1574	2.25327	100.00	(Pt), γ′t
43.3687	73.11	0.1968	2.08647	6.72	γ′t
47.0306	428.62	0.1181	1.93220	39.40	(Pt), γ′t
48.0304	410.82	0.2755	1.89429	37.76	γ′t
51.6645	84.01	0.1181	1.76927	5.98	-
51.5142	82.09	0.1968	1.77408	7.55	γ′t
52.8644	529.69	0.1968	1.73190	48.69	γ′t
53.8066	86.83	0.2362	1.70378	7.98	γ′t
56.9522	161.06	0.3936	1.61692	14.80	γ′t
68.6295	439.34	0.3149	1.36754	53.62	(Pt), γ′t
69.9009	62.60	0.2362	1.34575	5.75	γ′t
72.4037	70.56	0.1968	1.30528	6.49	γ′t
75.8685	27.80	0.3149	1.25405	2.56	γ′t
76.8252	90.14	0.3936	1.24081	8.29	γ′t
81.2565	64.61	0.3149	1.18396	5.94	γ′t
82.0264	87.69	0.3936	1.17479	8.06	γ′t
83.3670	69.19	0.3149	1.15928	6.36	(Pt), γ′t
84.4839	39.95	0.4723	1.14678	3.67	(Pt), γ′t
89.4473	19.64	0.1440	1.09466	1.81	γ′t
92.8018	17.50	0.4723	1.06456	1.61	γ′t
94.5182	162.73	0.1440	1.04884	14.96	γ′t
95.8980	47.94	0.2362	1.03823	4.41	γ′t
98.8661	56.10	0.4800	1.01402	5.16	γ′t

4.1.2.6 Nominal Pt_{85}:Al_7:Ru_3:Cr_5

Figure 4.56 (a) taken at the centre of the sample, showed a eutectic surrounded by a (Pt) matrix with ~Pt_3Al precipitates. No trace of the lighter regions were seen, which confirms that it was most likely a preparation artefact. Both the edge and centre microstructure consisted of rounded ~Pt_3Al precipitates in a (Pt) matrix (Figures 4.56 (b) and (c)). The precipitate volume fraction was 27 ± 6 % of the microstructure. Grain boundaries were also be seen (Figure 4.56 (b)). There was random alignment of the precipitates and their average size was 1.2 ± 0.6 µm.

The phase compositions are shown in Table 4.24, but the phases were too small to analyse accurately. Ru and Cr had limited solubility in the precipitates and partitioned preferentially to the (Pt). Aluminium was found to partition mostly to the ~Pt_3Al precipitates. The solubility of Ru and Cr in the eutectic/eutectoid part was comparable to that in the precipitates.

Table 4.24. EDX Phase compositions of nominal Pt_{85}:Al_7:Ru_3:Cr_5 in the heat treated

Phase description	Al	Ru	Cr	Pt	Phase
Overall	4.1 ± 0.6	1.6 ± 0.3	4.1 ± 0.3	90.2 ± 0.3	-
Dark (Precipitates)	14.1 ± 0.2	0.7 ± 0.2	1.8 ± 0.1	83.4 ± 0.2	~Pt_3Al
Light (Matrix)	5.3 ± 0.4	1.5 ± 0.1	4.1 ± 0.1	89.1 ± 0.4	(Pt)
Eutectic (Dark)	39.0 ± 0.8	0.9 ± 0.2	1.1 ± 0.2	59.0 ± 1.0	(Pt) + ~Pt_3Al

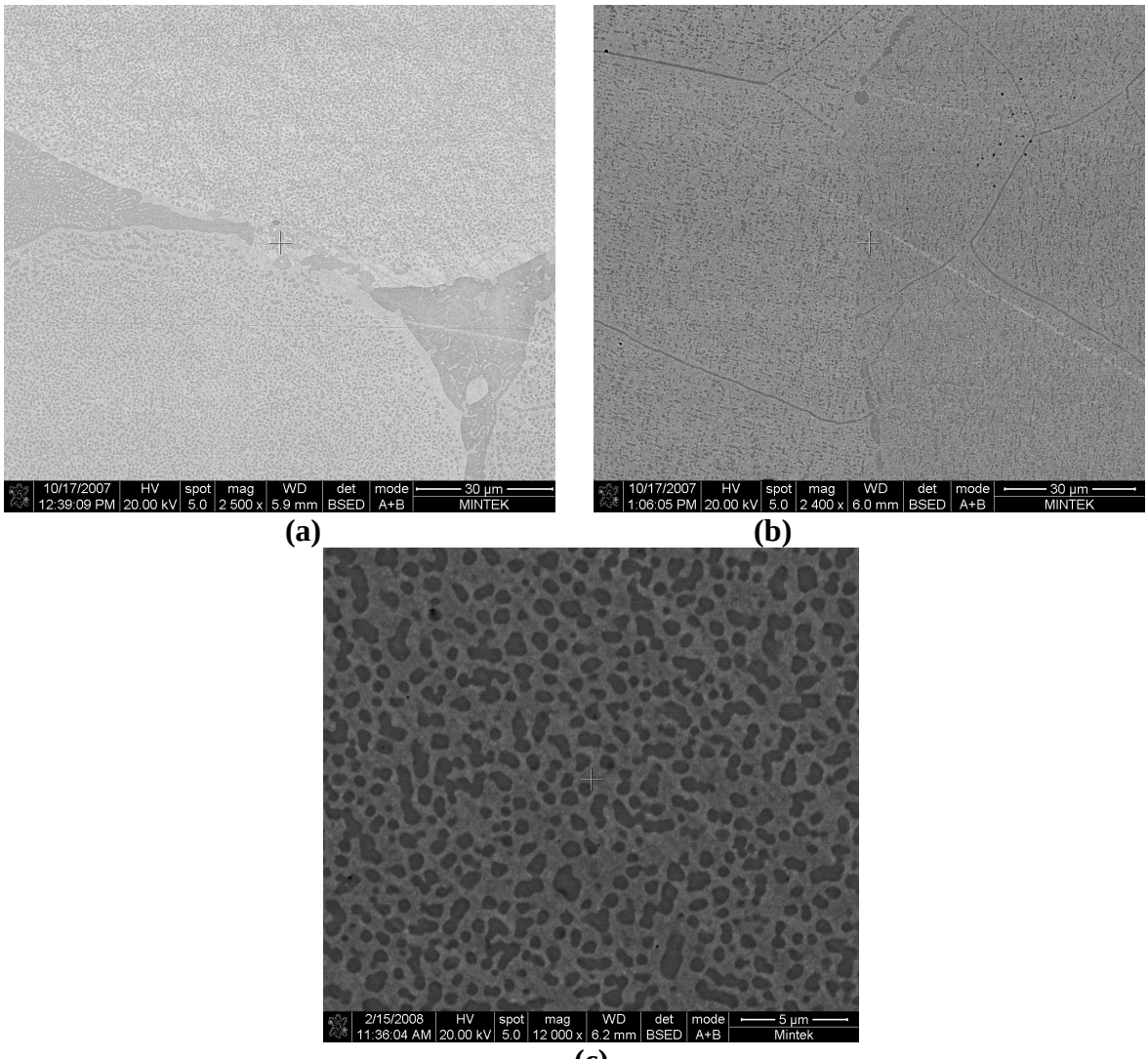

(a) **(b)**

(c)

Figure 4.56. HR-SEM-BSE image of nominal Pt_{85}:Al_7:Ru_3:Cr_5 after heat treatment, (a – b) taken from the centre showing remnants of the eutectic of (Pt) + ~Pt_3Al (dark) and grain boundaries, and (c) taken from edge showing also ~Pt_3Al precipitates (dark) in a (Pt) matrix (light).

The XRD spectrum had a high background. As with the rest of the alloys, similar observations were made of peaks shifting (Figures 4.57 to 4.59), and the (Pt) and DO′$_c$ - Pt_3Al database peaks agreed well with the XRD spectrum. Table 4.25 shows the peaks together with their d-spacings for (Pt) and DO′$_c$ - Pt_3Al, with $L1_2$ – ~Pt_3Al not present.

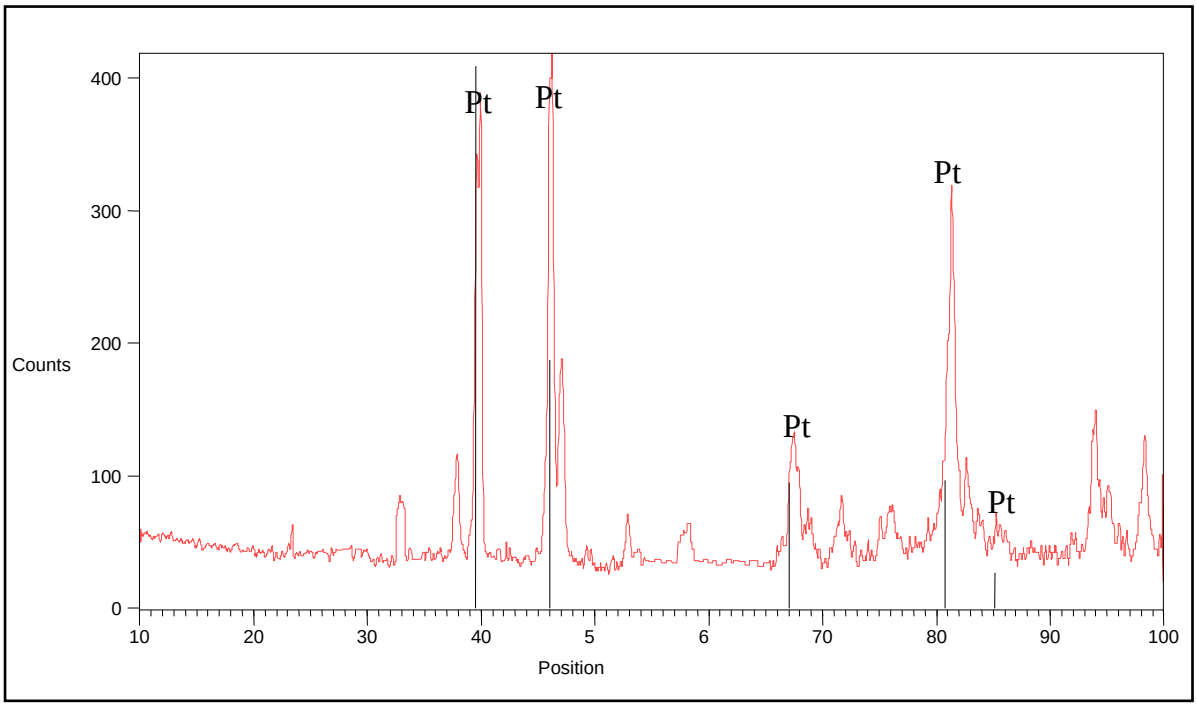

Figure 4.57. XRD Pattern of nominal Pt_{85}:Al_7:Ru_3:Cr_5 in the heat treated condition, showing identified Pt peaks.

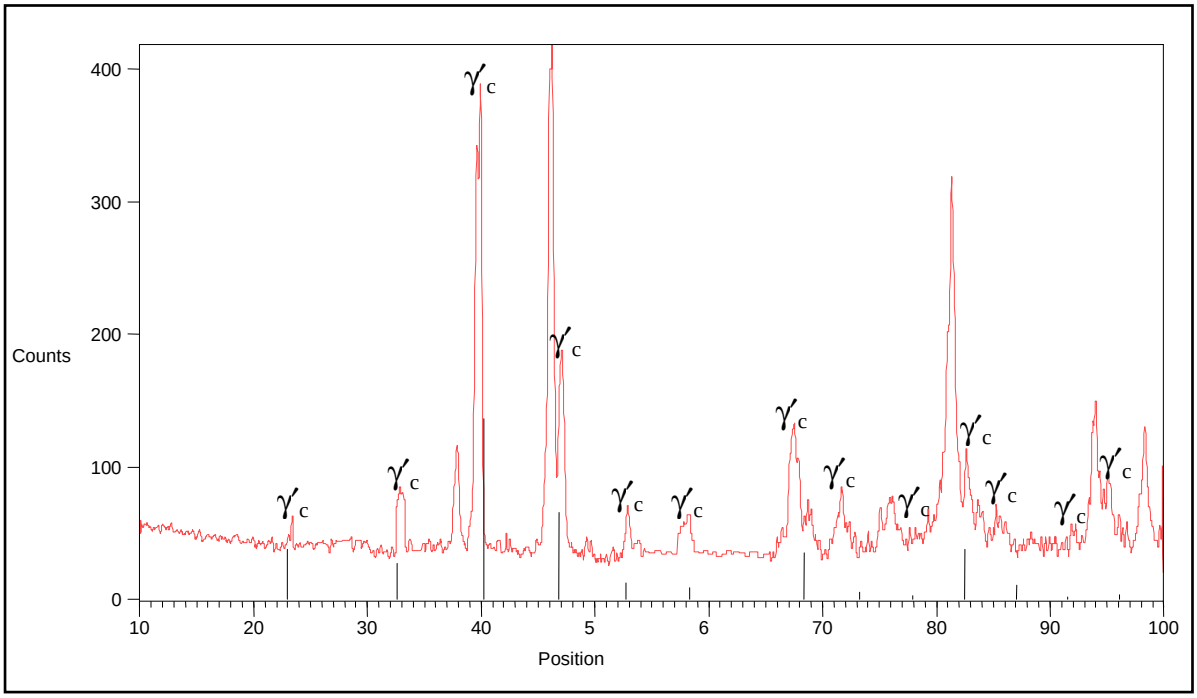

Figure 4.58. XRD Pattern of nominal Pt_{85}:Al_7:Ru_3:Cr_5 in the heat treated condition, showing apparent $L1_2$ – ~Pt_3Al peaks.

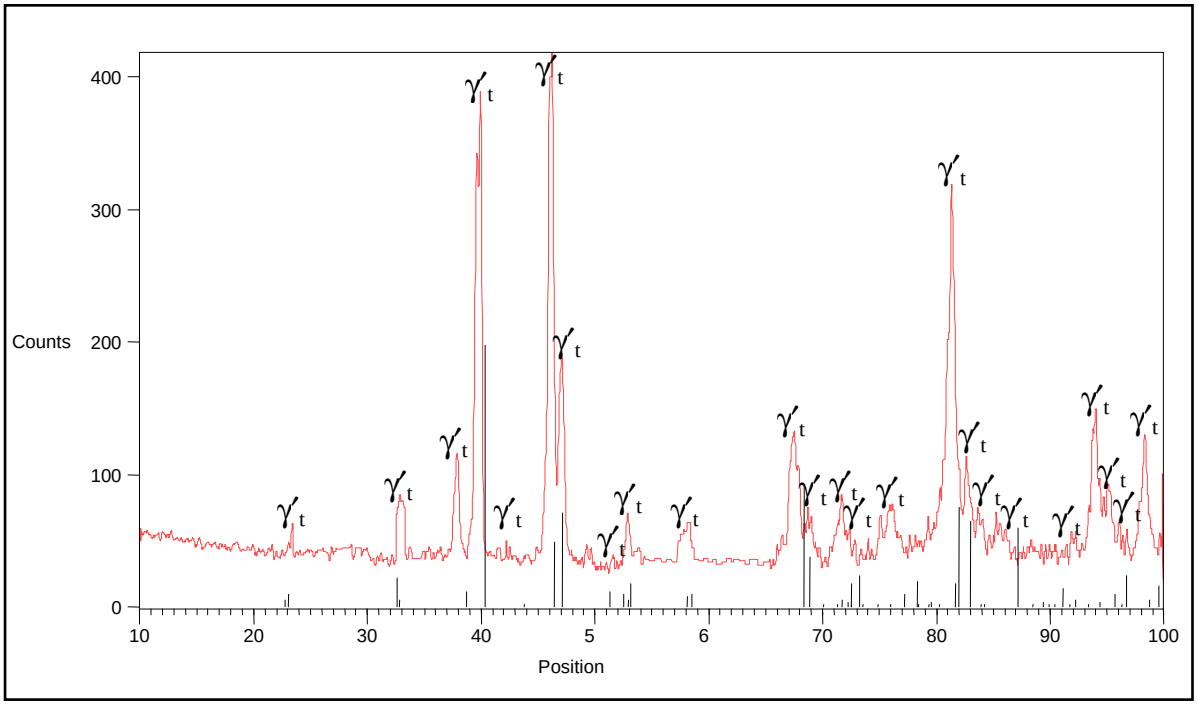

Figure 4.59. XRD Pattern of nominal Pt_{85}:Al_7:Ru_3:Cr_5 in the heat treated condition, showing identified DO'_c – ~Pt_3Al peaks.

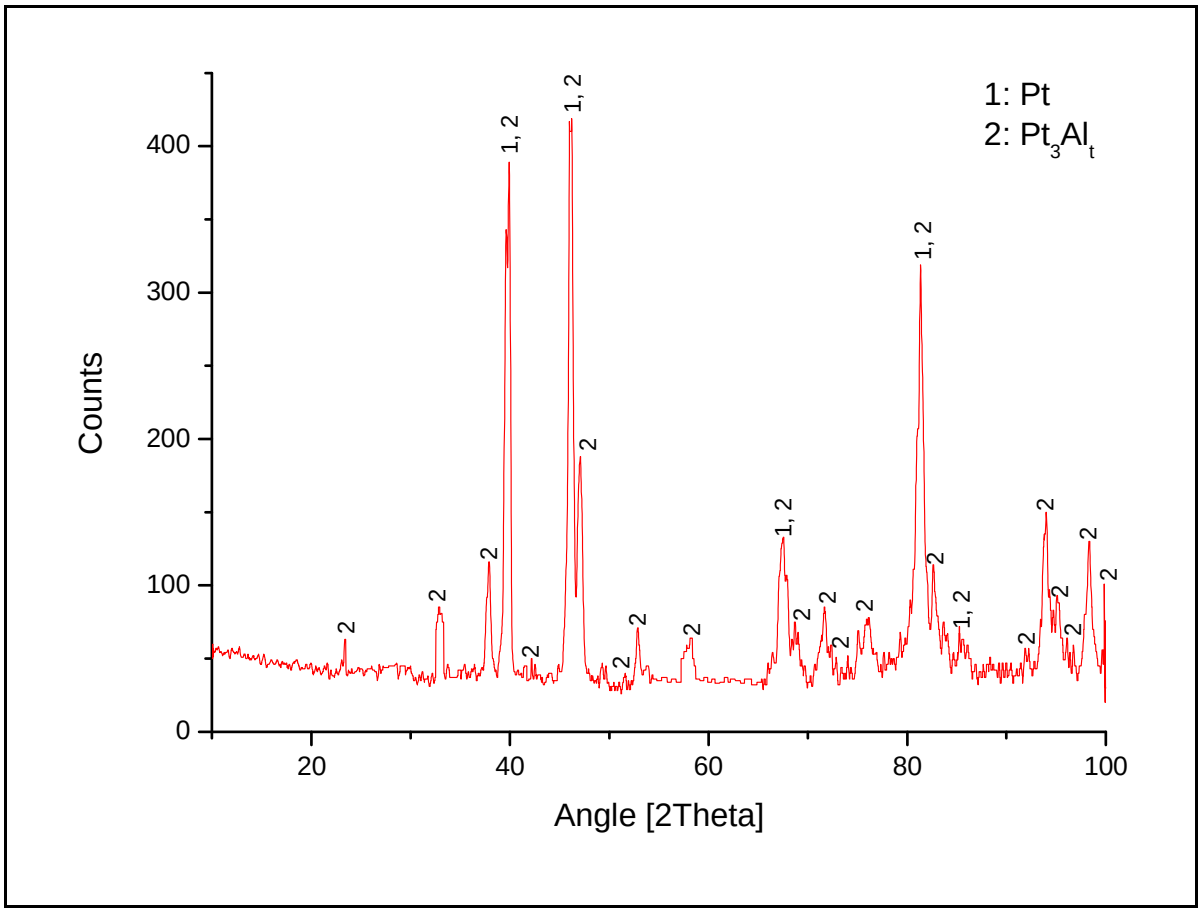

Figure 4.60. XRD pattern of nominal Pt_{85}:Al_7:Ru_3:Cr_5 in the heat treated condition, showing all identified phases.

Table 4.25. XRD peaks for Pt_{85}:Al_7:Ru_3:Cr_5 in the heat treated condition.

Position 2θ(°)	Height (counts)	Full-Width Half-Maximum 2θ(°)	d-spacing (Å)	Relative Intensity (%)	Phase (s)
22.8066	56.27	0.4723	3.89926	11.79	γ′t
32.9051	47.31	0.3936	2.72203	13.44	γ′t
33.1708	42.44	0.2362	2.70083	12.06	γ′t
37.8927	76.38	0.2362	2.37443	21.70	-
39.6336	298.98	0.3149	2.27406	84.95	γ′t
39.9276	346.70	0.2165	2.25799	98.51	(Pt), γ′t
41.0653	64.47	0.3936	2.25055	13.50	γ′t
46.1873	351.95	0.1574	1.96550	100.00	(Pt), γ′t
47.0797	142.91	0.2362	1.93030	40.60	γ′t
48.9090	48.17	0.1968	1.89881	12.80	-
52.8785	34.47	0.3149	1.73148	9.80	(Pt), γ′t
58.1217	21.73	0.4723	1.58714	6.17	γ′t
71.6758	35.81	0.3149	1.31673	10.18	γ′t
75.0969	25.90	0.3149	1.26501	7.36	γ′t
76.0052	28.93	0.4723	1.25214	8.22	γ′t
81.3434	237.91	0.2165	1.18292	67.60	(Pt), γ′t
81.4199	75.07	0.2362	1.18182	15.72	γ′t
82.0491	40.23	0.1920	1.17355	12.26	γ′t
82.6580	45.31	0.3149	1.16741	12.88	(Pt), γ′t
93.9338	90.18	0.3936	1.05469	25.62	γ′t
95.1722	39.18	0.3149	1.04422	11.13	γ′t
98.3195	79.35	0.3840	1.01819	22.55	γ′t

4.2 Second Batch of Samples

For the first batch of alloys, Pt_{85}:Al_7:Ru_3:Cr_5 was found to be the most promising alloy with a high volume fraction of ~Pt_3Al precipitates and with reasonable hardness. However, the alloy had a high Pt content, which is expensive. It also had a low content of Al (7 at.%) which could allow oxidation, since Mintek's work [2000Hil, 2001Süs] has shown that about 11 at.% Al is needed to establish the thin protective oxide coating at high temperatures. Thus, in an attempt to increase the volume fraction of precipitates at low Pt content with an Al content higher than 7 at.%, a second batch of alloys was manufactured. A total of six different alloy compositions were made with 11 at.% Al, with three samples of 80 at.% Pt and another three of 78 at.% Pt, and for both sets, the Ru and Cr contents were varied. Keeping the Al content constant (for six samples) and the Pt content constant (for three samples) and varying the Ru

and Cr contents would allow the effects of both elements (Ru and Cr) on the microstructure to be studied. The preparation, annealing, microstructural characterisation and mechanical test work were carried out as before. For all six alloys, the mass losses were found to be less than 1 % (Table 4.26).

Table 4.26. Mass before and after melting for the second batch of samples.

Alloy	Unmelted (g)	Melted (g)	% Weight Loss
$Pt_{80:}Al_{11}:Ru_5:Cr_4$	1.9912	1.9793	0.6
$Pt_{80}:Al_{11}:Ru_3:Cr_6$	2.0026	1.9866	0.8
$Pt_{80}:Al_{11}:Ru_6:Cr_3$	2.0009	1.9829	0.9
$Pt_{78}:Al_{11}:Ru_5:Cr_6$	1.9992	1.9892	0.5
$Pt_{78}:Al_{11}:Ru_3:Cr_8$	2.0015	1.9855	0.8
$Pt_{78}:Al_{11}:Ru_8:Cr_3$	2.0729	2.0584	0.7

XRD was also carried out for the second batch of samples to confirm the presence of (Pt) and ~Pt_3Al. For all samples the XRD spectrum had low counts, high background and wide peaks. For as-cast samples, the wide peaks were attributed to coring. The reason for the wide peaks in the annealed samples is not known. For some samples wide peaks were observed at high angles (i.e. $Pt_{80}:Al_{11}:Ru_6:Cr_3$). All three phases ((Pt), $L1_2$ - ~Pt_3Al and DO'_c - ~Pt_3Al) were matched in the XRD spectrum. Similar to the first batch of samples all observations made (i.e. the apparent $L1_2$ - ~Pt_3Al peaks shifting in both directions, the DO'_c - ~Pt_3Al phase peaks agreeing well with the spectrum and the high intensity peaks being a combination of both (Pt) and DO'_c - ~Pt_3Al) strongly suggested that the $L1_2$ - ~Pt_3Al phase was not present.

4.2.1 As-cast Alloys: Microstructural Characterisation

4.2.1.1 Nominal $Pt_{80}:Al_{11}:Ru_5:Cr_4$

HR-SEM-BSE images of nominal $Pt_{80}:Al_{11}:Ru_5:Cr_4$ in the as-cast condition are shown in Figure 4.61, taken at different areas of the sample. The centre of the alloy consisted of cored (Pt) dendrites surrounded by a darker (Pt) + ~Pt_3Al fine eutectic (Figure 4.61 (a)). The edge microstructure (Figures 4.61 (b)) was similar, confirming homogeneity of the sample. The dendrites were the major phase, taking 83 ± 7%, with an average arm spacing of about 9.3 ±

2.3 µm for both the centre and edge of the sample. The phase compositions are shown in Table 4.27. The overall Al content decreased the most, as expected, since some Al would have been lost during melting by evaporation. Ruthenium and Cr had very limited solubility in the ((Pt) + ~Pt_3Al) eutectic, while Ru partitioned almost exclusively to (Pt). The standard deviation of the measurements was below 1 at.%, except for light overall (1.3 at.%).

XRD results are shown in Figures 4.62 to 4.65 and Table 4.28, with the phases identified.

Table 4.27. EDX Phase compositions of nominal Pt_{80}:Al_{11}:Ru_5:Cr_4 in the as-cast condition.

Phase Description	Al	Ru	Cr	Pt	Phase
Overall	8.9 ± 0.3	4.2 ± 0.2	4.7 ± 0.5	82.2 ± 0.3	-
Dark (eutectic)	18.2 ± 0.7	0.2 ± 0.3	1.2 ± 0.2	80.6 ± 0.6	(Pt) + ~Pt_3Al
Dendrite overall	5.6 ± 1.3	5.6 ± 0.3	3.2 ± 0.4	85.7 ± 0.7	(Pt) + ~Pt_3Al
Dendrite inner (darker)	5.1 ± 0.8	9.9 ± 0.2	3.8 ± 0.2	81.2 ± 0.6	Cored (Pt) + ~Pt_3Al
Dendrite outer (lighter)	8.8 ± 0.8	0.7 ± 0.3	2.2 ± 0.6	88.3 ± 0.4	(Pt) + ~Pt_3Al

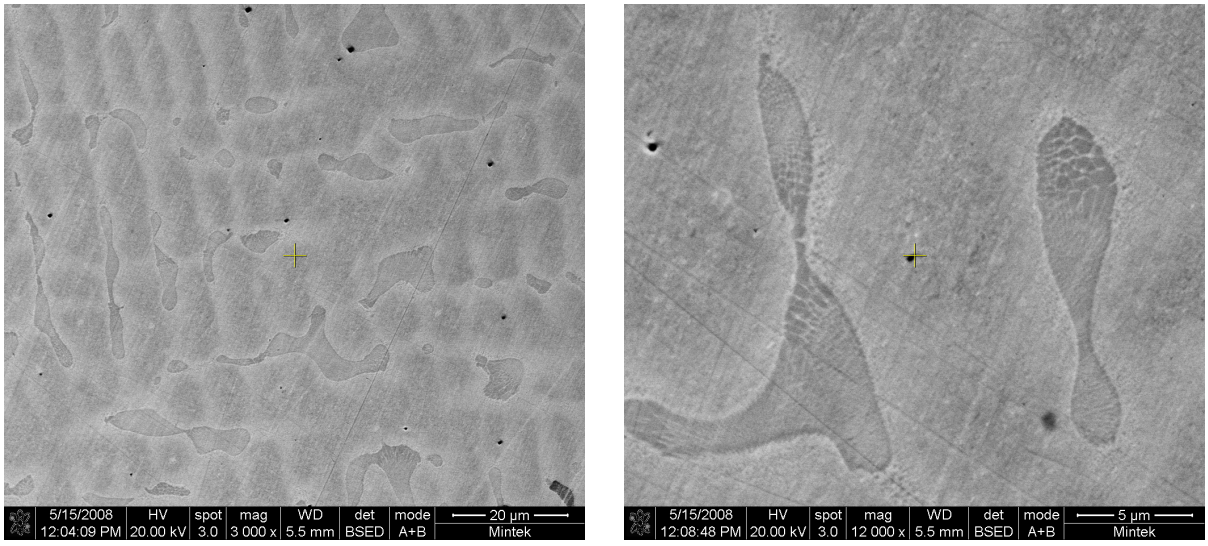

(a) **(b)**

Figure 4.61. HR-SEM-BSE image of nominal Pt_{80}:Al_{11}:Ru_5:Cr_4, as-cast condition, taken from the centre (a) and (b) edge showing (Pt) dendrites and a eutectic of (Pt) + ~Pt_3Al (dark).

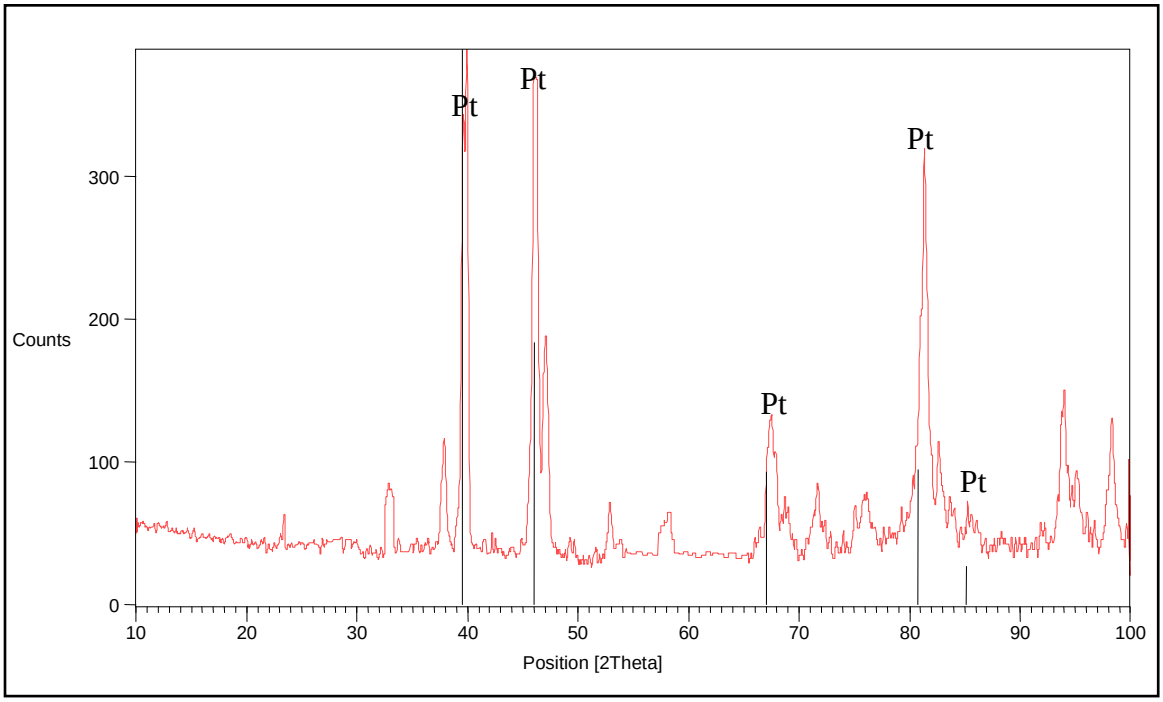

Figure 4.62. XRD Pattern of nominal Pt_{80}:Al_{11}:Ru_5:Cr_4 in the as-cast condition, showing identified Pt peaks.

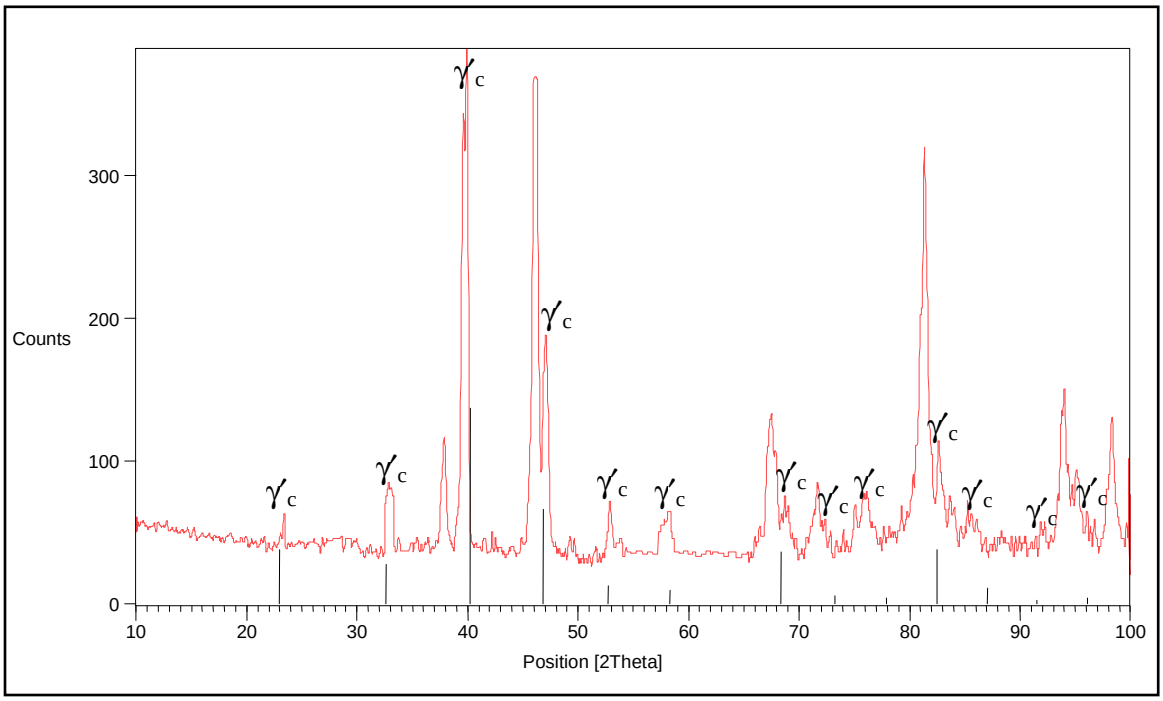

Figure 4.63. XRD Pattern of nominal Pt_{80}:Al_{11}:Ru_5:Cr_4 in the as-cast condition, showing apparent $L1_2$ – ~Pt_3Al peaks.

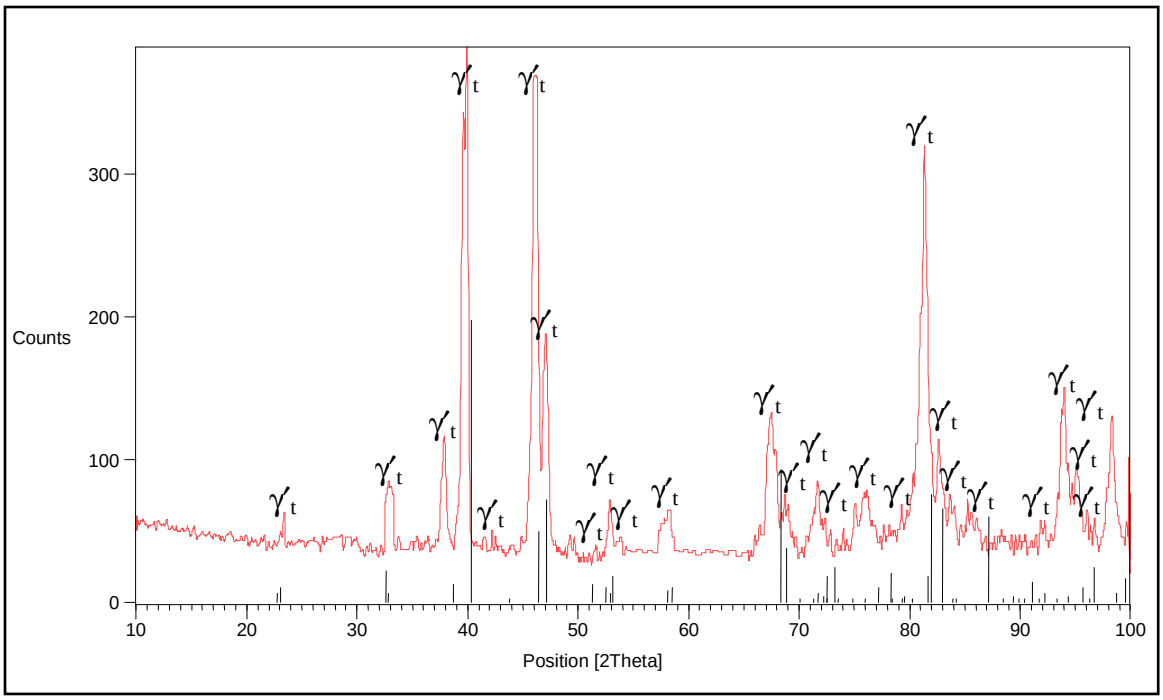

Figure 4.64. XRD Pattern of nominal $Pt_{80}:Al_{11}:Ru_5:Cr_4$ in the as-cast condition, showing identified DO'_c – ~Pt_3Al peaks.

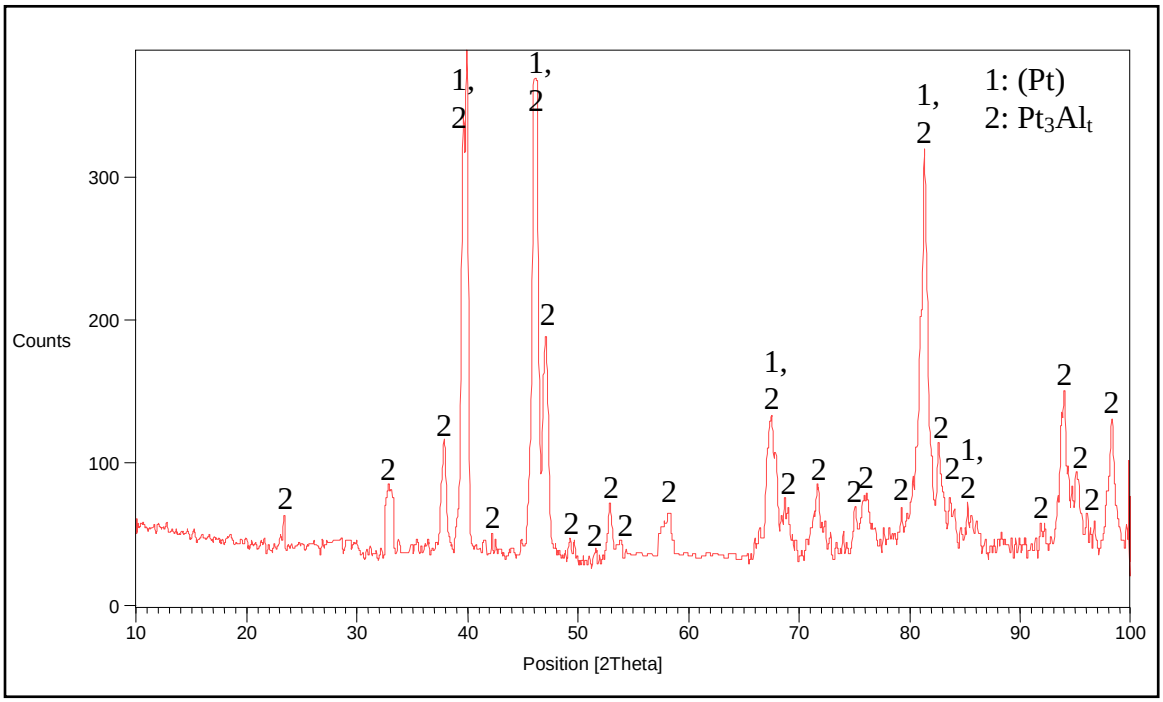

Figure 4.65. XRD pattern of nominal $Pt_{80}:Al_{11}:Ru_5:Cr_4$ in the as-cast condition, showing all identified phases.

Table 4.28. XRD peaks for Pt_{80}:Al_{11}:Ru_5:Cr_4 in the as-cast condition.

Position 2θ(°)	Height (counts)	Full-Width Half-Maximum 2θ(°)	d-spacing (Å)	Relative Intensity (%)	Phase (s)
22.8046	47.98	0.2362	3.89960	9.38	γ′t
32.9040	47.70	0.3936	2.72212	13.72	γ′t
33.1706	43.47	0.2362	2.70085	12.51	-
37.8917	76.15	0.2362	2.37449	21.91	-
39.6339	303.31	0.2755	2.27404	87.27	(Pt), γ′t
39.9269	347.56	0.2362	2.25803	100.00	γ′t
46.0243	335.84	0.1920	1.97045	96.63	(Pt), γ′t
46.2167	334.88	0.1574	1.96432	96.35	γ′t
47.0675	152.93	0.5510	1.93077	44.00	γ′t
52.8783	37.61	0.3149	1.73148	10.82	γ′t
58.1224	27.49	0.4723	1.58713	7.91	γ′t
67.1616	42.15	0.7972	1.38456	23.64	-
67.4616	82.15	0.7872	1.38835	23.64	(Pt), γ′t
71.6808	48.00	0.2755	1.31665	13.81	γ′t
75.0958	27.94	0.3149	1.26502	8.04	γ′t
76.0046	34.87	0.4723	1.25215	10.03	γ′t
81.3461	255.13	0.1968	1.18289	73.41	(Pt), γ′t
82.6581	57.24	0.3149	1.16741	16.47	
85.5736	16.16	0.9446	1.13495	4.65	(Pt), γ′t
93.9348	96.76	0.3936	1.05468	27.84	γ′t
95.1701	43.53	0.3149	1.04424	12.53	γ′t
98.3196	85.62	0.2880	1.01819	24.63	γ′t

4.2.1.2 Nominal $Pt_{80}:Al_{11}:Ru_3:Cr_6$

HR-SEM-BSE images in the as-cast condition of the centre and edge of the specimen are shown in Figure 4.66. There are cored dendrites (with a darker inner) and regions of dark and light eutectic. The centre and edge microstructure were similar, and consisted of cored (Pt) dendrites. Scratches can be seen, even though polishing time was increased. The dendrite centres were darker than in $Pt_{80}:Al_{11}:Ru_5:Cr_4$, and comprised 89 ± 6% of the microstructure with an arm spacing of 10.1 ± 2.2 µm. The phase compositions are shown in Table 4.29. The overall composition of the elements varied from the nominal composition, except for Ru. Ruthenium and Cr had very limited solubility in the ((Pt) + ~Pt_3Al) eutectic, and partitioned almost exclusively to (Pt). The standard deviation of the measurements was below 1 at.%.

Figures 4.67 to 4.69 shows the experimental XRD spectrum compared to the database lines for each phase. Figure 4.70 and Table 4.30 gives the identified phases.

Table 4.29. EDX Phase compositions of nominal $Pt_{80}:Al_{11}:Ru_3:Cr_6$ in the as-cast condition.

Phase Description	Al	Ru	Cr	Pt	Phase
Overall	8.6 ± 0.5	2.8 ± 0.8	4.1 ± 0.8	84.5 ± 1.2	-
Dark (eutectic)	17.7 ± 0.7	0.2 ± 0.6	2.2 ± 0.6	79.9 ± 0.3	(Pt) + ~Pt_3Al
Dendrite overall	5.3 ± 0.8	1.0 ± 0.9	6.9 ± 0.5	86.8 ± 0.9	(Pt) + ~Pt_3Al
Dendrite inner (darker)	4.6 ± 1.6	7.7 ± 0.3	1.9 ± 0.6	85.7 ± 0.8	Cored (Pt) + ~Pt_3Al
Dendrite outer (lighter)	8.1 ± 0.7	0.8 ± 0.5	5.4 ± 0.3	85.8 ± 0.6	(Pt) + ~Pt_3Al

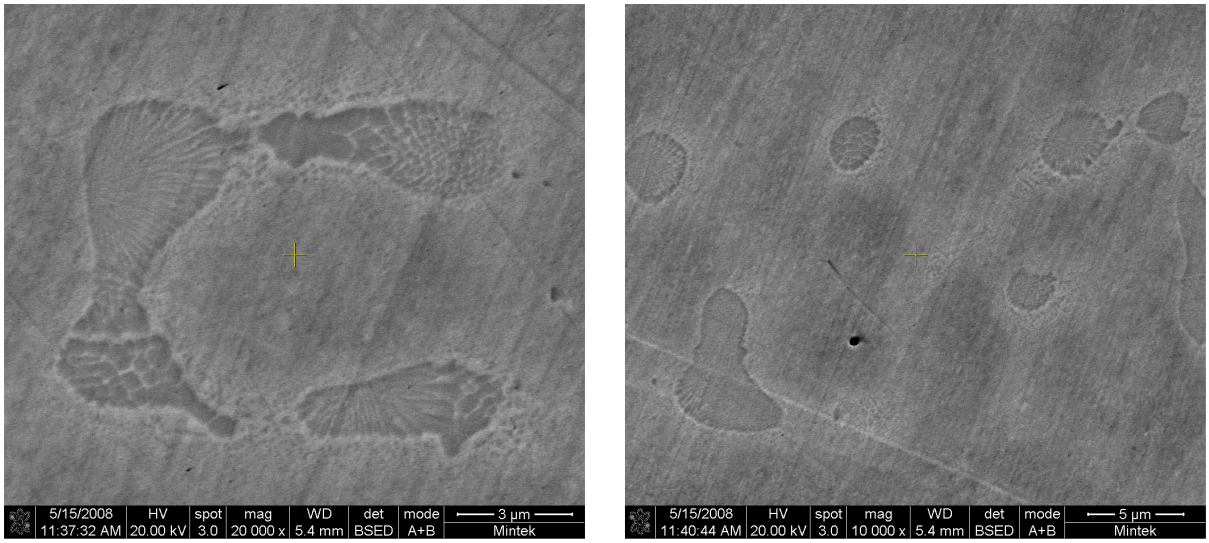

(a) **(b)**

Figure 4.66. HR-SEM-BSE image of nominal $Pt_{80}:Al_{11}:Ru_3:Cr_6$, as-cast condition, taken from the centre (a) and (b) edge showing cored (Pt) dendrites (light) with a fine eutectic of (Pt) + ~Pt_3Al (dark).

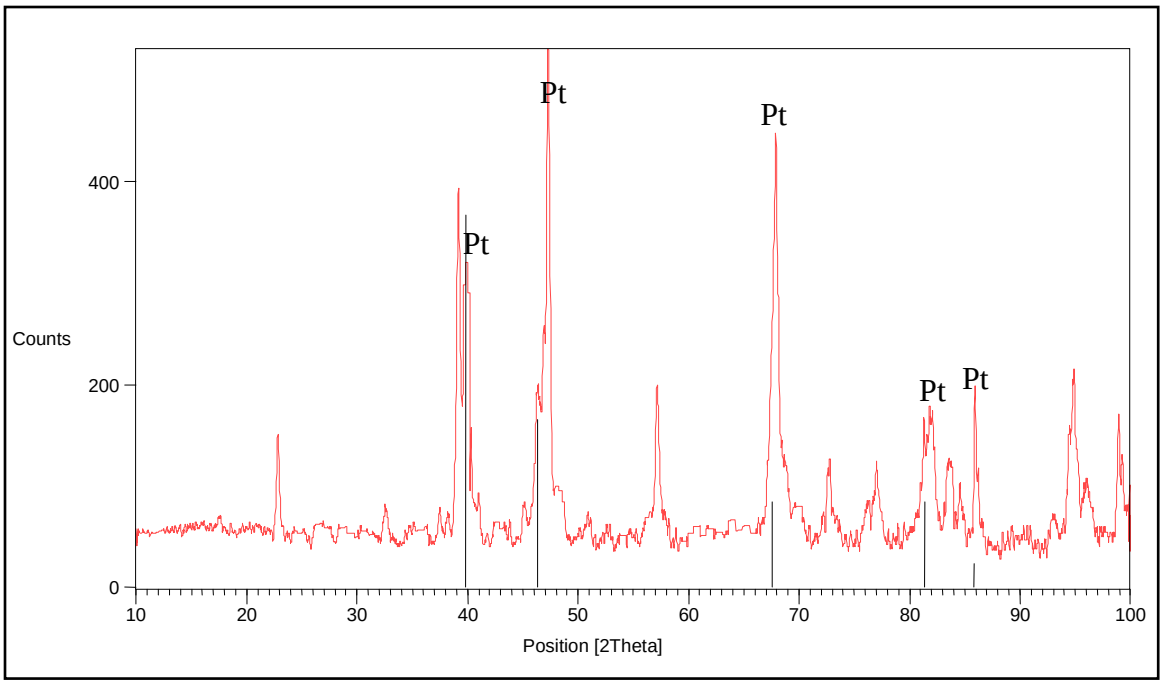

Figure 4.67. XRD Pattern of nominal Pt_{80}:Al_{11}:Ru_3:Cr_6 in the as-cast condition, showing identified Pt peaks.

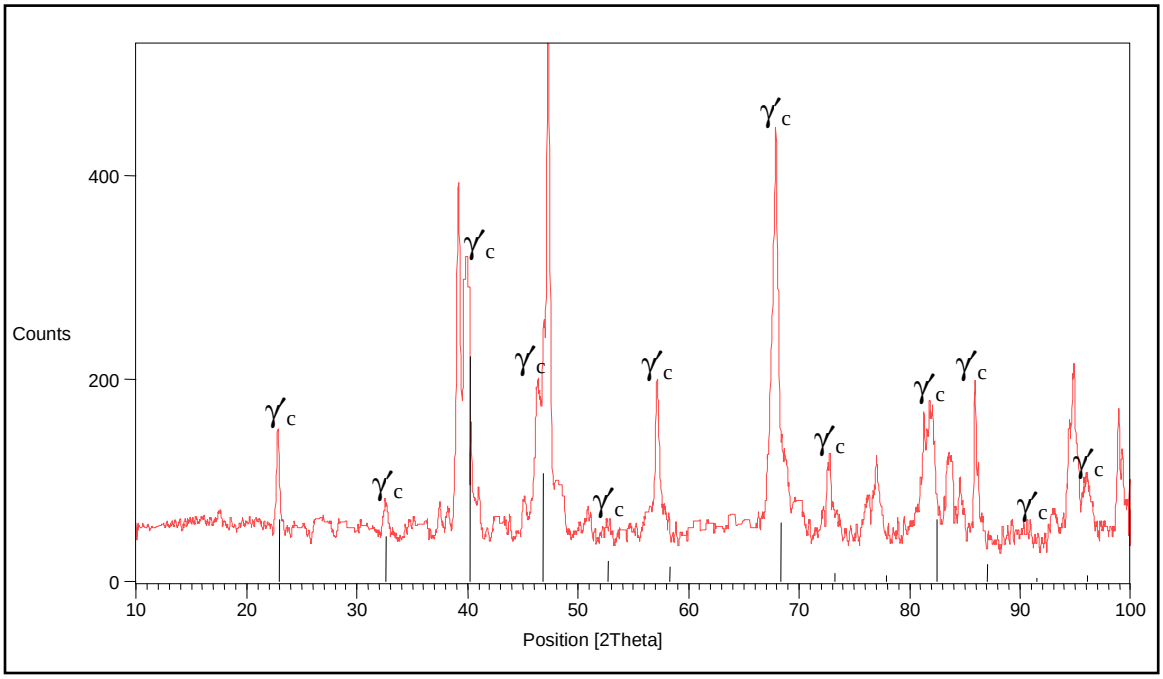

Figure 4.68. XRD Pattern of nominal Pt_{80}:Al_{11}:Ru_3:Cr_6 in the as-cast condition, showing apparent $L1_2$ – ~Pt_3Al peaks.

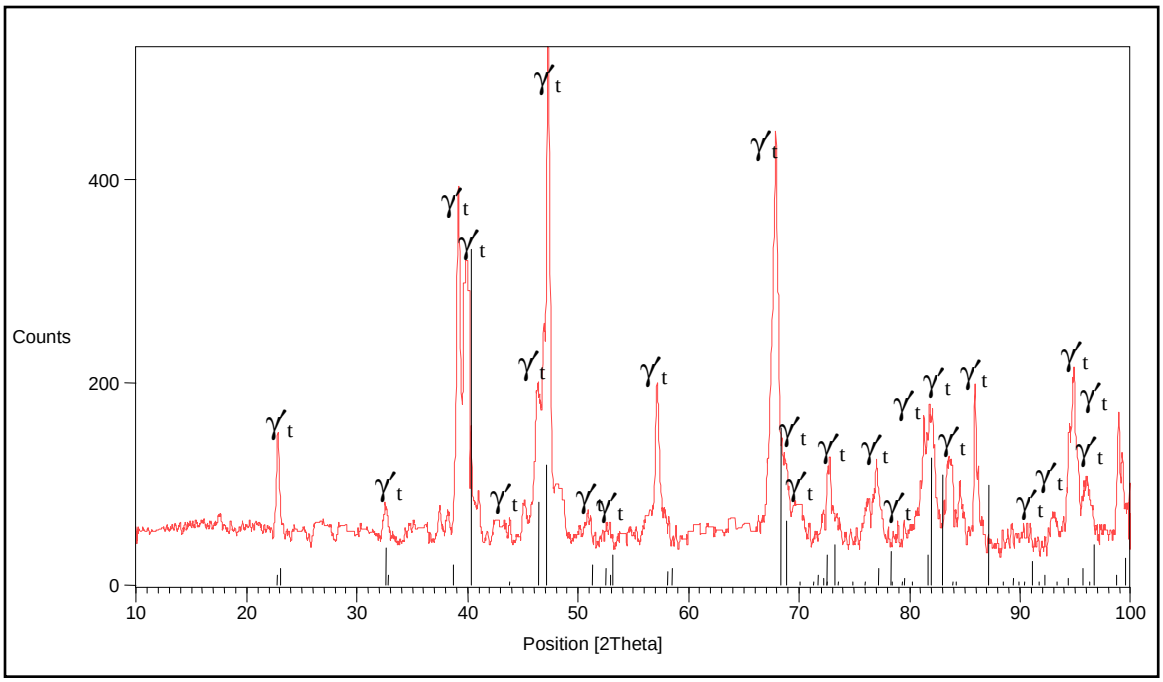

Figure 4.69. XRD Pattern of nominal Pt_{80}:Al_{11}:Ru_3:Cr_6 in the as-cast condition, showing identified DO'_c – ~Pt_3Al peaks.

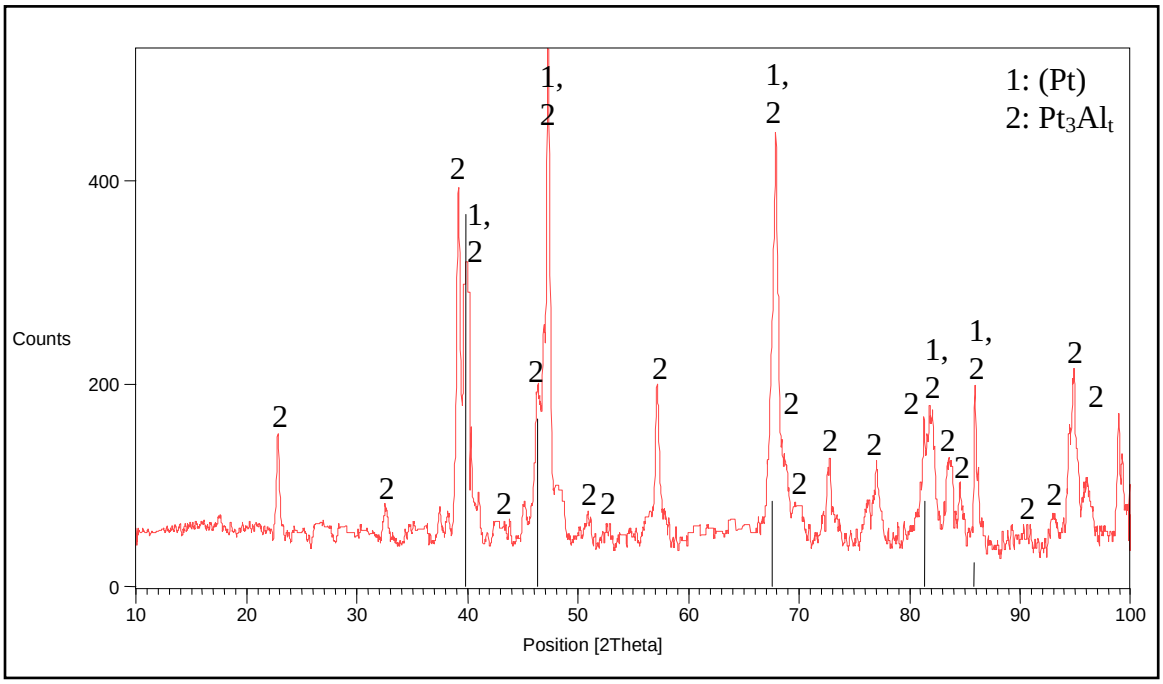

Figure 4.70. XRD pattern of nominal Pt_{80}:Al_{11}:Ru_3:Cr_6 in the as-cast condition, showing all identified phases.

Table 4.30. XRD peaks for Pt_{80}:Al_{11}:Ru_3:Cr_6 in the as-cast condition.

Position 2θ(°)	Height (counts)	Full-Width Half-Maximum 2θ(°)	d-spacing (Å)	Relative Intensity (%)	Phase (s)
22.8274	95.78	0.2362	3.89575	19.72	γ′t
26.8215	13.91	0.9446	3.32400	2.86	-
32.5989	31.85	0.3936	2.74690	6.56	γ′t
37.4682	29.30	0.2362	2.40035	6.03	-
39.1754	346.47	0.2755	2.29959	71.32	γ′t
39.8647	268.14	0.2362	2.26141	55.19	(Pt), γ′t
40.1003	242.50	0.2362	2.24866	49.92	γ′t
40.9545	43.11	0.2362	2.20371	8.87	γ′t
42.9488	15.87	0.9446	2.10589	3.27	γ′t
45.1443	39.43	0.3149	2.00845	8.12	γ′t
45.5002	30.86	0.3936	2.00316	4.53	-
46.3358	152.17	0.2755	1.95954	31.32	(Pt), γ′t
47.2926	485.81	0.2558	1.92211	100.00	γ′t
48.4707	48.69	0.4723	1.87811	10.02	-
50.9588	22.28	0.5510	1.79210	4.59	γ′t
52.6924	13.84	0.6298	1.73715	2.85	γ′t
57.1468	151.48	0.1968	1.61188	31.18	γ′t
67.8865	383.61	0.1574	1.38069	78.96	(Pt), γ′t
69.8869	27.84	0.6298	1.34598	5.73	γ′t
72.7030	67.86	0.3149	1.30064	13.97	γ′t
77.0071	70.16	0.3149	1.23833	14.44	γ′t
81.3132	111.00	0.1440	1.18230	22.85	(Pt), γ′t
81.9421	116.55	0.4723	1.17579	23.99	γ′t
83.7244	74.91	0.2362	1.15524	15.42	γ′t
84.5927	53.35	0.2362	1.14558	10.98	(Pt), γ′t
85.9315	155.30	0.1771	1.13113	31.97	γ′t
92.9988	33.59	0.5510	1.06282	6.91	γ′t
94.8628	172.90	0.2362	1.04680	35.59	γ′t
96.0290	64.90	0.4723	1.03716	13.36	γ′t
98.9414	133.37	0.1680	1.01345	27.45	γ′t

4.2.1.3 Nominal $Pt_{80}:Al_{11}:Ru_6:Cr_3$

HR-SEM-BSE images of the edge and centre microstructure in the as-cast condition are shown in Figure 4.71 and both consisted of cored (Pt) dendrites with a (Pt) + ~Pt_3Al eutectic. ~Pt_3Al precipitates in the dendrites were finer in the centres. The microstructure consisted of 82 ± 6% dendrites with an arm spacing of 10.9 ± 1.9 µm. The phase compositions are shown in Table 4.31. As with the other samples, Ru and Cr had limited solubility in the ((Pt) + ~Pt_3Al) eutectic, and partitioned almost exclusively to (Pt). The darker inner part of the dendrites had more Ru compared to the lighter outer part.

All three phases database lines were matched with the experimental XRD spectrum (Figure 4.72 to 4.74) and Figure 4.75 together with Table 4.32 gives the identified phases.

Table 4.31. EDX Phase compositions of nominal $Pt_{80}:Al_{11}:Ru_6:Cr_3$ in the as-cast condition.

Phase Description	Al	Ru	Cr	Pt	Phase
Overall	7.9 ± 0.5	4.7 ± 0.6	5.8 ± 0.2	81.6 ± 0.8	-
Dark (Eutectic)	18.2 ± 0.4	0.2 ± 0.5	1.2 ± 0.3	80.6 ± 0.6	(Pt) + ~Pt_3Al
Dendrite overall	3.8 ± 0.5	5.6 ± 0.3	3.1 ± 0.1	87.5 ± 0.9	(Pt) + ~Pt_3Al
Dendrite inner (darker)	5.2 ± 0.2	10.0 ± 0.7	2.9 ± 0.4	81.9 ± 0.5	Cored (Pt) + ~Pt_3Al
Dendrite outer (lighter)	12.0 ± 0.7	0.6 ± 0.5	3.0 ± 0.8	84.4 ± 0.3	(Pt) + ~Pt_3Al

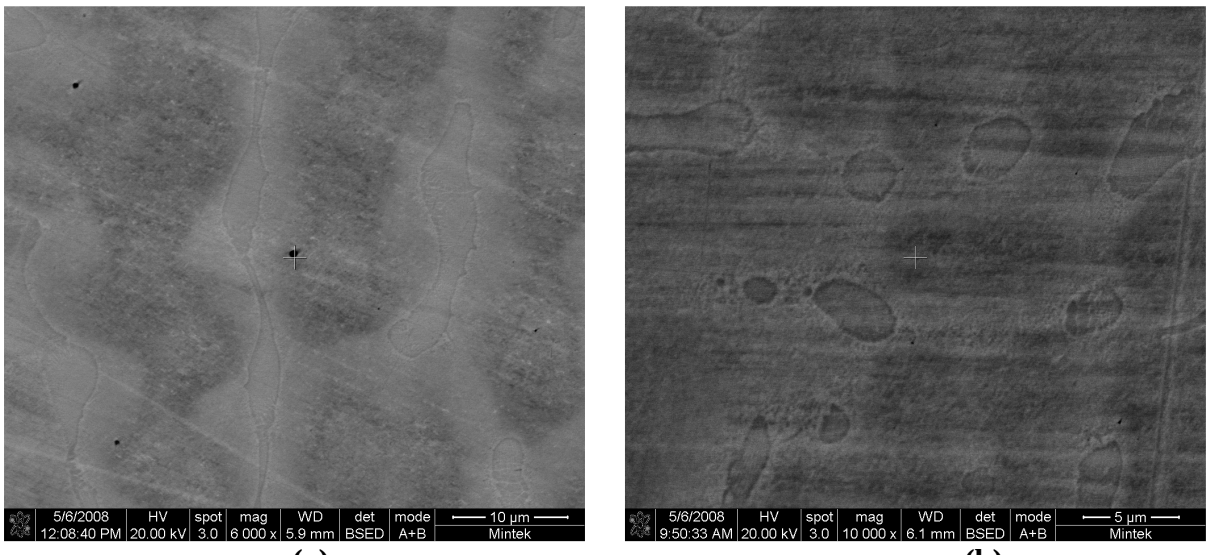

(a) **(b)**

Figure 4.71. HR-SEM-BSE image of nominal $Pt_{80}:Al_{11}:Ru_6:Cr_3$, as-cast condition, a) taken from the centre and (b) edge, showing cored (Pt) dendrites (light) with ~Pt_3Al precipitates and a eutectic of (Pt) + ~Pt_3Al (dark).

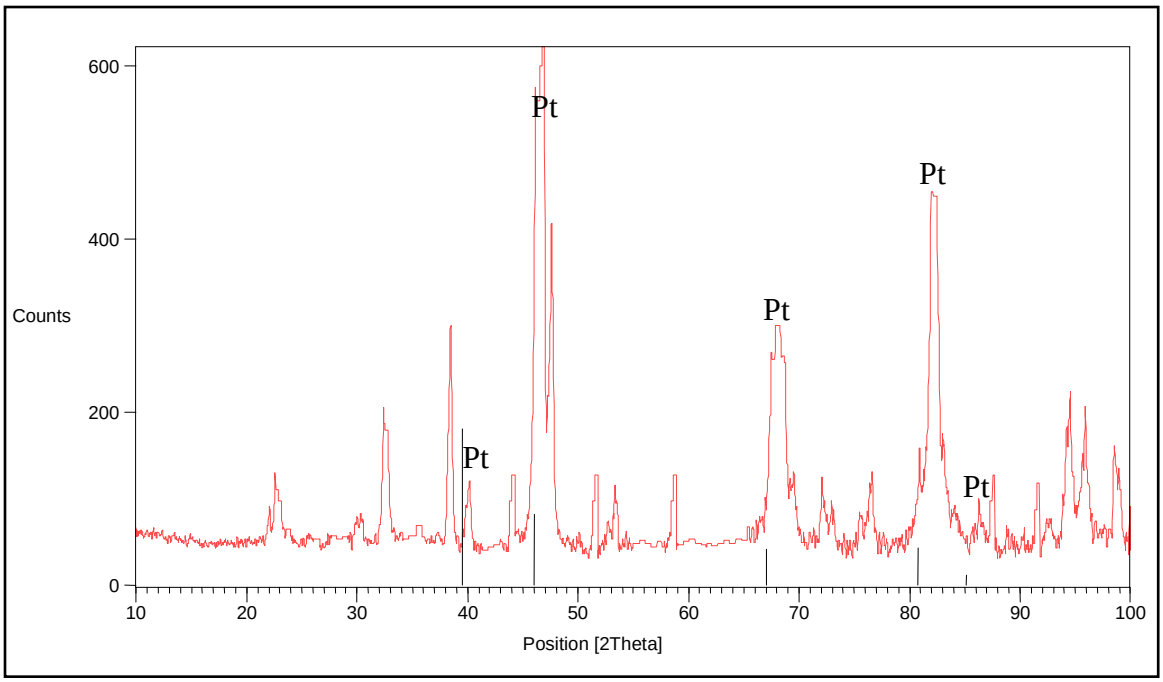

Figure 4.72. XRD Pattern of nominal Pt_{80}:Al_{11}:Ru_6:Cr_3 in the as-cast condition, showing identified Pt peaks.

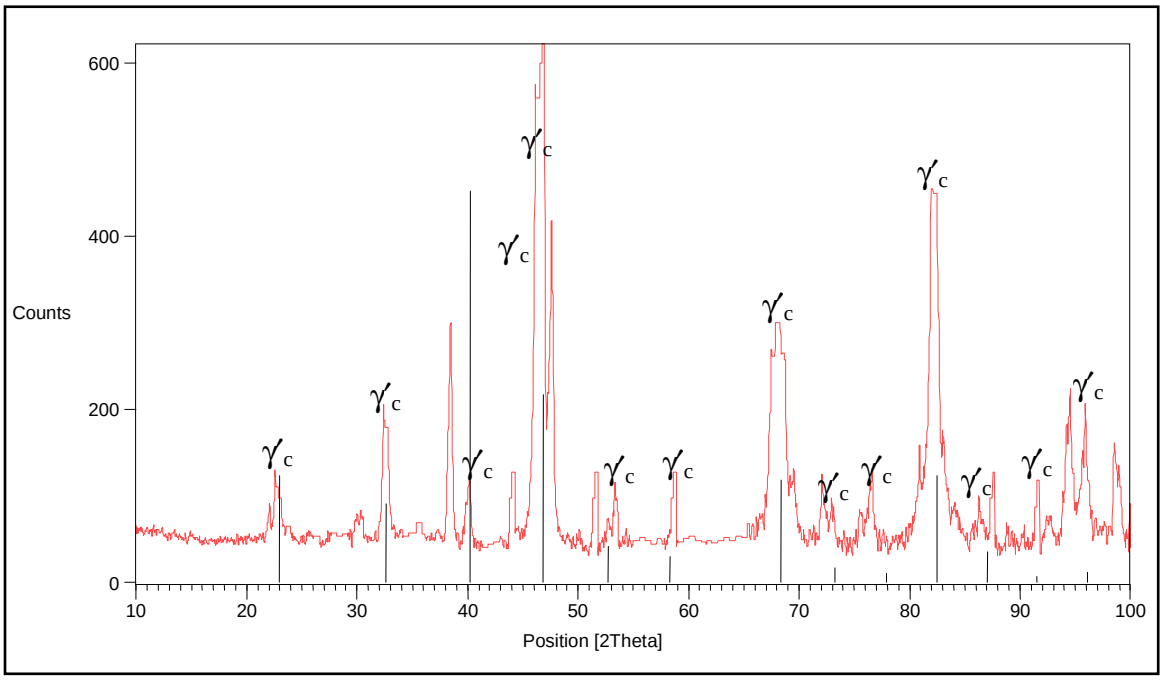

Figure 4.73. XRD Pattern of nominal Pt_{80}:Al_{11}:Ru_6:Cr_3 in the as-cast condition, showing apparent $L1_2$ – ~Pt_3Al peaks.

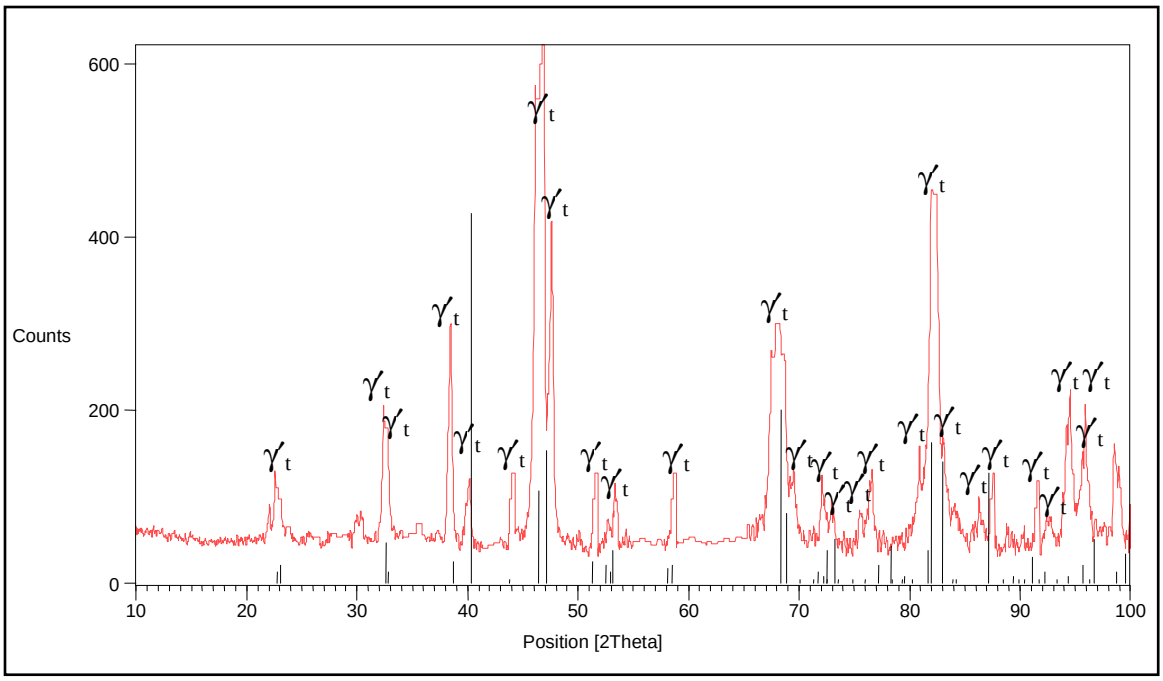

Figure 4.74. XRD Pattern of nominal Pt_{80}:Al_{11}:Ru_6:Cr_3 in the as-cast condition, showing identified DO'_c – ~Pt_3Al peaks.

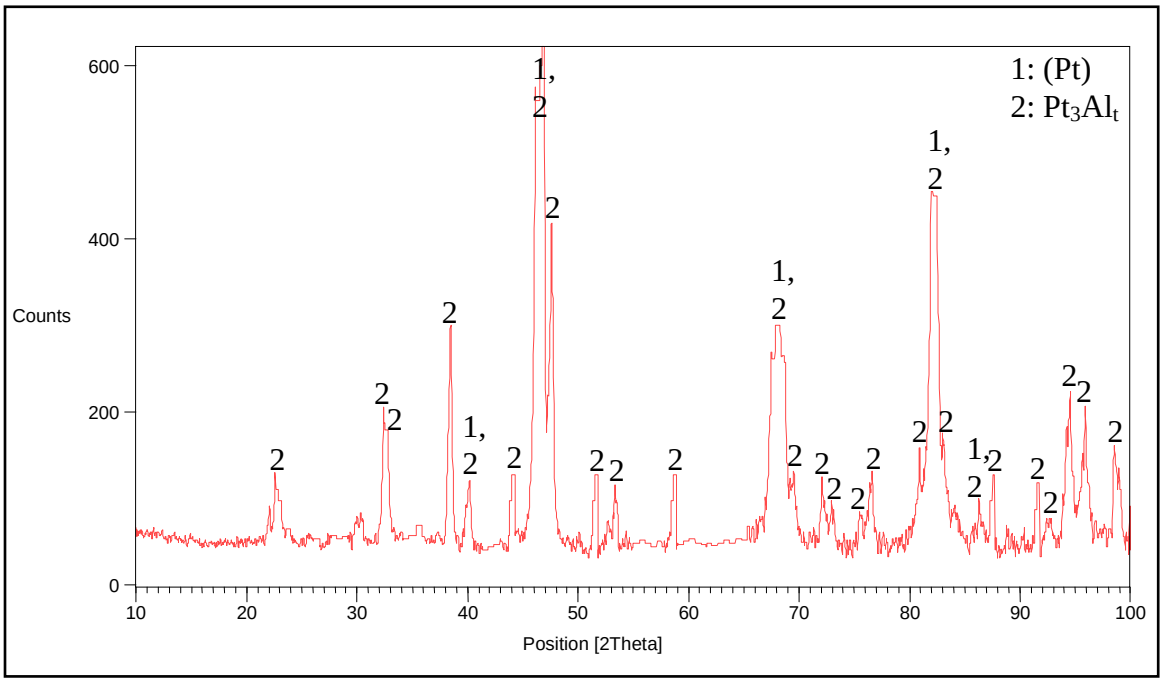

Figure 4.75. XRD pattern of nominal Pt_{80}:Al_{11}:Ru_6:Cr_3 in the as-cast condition, showing all identified phases.

Table 4.32. XRD peaks for Pt_{80}:Al_{11}:Ru_6:Cr_3 in the as-cast condition.

Position 2θ(°)	Height (counts)	Full-Width Half-Maximum 2θ(°)	d-spacing (Å)	Relative Intensity (%)	Phase (s)
22.0432	34.89	0.2362	4.03253	6.08	-
22.6925	55.91	0.3149	3.91861	9.74	γ′t
30.1869	21.07	0.6298	2.96066	3.67	-
32.4332	135.79	0.1968	2.76055	23.65	-
32.7586	123.94	0.2362	2.73387	21.59	γ′t
38.4615	251.54	0.1574	2.34062	43.81	γ′t
40.1688	75.66	0.2165	2.24498	13.18	(Pt), γ′t
44.1842	80.56	0.1181	2.04984	14.03	γ′t
46.1976	512.07	0.1968	1.96508	89.18	(Pt), γ′t
46.9500	574.21	0.0720	1.93373	100.00	γ′t
47.6012	367.72	0.2755	1.91037	64.04	γ′t
51.6645	85.05	0.1181	1.76927	14.81	γ′t
53.4050	56.98	0.3936	1.71564	9.92	γ′t
58.7858	78.54	0.1181	1.57079	13.68	γ′t
66.1616	42.15	0.7872	1.38835	23.64	-
67.4778	190.44	0.2362	1.38805	33.17	(Pt), γ′t
68.6671	203.69	0.1574	1.36689	35.47	γ′t
69.4509	69.01	0.3149	1.35336	12.02	γ′t
72.0823	76.90	0.1440	1.30922	13.39	γ′t
72.9896	42.40	0.3936	1.29624	7.38	γ′t
75.5812	38.03	0.2362	1.25810	6.62	γ′t
76.5252	74.32	0.3936	1.24492	12.94	γ′t
80.9122	99.46	0.1440	1.18715	17.32	(Pt), γ′t
82.0155	386.28	0.2880	1.17395	67.27	γ′t
82.4845	354.30	0.3149	1.16943	61.70	γ′t
86.4044	32.37	0.6298	1.12615	5.64	(Pt), γ′t
87.6029	84.66	0.1920	1.11289	14.74	γ′t
91.6623	71.14	0.1968	1.07479	12.39	γ′t
92.6166	26.49	0.4723	1.06620	4.61	γ′t
94.2123	134.89	0.1920	1.05144	23.49	γ′t
94.5258	172.01	0.1920	1.04877	29.96	γ′t
95.9047	157.17	0.1680	1.03732	27.37	γ′t
98.5453	106.95	0.2400	1.01646	18.63	γ′t

4.2.1.4. Nominal $Pt_{78}:Al_{11}:Ru_5:Cr_6$

HR-SEM-BSE images of the centre and edge microstructure in the as-cast condition are shown in Figure 4.76 and consisted of cored (Pt) dendrites (with dark inner dendrites) and a eutectic of (Pt) + ~Pt_3Al. ~Pt_3Al precipitates can be seen in the dendrites but not so clearly. The dendrites were the major phase taking 84 ± 7% of the microstructure. The average dendrite arm spacing was about 8.9 ± 1.3 µm. The overall composition was comparable to the EDX composition of the as-cast sample (Table 4.33). The interdendritic eutectic ((Pt) + ~Pt_3Al) comprised about 18 at.% Al and the cored (Pt) phase had about 6 at.% Al. Ru and Cr had very limited solubility in the ((Pt) + ~Pt_3Al) eutectic, and partitioned to (Pt). The darker part of the dendrites had a high solubility of Ru (~8.0 at.%) compared to the lighter part.

Comparison of experimental XRD spectrum with database lines are shown in Figures 4.77 to 4.49 and the identified phases are given in Figure 4.50 and Table 4.34.

Table 4.33. EDX Phase compositions of nominal $Pt_{78}:Al_{11}:Ru_5:Cr_6$ in the as-cast condition.

Phase Description	Al	Ru	Cr	Pt	Phase
Overall	9.9 ± 0.7	3.7 ± 0.8	4.4 ± 0.5	82.0 ± 0.6	-
Dark (Eutectic)	18.1 ± 0.4	0.30 ± 0.0	2.3 ± 0.2	79.4 ± 0.3	(Pt) + ~Pt_3Al
Dendrite overall	6.4 ± 0.7	2.9 ± 0.2	6.7 ± 0.3	84.0 ± 0.4	(Pt) + ~Pt_3Al
Dendrite inner (darker)	5.1 ± 0.5	7.7 ± 0.3	4.9 ± 0.6	82.4 ± 0.8	Cored (Pt) + ~Pt_3Al
Dendrite outer (lighter)	10.4 ± 0.4	0.6 ± 0.2	5.1 ± 0.7	83.9 ± 0.4	(Pt) + ~Pt_3Al

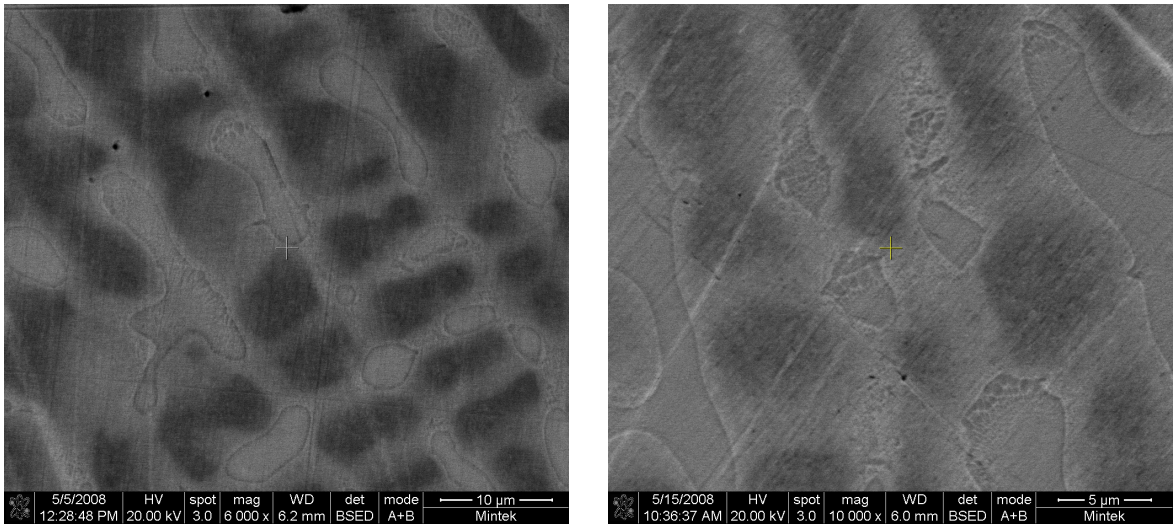

(a) **(b)**

Figure 4.76. HR-SEM-BSE image of nominal $Pt_{78}:Al_{11}:Ru_5:Cr_6$, as-cast condition, a) taken from the centre and b) edge showing cored (Pt) dendrites with a eutectic of (Pt) + ~Pt_3Al.

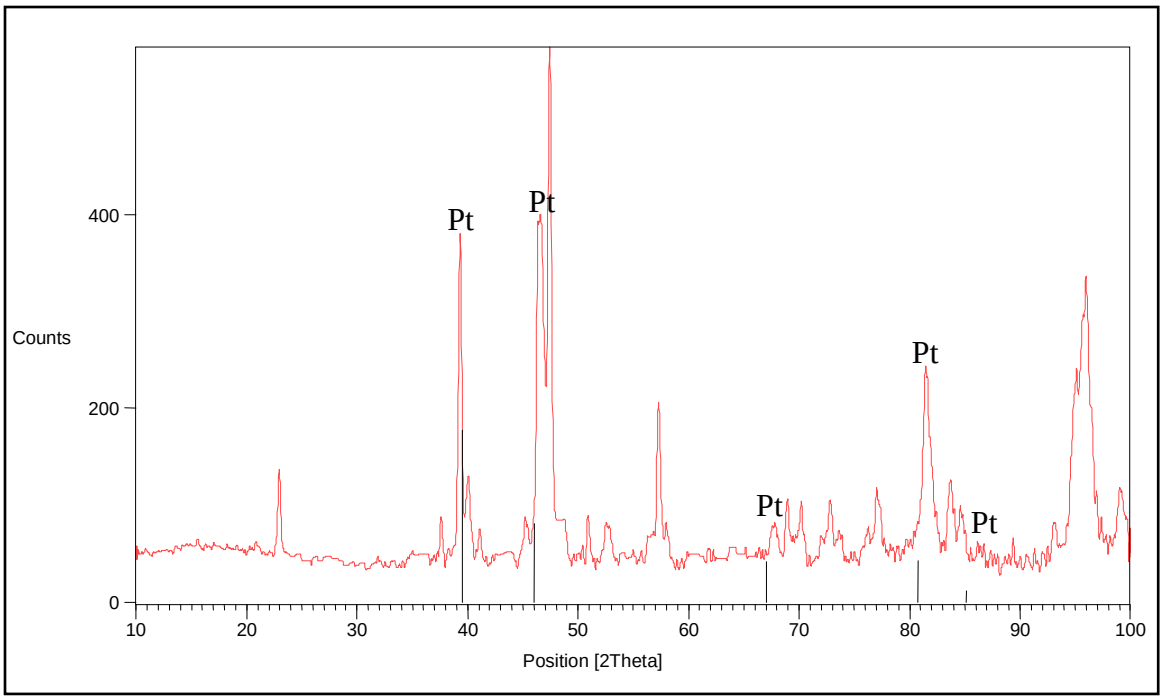

Figure 4.77. XRD Pattern of nominal Pt_{78}:Al_{11}:Ru_5:Cr_6 in the as-cast condition, showing identified Pt peaks.

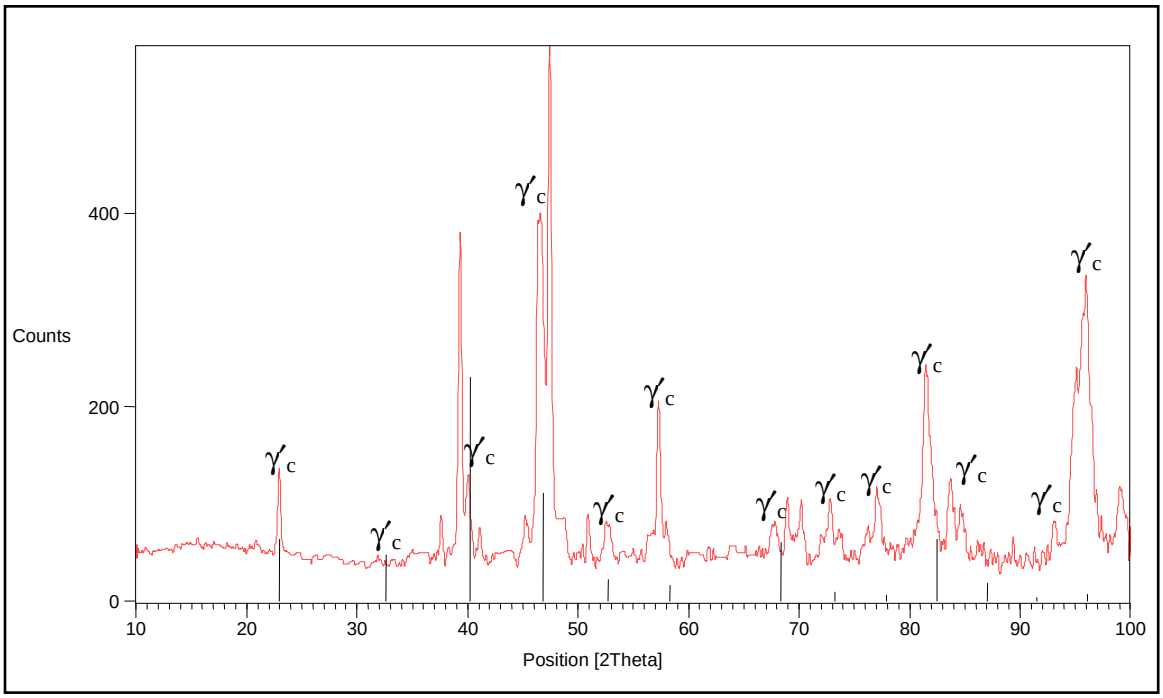

Figure 4.78. XRD Pattern of nominal Pt_{78}:Al_{11}:Ru_5:Cr_6 in the as-cast condition, showing apparent $L1_2$ – ~Pt_3Al peaks.

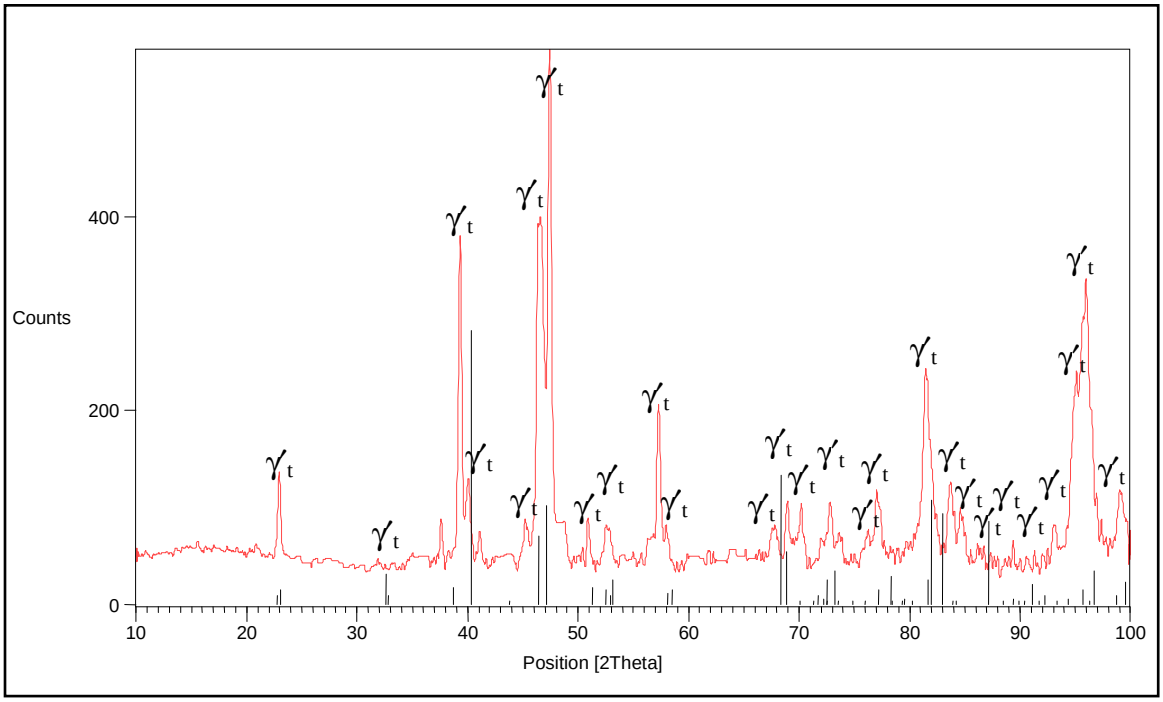

Figure 4.79. XRD Pattern of nominal $Pt_{78}:Al_{11}:Ru_5:Cr_6$ in the as-cast condition, showing identified DO'_c – ~Pt_3Al peaks.

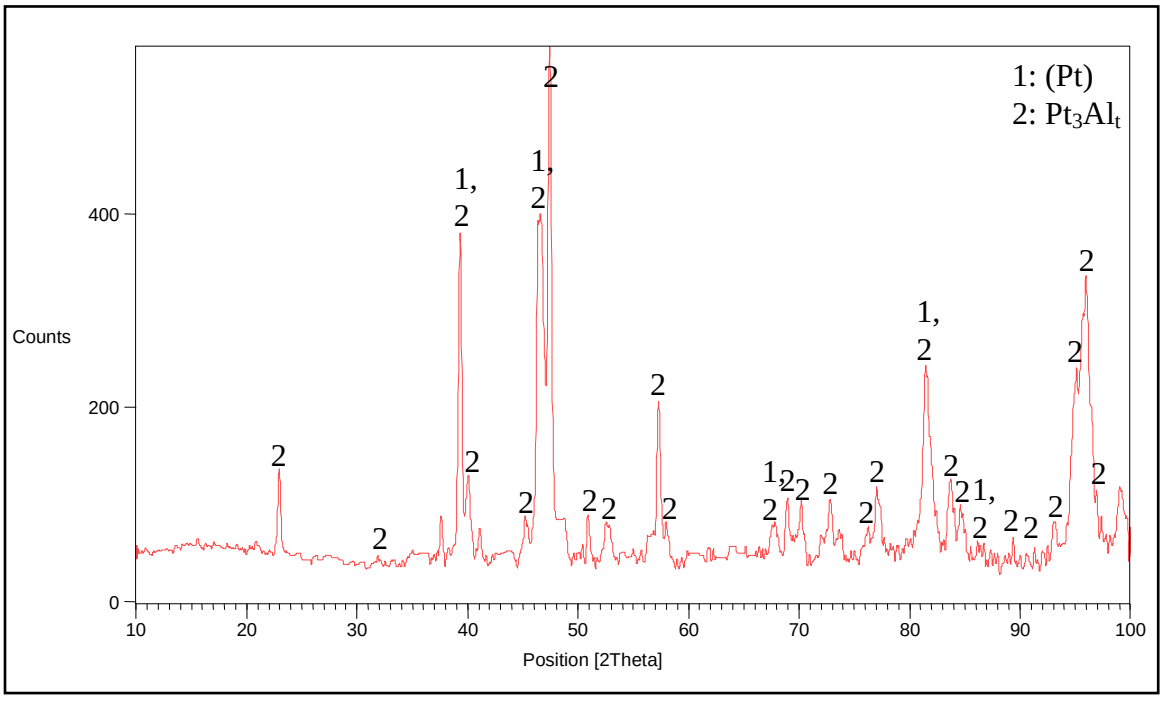

Figure 4.80. XRD pattern of nominal $Pt_{78}:Al_{11}:Ru_5:Cr_6$ in the as-cast condition, showing all identified phases.

Table 4.34. XRD peaks for Pt_{78}:Al_{11}:Ru_5:Cr_6 in the as-cast condition.

Position 2θ(°)	Height (counts)	Full-Width Half-Maximum 2θ(°)	d-spacing (Å)	Relative Intensity (%)	Phase (s)
22.9475	86.93	0.2558	3.87563	16.30	γ′t
32.7424	52.78	0.1181	2.73518	10.48	γ′t
37.5825	43.50	0.1968	2.39331	8.16	-
39.3321	338.67	0.2755	2.29079	63.51	(Pt), γ′t
40.0671	87.77	0.2165	2.25045	16.46	γ′t
41.1037	33.07	0.3149	2.19606	6.20	γ′t
43.8055	11.31	0.8659	2.06668	2.12	-
45.2802	30.86	0.3936	2.00316	4.53	γ′t
46.3779	352.11	0.1920	1.95624	66.03	(Pt), γ′t
46.5678	359.04	0.2755	1.95032	67.33	γ′t
47.4349	533.27	0.3149	1.91667	100.00	γ′t
48.5378	43.10	0.4723	1.87567	8.08	γ′t
50.8876	47.71	0.2362	1.79444	8.95	γ′t
52.6775	36.76	0.6298	1.73761	6.89	γ′t
57.2943	163.82	0.3542	1.60808	30.72	γ′t
67.7409	33.95	0.7085	1.38330	6.37	(Pt), γ′t
68.9582	62.15	0.3542	1.36183	11.66	γ′t
70.1809	58.41	0.2362	1.34107	10.95	γ′t
72.8285	62.04	0.3542	1.29871	11.63	-
73.6595	27.01	0.4723	1.28610	5.07	γ′t
75.5812	38.03	0.2362	1.25810	6.62	-
77.0723	64.93	0.3149	1.23744	12.18	γ′t
81.4618	186.01	0.3149	1.18150	34.88	(Pt), γ′t
83.6940	75.59	0.5510	1.15558	14.17	γ′t
84.6668	47.45	0.3936	1.14477	8.90	(Pt), γ′t
86.3841	12.00	0.4723	1.12637	2.25	γ′t
89.3849	27.42	0.1968	1.09617	5.14	γ′t
93.1206	38.56	0.3936	1.06175	7.23	γ′t
95.0700	190.10	0.5510	1.04507	35.65	γ′t
95.9776	289.22	0.3840	1.03672	54.24	γ′t
96.5470	141.23	0.3120	1.03468	26.48	γ′t
99.1015	72.79	0.4800	1.01224	13.65	γ′t

4.2.1.5. Nominal $Pt_{78}:Al_{11}:Ru_3:Cr_8$

HR-SEM-BSE images of the centre and edge microstructures are shown in Figure 4.81 and both consisted of cored (Pt) dendrites with precipitates and a eutectic of (Pt) + ~Pt_3Al. The dendrite inner were darker in contrast than the outer dendrites. Similarities of the microstructures confirmed the homogeneity of the sample. The eutectic was lighter than the dendrite centres. The proportion of the dendrites was 82 ± 9% of the sample microstructure and the dendrite arm spacing was 8.2 ± 2.9 µm. The phase compositions are shown in Table 4.35. Ru and Cr had limited solubility in the ((Pt) + ~Pt_3Al) eutectic, and partitioned mostly to (Pt). The darker inner part of the dendrites had a higher solubility of Ru compared to the lighter outer part, and was darkest in the microstructure.

XRD results and phases identified are shown in Figures 4.82 to 4.85 and Table 4.36

Table 4.35. EDX Phase compositions of nominal $Pt_{78}:Al_{11}:Ru_3:Cr_8$ in the as-cast condition.

Phase Description	Al	Ru	Cr	Pt	Phase
Overall	9.4 ± 0.4	4.9 ± 0.3	3.1 ± 0.4	82.6 ± 0.6	-
Dark (Eutectic)	18.2 ± 0.1	0.2 ± 0.2	1.2 ± 0.3	80.6 ± 0.2	(Pt) + ~Pt_3Al
Dendrite overall	3.7 ± 0.7	5.2 ± 0.1	3.4 ± 0.3	87.7 ± 0.8	(Pt) + ~Pt_3Al
Dendrite inner (darker)	6.2 ± 0.3	9.1 ± 0.4	3.2 ± 0.2	81.5 ± 0.5	Cored (Pt) + ~Pt_3Al
Dendrite outer (lighter)	10.9 ± 0.7	0.7 ± 0.3	3.2± 0.6	85.2 ± 0.4	(Pt) + ~Pt_3Al

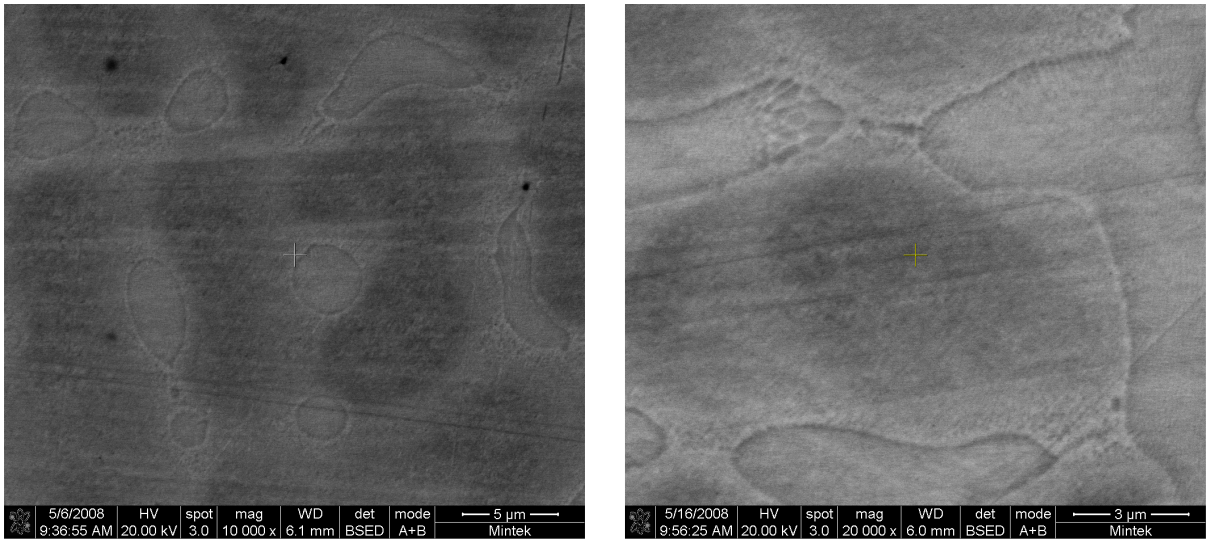

(a) **(b)**

Figure 4.81. HR-SEM-BSE image of nominal $Pt_{78}:Al_{11}:Ru_3:Cr_8$, as-cast condition, a) taken from the centre and b) edge showing cored (Pt) dendrites with a eutectic of (Pt) + ~Pt_3Al.

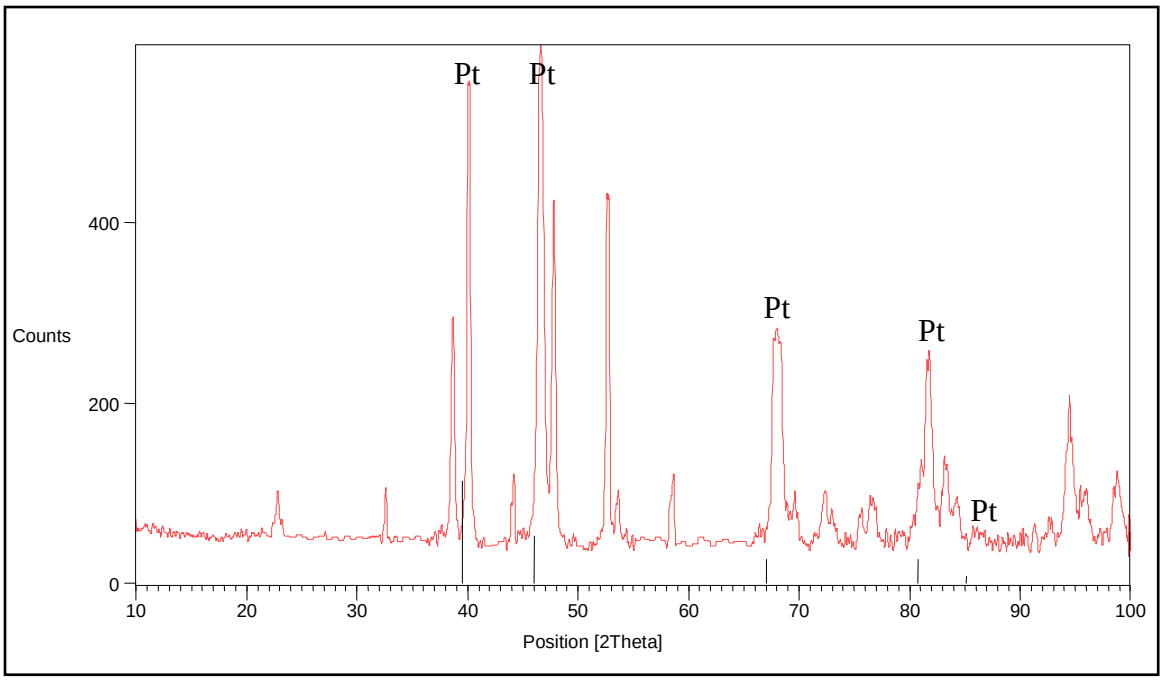

Figure 4.82. XRD Pattern of nominal Pt_{78}:Al_{11}:Ru_3:Cr_8 in the as-cast condition, showing identified Pt peaks.

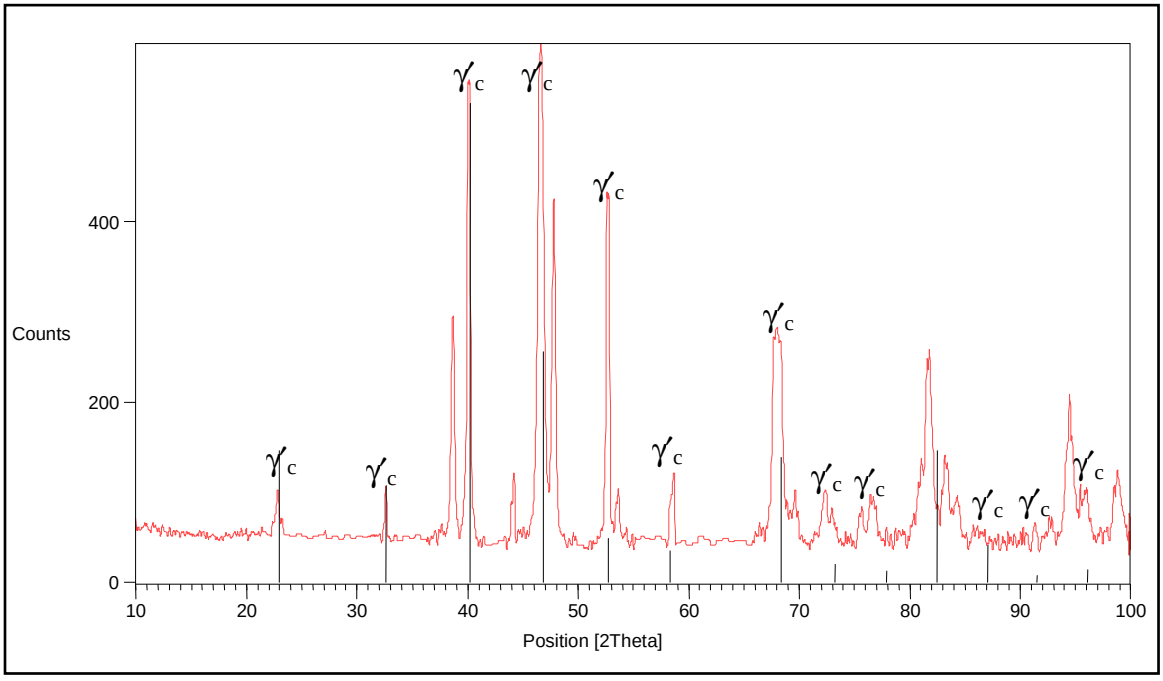

Figure 4.83. XRD Pattern of nominal Pt_{78}:Al_{11}:Ru_3:Cr_8 in the as-cast condition, showing apparent $L1_2$ – ~Pt_3Al peaks.

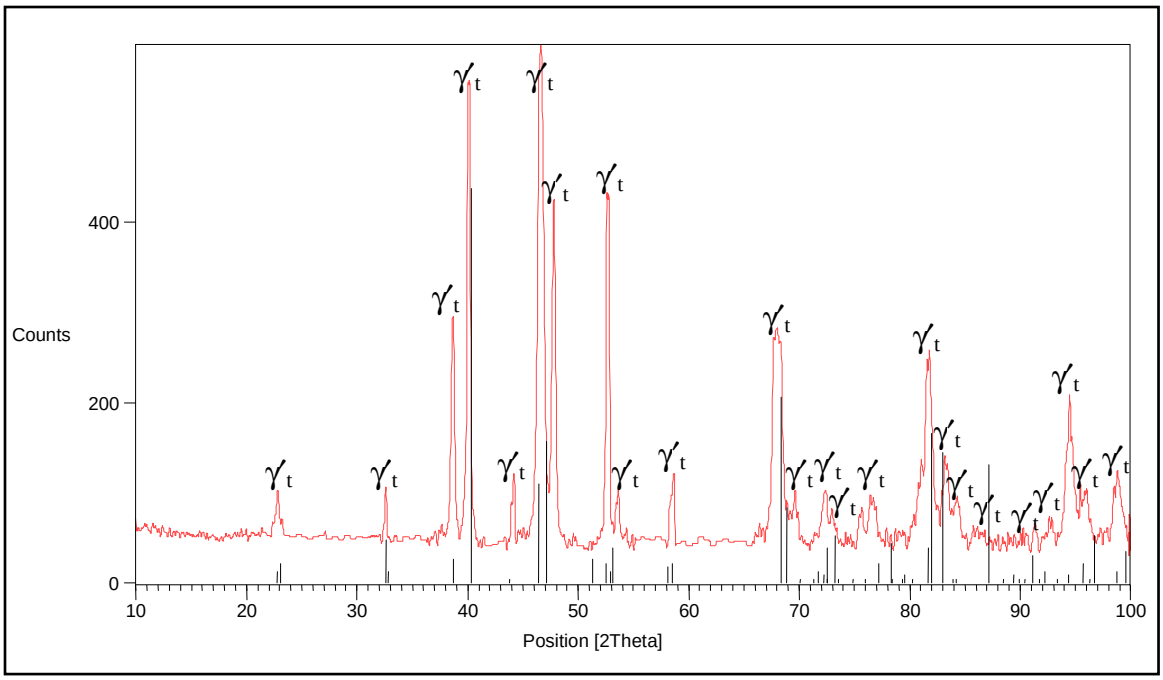

Figure 4.84. XRD Pattern of nominal Pt_{78}:Al_{11}:Ru_3:Cr_8 in the as-cast condition, showing identified DO'_c – ~Pt_3Al peaks.

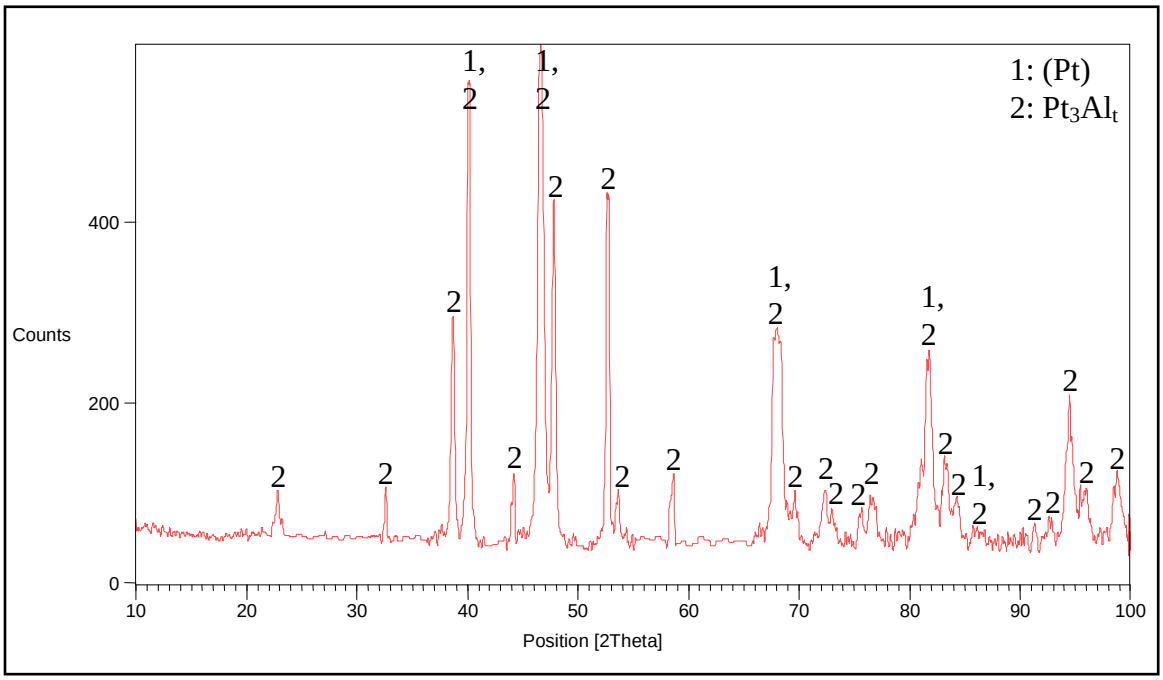

Figure 4.85. XRD pattern of nominal Pt_{78}:Al_{11}:Ru_3:Cr_8 in the as-cast condition, showing all identified phases.

Table 4.36. XRD peaks for Pt_{78}:Al_{11}:Ru_3:Cr_8 in the as-cast condition.

Position 2θ(°)	Height (counts)	Full-Width Half-Maximum 2θ(°)	d-spacing (Å)	Relative Intensity (%)	Phase (s)
22.8046	47.98	0.2362	3.89960	9.38	γ′t
32.6127	57.47	0.1771	2.74576	11.24	γ′t
38.4682	29.30	0.2362	2.40035	6.03	-
38.6687	247.06	0.3346	2.32855	48.32	γ′t
40.1556	511.27	0.1181	2.24569	100.00	(Pt), γ′t
44.1971	77.55	0.1968	2.04927	15.17	γ′t
45.1443	39.43	0.3149	2.00845	4.12	-
46.4476	504.84	0.1771	1.95508	98.74	(Pt), γ′t
46.7821	479.41	0.3149	1.94188	93.77	γ′t
47.8002	381.81	0.3346	1.90288	74.68	γ′t
52.6200	389.84	0.1440	1.73793	76.25	γ′t
52.7522	389.02	0.1378	1.73532	76.09	γ′t
53.5752	52.95	0.3149	1.71059	10.36	γ′t
58.6613	75.78	0.1771	1.57383	14.82	γ′t
66.8865	33.61	0.1574	1.38069	5.96	-
67.7381	224.61	0.1574	1.38335	43.93	(Pt), γ′t
68.2923	221.32	0.2165	1.37347	43.29	γ′t
69.6029	55.44	0.3149	1.35078	10.84	γ′t
72.3801	58.57	0.3149	1.30564	11.46	γ′t
75.6079	33.19	0.3936	1.25772	6.49	γ′t
76.6195	45.89	0.6298	1.24362	8.98	γ′t
81.6981	190.70	0.6298	1.17868	37.30	(Pt), γ′t
83.2751	80.20	0.5510	1.16032	15.69	γ′t
84.2584	45.20	0.3936	1.14927	8.84	(Pt), γ′t
91.3217	21.81	0.3149	1.07791	4.27	γ′t
92.7216	23.65	0.6298	1.06527	4.63	γ′t
94.4665	161.04	0.1440	1.04928	31.50	γ′t
95.8065	45.63	0.7680	1.03812	8.93	γ′t

4.2.1.6. Nominal $Pt_{78}:Al_{11}:Ru_8:Cr_3$

HR-SEM-BSE images are shown in Figure 4.86, taken at the centre and edge of the sample. The microstructure consisted of cored (Pt) dendrites with precipitates and a lighter region of the (Pt) + ~Pt_3Al eutectic. Once again, the dendrite inner were darker than the rest of the dendrite. The sample microstructure consisted of 86 ± 5% dendrites with an average arm spacing of 5.9 ± 2.1 µm. The phase compositions are shown in Table 4.37. Similar to the other samples, a decrease in Al was observed compared to the targeted composition. Ru and Cr had limited solubility in the ((Pt) + ~Pt_3Al) eutectic, and partitioned mostly to (Pt).

Figures 4.87 to 4.89 shows the experimental XRD spectrum compared with the database lines for Pt, $L1_2$ and DO'_c - Pt_3Al. The identified phases are shown in Figure 4.90 and Table 4.38.

Table 4.37. EDX Phase compositions of nominal $Pt_{78}:Al_{11}:Ru_8:Cr_3$ in the as-cast condition.

Phase Description	Al	Ru	Cr	Pt	Phase
Overall	9.2 ± 0.4	4.9 ± 0.3	3.1 ± 0.4	82.8 ± 0.6	-
Dark (Eutectic)	19.0 ± 0.1	0.2 ± 0.2	1.2 ± 0.3	79.8 ± 0.2	(Pt) + ~Pt_3Al
Dendrite overall	7.6 ± 0.3	6.5 ± 0.4	3.1 ± 0.2	83.2 ± 0.5	(Pt) + ~Pt_3Al
Dendrite inner (darker)	4.4 ± 0.7	11.6 ± 0.1	3.6 ± 0.3	80.4 ± 0.8	Cored (Pt) + ~Pt_3Al
Dendrite outer (lighter)	12.7 ± 0.7	0.7 ± 0.1	2.3 ± 0.3	84.3 ± 0.8	(Pt) + ~Pt_3Al

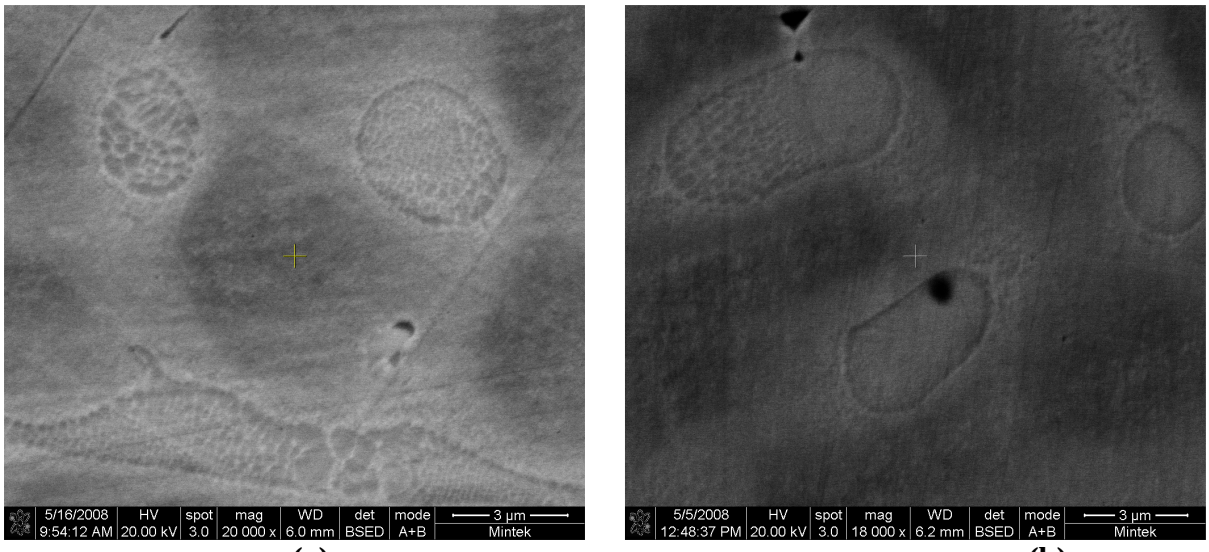

(a) **(b)**

Figure 4.86. HR-SEM-BSE image of nominal $Pt_{78}:Al_{11}:Ru_8:Cr_3$, as-cast condition, a) taken from the centre and b) edge showing cored (Pt) dendrites with fine ~Pt_3Al precipitates and a eutectic of (Pt) + ~Pt_3Al.

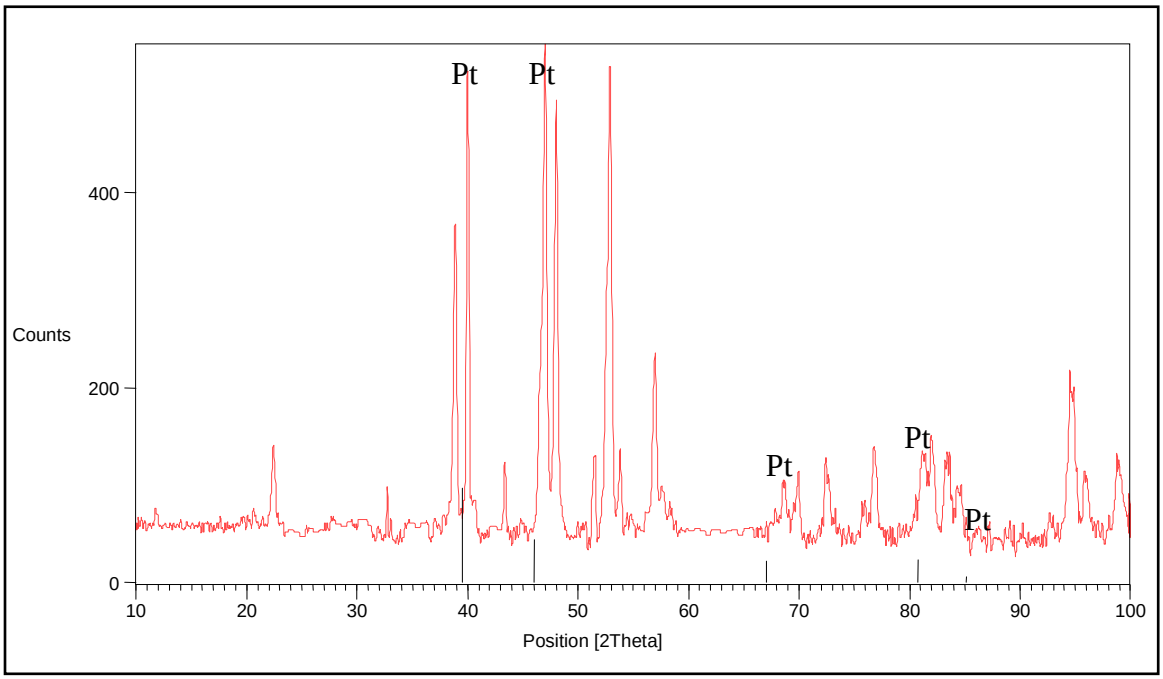

Figure 4.87. XRD Pattern of nominal Pt_{78}:Al_{11}:Ru_8:Cr_3 in the as-cast condition, showing identified Pt peaks.

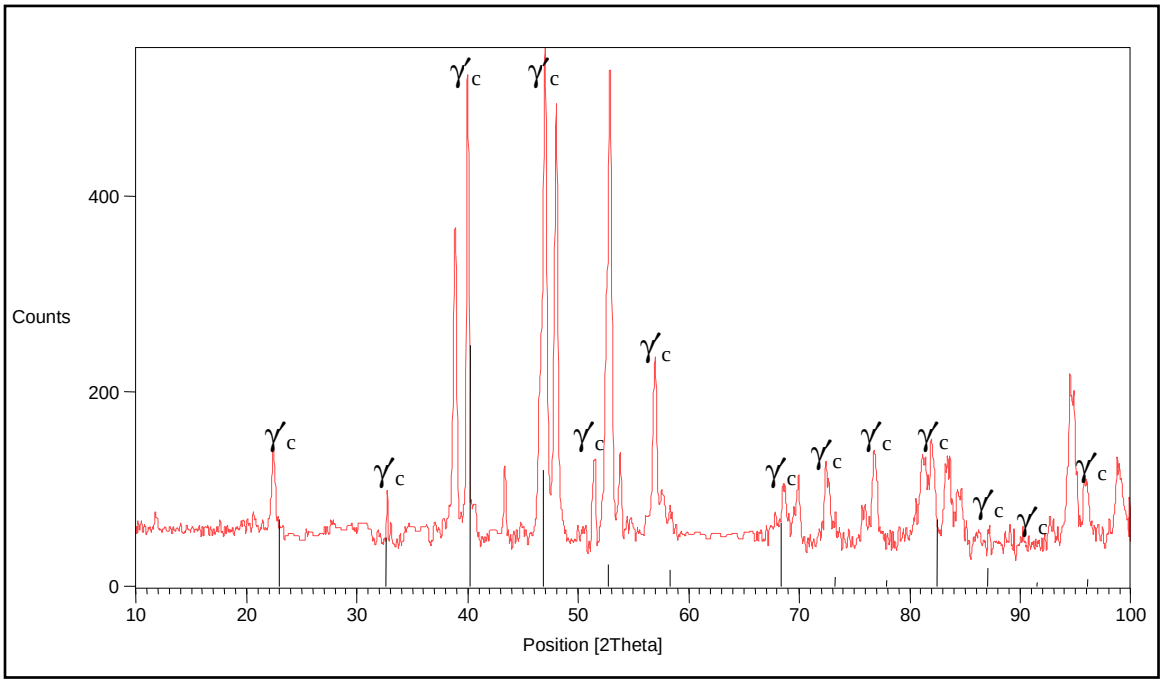

Figure 4.88. XRD Pattern of nominal Pt_{78}:Al_{11}:Ru_8:Cr_3 in the as-cast condition, showing apparent $L1_2$ – ~Pt_3Al peaks.

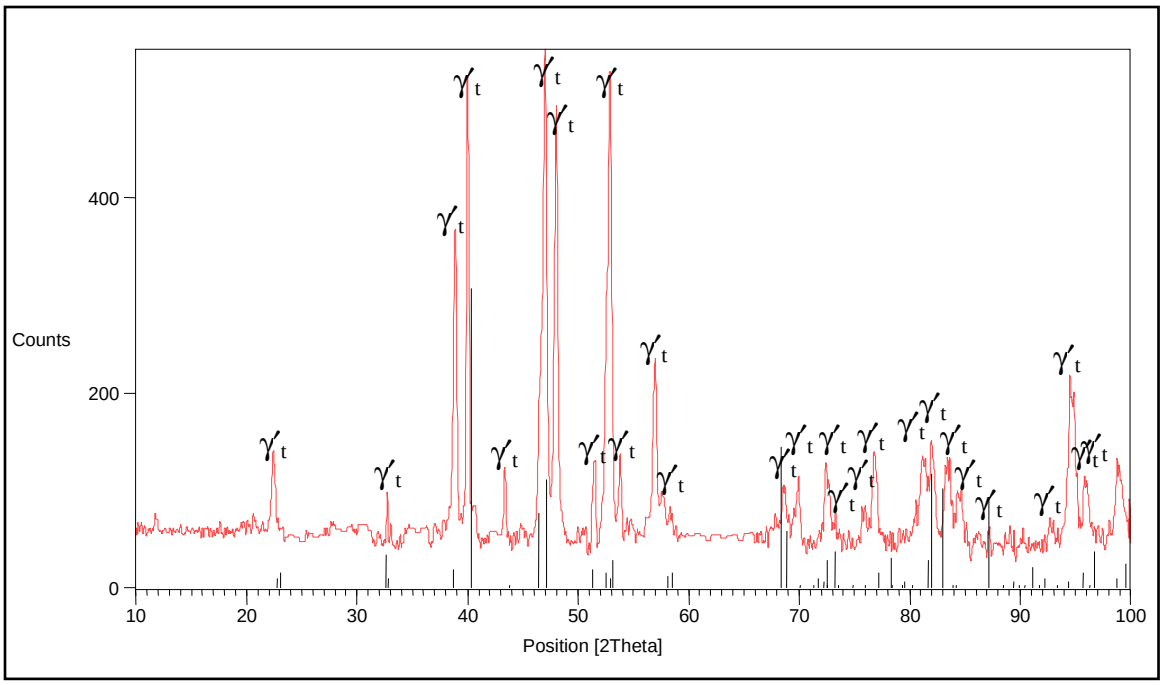

Figure 4.89. XRD Pattern of nominal Pt_{78}:Al_{11}:Ru_8:Cr_3 in the as-cast condition, showing identified DO'_c – ~Pt_3Al peaks.

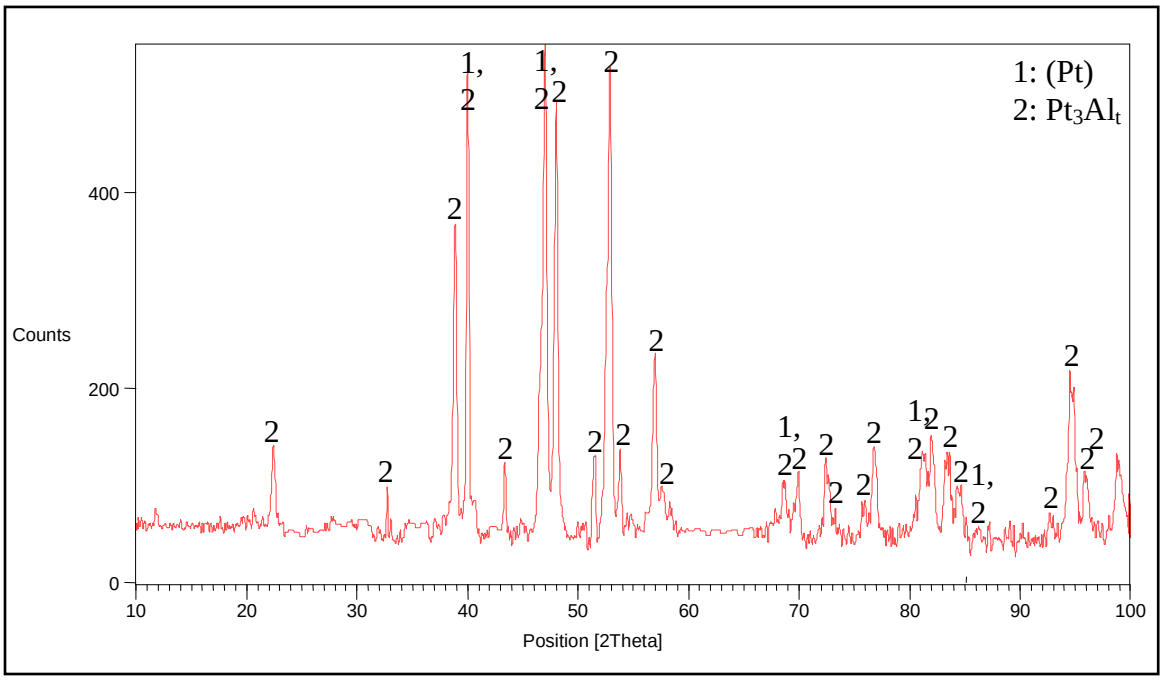

Figure 4.90. XRD pattern of nominal Pt_{78}:Al_{11}:Ru_8:Cr_3 in the as-cast condition, showing all identified phases.

Table 4.38. XRD peaks for Pt_{78}:Al_{11}:Ru_8:Cr_3 in the as-cast condition.

Position 2θ(°)	Height (counts)	Full-Width Half-Maximum 2θ(°)	d-spacing (Å)	Relative Intensity (%)	Phase (s)
22.4285	84.29	0.2755	3.96412	16.74	γ′t
32.7424	52.78	0.1181	2.73518	10.48	γ′t
35.0298	13.39	0.9446	2.56165	2.66	-
38.8637	313.96	0.3149	2.31732	62.35	-
39.9793	473.17	0.2160	2.25332	93.97	γ′t
40.1324	324.21	0.1200	2.25066	64.38	(Pt), γ′t
43.3680	73.62	0.2400	2.08478	14.62	γ′t
46.595	27.01	0.4723	2.07610	5.07	-
47.0207	503.56	0.2880	1.93099	100.00	(Pt), γ′t
48.0284	447.42	0.3120	1.89280	88.85	γ′t
51.5080	83.77	0.2400	1.77281	16.64	γ′t
52.8669	480.92	0.3360	1.73039	95.51	γ′t
53.8056	86.33	0.2880	1.70240	17.14	γ′t
56.9511	172.76	0.4800	1.61562	34.31	γ′t
68.6294	53.04	0.3840	1.36641	10.53	(Pt), γ′t
69.9305	68.13	0.3360	1.34414	13.53	γ′t
72.4044	81.65	0.2400	1.30418	16.21	γ′t
75.8699	28.30	0.3840	1.25299	5.62	γ′t
76.8016	93.87	0.4320	1.24010	18.64	γ′t
81.2549	78.21	0.6720	1.18300	15.53	(Pt), γ′t
82.0268	101.01	0.4800	1.17381	20.06	γ′t
83.3722	80.53	0.3840	1.15826	15.99	γ′t
84.4846	53.99	0.5760	1.14582	10.72	(Pt), γ′t
87.2094	17.16	0.2400	1.11689	3.41	γ′t
92.8041	21.38	0.5760	1.06366	4.25	γ′t
94.5212	172.35	0.1440	1.04881	34.23	γ′t
95.8984	63.75	0.2880	1.03737	12.66	γ′t
98.8663	77.23	0.4800	1.01402	15.34	γ′t

4.2.2. Heat Treated Alloys: Microstructural Characterisation

4.2.2.1. Nominal $Pt_{80}:Al_{11}:Ru_5:Cr_4$

A representative HR-SEM-BSE image is shown in Figure 4.91. The microstructure shows fine ~Pt_3Al precipitates in a (Pt) matrix, which were very difficult to discern under the HR-SEM due to the scracthes. The overall composition (Table 4.39) was different from the targeted and as-cast composition. The fineness of the microstructure and scratches did not allow accurate analysis. A decrease in Al was noticed.

XRD results are shown in Figures 4.92 to 4.95 and Table 4.40, with the phases identified.

Table 4.39. EDX overall composition of nominal $Pt_{80}:Al_{11}:Ru_5:Cr_4$ in the heat treated condition.

Phase Description	Al	Ru	Cr	Pt	Phase
Overall	8.9 ± 0.8	3.9 ± 0.6	3.1 ± 0.9	84.1 ± 0.7	-

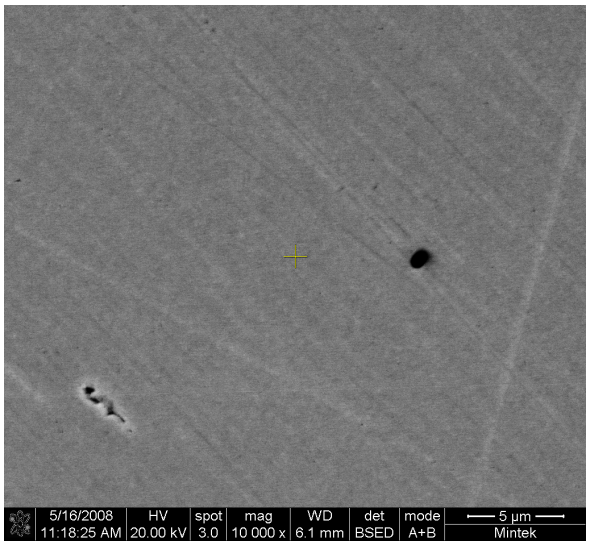

Figure 4.91. HR-SEM-BSE image of nominal $Pt_{80}:Al_{11}:Ru_5:Cr_4$ after heat treatment, showing very fine ~Pt_3Al precipitates (dark) in a (Pt) matrix (light).

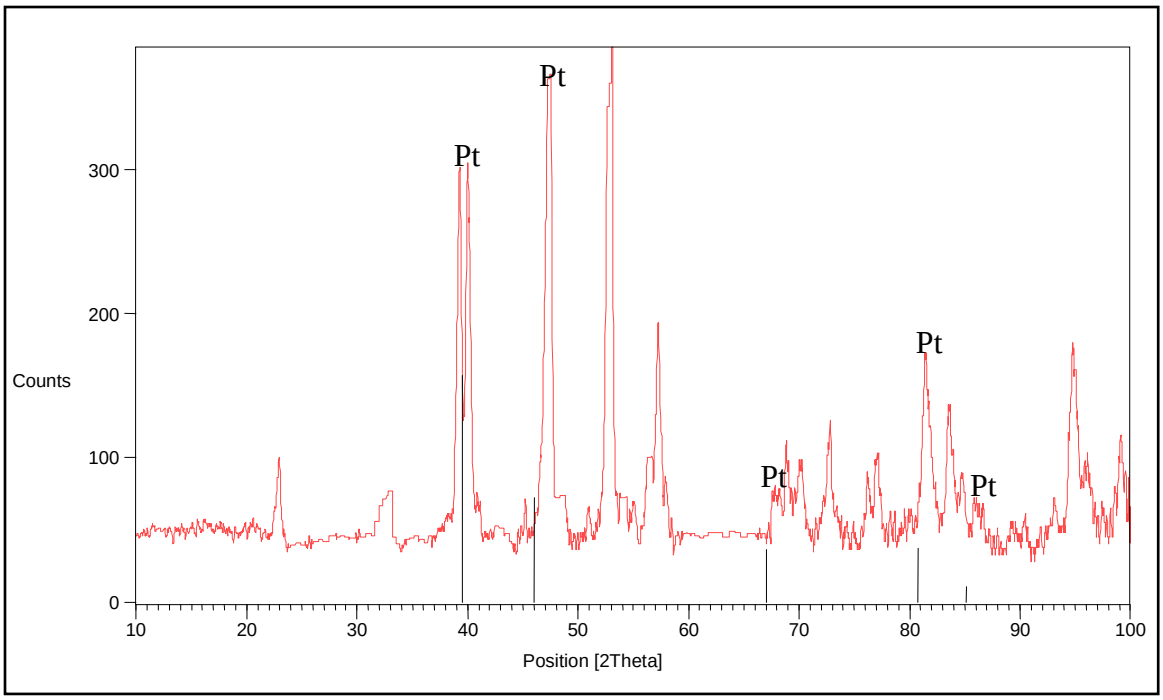

Figure 4.92. XRD Pattern of nominal Pt_{80}:Al_{11}:Ru_5:Cr_4 in the heat treated condition, showing identified Pt peaks.

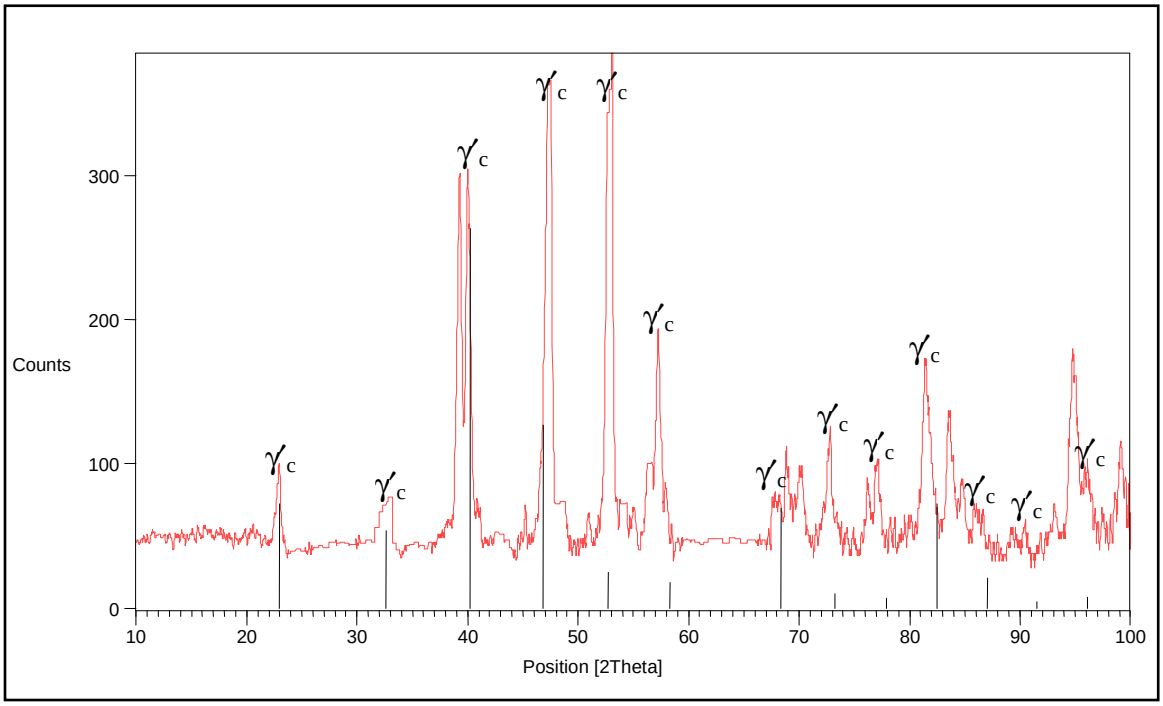

Figure 4.93. XRD Pattern of nominal Pt_{80}:Al_{11}:Ru_5:Cr_4 in the heat treated condition, showing apparent $L1_2$ – ~Pt_3Al peaks.

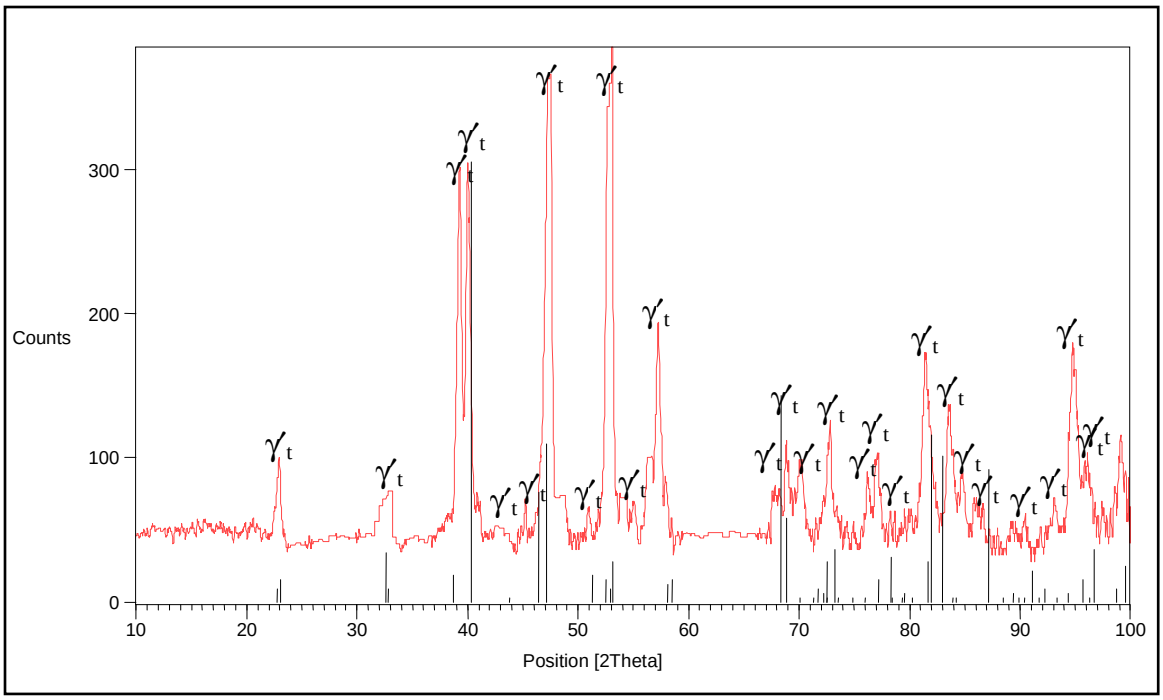

Figure 4.94. XRD Pattern of nominal Pt_{80}:Al_{11}:Ru_5:Cr_4 in the heat treated condition, showing identified DO'_c – ~Pt_3Al peaks.

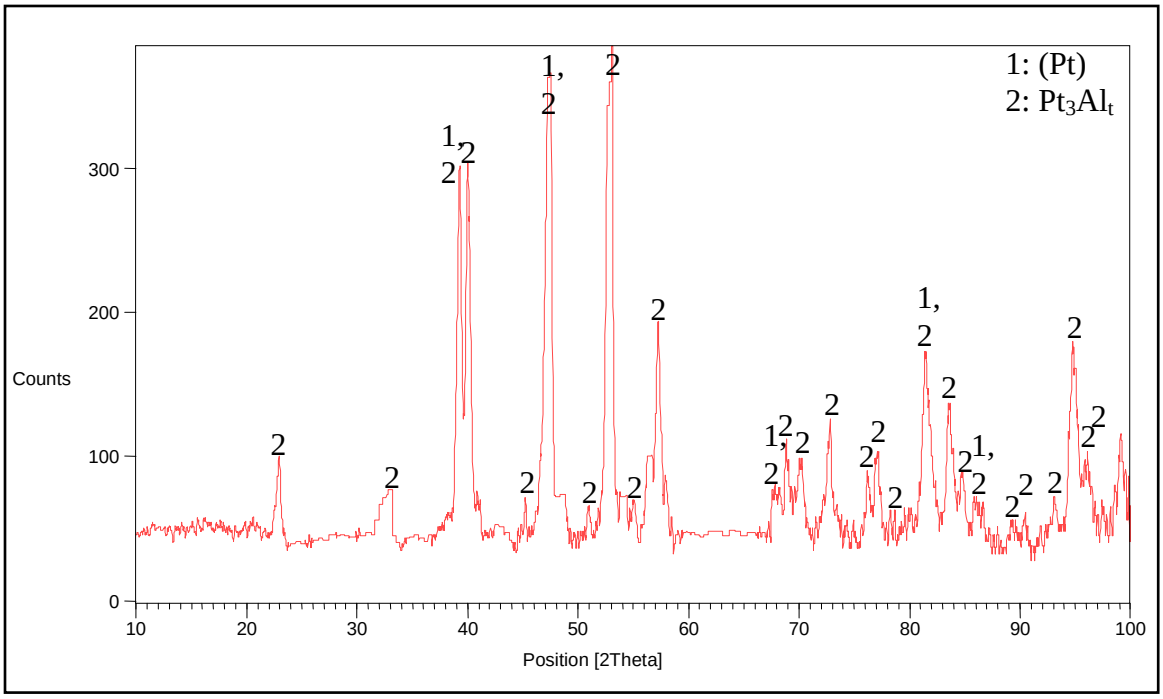

Figure 4.95. XRD pattern of nominal Pt_{80}:Al_{11}:Ru_5:Cr_4 in the heat treated condition, showing all identified phases.

Table 4.40. XRD peaks for Pt_{80}:Al_{11}:Ru_5:Cr_4 in the heat treated condition.

Position 2θ(°)	Height (counts)	Full-Width Half-Maximum 2θ(°)	d-spacing (Å)	Relative Intensity (%)	Phase (s)
22.9889	54.91	0.1574	3.86874	16.04	γ′t
33.0387	35.33	0.3149	2.71133	10.32	γ′t
39.2912	249.99	0.1378	2.29308	73.02	γ′t
39.9816	244.43	0.1771	2.25506	71.40	(Pt), γ′t
42.9418	9.26	0.9446	2.10622	2.71	γ′t
45.2243	30.57	0.1378	2.00509	8.93	γ′t
47.2385	322.34	0.1574	1.92418	94.15	(Pt), γ′t
47.5568	327.78	0.1181	1.91204	95.74	γ′t
48.8406	30.53	0.5510	1.86475	8.92	γ′t
50.9286	21.63	0.2755	1.79309	6.32	γ′t
52.6217	301.42	0.1771	1.73932	88.04	γ′t
53.0643	342.35	0.0960	1.72442	100.00	γ′t
54.1490	28.96	0.3149	1.69381	8.46	γ′t
55.0049	24.93	0.2362	1.66947	7.28	γ′t
56.2937	56.01	0.3149	1.63427	16.36	γ′t
57.3053	144.55	0.2165	1.60780	42.22	γ′t
67.6696	28.37	0.2362	1.38458	8.29	(Pt), γ′t
68.8160	61.90	0.1574	1.36429	18.08	γ′t
70.1423	48.94	0.4723	1.34171	14.29	γ′t
72.8263	81.18	0.1440	1.29766	23.71	γ′t
76.2303	43.34	0.2362	1.24900	12.66	γ′t
77.0036	57.52	0.3936	1.23837	16.80	γ′t
78.2446	20.34	0.2400	1.22080	5.94	γ′t
78.6479	20.94	0.1440	1.21857	6.12	γ′t
81.4359	129.22	0.2400	1.18083	37.74	(Pt), γ′t
83.6341	95.31	0.4320	1.15530	27.84	γ′t
84.8123	45.15	0.3840	1.14223	13.19	γ′t
85.9830	26.83	0.5760	1.12965	7.84	(Pt), γ′t
89.2924	16.15	0.5760	1.09616	4.72	γ′t
90.3981	20.87	0.3840	1.08560	6.10	γ′t
93.1728	32.87	0.3840	1.06042	9.60	γ′t
94.8489	131.86	0.4800	1.04605	38.52	γ′t
96.1375	56.98	0.5760	1.03542	16.64	γ′t
96.8208	27.98	0.1920	1.02992	8.17	γ′t
98.6660	38.57	0.2400	1.01554	11.27	γ′t
99.0951	76.06	0.3840	1.01229	22.22	γ′t

4.2.2.2 Nominal Pt_{80}:Al_{11}:Ru_3:Cr_6

HR-SEM-BSE images are shown in Figure 4.96, showing the centre and edge microstructures consisting of rounded ~Pt_3Al precipitates (dark) in a (Pt) matrix (light). Subgrain boundaries were seen, where ~Pt_3Al was precipitated in the solid state. The average size of the ~Pt_3Al phase was 1.2 ± 0.6 µm. The precipitates were 10 ± 5 % of the microstructure. The overall composition (Table 4.41) had decreased Al compared to the as-cast sample. The ~Pt_3Al precipitates could not be measured accurately since they were too small, although the standard deviation is acceptable, which is due to similar areas being measured. Ruthenium and Cr had limited solubility in the precipitates and partitioned preferentially to (Pt). The composition of the (Pt) phase was very close to the overall composition, which is expected since most of the sample is the matrix. The standard deviation of the measurements was below 1 %.

The database lines and the experimental XRD spectrum for each phase and identified peaks are shown in Figures 4.97 to 4.100 and Table 4.42.

Table 4.41. EDX phase compositions of nominal Pt_{80}:Al_{11}:Ru_3:Cr_6 in the heat treated condition.

Phase Description	Al	Ru	Cr	Pt	Phase
Overall	8.1 ± 0.2	2.8 ± 0.2	5.7 ± 0.4	83.4 ± 0.5	-
Dark (Precipitates)	21.6 ± 0.3	0.7 ± 0.3	2.9 ± 0.3	74.8 ± 0.5	~Pt_3Al
Light (Matrix)	9.0 ± 0.7	2.8 ± 0.2	4.1 ± 0.1	84.2 ± 0.9	(Pt)

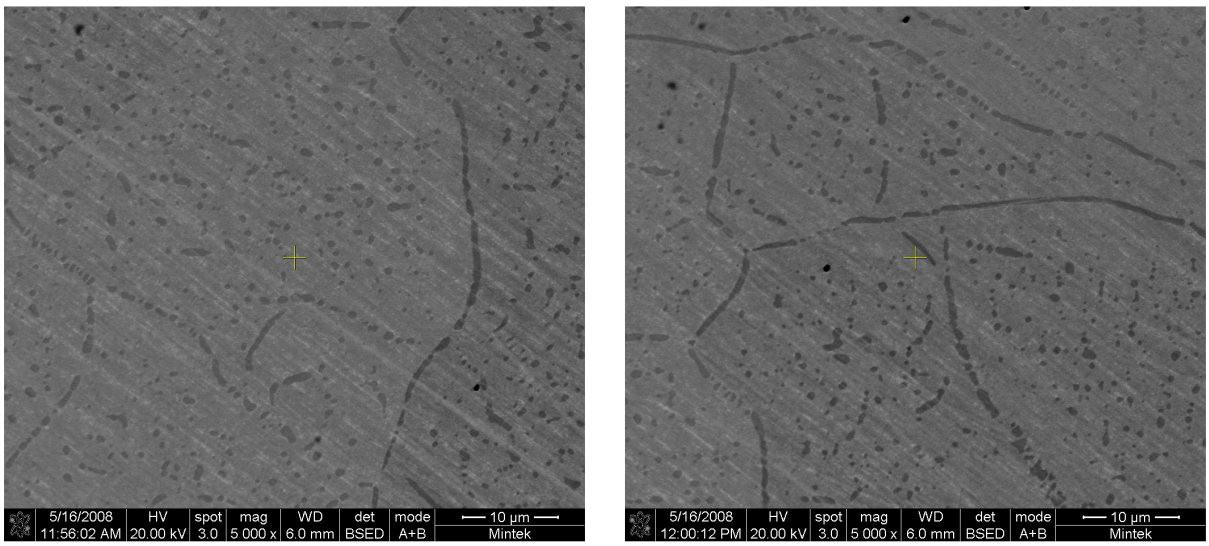

(a) **(b)**

Figure 4.96. HR-SEM-BSE image of nominal Pt_{80}:Al_{11}:Ru_3:Cr_6 after heat treatment, a) taken from the centre and b) edge, showing ~Pt_3Al precipitates (dark) in a (Pt) matrix (light).

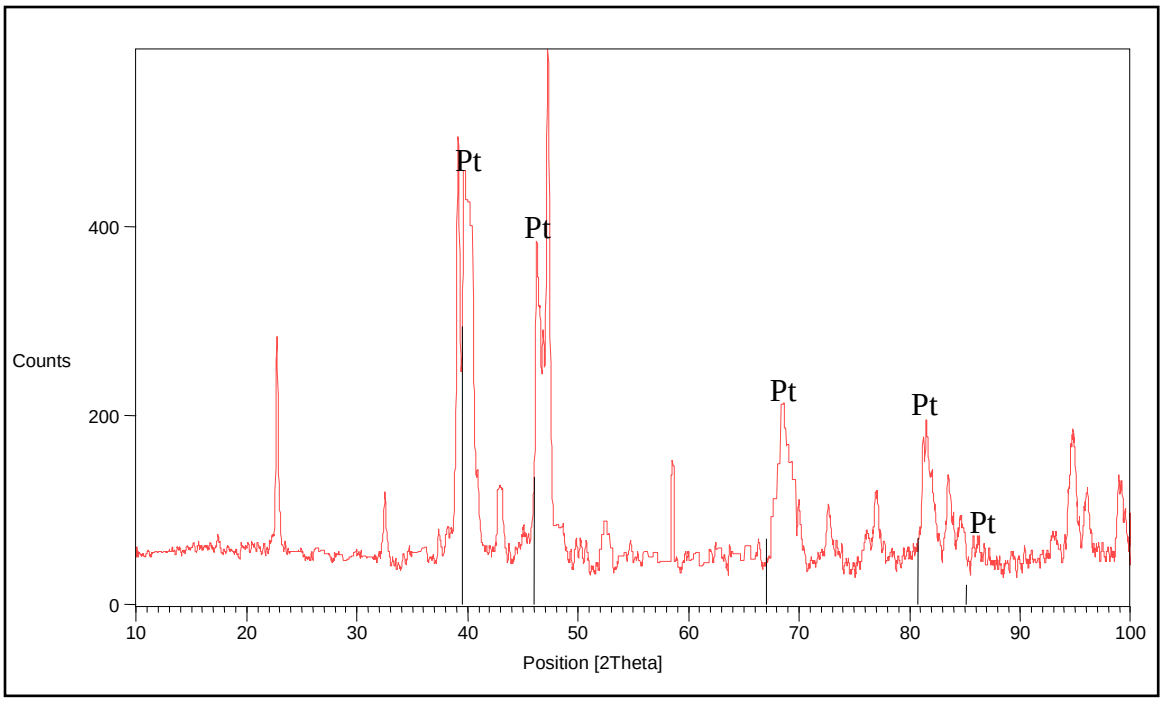

Figure 4.97. XRD Pattern of nominal Pt_{80}:Al_{11}:Ru_3:Cr_6 in the heat treated condition, showing identified Pt peaks.

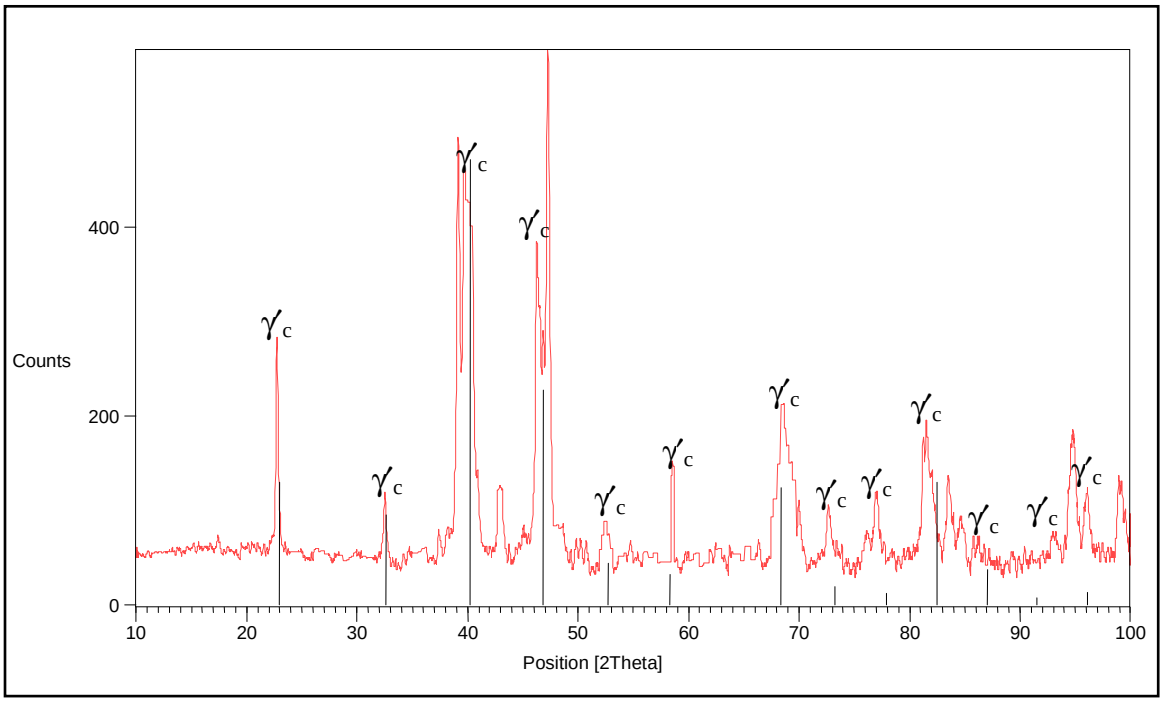

Figure 4.98. XRD Pattern of nominal Pt_{80}:Al_{11}:Ru_3:Cr_6 in the heat treated condition, showing apparent $L1_2$ – ~Pt_3Al peaks.

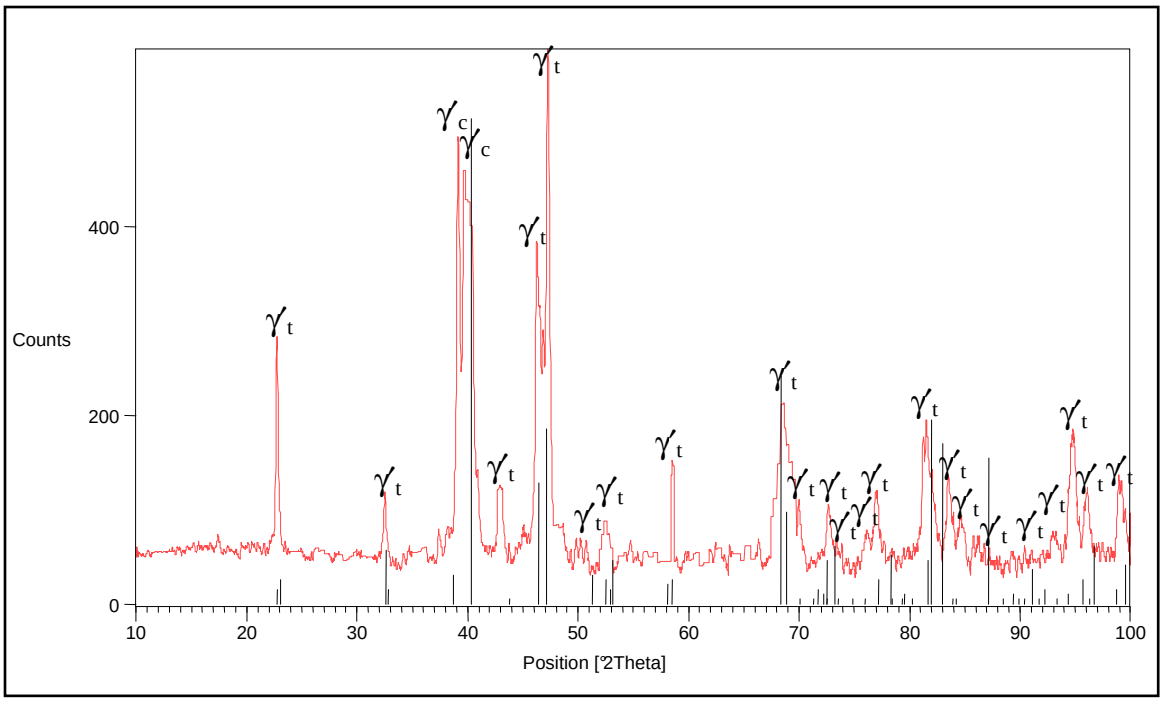

Figure 4.99. XRD Pattern of nominal Pt_{80}:Al_{11}:Ru_3:Cr_6 in the heat treated condition, showing identified DO'_c – ~Pt_3Al peaks.

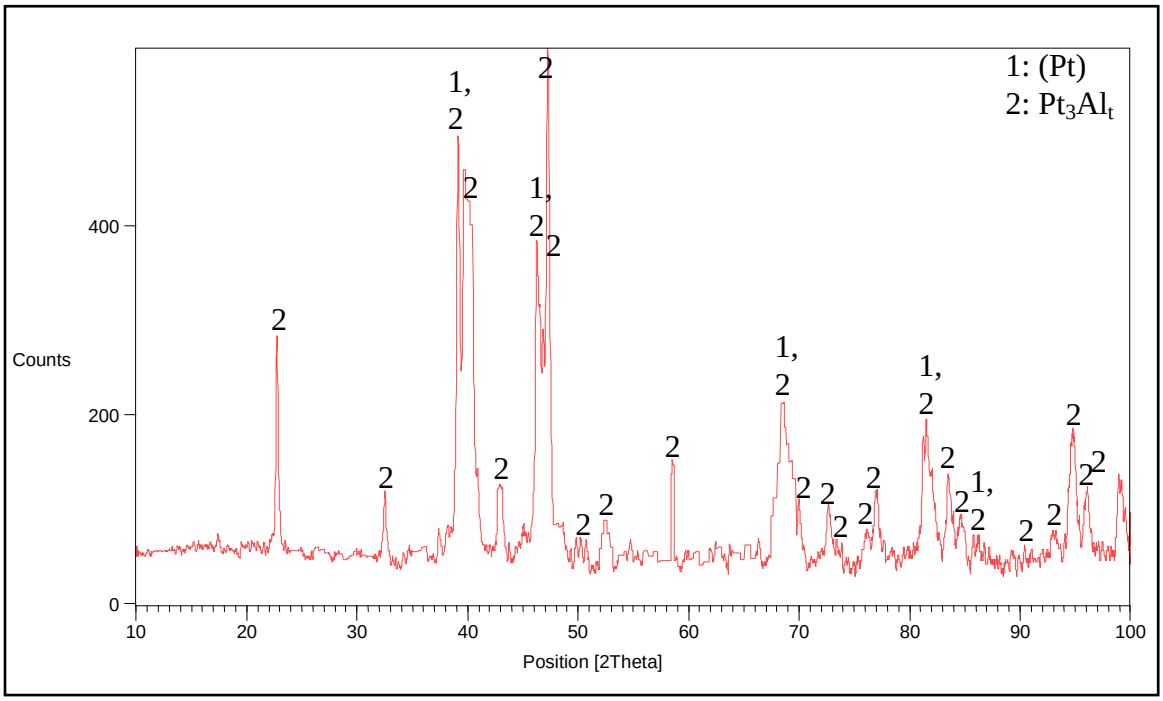

Figure 4.100. XRD pattern of nominal Pt_{80}:Al_{11}:Ru_3:Cr_6 in the heat treated condition, showing all identified phases.

Table 4.42. XRD peaks for Pt_{80}:Al_{11}:Ru_3:Cr_6 in the heat treated condition.

Position 2θ(°)	Height (counts)	Full-Width Half-Maximum 2θ(°)	d-spacing (Å)	Relative Intensity (%)	Phase (s)
17.4352	14.26	0.2362	5.08653	2.61	-
22.7637	221.66	0.1771	3.90652	40.63	γ′t
26.6127	8.84	0.6298	3.34960	1.62	-
32.5079	74.19	0.1771	2.75438	13.60	γ′t
39.1127	432.96	0.2558	2.30313	79.35	-
39.6621	414.10	0.2362	2.27249	75.90	(Pt), γ′t
40.4632	356.63	0.0720	2.22748	65.36	γ′t
43.1028	81.23	0.2755	2.09873	14.89	γ′t
43.7197	21.67	0.1378	2.07053	3.97	γ′t
46.2302	140.04	0.2755	1.96377	3.68	-
46.2565	343.17	0.1771	1.96272	62.90	(Pt), γ′t
46.8676	248.80	0.1378	1.93854	45.60	γ′t
47.2516	545.60	0.2755	1.92368	100.00	γ′t
48.5054	44.06	0.4723	1.87685	8.08	γ′t
49.8406	30.41	0.1968	1.82965	5.57	γ′t
50.2320	28.52	0.1968	1.81631	5.23	γ′t
50.7506	26.51	0.2362	1.79896	4.86	γ′t
52.4775	51.31	0.3936	1.74376	9.40	γ′t
54.7381	28.75	0.2362	1.67697	5.27	γ′t
56.5757	14.09	0.9446	1.62679	2.58	γ′t
58.4854	97.59	0.1440	1.57683	17.89	γ′t
58.6345	108.65	0.0960	1.57709	19.91	γ′t
60.7630	17.35	0.4800	1.52307	3.18	γ′t
61.9546	20.02	0.2880	1.49660	3.67	γ′t
62.6839	20.79	0.7680	1.48093	3.81	γ′t
65.3485	23.96	0.3840	1.42684	4.39	γ′t
66.3958	27.33	0.2880	1.40685	5.01	γ′t
68.3863	175.32	0.1440	1.37068	32.13	(Pt), γ′t
69.6492	94.70	0.1440	1.34888	17.36	γ′t
69.9735	70.30	0.2400	1.34342	12.89	γ′t
72.6317	68.37	0.2880	1.30066	12.53	γ′t
73.9039	25.10	0.1920	1.28139	4.60	γ′t
74.9964	1.93	0.2160	1.26541	0.35	γ′t
76.1197	33.16	0.6720	1.24950	6.08	γ′t
76.9908	72.47	0.4800	1.23752	13.28	γ′t
81.2113	125.17	0.2160	1.18353	22.94	(Pt), γ′t
81.4813	145.53	0.1920	1.18029	26.67	γ′t
83.4934	89.34	0.2400	1.15689	16.37	γ′t
84.6033	46.26	0.3840	1.14452	8.48	γ′t
85.0642	21.23	0.2880	1.14232	3.89	(Pt), γ′t

Table4.42. Continued: XRD peaks for Pt_{80}:Al_{11}:Ru_3:Cr_6 in the heat treated condition.					
Position 2θ(°)	**Height (counts)**	**Full-Width Half-Maximum 2θ(°)**	**d-spacing (Å)**	**Relative Intensity (%)**	**Phase (s)**
85.8022	24.86	0.3360	1.13157	4.56	γ't
86.2444	26.27	0.2880	1.12690	4.81	γ't
89.2746	17.85	0.3840	1.09633	3.27	γ't
90.4254	22.46	0.2880	1.08535	4.12	γ't
91.0406	20.72	0.2880	1.07961	3.80	γ't
93.1089	35.88	0.7680	1.06098	6.58	γ't
94.8829	137.49	0.4320	1.04577	25.20	γ't
96.0745	83.00	0.5760	1.03593	15.21	γ't
98.9098	87.87	0.4800	1.01369	16.11	γ't

4.2.2.3 Nominal Pt_{80}:Al_{11}:Ru_6:Cr_3

HR-SEM-BSE images taken at the centre and edge of the sample are shown Figure 4.101. The centre of the sample (Figure 4.101 (a)) had ~Pt_3Al precipitates in a (Pt) matrix, with subgrain boundaries. Shown also are rounded and some cubic ~Pt_3Al precipitates. The edge microstructure (Figure 4.101 (b)) was similar to the centre, thus confirming homogeneity of the sample. However, cross-like shaped precipitates were observed at the edge (Figure 4.101 (c)). The distribution of the ~Pt_3Al phase was random and the average size was 1.8 ± 0.4 µm and the proportion was 6 ± 4 %. The phase compositions are shown in Table 4.43 and the overall composition was comparable to the as-cast composition. Ruthenium and Cr had limited solubility in the ~Pt_3Al precipitates and partitioned mostly to (Pt). The standard deviation of all measurements was well below 1 at.%.

Figures 4.102 to 4.105 show the XRD results and identified phases are given in Table 4.43.

Table 4.43. EDX phase compositions of nominal Pt_{80}:Al_{11}:Ru_6:Cr_3 in the heat treated condition.

Phase Description	Al	Ru	Cr	Pt	Phase
Overall	7.8 ± 0.6	4.8 ± 0.3	3.6 ± 0.3	83.8 ± 0.3	-
Dark (Precipitates)	18.9 ± 0.2	0.8 ± 0.2	2.1 ± 0.1	78.2 ± 0.2	~Pt_3Al
Light (Matrix)	7.8 ± 0.4	1.7 ± 0.1	5.1 ± 0.1	85.4 ± 0.4	(Pt)

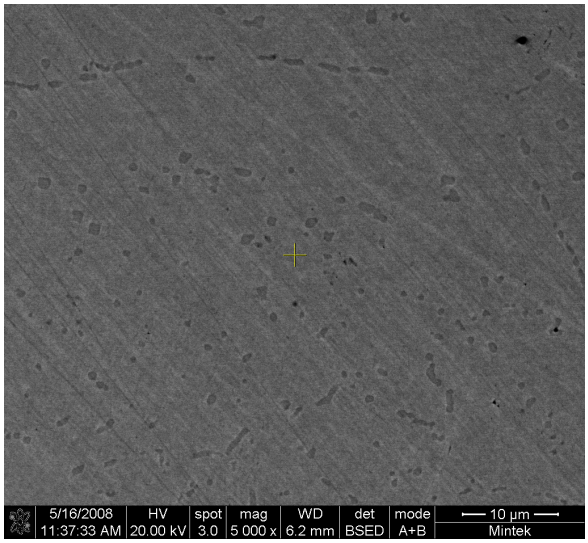

(a)

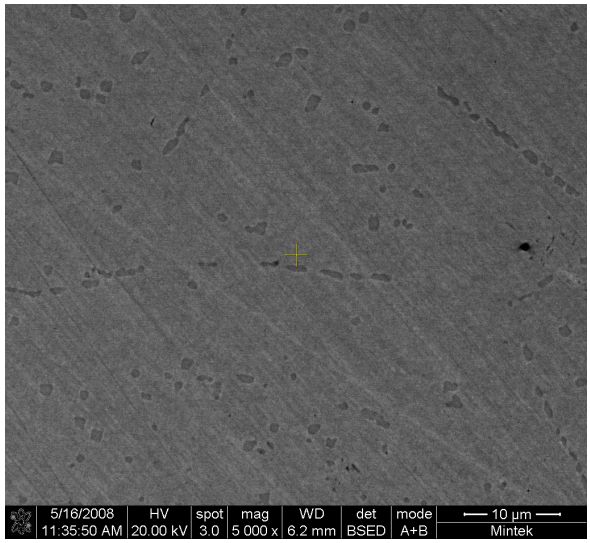

(b)

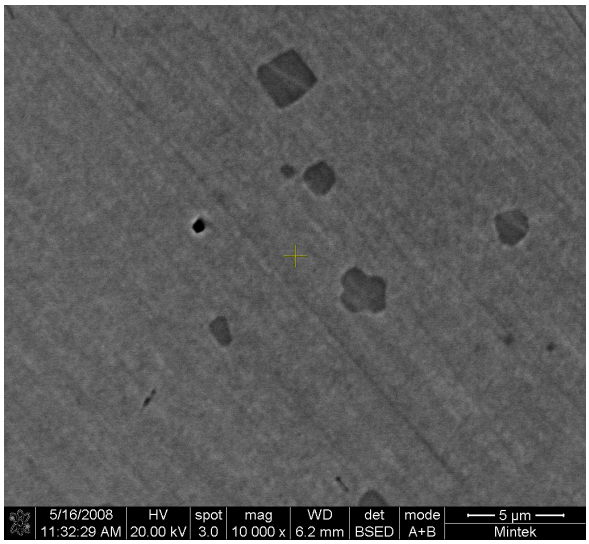

(c)

Figure 4.101. HR-SEM-BSE image of nominal Pt_{80}:Al_{11}:Ru_6:Cr_3 after heat treatment, a) taken at the centre and (b - c) edge, showing rounded, cubic and Maltese cross-like ~Pt_3Al precipitates (dark) in a (Pt) matrix (light).

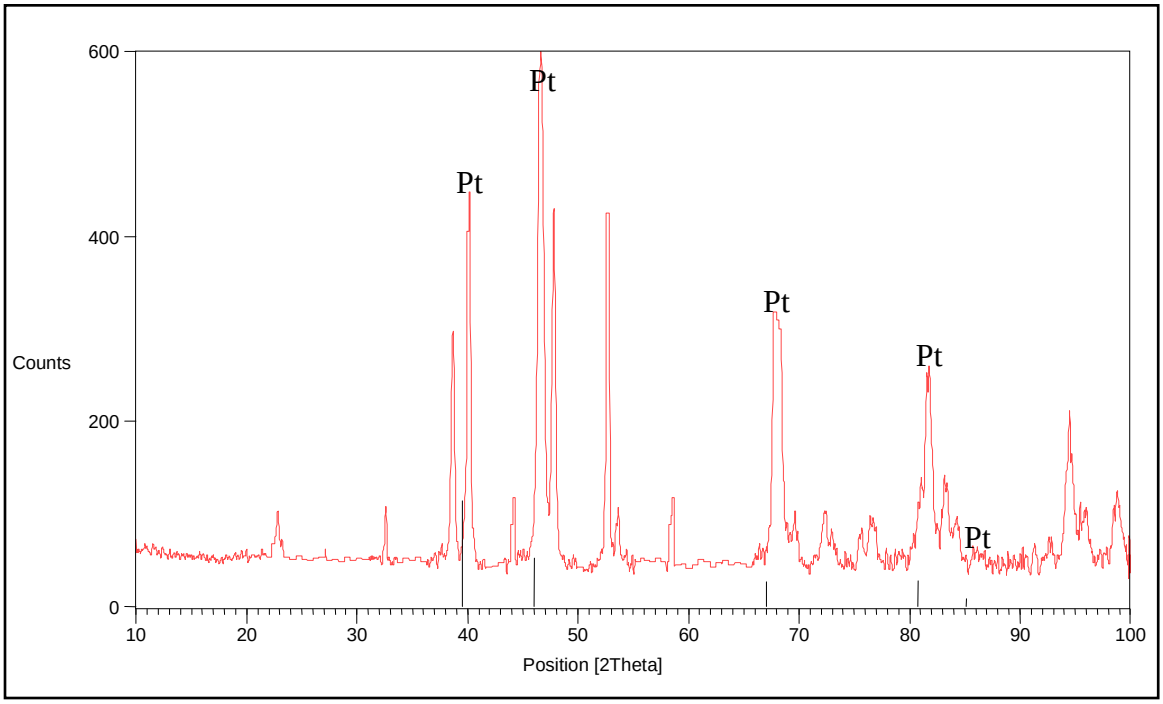

Figure 4.102. XRD Pattern of nominal Pt_{80}:Al_{11}:Ru_6:Cr_3 in the heat treated condition, showing identified Pt peaks.

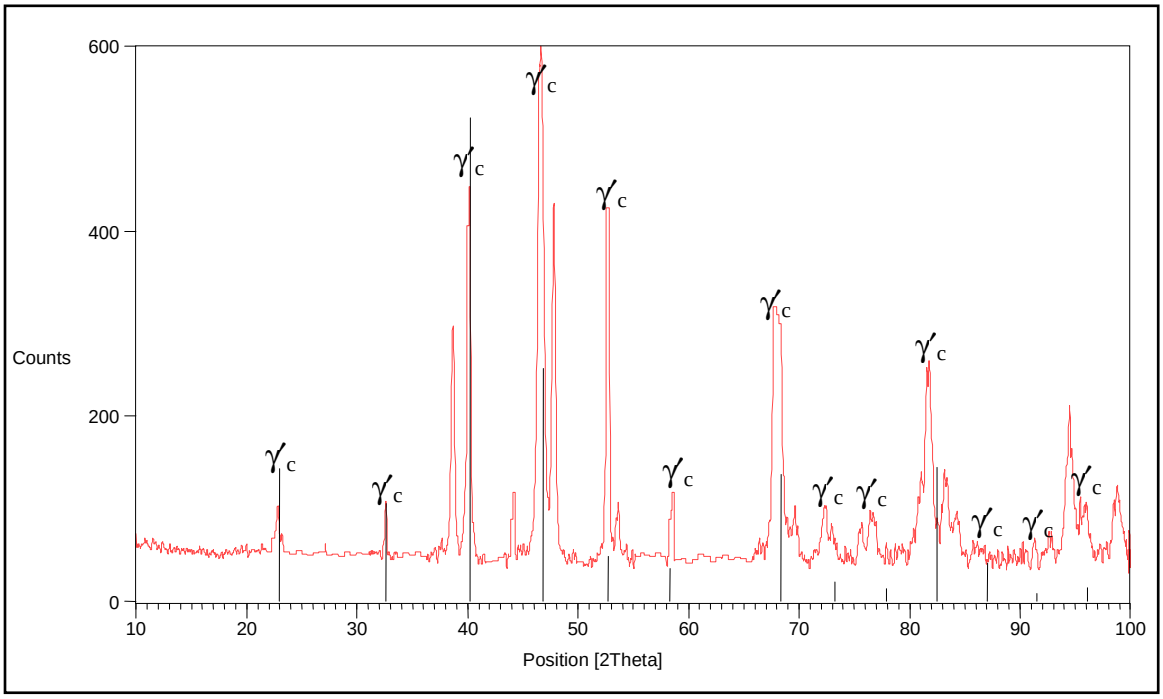

Figure 4.103. XRD Pattern of nominal Pt_{80}:Al_{11}:Ru_6:Cr_3 in the heat treated condition, showing apparent $L1_2$ – ~Pt_3Al peaks.

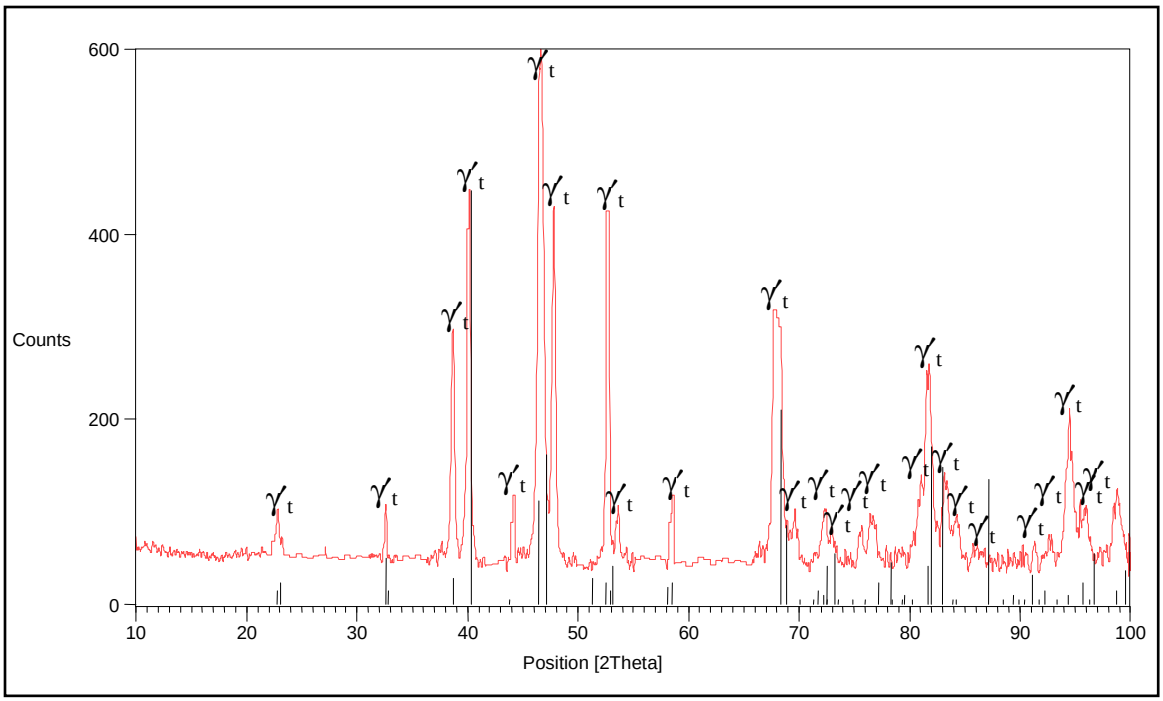

Figure 4.104. XRD Pattern of nominal Pt_{80}:Al_{11}:Ru_6:Cr_3 in the heat treated condition, showing identified DO'_c – ~Pt_3Al peaks.

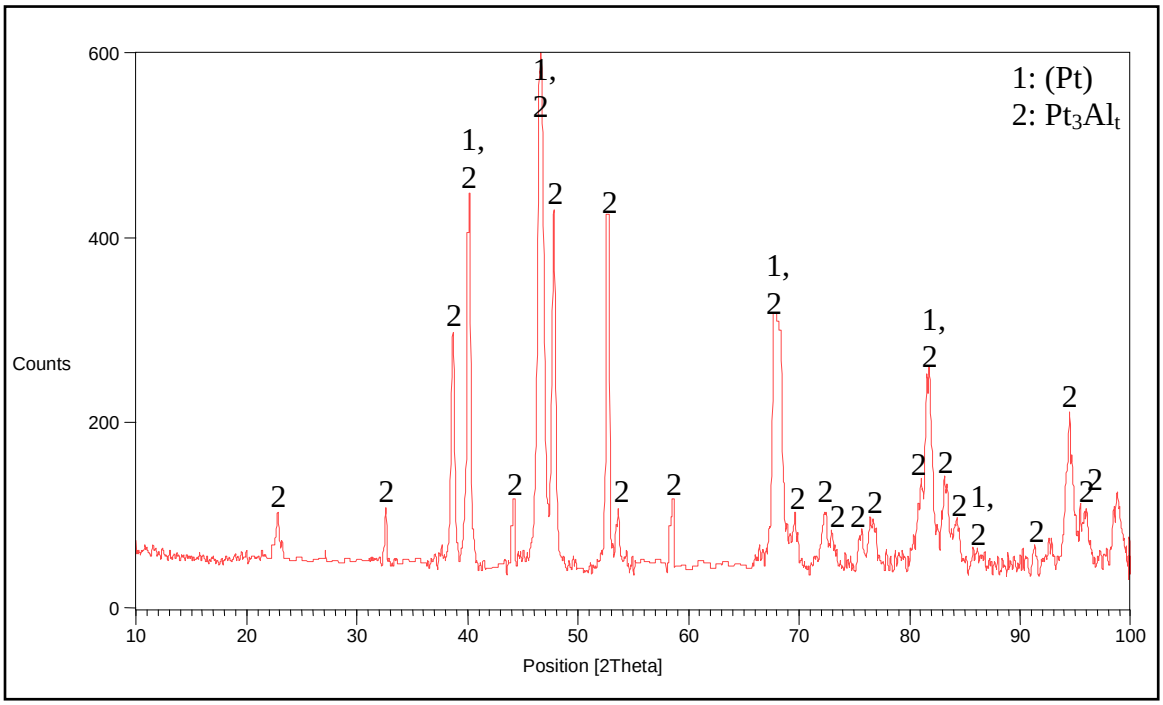

Figure 4.105. XRD pattern of nominal Pt_{80}:Al_{11}:Ru_6:Cr_3 in the heat treated condition, showing all identified phases.

Table 4.44. XRD peaks for Pt_{80}:Al_{11}:Ru_6:Cr_3 in the heat treated condition.

Position 2θ(°)	Height (counts)	Full-Width Half-Maximum 2θ(°)	d-spacing (Å)	Relative Intensity (%)	Phase (s)
22.8183	50.45	0.1574	3.89729	9.90	γ′t
32.6351	57.17	0.1771	2.74393	11.21	γ′t
37.0803	11.15	0.2362	2.42457	2.19	-
38.7464	222.27	0.3346	2.32406	43.60	γ′t
39.9554	360.34	0.0720	2.25462	70.69	γ′t
40.2309	413.06	0.1378	2.24166	81.03	(Pt), γ′t
44.2054	75.13	0.1574	2.04891	14.74	γ′t
46.4481	509.78	0.1378	1.95507	100.00	(Pt), γ′t
46.8235	449.90	0.3149	1.94027	88.26	γ′t
47.7997	385.81	0.1968	1.90290	75.68	γ′t
51.9554	360.34	0.0720	1.85462	6.69	-
52.5614	384.09	0.0960	1.73973	75.35	γ′t
52.8165	367.95	0.0984	1.73336	72.18	γ′t
53.6561	60.62	0.1181	1.70820	11.89	γ′t
58.6713	73.20	0.1574	1.57358	14.36	γ′t
67.6990	271.70	0.1968	1.38406	53.30	-
68.3612	252.67	0.1378	1.37225	49.57	(Pt), γ′t
69.6383	58.26	0.1378	1.35018	11.43	γ′t
72.4499	59.88	0.2755	1.30456	11.75	γ′t
72.9897	39.66	0.2362	1.29624	7.78	γ′t
75.6052	34.02	0.3936	1.25776	6.67	γ′t
76.3930	51.79	0.3936	1.24674	10.16	γ′t
77.8997	20.48	0.1680	1.22534	4.02	γ′t
79.2373	11.72	0.6298	1.20898	2.30	γ′t
81.5485	202.06	0.2400	1.17949	39.64	γ′t
81.7808	216.56	0.1680	1.17672	42.48	γ′t
83.1672	97.95	0.1680	1.16059	19.21	γ′t
84.4193	41.65	0.3936	1.14749	8.17	γ′t
85.8743	12.87	0.6298	1.13174	2.53	(Pt), γ′t
91.2757	20.31	0.3936	1.07833	3.98	γ′t
92.6516	30.96	0.1920	1.06501	6.07	γ′t
94.4752	167.75	0.1680	1.04920	32.91	γ′t
95.4493	69.52	0.1200	1.04106	13.64	γ′t
95.9983	58.97	0.3149	1.03741	11.57	γ′t
98.8659	75.04	0.2880	1.01402	14.72	γ′t

4.2.2.4. Nominal $Pt_{78}:Al_{11}:Ru_5:Cr_6$

HR-SEM-BSE images are shown in Figure 4.106. Figure 4.106 (a) shows the centre microstructure with a volume fraction of 24 ± 3 %, and rounded and aligned ~Pt_3Al precipitates in a (Pt) matrix. The edge microstructure (Figure 4.106 (b)) was similar to the centre. Subgrain boundaries were observed together with black spots showing porosity. The average precipitate size was 0.8 ± 0.4 µm. The phase compositions are shown in Table 4.45, and the overall composition was comparable with that of the as-cast sample. Aluminium was found to partition mostly to the ~Pt_3Al precipitates compared to the (Pt) phase. Ruthenium and Cr had limited solubility in the precipitates and partitioned preferentially to the (Pt).

All three phases (Pt, $L1_2$ - ~Pt_3Al and DO'_c - ~Pt_3Al) database lines were matched with the XRD spectrum (Figures 4.107 to 4.109) and Pt, $L1_2$ - ~Pt_3Al were identified (Figure 4.110 and Table 4.46).

Table 4.45. EDX phase compositions of nominal $Pt_{78}:Al_{11}:Ru_5:Cr_6$ in the heat treated condition.

Phase Description	Al	Ru	Cr	Pt	Phase
Overall	9.0 ± 0.2	3.4 ± 0.2	6.2 ± 0.4	81.4 ± 0.5	-
Dark (Precipitates)	19.9 ± 0.3	0.6 ± 0.3	2.8 ± 0.3	76.7 ± 0.5	~Pt_3Al
Light (Matrix)	8.7 ± 0.7	2.7 ± 0.2	4.2 ± 0.1	84.6 ± 0.9	(Pt)

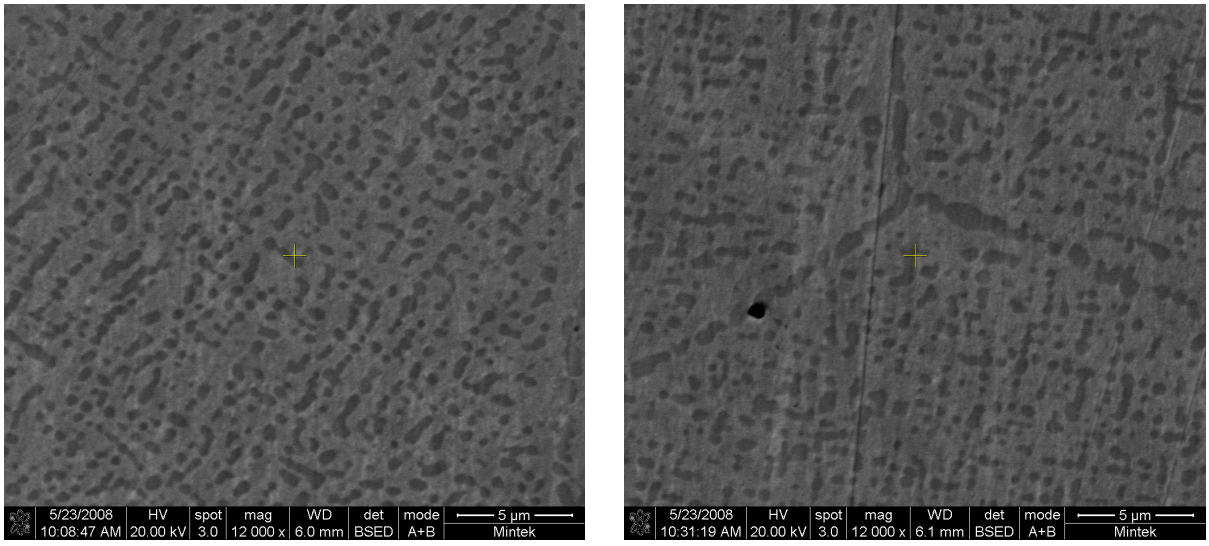

(a) **(b)**

Figure 4.106. HR-SEM-BSE image of nominal $Pt_{78}:Al_{11}:Ru_5:Cr_6$ after heat treatment, a) taken at the centre and b) edge, showing ~Pt_3Al precipitates (dark) in a (Pt) matrix (light) and a triple subgrain boundary.

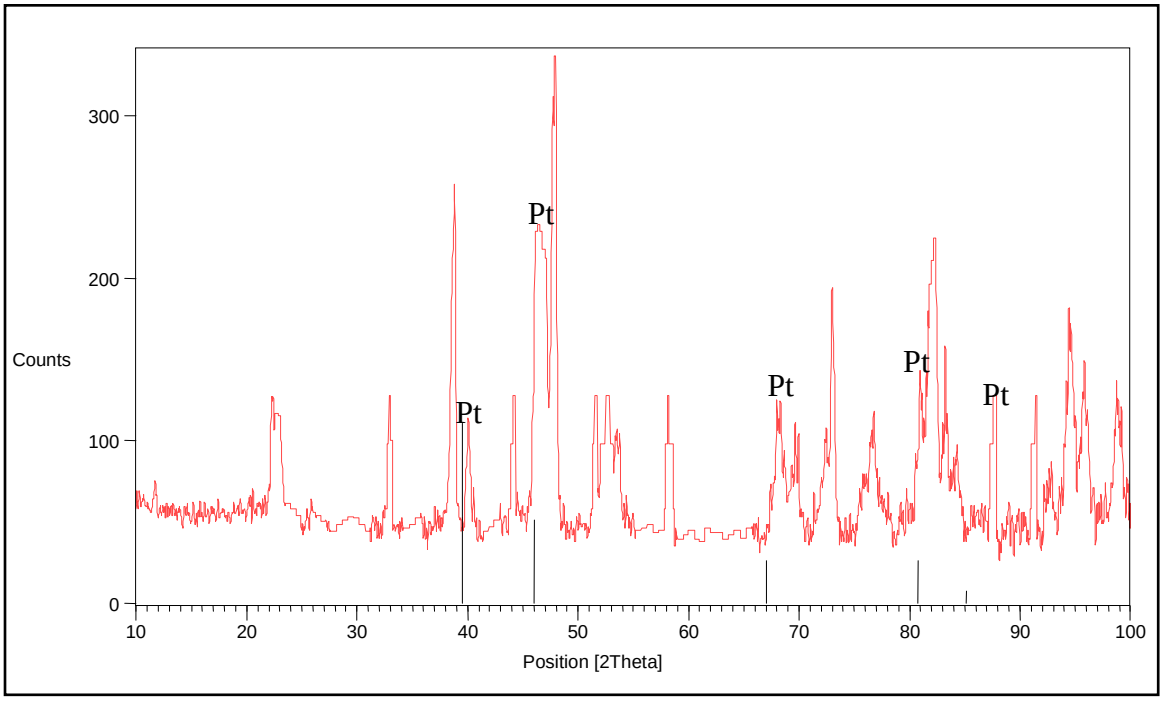

Figure 4.107. XRD Pattern of nominal Pt_{78}:Al_{11}:Ru_5:Cr_6 in the heat treated condition, showing identified Pt peaks.

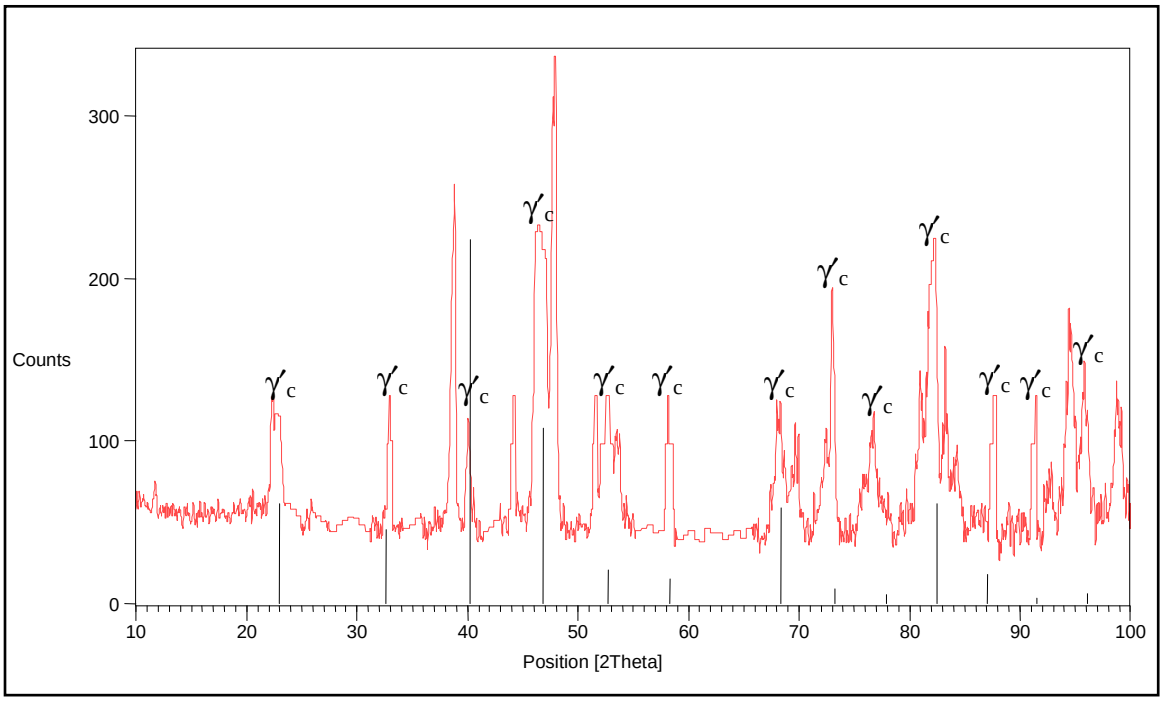

Figure 4.108. XRD Pattern of nominal Pt_{78}:Al_{11}:Ru_5:Cr_6 in the heat treated condition, showing apparent $L1_2$ – ~Pt_3Al peaks.

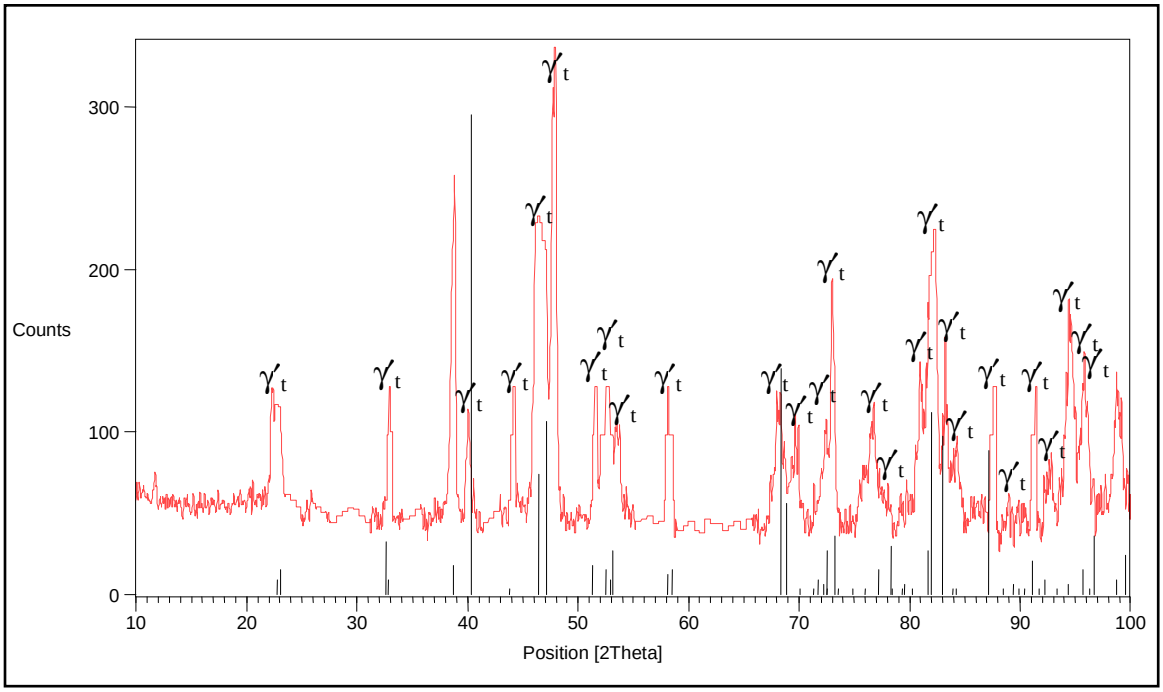

Figure 4.109. XRD Pattern of nominal Pt_{78}:Al_{11}:Ru_5:Cr_6 in the heat treated condition, showing identified DO'_c – ~Pt_3Al peaks.

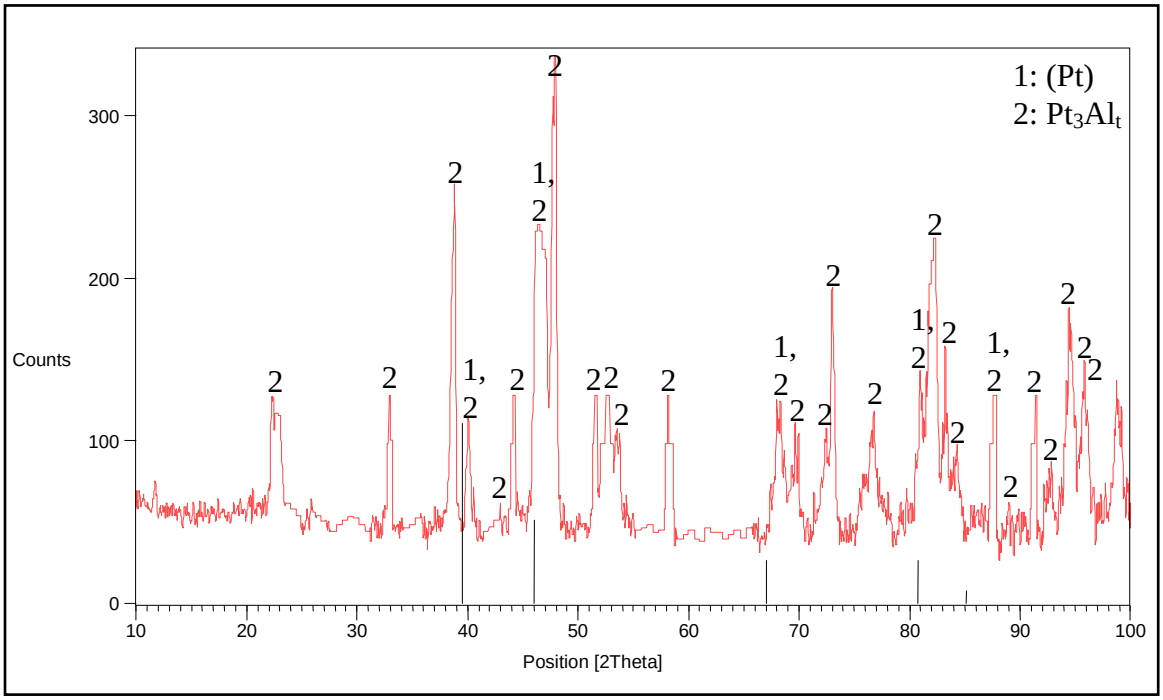

Figure 4.110. XRD pattern of nominal Pt_{78}:Al_{11}:Ru_5:Cr_6 in the heat treated condition, showing all identified phases.

Table 4.46. XRD peaks for Pt_{78}:Al_{11}:Ru_5:Cr_6 in the heat treated condition.

Position 2θ(°)	Height (counts)	Full-Width Half-Maximum 2θ(°)	d-spacing (Å)	Relative Intensity (%)	Phase (s)
11.7263	14.54	0.2362	7.54693	4.99	-
22.2714	67.71	0.1574	3.99173	23.24	γ′t
26.1419	8.97	0.9446	3.40885	3.08	-
32.9403	87.70	0.1181	2.71920	30.10	γ′t
38.8290	206.68	0.1378	2.31931	70.95	-
40.0671	67.29	0.1574	2.25045	23.10	(Pt), γ′t
44.2770	79.94	0.2362	2.04576	27.44	γ′t
46.1205	183.71	0.1181	1.96819	63.06	(Pt), γ′t
47.1319	166.81	0.1574	1.92829	57.26	γ′t
47.7200	265.64	0.2160	1.90431	91.18	γ′t
47.9630	291.32	0.1574	1.89680	100.00	γ′t
51.6787	80.46	0.2362	1.76882	27.62	γ′t
52.6668	79.99	0.3149	1.73793	27.46	γ′t
53.7365	53.79	0.3936	1.70584	18.46	γ′t
58.1296	90.42	0.1181	1.58695	31.04	γ′t
58.5178	57.48	0.1574	1.57734	19.73	γ′t
67.9714	14.38	0.1440	1.37803	8.96	-
68.3008	83.58	0.1378	1.37332	28.69	(Pt), γ′t
69.6466	69.19	0.1440	1.34892	23.75	γ′t
69.9508	61.71	0.1440	1.34380	21.18	γ′t
72.4300	62.23	0.2362	1.30487	21.36	γ′t
76.7396	64.23	0.3149	1.24197	22.05	γ′t
79.2599	8.86	0.3840	1.20769	3.04	γ′t
79.7286	25.97	0.1680	1.20177	8.91	γ′t
80.5406	45.87	0.1440	1.19169	15.75	γ′t
80.9498	98.07	0.1440	1.18669	33.66	(Pt), γ′t
81.8048	146.39	0.3936	1.17741	50.25	γ′t
82.3664	178.84	0.2362	1.17080	61.39	γ′t
83.2451	112.79	0.1200	1.15970	38.72	γ′t
84.3142	47.41	0.3149	1.14865	16.27	γ′t
87.3483	52.04	0.1920	1.11548	17.86	(Pt), γ′t
87.7562	83.35	0.2362	1.11226	28.61	γ′t
89.0315	19.27	0.1680	1.09869	6.62	γ′t
91.1222	56.67	0.1920	1.07885	19.45	γ′t
92.8054	35.28	0.4800	1.06365	12.11	γ′t
94.5143	123.45	0.6720	1.04887	42.38	γ′t
95.7697	94.62	0.3840	1.03842	32.48	γ′t
96.7257	26.49	0.2160	1.03068	9.09	γ′t
98.7663	85.74	0.2880	1.01478	29.43	γ′t
99.1785	79.60	0.1680	1.01167	27.32	γ′t

4.2.2.5. Nominal $Pt_{78}:Al_{11}:Ru_3:Cr_8$

HR-SEM-BSE images of the edge and centre microstructure are shown in Figure 4.111, both with rounded ~Pt_3Al precipitates in a (Pt) matrix. The precipitate proportion was 20 ± 3 % of the microstructure. Subgrain boundaries were also seen (Figure 4.111 (a)). The precipitates were not aligned and their average size was about 1.6 ± 0.7 µm. The phase compositions are shown in Table 4.47 and the overall composition for Al and Pt were comparable with those of the as-cast sample. Ru and Cr had limited solubility in the ~Pt_3Al precipitates and partitioned mostly to (Pt). The composition of the (Pt) phase was comparable to the overall composition.

XRD results are shown in Figures 4.112 to 4.115 and Table 4.48, with the phases identified.

Table 4.47. EDX phase compositions of nominal $Pt_{78}:Al_{11}:Ru_3:Cr_8$ in the heat treated condition.

Phase Description	Al	Ru	Cr	Pt	Phase
Overall	8.0 ± 0.3	2.2 ± 0.6	7.1 ± 0.4	82.5 ± 0.5	-
Dark (Precipitates)	19.7 ± 0.4	0.5 ± 0.2	2.5 ± 0.1	77.3 ± 0.4	~Pt_3Al
Light (Matrix)	7.1 ± 0.3	2.1 ± 0.1	6.0 ± 0.2	84.7 ± 0.5	(Pt)

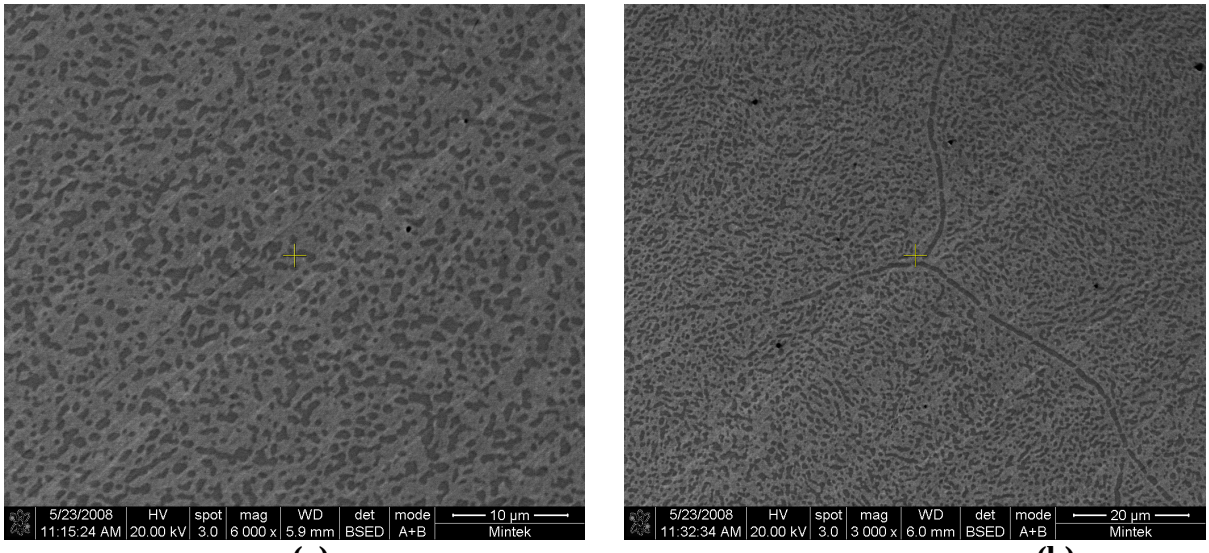

(a) **(b)**

Figure 4.111. HR-SEM-BSE image of nominal $Pt_{78}:Al_{11}:Ru_3:Cr_8$ after heat treatment, a) taken from the centre and b) edge, showing ~Pt_3Al precipitates (dark) in a (Pt) matrix (light) and subgrain boundaries.

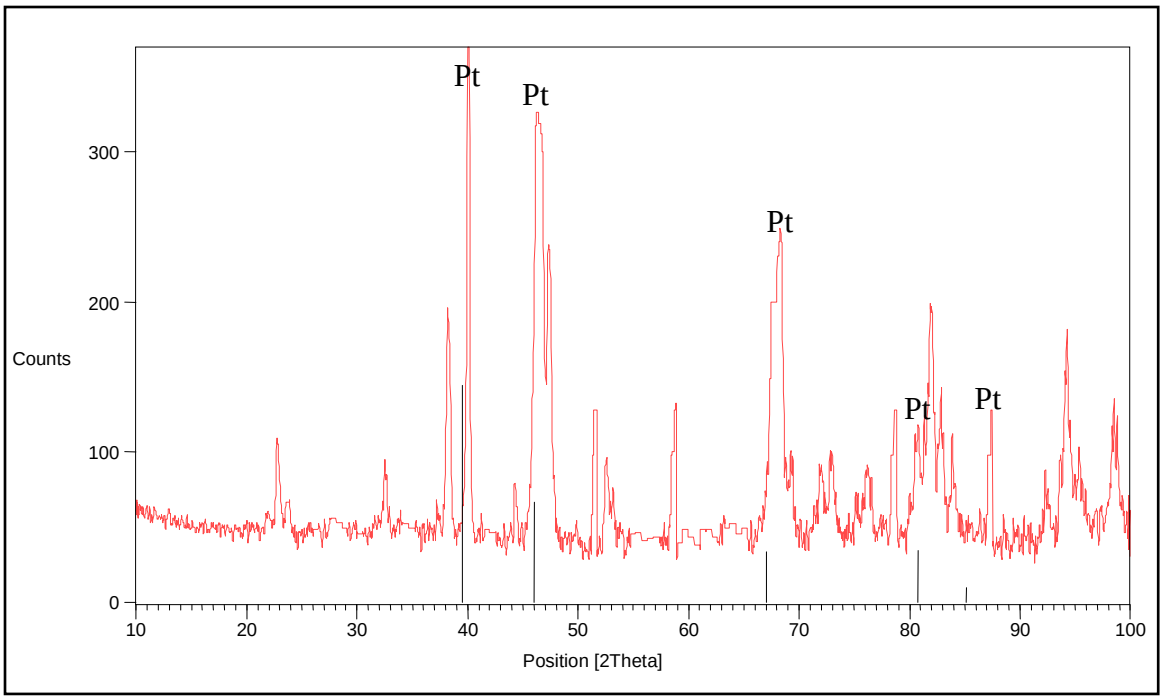

Figure 4.112. XRD Pattern of nominal Pt_{78}:Al_{11}:Ru_3:Cr_8 in the heat treated condition, showing identified Pt peaks.

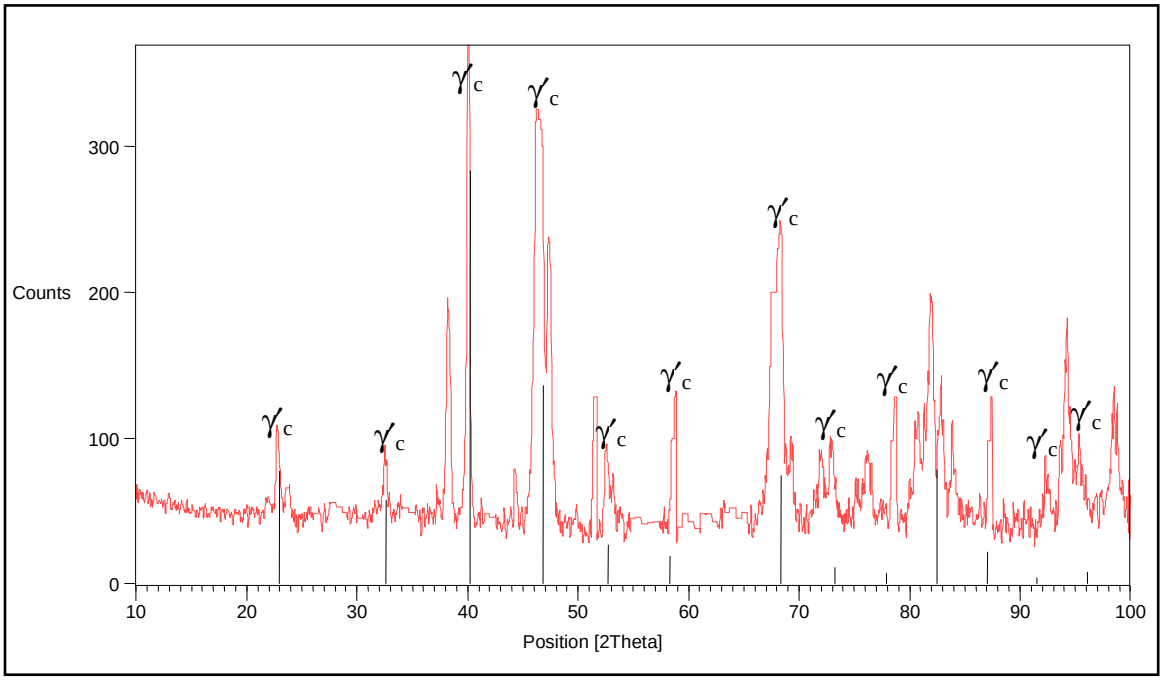

Figure 4.113. XRD Pattern of nominal Pt_{78}:Al_{11}:Ru_3:Cr_8 in the heat treated condition, showing apparent $L1_2$ – ~Pt_3Al peaks.

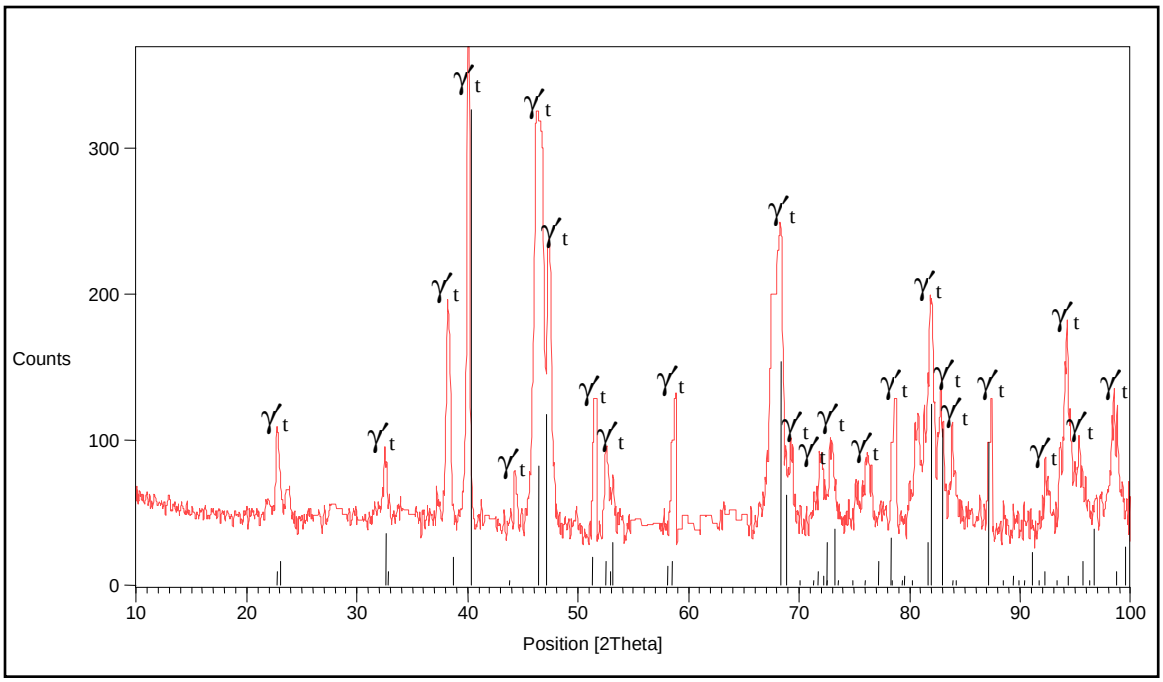

Figure 4.114. XRD Pattern of nominal Pt_{78}:Al_{11}:Ru_3:Cr_8 in the heat treated condition, showing identified DO'_c – ~Pt_3Al peaks.

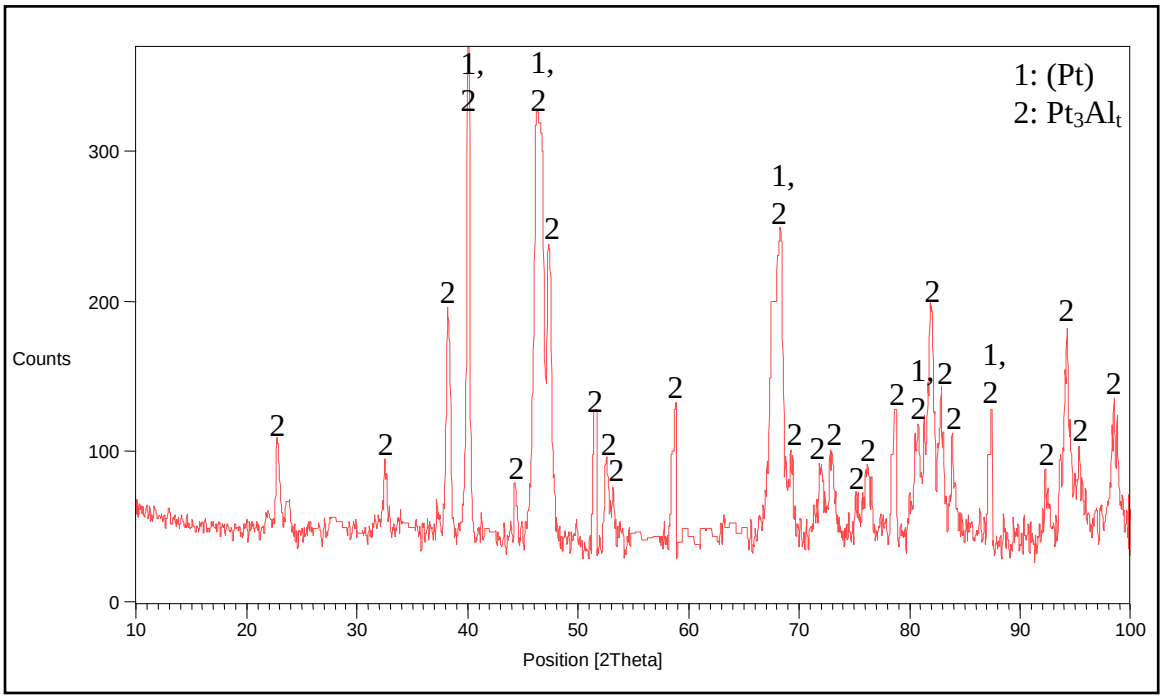

Figure 4.115. XRD pattern of nominal Pt_{78}:Al_{11}:Ru_3:Cr_8 in the heat treated condition, showing all identified phases.

Table 4.48. XRD peaks for Pt_{78}:Al_{11}:Ru_3:Cr_8 in the heat treated condition.

Position 2θ(°)	Height (counts)	Full-Width Half-Maximum 2θ(°)	d-spacing (Å)	Relative Intensity (%)	Phase (s)
22.7445	62.58	0.2755	3.90976	18.85	γ′t
28.0038	10.09	0.9446	3.18629	3.04	-
32.5660	40.32	0.2362	2.74959	12.15	γ′t
38.1918	149.94	0.1378	2.35652	45.17	-
38.4205	112.97	0.1574	2.34302	34.03	γ′t
39.9882	331.96	0.0960	2.25284	100.00	(Pt), γ′t
40.1583	319.25	0.1378	2.24555	96.17	γ′t
44.2660	38.53	0.1574	2.04624	11.61	-
46.1624	278.91	0.1968	1.96650	84.02	γ′t
46.8138	258.22	0.3542	1.94064	77.79	(Pt), γ′t
47.2607	184.18	0.1574	1.92333	55.48	γ′t
47.5511	153.17	0.1771	1.91226	46.14	γ′t
51.5958	92.28	0.1968	1.77146	27.80	γ′t
52.4920	55.70	0.1968	1.74331	16.78	γ′t
53.1949	36.54	0.2362	1.72192	11.01	γ′t
58.9091	87.04	0.1181	1.56780	26.22	γ′t
62.9172	9.30	0.1378	1.47722	2.80	-
67.5011	154.47	0.3149	1.38763	46.53	(Pt), γ′t
68.3963	201.03	0.2755	1.37164	60.56	γ′t
69.3160	52.85	0.2362	1.35567	15.92	γ′t
71.9653	46.92	0.3149	1.31214	14.13	γ′t
72.9243	52.90	0.3936	1.29724	15.93	γ′t
75.1012	28.59	0.1440	1.26390	8.61	γ′t
76.5683	39.69	0.1440	1.24330	11.96	γ′t
78.7625	85.04	0.2362	1.21507	25.62	γ′t
80.4991	67.38	0.1440	1.19220	20.30	γ′t
81.8832	155.05	0.1920	1.17551	46.71	(Pt), γ′t
82.8536	96.11	0.1440	1.16419	28.95	γ′t
83.0867	66.27	0.1440	1.16440	19.96	γ′t
83.8511	66.07	0.1680	1.15286	19.90	γ′t
87.1237	57.56	0.1440	1.11777	17.34	(Pt), γ′t
87.4320	88.75	0.1440	1.11462	26.74	γ′t
92.2866	49.95	0.1680	1.06827	15.05	γ′t
93.6382	58.83	0.1920	1.05637	17.72	γ′t
94.2395	144.16	0.1440	1.05120	43.43	γ′t
95.3602	64.35	0.1440	1.04179	19.39	γ′t
96.9536	22.91	0.2880	1.02887	6.90	γ′t
97.3631	24.96	0.1920	1.02818	7.52	γ′t
98.5340	94.34	0.1440	1.01655	28.42	γ′t
98.8084	86.74	0.1200	1.01446	26.13	γ′t

4.2.2.6. Nominal $Pt_{78}:Al_{11}:Ru_8:Cr_3$

HR-SEM-BSE images taken at the centre and edge of the sample are shown in Figure 4.116 which show that the alloy is fairly homogenous. The microstructure consisted of aligned ~Pt_3Al precipitates in a (Pt) matrix. Figure 4.116 (a) shows two grains differing contrast, due to orientation. Most of the precipitates were rounded, with an average size of 0.7 ± 0.3 µm and the proportion was about 10 ± 5 % volume fraction. The ~Pt_3Al phase also precipitated in the solid state on the grain boundaries in both the centre and edge microstructure. The phase compositions are shown in Table 4.49. The ~Pt_3Al and (Pt) phases were too fine for accurate analysis. Ru and Cr had limited solubility in the precipitates and partitioned preferentially to (Pt). The standard deviation of the measurements was well below 1 %.

Figures 4.117 to 4.120 shows the XRD results and the identified phases are given in Table 4.50. The peak at about 2θ = 39° belongs to DO'_c - ~Pt_3Al and the plasticine (spectrum shown in Appendix A), although this still does not explain the high intensity peak at 2θ = 39°. The plasticine was placed inside the aluminium holder to prevent contact between the sample and the Al holder.

Table 4.49. EDX phase compositions of nominal $Pt_{78}:Al_{11}:Ru_8:Cr_3$ in the heat treated condition.

Phase Description	Al	Ru	Cr	Pt	Phase
Overall	8.6 ± 0.5	4.6 ± 0.1	4.9 ± 0.1	81.9 ± 0.5	-
Dark (Precipitates)	20.5 ± 0.3	0.4 ± 0.3	1.9 ± 0.1	77.2 ± 0.1	~Pt_3Al
Light (Matrix)	10.3 ± 0.5	2.5 ± 0.2	4.8 ± 0.2	82.5 ± 0.2	(Pt)

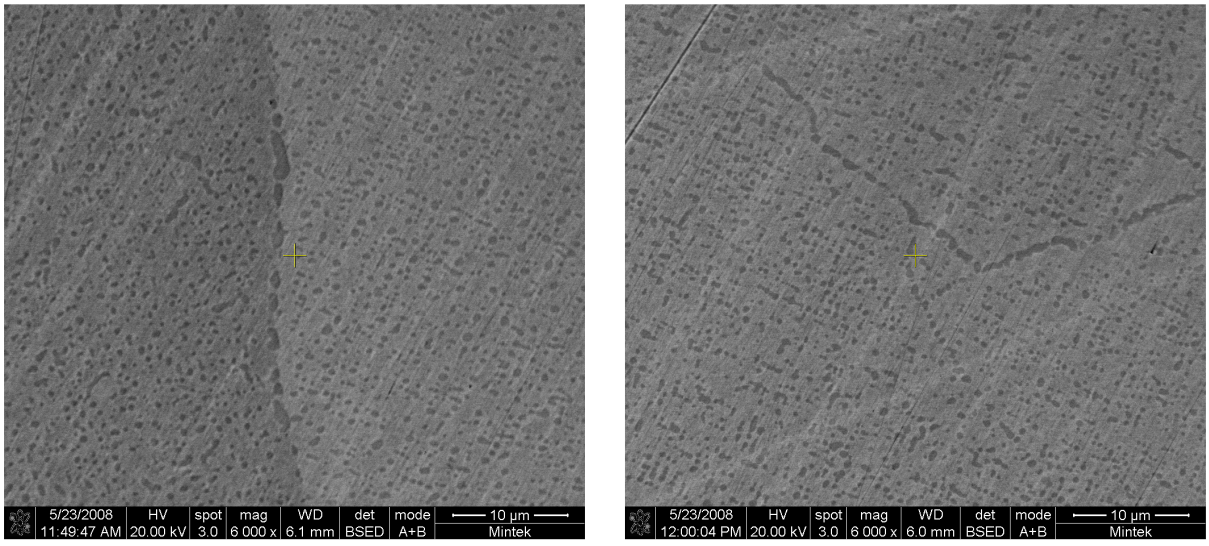

(a) **(b)**

Figure 4.116. HR-SEM-BSE image of nominal $Pt_{78}:Al_{11}:Ru_8:Cr_3$ after heat treatment, a) taken at the centre showing grains and b) edge, showing ~Pt_3Al precipitates (dark) in a (Pt) matrix (light) and subgrain boundaries.

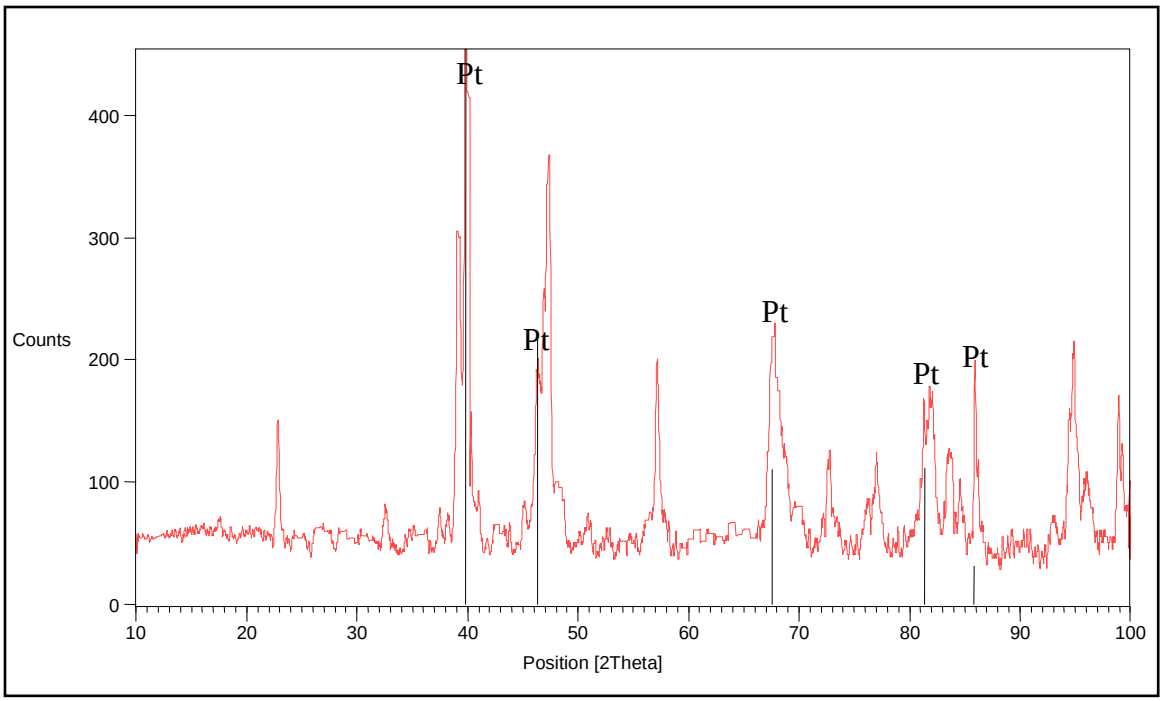

Figure 4.117. XRD Pattern of nominal Pt_{78}:Al_{11}:Ru_8:Cr_3 in the heat treated condition, showing identified Pt peaks.

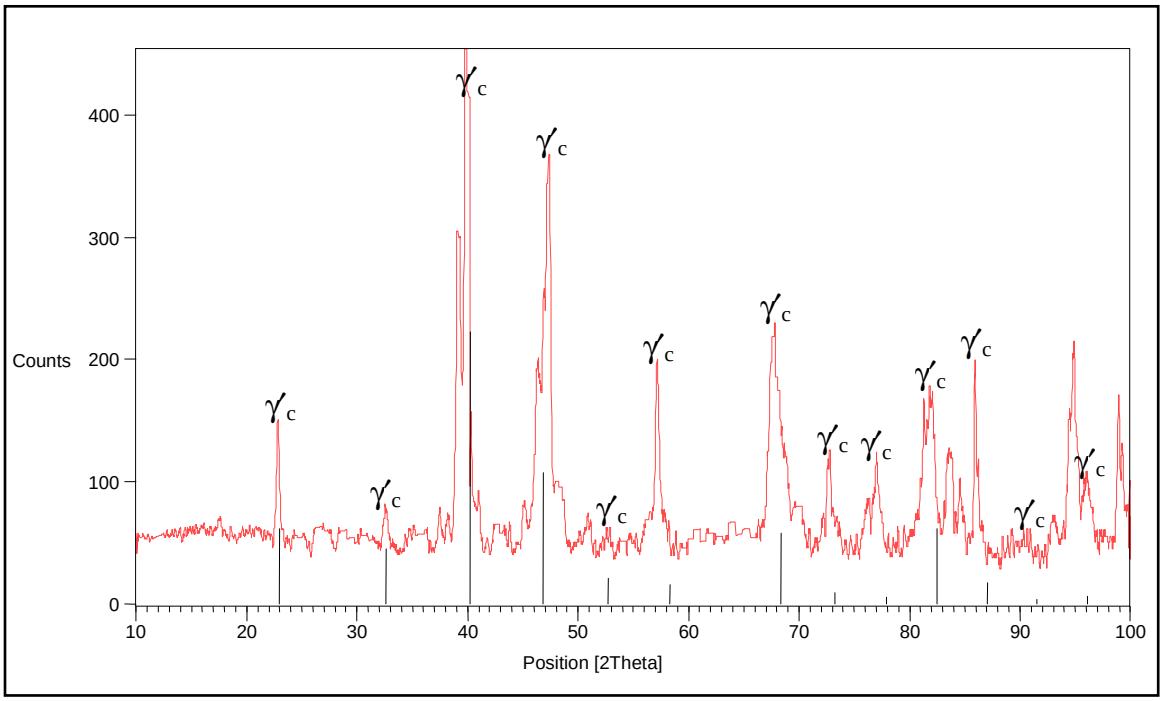

Figure 4.118. XRD Pattern of nominal Pt_{78}:Al_{11}:Ru_8:Cr_3 in the heat treated condition, showing apparent $L1_2$ – ~Pt_3Al peaks.

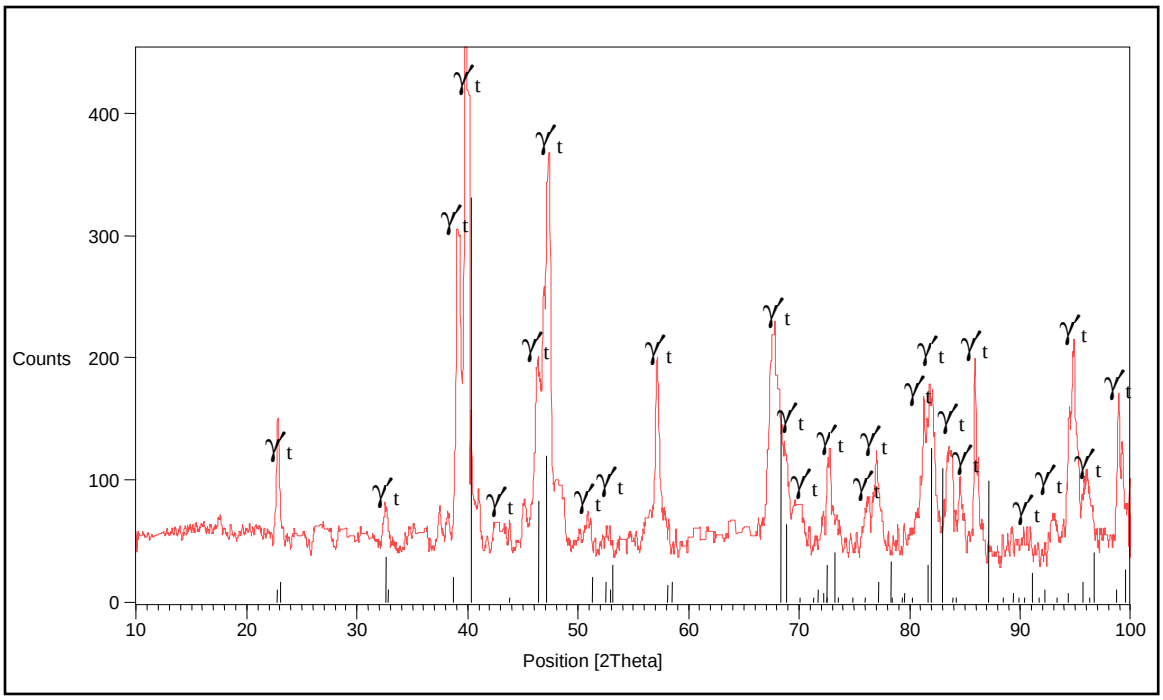

Figure 4.119. XRD Pattern of nominal Pt_{78}:Al_{11}:Ru_8:Cr_3 in the heat treated condition, showing identified DO'_c – ~Pt_3Al peaks.

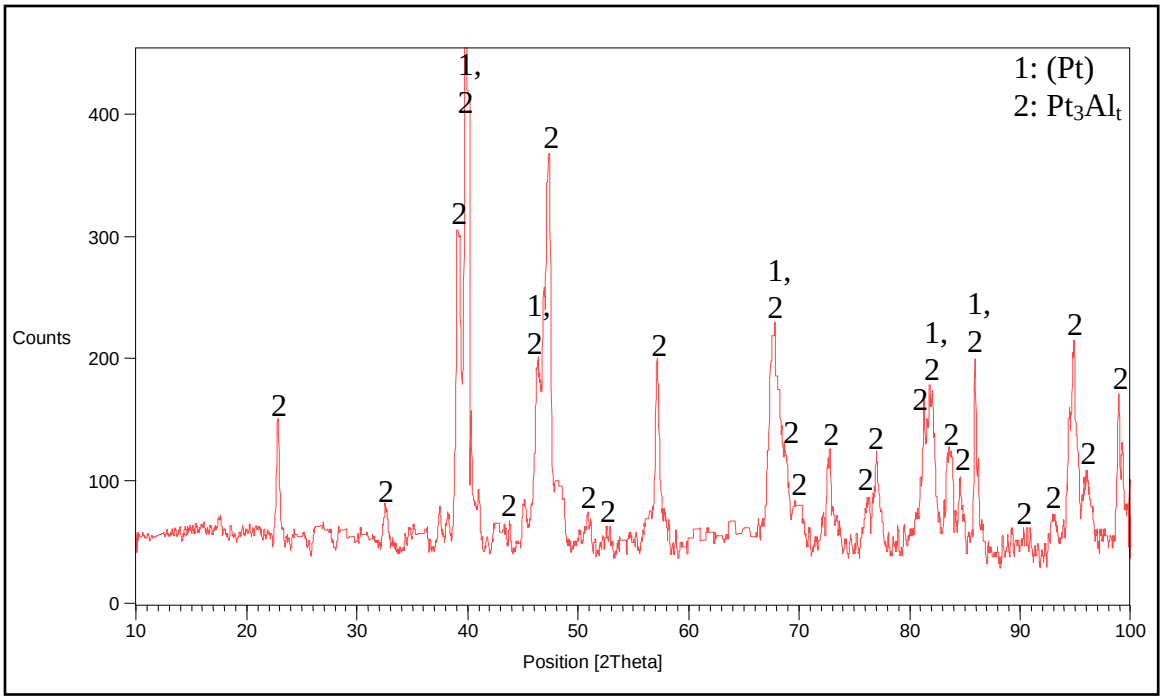

Figure 4.120. XRD pattern of nominal Pt_{78}:Al_{11}:Ru_8:Cr_3 in the heat treated condition, showing all identified phases.

Table 4.50. XRD peaks for Pt_{78}:Al_{11}:Ru_{8}:Cr_{3} in the heat treated condition.

Position 2θ(°)	Height (counts)	Full-Width Half-Maximum 2θ(°)	d-spacing (Å)	Relative Intensity (%)	Phase (s)
22.8154	96.77	0.2362	3.89778	23.27	γ′t
26.3325	14.09	0.7872	3.38461	3.39	-
28.5574	10.50	0.6298	3.12578	2.52	γ′t
32.6144	30.63	0.3936	2.74562	7.37	γ′t
37.4468	29.64	0.1968	2.40167	7.13	γ′t
38.2413	26.12	0.2755	2.35359	6.28	-
39.2747	257.01	0.1181	2.29401	61.81	γ′t
39.7464	415.81	0.0720	2.26599	100.00	(Pt), γ′t
41.0231	45.62	0.1574	2.20019	10.97	-
42.5835	19.84	0.3149	2.12311	4.77	γ′t
43.8054	21.18	0.1771	2.06668	5.09	γ′t
45.1810	39.04	0.3149	2.00691	9.39	-
46.2302	140.04	0.2755	1.96377	33.68	(Pt), γ′t
47.4281	322.31	0.1968	1.91693	77.51	γ′t
48.6600	39.56	0.4723	1.87125	9.51	γ′t
51.0355	19.62	0.5510	1.78959	4.72	γ′t
52.9391	9.00	0.5510	1.72964	2.16	γ′t
57.0432	124.21	0.1968	1.61456	29.87	γ′t
60.7376	9.08	0.6298	1.52490	2.18	-
63.9190	11.53	0.4723	1.45647	2.77	-
67.7648	168.60	0.2362	1.38287	40.55	(Pt), γ′t
70.1334	29.05	0.6298	1.34186	6.99	γ′t
72.2288	23.55	0.2755	1.30801	5.66	γ′t
72.7902	79.61	0.1680	1.29822	19.14	γ′t
76.3430	39.66	0.3149	1.24744	9.54	γ′t
77.0178	71.49	0.3149	1.23818	17.19	γ′t
81.2837	109.77	0.1680	1.18266	26.40	γ′t
81.9699	117.16	0.4723	1.17546	28.18	(Pt), γ′t
83.4892	74.45	0.2880	1.15693	17.91	γ′t
83.9102	63.38	0.2400	1.15506	15.24	γ′t
84.5598	56.19	0.1920	1.14500	13.51	γ′t
85.9366	158.24	0.2160	1.13014	38.05	(Pt), γ′t
88.4479	19.45	0.1920	1.10443	4.68	γ′t
90.6493	16.30	1.1520	1.08325	3.92	γ′t
92.9611	34.87	0.6720	1.06228	8.39	γ′t
94.4209	117.48	0.1920	1.04966	28.25	γ′t
94.8785	175.87	0.2880	1.04581	42.30	γ′t
96.0061	65.98	0.5760	1.03649	15.87	γ′t
98.9400	134.79	0.1680	1.01346	32.42	γ′t
99.2751	91.01	0.1680	1.01345	21.89	γ′t

4.3 Mechanical Tests

4.3.1 First Batch of Samples

4.3.1.1 Hardness

The results of the Vickers hardness measurements on both as-cast and heat treated samples are given in Table 4.51. The hardnesses quoted are the average of at least five determinations on different areas. Four of the alloys hardnesses increased after heat treatment, except Pt_{84}:Al_{11}:Ru_2:Cr_3 and Pt_{85}:Al_7:Ru_3:Cr_5.

4.3.1.1 Toughness

Photographs of the hardness indentions of both as-cast and heat treated samples were taken using an optical microscope (Figures 4.121 to 4.132) to obtain a qualitative evaluation of the alloys toughness and, where possible, slip modes. Micrographs were taken at low and high magnifications, firstly to have most of the indentations' surrounding area and secondly to increase the visibility of the slip mode. Cracking around an indentation is an indication of brittleness, while the slip mode around indentations shows whether the alloy has reasonable toughness shown by planar slip or wavy slip indicating much better resistance.

Wavy slip was observed around hardness indentations in five of the as-cast alloys, with the exception of Pt_{85}:Al_7:Ru_3:Cr_5 which showed planar slip. Cracking around the indention was observed in four samples (Pt_{80}:Al_{14}:Ru_3:Cr_3, $Pt_{81.5}$:$Al_{11.5}$:$Ru_{2.5}$:$Cr_{4.5}$, Pt_{84}:Al_{11}:Ru_2:Cr_3 and Pt_{85}:Al_7:Ru_3:Cr_5). Barrelling was observed in five samples, except $Pt_{81.5}$:$Al_{11.5}$:$Ru_{2.5}$:$Cr_{4.5}$ which had pincushioning. Indentation distortion was observed in Pt_{84}:Al_{11}:Ru_2:Cr_3 probably due to sample surface not being totally flat.

Three of the heat treated samples (Pt_{80}:Al_{14}:Ru_3:Cr_3, $Pt_{81.5}$:$Al_{11.5}$:$Ru_{2.5}$:$Cr_{4.5}$ and Pt_{84}:Al_{11}:Ru_2:Cr_3) had distorted indentations possibly due to the sample surface not being absolutely flat. Wavy slip was observed for all heat treated samples. Barrelling was observed in five samples, except Pt_{85}:Al_7:Ru_3:Cr_5 with pincushioning and minor cracking observed in Pt_{80}:Al_{14}:Ru_3:Cr_3.

Table 4.51. Hardness values of first batch of samples in the as-cast and heat treated conditions (HV_{10}).

	As-cast		Heat treated	
Alloy	**Hardness (HV_{10})**	**Deformation**	**Hardness (HV_{10})**	**Deformation**
$Pt_{78}:Al_{15.5}:Ru_2:Cr_{4.5}$	453 ± 26	Wavy slip	164 ± 5	Wavy slip
$Pt_{80}:Al_{14}:Ru_3:Cr_3$	390 ± 25	Wavy slip	361 ± 24	Wavy slip
$Pt_{81.5}:Al_{11.5}:Ru_{2.5}:Cr_{4.5}$	399 ± 20	Wavy slip	391 ± 24	Wavy slip
$Pt_{82}:Al_{12}:Ru_2:Cr_4$	367 ± 16	Wavy slip	378 ± 4	Wavy slip
$Pt_{84}:Al_{11}:Ru_2:Cr_3$	348 ± 53	Wavy slip	395 ± 27	Wavy slip
$Pt_{85}:Al_7:Ru_3:Cr_5$	307 ± 9	Planar slip	380 ± 17	Wavy slip

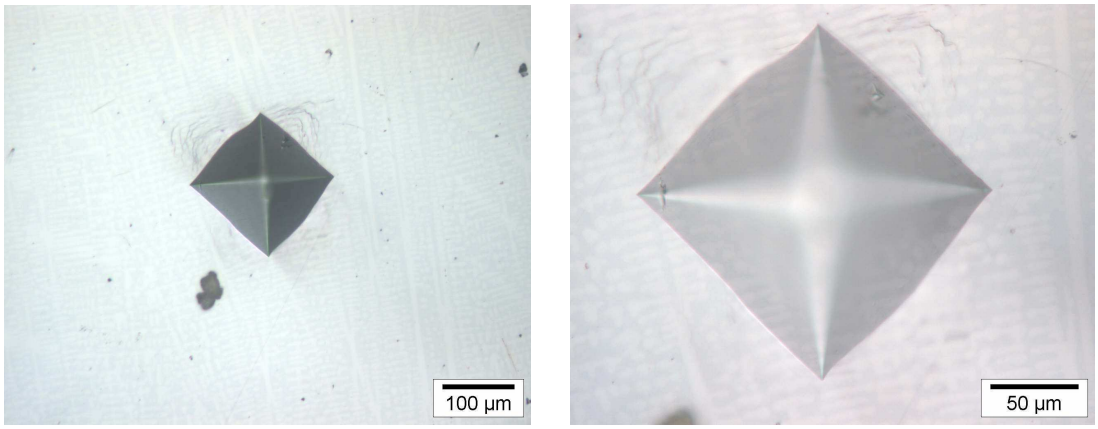

(a) **(b)**

Figure 4.121. Hardness indentation micrographs for $Pt_{78}:Al_{15.5}:Ru_2:Cr_{4.5}$ in the as-cast condition (a) and (b) taken at different magnifications showing wavy slip and slight barrelling.

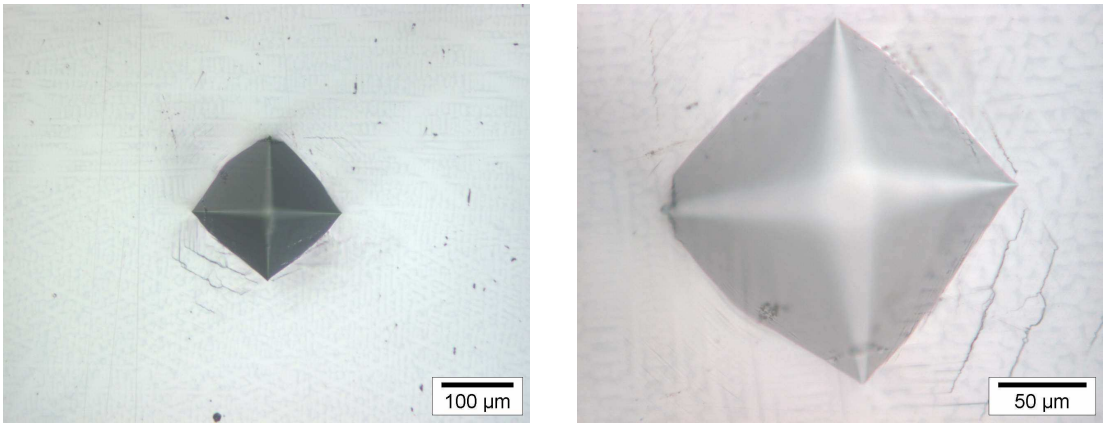

(a) **(b)**

Figure 4.122. Hardness indentation micrographs for $Pt_{80}:Al_{14}:Ru_3:Cr_3$ in the as-cast condition (a) and (b) taken at different magnifications showing wavy slip, cracking and barrelling.

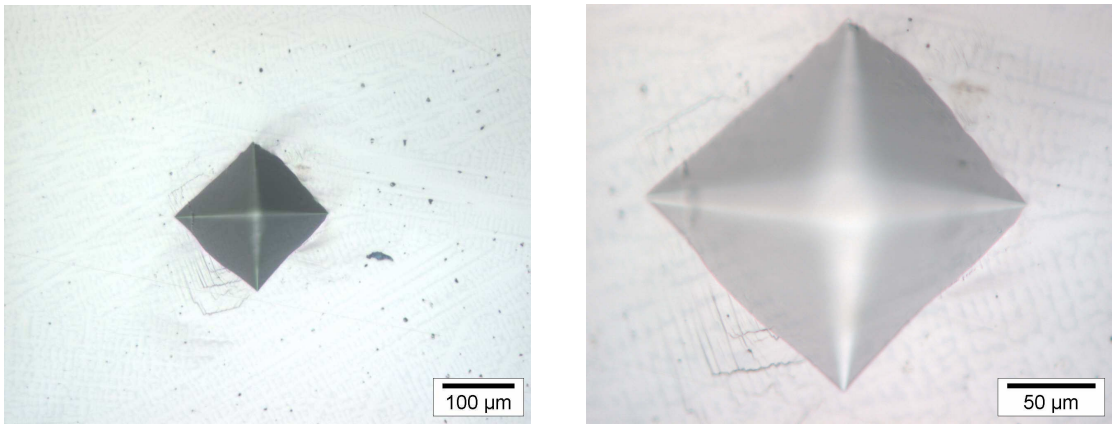

(a) **(b)**

Figure 4.123. Hardness indentation micrographs for $Pt_{81.5}$:$Al_{11.5}$:$Ru_{2.5}$:$Cr_{4.5}$ in the as-cast condition (a) and (b) taken at different magnifications showing wavy slip, minor cracking and slight pincushioning.

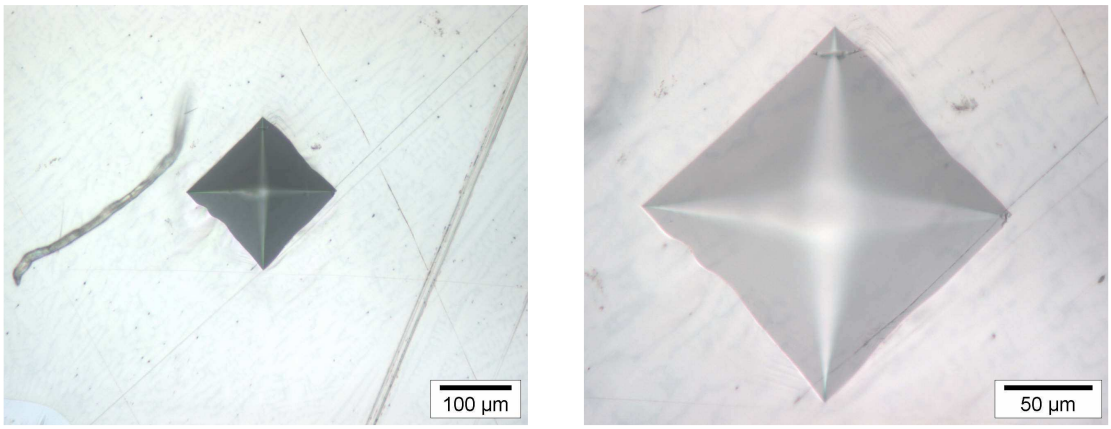

(a) **(b)**

Figure 4.124. Hardness indentation micrographs for Pt_{82}:Al_{12}:Ru_{2}:Cr_{4} in the as-cast condition (a) and (b) taken at different magnifications showing minor wavy slip.

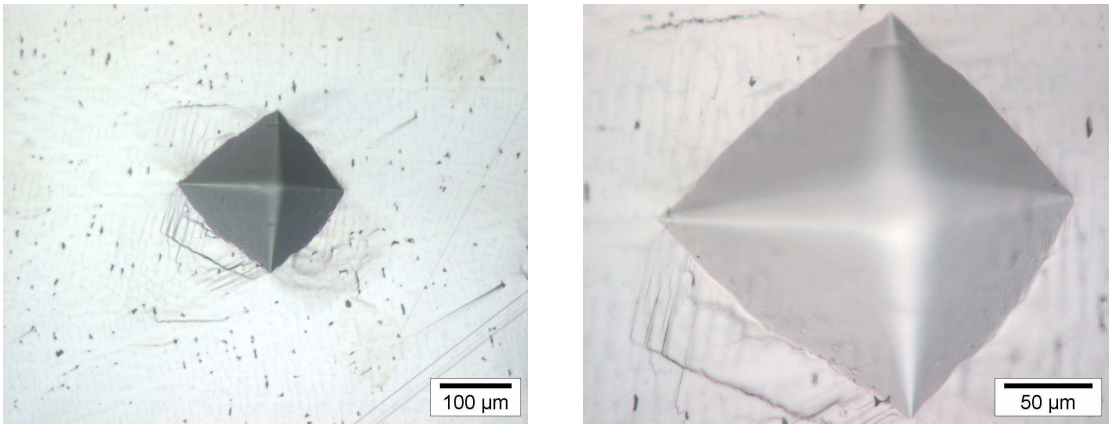

(a) **(b)**

Figure 4.125. Hardness indentation micrographs for Pt_{84}:Al_{11}:Ru_{2}:Cr_{3} in the as-cast condition (a) and (b) taken at different magnifications showing wavy slip, cracking and barrelling.

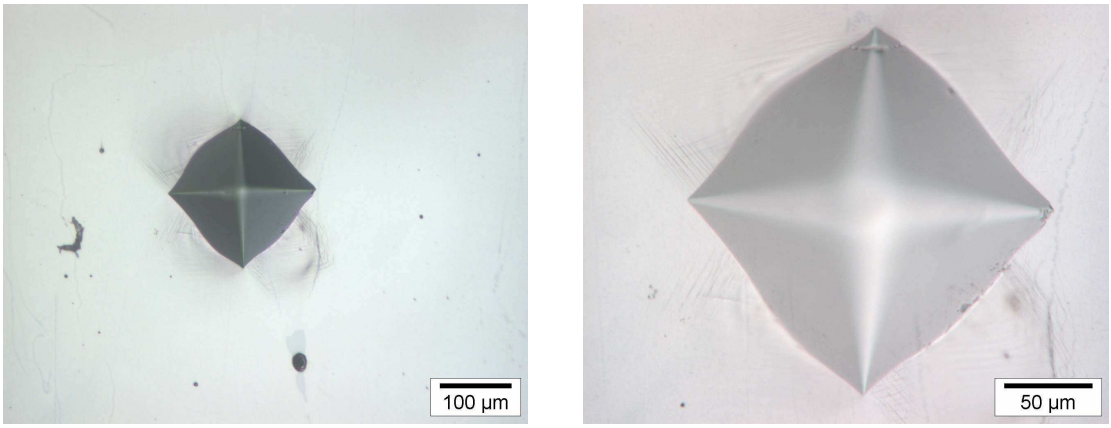

(a) **(b)**

Figure 4.126. Hardness indentation micrographs for Pt_{85}:Al_7:Ru_3:Cr_5 in the as-cast condition (a) and (b) taken at different magnifications showing planar slip, minor cracking and barrelling.

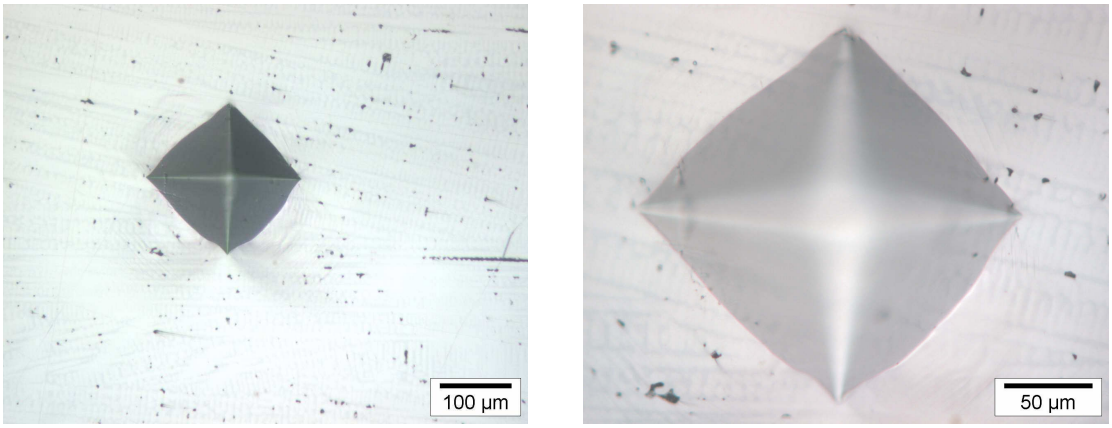

(a) **(b)**

Figure 4.127. Hardness indentation micrographs for Pt_{78}:$Al_{15.5}$:Ru_2:$Cr_{4.5}$ in the heat treated condition (a) and (b) taken at different magnifications showing minor wavy slip and slight barrelling.

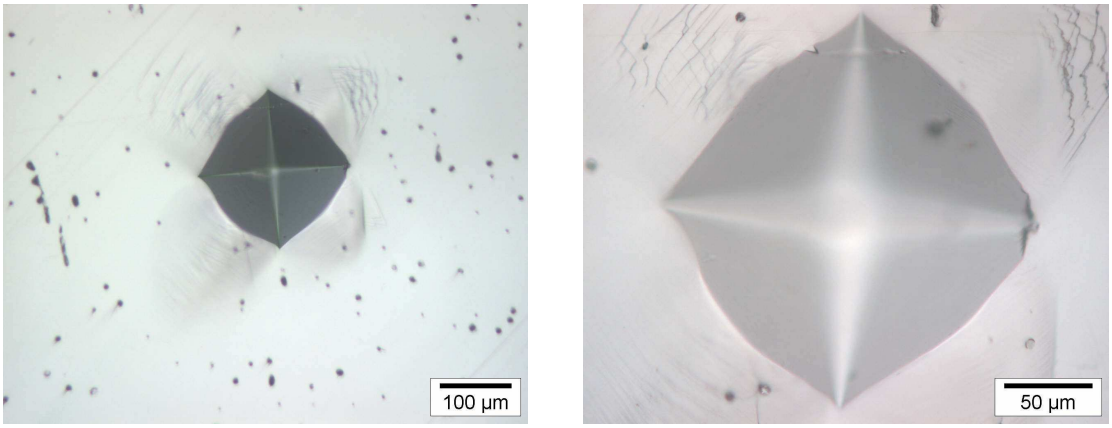

(a) **(b)**

Figure 4.128. Hardness indentation micrographs for Pt_{80}:Al_{14}:Ru_3:Cr_3 in the heat treated condition (a) and (b) taken at different magnifications showing wavy slip, cracking, barrelling and minor cracking.

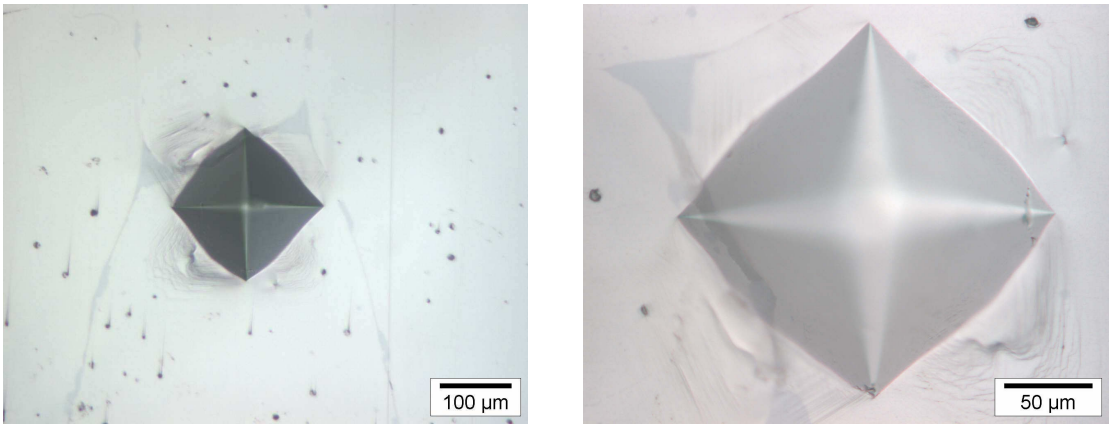

(a) **(b)**

Figure 4.129. Hardness indentation micrographs for $Pt_{81}:Al_{11.5}:Ru_{2.5}:Cr_{4.5}$ in the heat treated condition (a) and (b) taken at different magnifications showing wavy slip and barrelling.

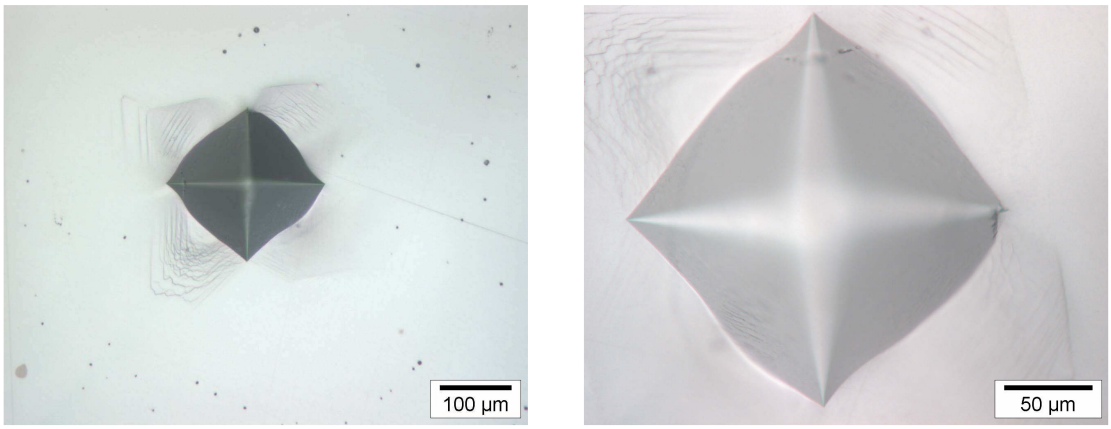

(a) **(b)**

Figure 4.130. Hardness indentation micrographs for $Pt_{82}:Al_{12}:Ru_{2}:Cr_{4}$ in the heat treated condition (a) and (b) taken at different magnifications showing wavy slip and barrelling.

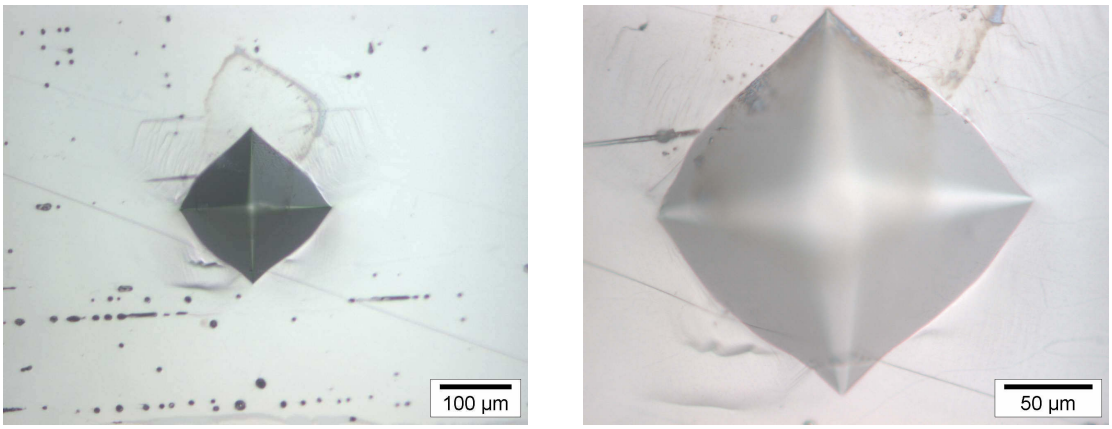

(a) **(b)**

Figure 4.131. Hardness indentation micrographs for $Pt_{84}:Al_{11}:Ru_{2}:Cr_{3}$ in the heat treated condition (a) and (b) taken at different magnifications showing wavy slip and barrelling.

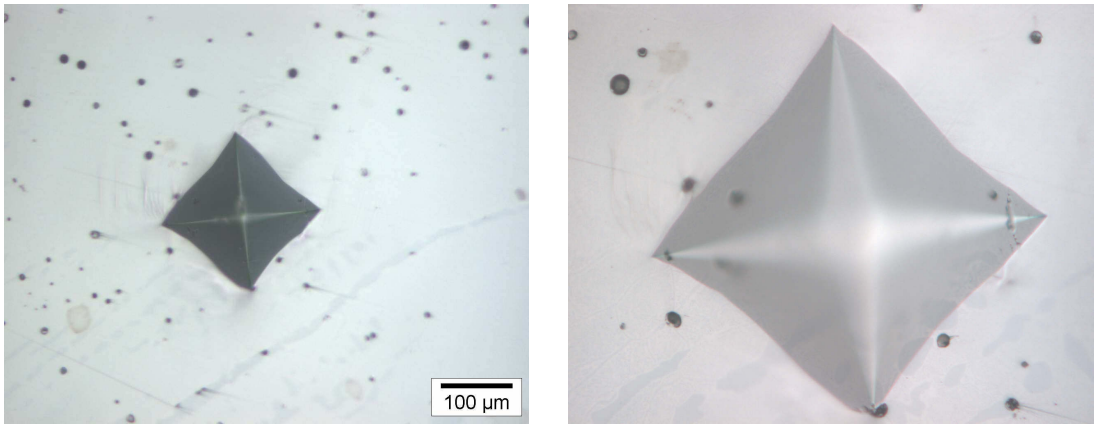

(a) **(b)**

Figure 4.132. Hardness indentation micrographs for $Pt_{85}:Al_7:Ru_3:Cr_5$ in the heat treated condition (a) and (b) taken at different magnifications showing minor wavy slip and pincushioning.

4.3.2 Second Batch of Samples

4.3.2.1 Hardness

The results of the Vickers hardness measurements (average of at least five determinations on different areas) of both as-cast and heat treated samples are given in Table 4.52. The slip modes are also given.

4.3.2.2 Toughness

The hardness indentions for all alloys are shown in Figures 4.133 to 4.144. Wavy slip was observed around macrohardness indentations of all as-cast alloys. Cracking was seen in two samples ($Pt_{80}:Al_{11}:Ru_5:Cr_4$ and $Pt_{78}:Al_{11}:Ru_8:Cr_3$). Indentation distortion was also observed in four samples ($Pt_{80}:Al_{11}:Ru_3:Cr_6$, $Pt_{78}:Al_{11}:Ru_5:Cr_6$, $Pt_{78}:Al_{11}:Ru_3:Cr_8$ and $Pt_{78}:Al_{11}:Ru_8:Cr_3$), probably due to the surface of the sample not being perfectly flat. Pincushioning was seen in $Pt_{80}:Al_{11}:Ru_6:Cr_3$ and $Pt_{78}:Al_{11}:Ru_3:Cr_8$, and barrelling was observed for $Pt_{80}:Al_{11}:Ru_5:Cr_4$.

All heat treated alloys had planar slip. Pincushioning was observed for $Pt_{80}:Al_{11}:Ru_3:Cr_6$ and $Pt_{80}:Al_{11}:Ru_6:Cr_3$. $Pt_{78}:Al_{11}:Ru_5:Cr_6$ had distortion of the indentations. Barrelling was observed in three samples ($Pt_{80}:Al_{11}:Ru_5:Cr_4$, $Pt_{78}:Al_{11}:Ru_3:Cr_8$, $Pt_{78}:Al_{11}:Ru_8:Cr_3$ and $Pt_{78}:Al_{11}:Ru_5:Cr_6$). Minor cracking was seen in $Pt_{80}:Al_{11}:Ru_6:Cr_3$.

Table 4. 52. Hardness values of second batch of samples in the as-cast and heat treated conditions (HV_{10}).

	As-cast		Heat treated	
Alloy	**Hardness (HV_{10})**	**Deformation**	**Hardness (HV_{10})**	**Deformation**
Pt_{80}:Al_{11}:Ru_5:Cr_4	409 ± 19	Wavy slip	247 ± 13	Planar Slip
Pt_{80}:Al_{11}:Ru_3:Cr_6	330 ± 30	Wavy slip	237 ± 22	Planar Slip
Pt_{80}:Al_{11}:Ru_6:Cr_3	383 ± 23	Wavy slip	226 ± 9	Planar Slip
Pt_{78}:Al_{11}:Ru_5:Cr_6	363 ± 27	Wavy slip	357 ± 4	Planar Slip
Pt_{78}:Al_{11}:Ru_3:Cr_8	367 ± 36	Wavy slip	354 ± 26	Planar Slip
Pt_{78}:Al_{11}:Ru_8:Cr_3	413 ± 18	Wavy slip	396 ± 17	Planar Slip

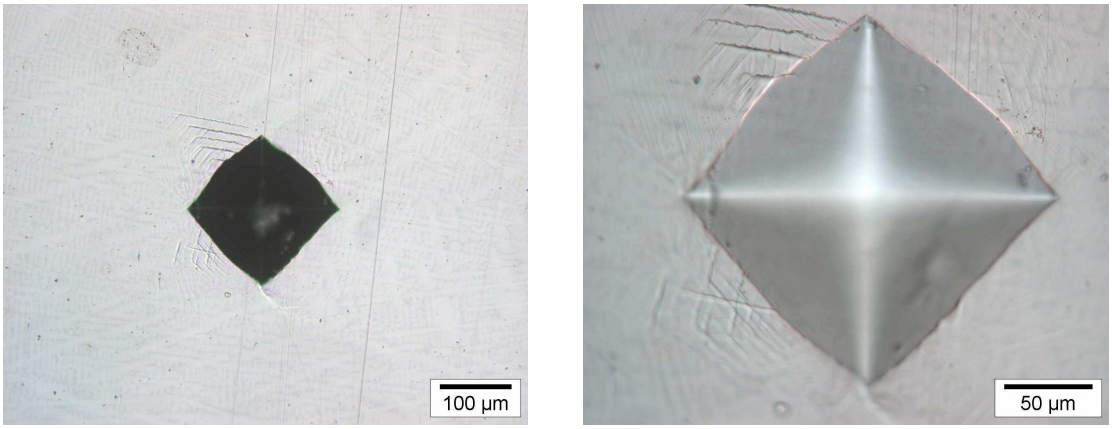

(a) **(b)**

Figure 4.133. Hardness indentation micrographs for Pt_{80}:Al_{11}:Ru_5:Cr_4 in the as-cast condition (a) and (b) taken at different magnifications showing wavy slip, cracking and slight barrelling.

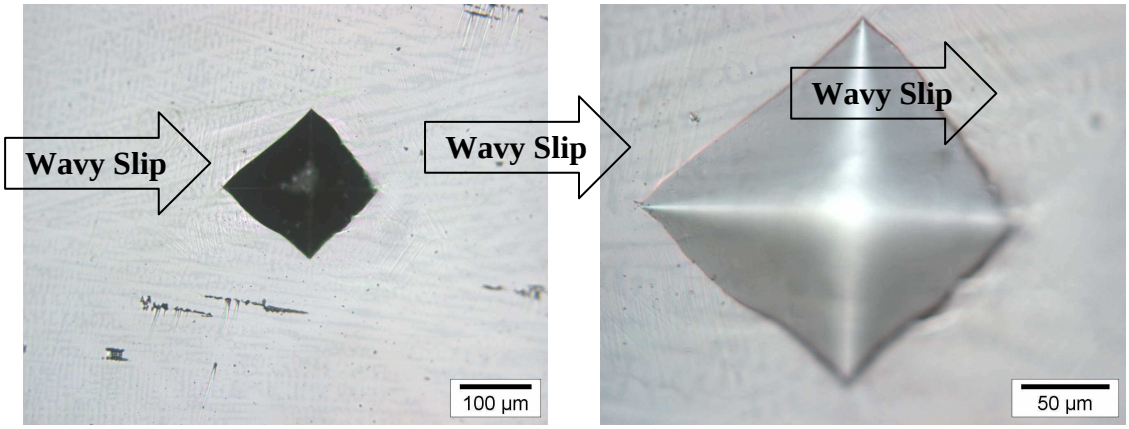

(a) **(b)**

Figure 4.134. Hardness indentation micrographs for Pt_{80}:Al_{11}:Ru_3:Cr_6 in the as-cast condition (a) and (b) taken at different magnifications showing minor wavy slip.

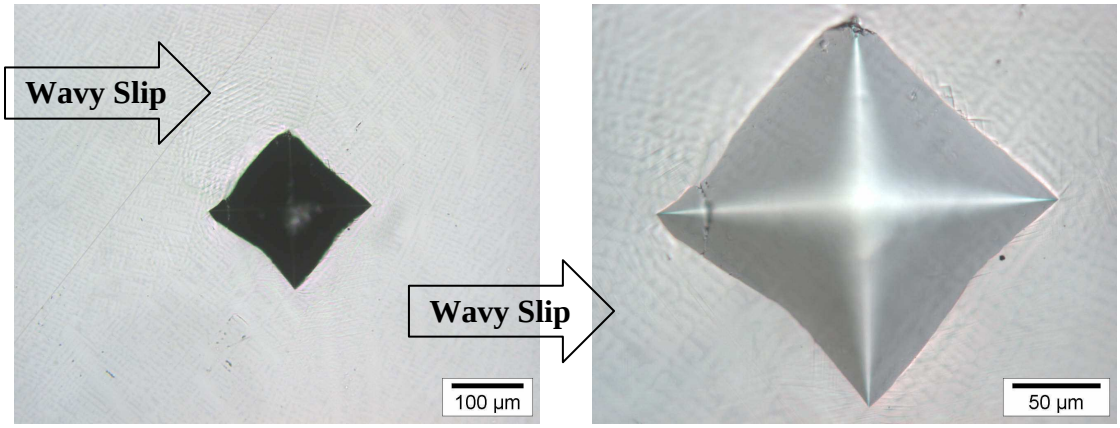

(a) **(b)**

Figure 4.135. Hardness indentation micrographs for Pt_{80}:Al_{11}:Ru_6:Cr_3 in the as-cast condition (a) and (b) taken at different magnifications showing minor wavy slip and pincushioning.

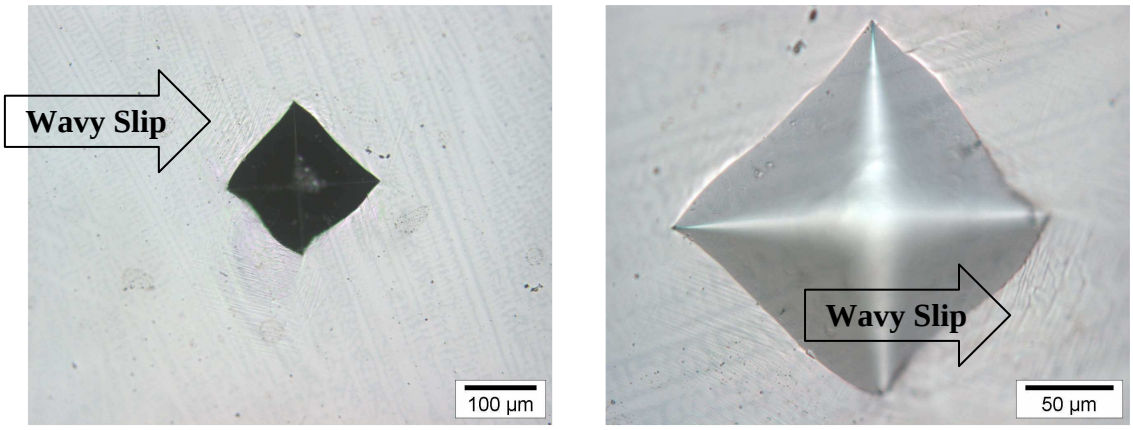

(a) **(b)**

Figure 4.136. Hardness indentation micrographs for Pt_{78}:Al_{11}:Ru_5:Cr_6 in the as-cast condition (a) and (b) taken at different magnifications showing wavy slip.

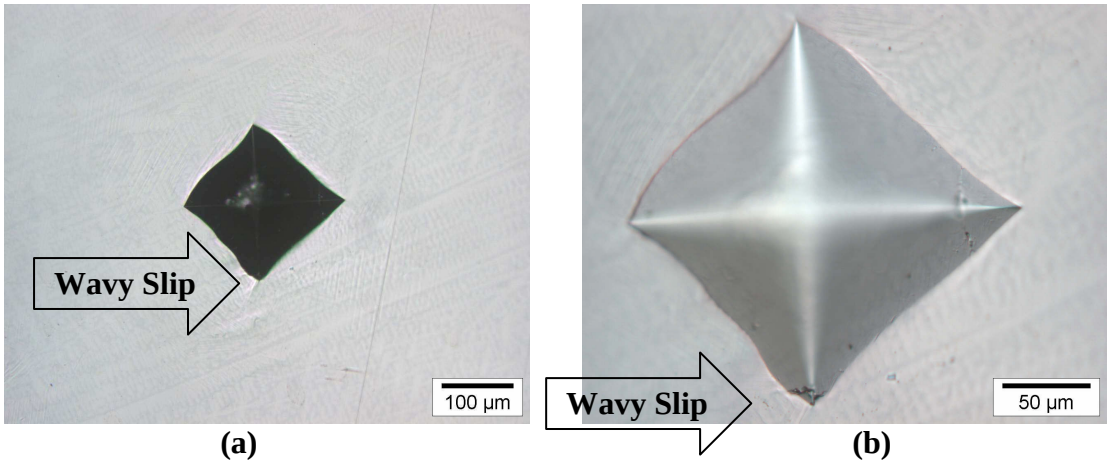

(a) **(b)**

Figure 4.137. Hardness indentation micrographs for Pt_{78}:Al_{11}:Ru_3:Cr_8 in the as-cast condition (a) and (b) taken at different magnifications showing minor wavy slip and pincushioning.

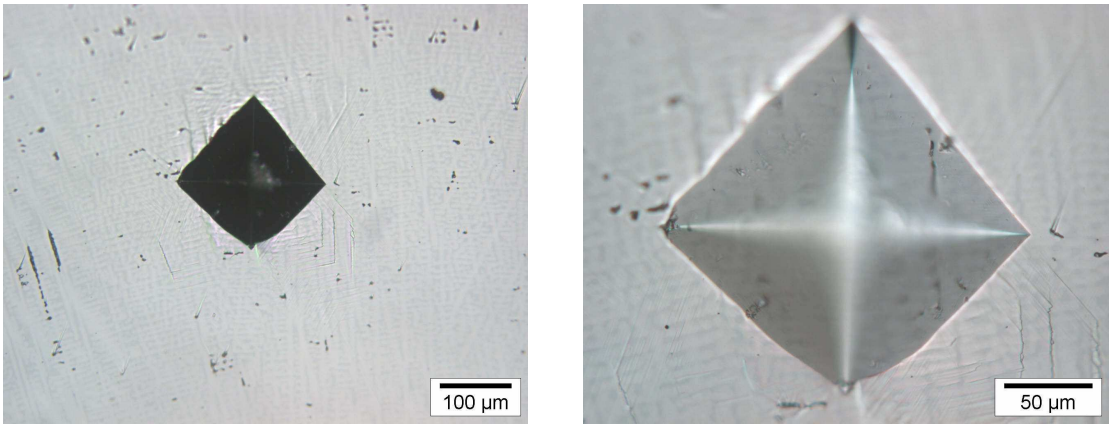

(a) **(b)**

Figure 4.138. Hardness indentation micrographs for Pt_{78}:Al_{11}:Ru_8:Cr_3 in the as-cast condition. (a) and (b) taken at different magnifications showing wavy slip and cracking.

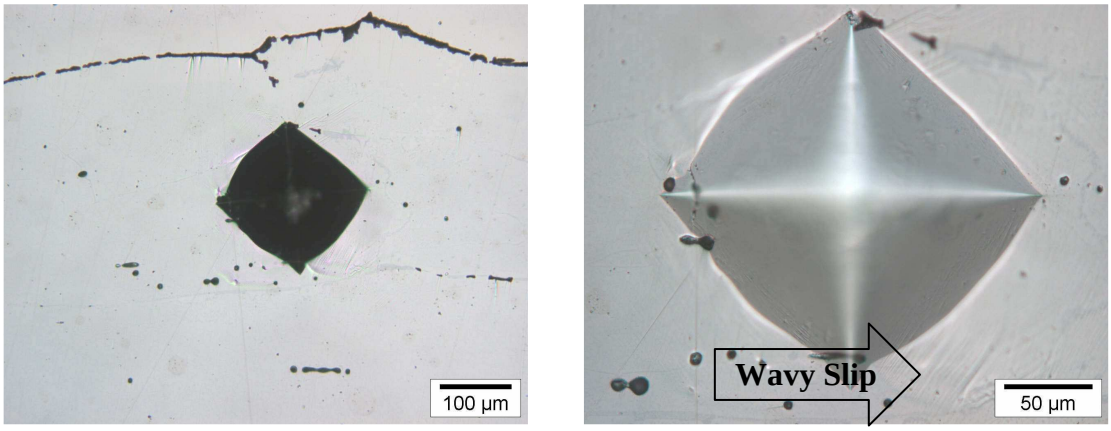

(a) **(b)**

Figure 4.139. Hardness indentation micrographs for Pt_{80}:Al_{11}:Ru_5:Cr_4 in the heat treated condition. (a) and (b) taken at different magnifications showing minor planar slip and barrelling.

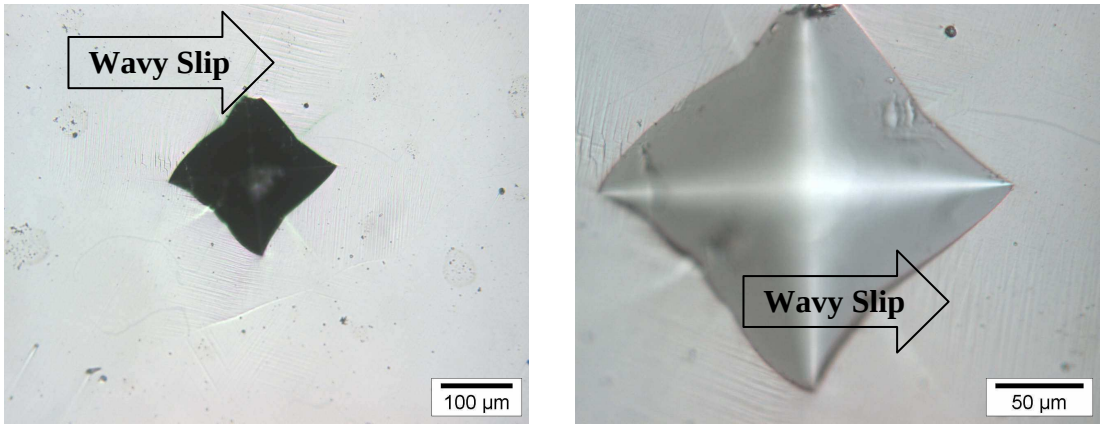

(a) **(b)**

Figure 4.140. Hardness indentation micrographs for Pt_{80}:Al_{11}:Ru_3:Cr_6 in the heat treated condition (a) and (b) taken at different magnifications showing planar slip and pincushioning.

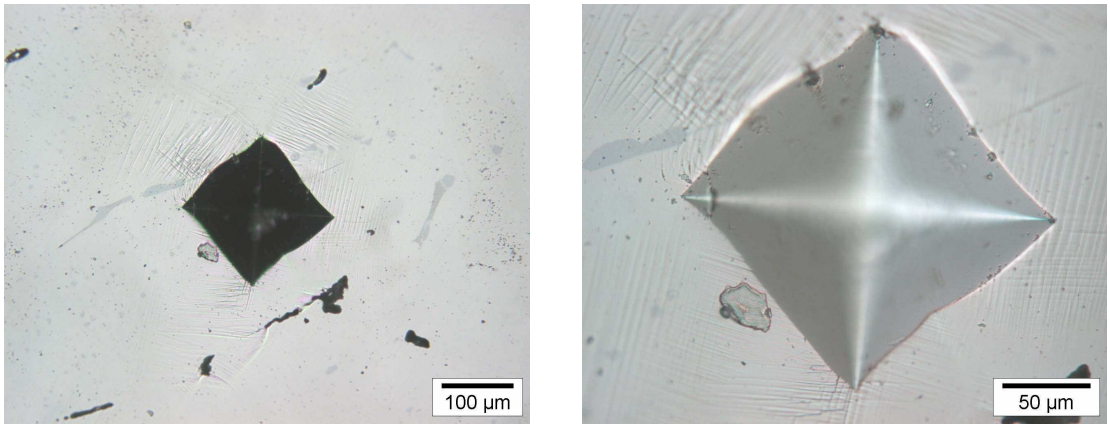

(a) (b)

Figure 4.141. Hardness indentation micrographs for Pt_{80}:Al_{11}:Ru_6:Cr_3 in the heat treated condition (a) and (b) taken at different magnifications showing planar slip, cracking and pincushioning.

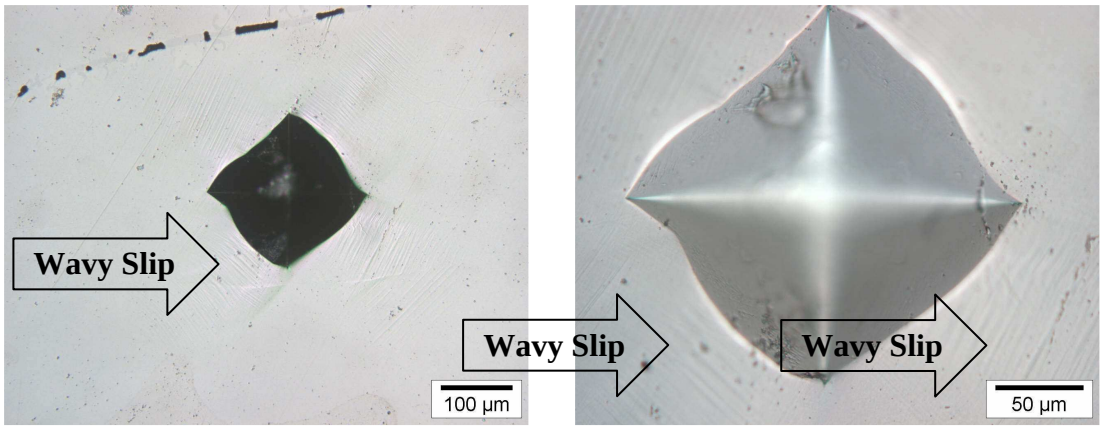

(a) (b)

Figure 4.142. Hardness indentation micrographs for Pt_{78}:Al_{11}:Ru_5:Cr_6 in the heat treated condition (a) and (b) taken at different magnifications showing minor planar slip and barrelling.

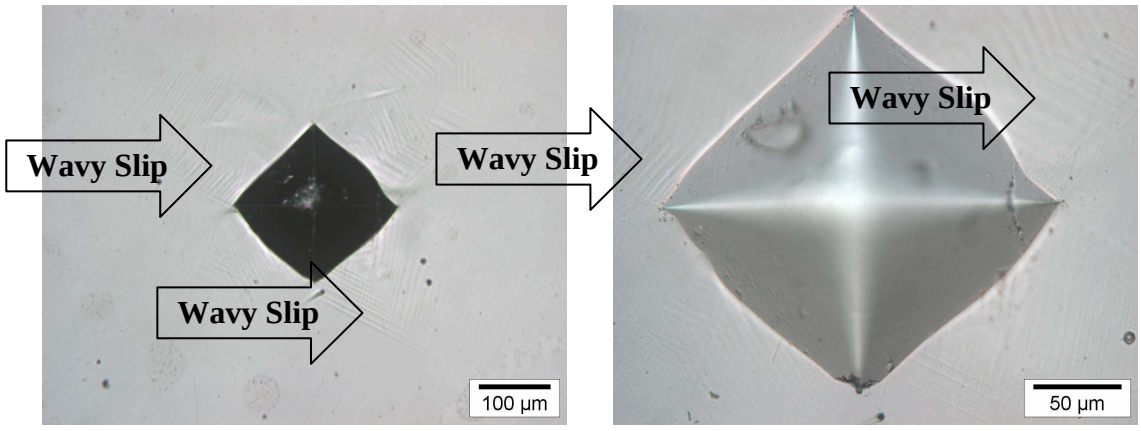

(a) (b)

Figure 4.143. Hardness indentation micrographs for Pt_{78}:Al_{11}:Ru_3:Cr_8 in the heat treated condition (a) and (b) taken at different magnifications showing minor planar slip and barrelling.

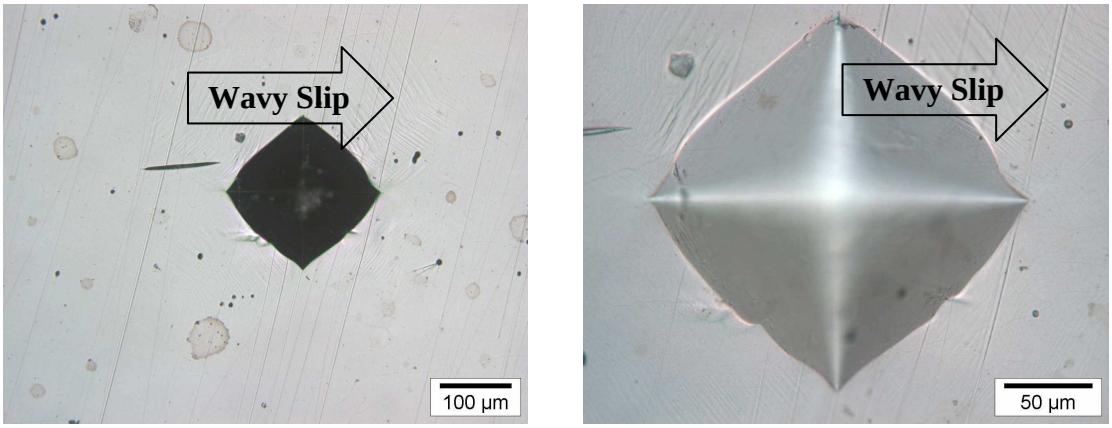

(a) **(b)**

Figure 4.144. Hardness indentation micrographs for Pt_{78}:Al_{11}:Ru_8:Cr_3 in the heat treated condition (a) and (b) taken at different magnifications showing planar slip and barrelling.

CHAPTER FIVE

DISCUSSION

5.1 First Batch of Samples

The compositions of the first batch of samples were selected using the original optimum composition (Pt_{84}:Al_{11}:Ru_2:Cr_3) [2002Cor]. The Pt and Al contents were varied to evaluate the effect of both elements on the as-cast and heat treated samples microstructures, with Ru and Cr being kept similar for each of the samples.

Sample preparation was a problem. Some scratches can be seen on the microstructure, although sample preparation was improved slightly by carrying out polishing for longer times. However, it was likely that the deeper deformation due to earlier grinding had not been totally removed. Image analysis could not be done on the samples as there was insufficient contrast between the phases.

5.1.1 As-cast samples

All the as-cast samples were fairly homogenous as shown by the similarities of their edge and centre microstructures and compositional analyses. The proportion of the dendrites was higher than the eutectic phase and the dendrite proportion increased with increasing Pt content and decreasing Al content. Some ~Pt_3Al precipitates were observed in the dendrites, particularly close to the dendrite edges, in agreement to the results of Marekwa *et al.* [2007Mar] and Wenderoth *et al.* [2005Wen]. The dendrites were cored with a low Al content in the centre and higher towards the edges, which explains why there were more precipitates at the dendrite edges. The precipitates were coarse on the dendrite edges and finer towards the centre of the dendrites for all alloys, and the majority were rounded in shape. This was unexpected since Tshawe et al. [2006Tsh] observed cubic precipitates, although the latter were for Pt-Al alloys. The largest precipitates were approximately 500 nm, and the finest observed approximately 50 nm (although there might be smaller precipitates which were not seen).

Three of the alloys (Pt_{80}:Al_{14}:Ru_3:Cr_3, Pt_{82}:Al_{12}:Ru_2:Cr_4, and Pt_{84}:Al_{11}:Ru_2:Cr_3) had compositions close to those targeted, while the other three alloys (Pt_{78}:$Al_{15.5}$:Ru_2:$Cr_{4.5}$, Pt_{81}:$Al_{11.5}$:$Ru_{2.5}$:$Cr_{4.5}$ and Pt_{85}:Al_7:Ru_3:Cr_5) varied from the targeted composition. Aluminium

was found to partition mostly to the interdendritic eutectic ((Pt) + ~Pt_3Al) with limited solubility in the (Pt) phase. The solubility range of Al was 13 to 22 at.% in the eutectic, and 3 to 11 at.% Al for the (Pt) dendrites. Ruthenium and Cr had limited solubility in the ((Pt) + ~Pt_3Al) eutectic, and partitioned preferentially to the (Pt). The solubility ranges were 0.5 to 0.7 at.% Ru and 1.2 to 1.7 at.% Cr for the eutectic, and between 1.4 to 3.2 at.% Ru and 2.4 to 5.4 at.% Cr for the (Pt) phase. The partitioning behaviour of Ru and Cr agreed with the results from Universities of Jena and Bayreuth, Germany [2004Vor, 2005Wen] and earlier work done at Mintek [2002Cor, 2003Cor, 2007Mar]. The work on Pt-based superalloys by Wenderoth *et al.* [2005Wen] had nickel additions and EDX measurements confirmed the preferential partitioning of Ni to the matrix phase, and Ni additions were found to decrease the absolute lattice misfit in Pt-Al-Cr-Ni alloys.

5.1.2 Heat Treated Samples

The heat treated overall compositions were different from the nominal and actual composition of the as-cast samples (Table 5.1). A marked decrease in Al was seen in all heat treated samples. The nominal Pt_{78}:$Al_{15.5}$:Ru_2:$Cr_{4.5}$ sample had the highest Al decrease of about 6 at.%, agreeing with the highest weight loss after melting (Table 4.1), thus confirming the loss of Al. Similar to the as-cast samples, the heat treated samples were also fairly homogenous. Pt_{78}:$Al_{15.5}$:Ru_2:$Cr_{4.5}$ and Pt_{80}:Al_{14}:Ru_3:Cr_3 had the finest ~Pt_3Al precipitates, which were very difficult to discern under the HR-SEM. The rest of the samples (Pt_{81}:$Al_{11.5}$:$Ru_{2.5}$:$Cr_{4.5}$, Pt_{82}:Al_{12}:Ru_2:Cr_4, Pt_{84}:Al_{11}:Ru_2:Cr_3 and Pt_{85}:Al_7:Ru_3:Cr_5) had visible rounded precipitates. Pt_{85}:Al_7:Ru_3:Cr_5 had retained areas of a eutectic even after heat treatment and according to Belov [1995Bel], the presence of brittle particles of the eutectic phase can affect negatively the fracture toughness and increases the capacity of the alloy for intergrain fracture. Douglas *et al.* [2006Dou2] also found that crack propagation occurred in the interdendritic areas that comprised (Pt) + ~Pt_3Al eutectic regions. It is therefore expected the retained eutectic may affect negatively the fracture toughness of the Pt-Al-Ru-Cr alloy.

Considering the alloys' compositions, the results show that higher Cr contents stabilise the ~Pt_3Al phase, similar to the findings of Hill *et al.* [200Hil3] and Wenderoth *et al.* [2005Wen] The average precipitate size for all samples was 0.95 µm, slightly above the average precipitate size found by Hüller *et al.* of 0.5 µm [2005Hül] and Wenderoth *et al.* of 0.7 µm [2005Wen] for Pt-Al-Cr-Ni alloys. Nominal Pt_{85}:Al_7:Ru_3:Cr_5 had the highest proportion of

~Pt_3Al (27 ± 6%). The proportion of the ~Pt_3Al volume fraction was similar to the results reported by Huller *et al.* [2005Hül] and those found at Mintek by Cornish *et al.* [2002Cor]. However, the volume fraction fraction is still small compared to the ~70-80% [1987Sim] value for NBSAs.

The microstructure was too fine to analyse the components phases accurately. However, the EDX measurements were useful for accessing trends on the solubility of the elements in the (Pt) and ~Pt_3Al phase. Aluminium was found to partition mostly to the ~Pt_3Al precipitates with limited solubility in the (Pt) phase. The solubility range of Al was 14 to 22 at.% in the precipitates, and 5 to 8.5 at.% Al in (Pt). Ruthenium had an extremely limited solubility in the ~Pt_3Al precipitates and partitioned almost exclusively to (Pt), in agreement with the results found at Mintek [2002Cor, 2007Mar] and Wenderoth *et al.* [2007Wen]. Chromium showed solubility in both phases, but partitioned preferentially to (Pt). The solubility ranges of Ru and Cr were found to be 0.5 to 0.7 at.% Ru and 1.3 to 1.8 at.% Cr for the precipitates, while for (Pt) it was between 1.2 to 2.4 at.% Ru and 2.7 to 4.6 at.% Cr. The solubility of Al in ~Pt_3Al decreased with Ru and Cr additions (Figures 5.1 and 5.2).

Table 5.1. Summary of overall EDX compositions (at.%) and approximate ~Pt_3Al volume fractions (%) for the first batch of heat treated samples (at.%).

Nominal alloy (at.%)	Actual compositions (at.%)				Approximate precipitate volume fraction (%)
	Pt	Al	Ru	Cr	
$Pt_{78}:Al_{15.5}:Ru_2:Cr_{4.5}$	84.9	9.8	1.5	3.8	~Pt_3Al indiscernible
$Pt_{80}:Al_{14}:Ru_3:Cr_3$	87	8.6	2	2.4	~Pt_3Al indiscernible
$Pt_{81}:Al_{11.5}:Ru_{2.5}:Cr_{4.5}$	86.2	8.6	1.4	3.8	12 ± 6
$Pt_{82}:Al_{12}:Ru_2:Cr_4$	85.3	10.3	0.9	3.5	10 ± 5
$Pt_{84}:Al_{11}:Ru_2:Cr_3$	86.8	8.7	1.8	2.7	12 ± 5
$Pt_{85}:Al_7:Ru_3:Cr_5$	90.2	4.1	1.6	4.1	27 ± 6

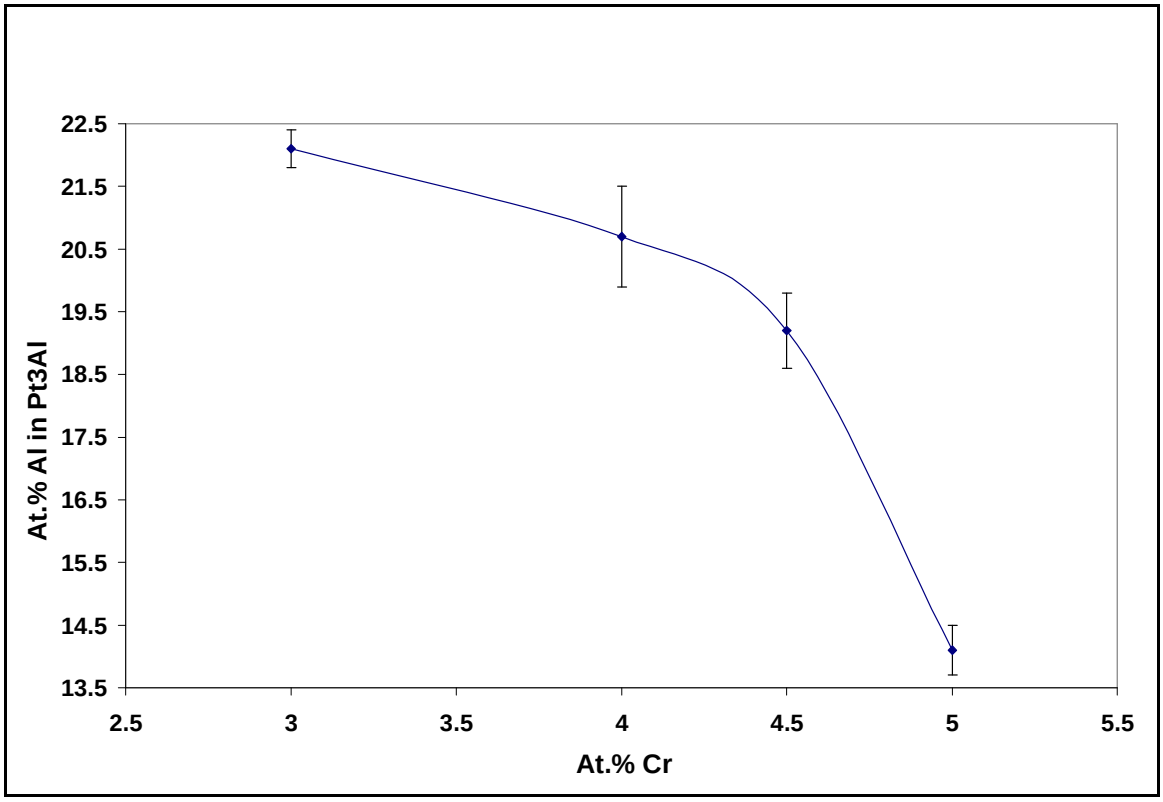

Figure 5.1. Solubility of Al in ~Pt_3Al with Cr additions (first batch).

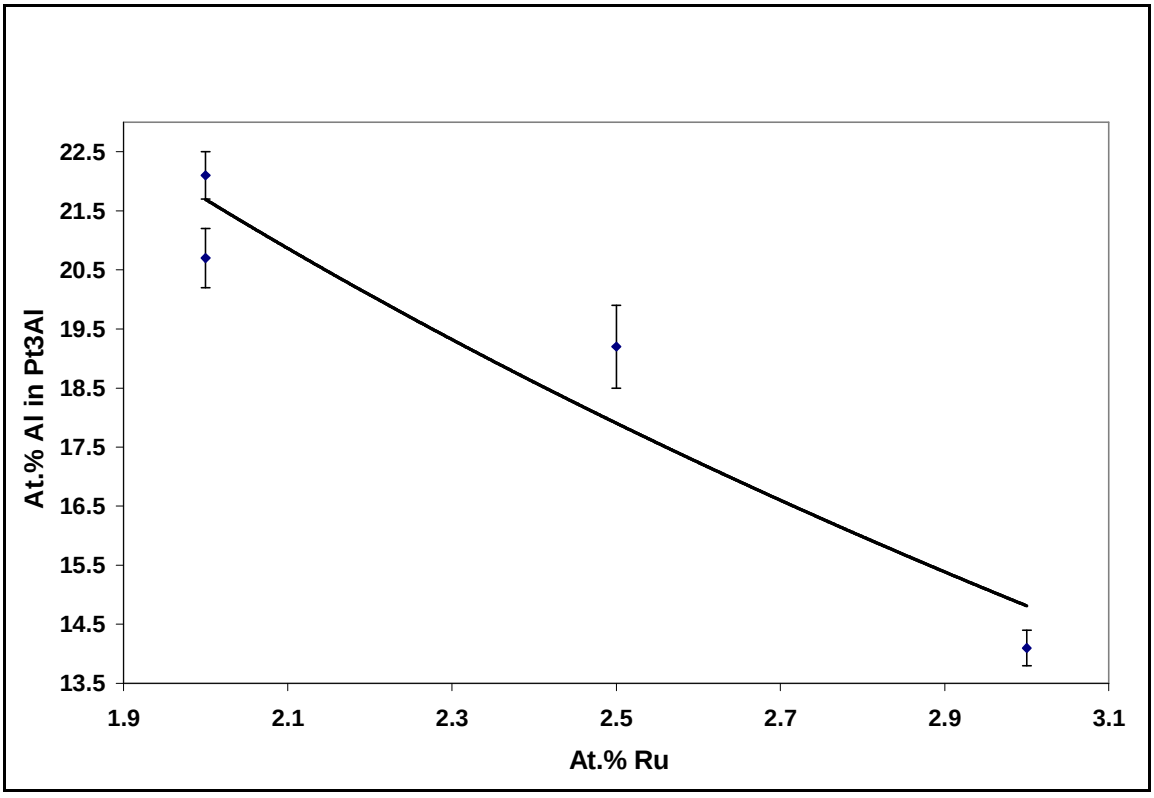

Figure 5.2. Solubility of Al in ~Pt_3Al with Ru additions (first batch).

5.1.3 Mechanical Properties

The Pt_{85}:Al_7:Ru_3:Cr_5 alloy had a planar slip mode which was different from the other five as-cast samples (which had wavy slip), probably due to its low hardness relative to the rest of the alloys. Barrelling was observed in five samples, except Pt_{85}:Al_7:Ru_3:Cr_5 with pincushioning and according to Chaudhri and Winter [1988Cha] when the sample is fully annealed, generally there is no barrelling (pile-up), but the surface of the indentation sinks in (pincushioning). For all the as-cast samples, the hardness increased with increasing eutectic proportion (Figure 5.3), although there was much scatter. Figure 5.4 shows a comparison of hardnesses for as-cast and heat treated samples. The hardness increased with decreasing Pt content, which would be expected since Pt is softer, and more Al gives more ~Pt_3Al precipitates. Pt_{78}:$Al_{15.5}$:Ru_2:$Cr_{4.5}$ had the largest decrease of about 290 HV_{10} after heat treatment and the decrease is thought to be due to very few precipitates and changes in composition. Three samples (Pt_{82}:Al_{12}:Ru_2:Cr_4, Pt_{84}:Al_{11}:Ru_2:Cr_3 and Pt_{85}:Al_7:Ru_3:Cr_5) increased in hardness compared to the heat treated samples (Tables 5.2 and 5.3). All heat treated samples had wavy slip. The hardness values for all samples were lower than those found by Cornish *et al.* [2002Cor], and a comparison of Pt_{84}:Al_{11}:Ru_2:Cr_3 with the same composition as that investigated by Cornish *et al.* [2002Cor] show differences in the microstructure. Pt_{84}:Al_{11}:Ru_2:Cr_3 for this investigation had coarser precipitates and a lower volume fraction of ~Pt_3Al (12 ± 5%) while for Cornish *et al.* [2002Cor] the precipitates where finer with a higher volume fraction (25 – 30%). The differences in microstructure are thought to be due to the different heat treatments and slight changes in composition that occurred after melting. A two-step heat treatment in air was carried out in this investigation for 18 hours at 1500°C and with quenching in water, followed by 1100°C for 120 hours and air cooling. On the other hand, Cornish *et al.* [2002Cor] conducted a single step heat treatment at 1350°C in argon for 96 hours followed by air cooling. It is likely that the Ar atmosphere protected the specimens against loss, especially given that the German researchers also used an argon atmosphere [2004Vor, 2005Wen, 2005Völ].

The four alloys (Pt_{81}:$Al_{11.5}$:$Ru_{2.5}$:$Cr_{4.5}$, Pt_{82}:Al_{12}:Ru_2:Cr_4, Pt_{84}:Al_{11}:Ru_2:Cr_3 and Pt_{85}:Al_7:Ru_3:Cr_5) with a high volume fraction of ~Pt_3Al precipitates had the highest hardness values compared to the two samples with very fine precipitates which were difficult to discern. Considering the precipitate volume fractions, given that ~Pt_3Al is harder than (Pt), it would be expected that higher precipitate volume fractions would give higher hardnesses. Figure 5.5 shows that the hardness increases with increasing precipitate volume fraction,

although there was much scatter. Pt_{85}:Al_7:Ru_3:Cr_5 is promising with its hardness, as one of the objectives is to improve the hardness of the quaternary and also had minor wavy slip, an indication that the alloy has good toughness.

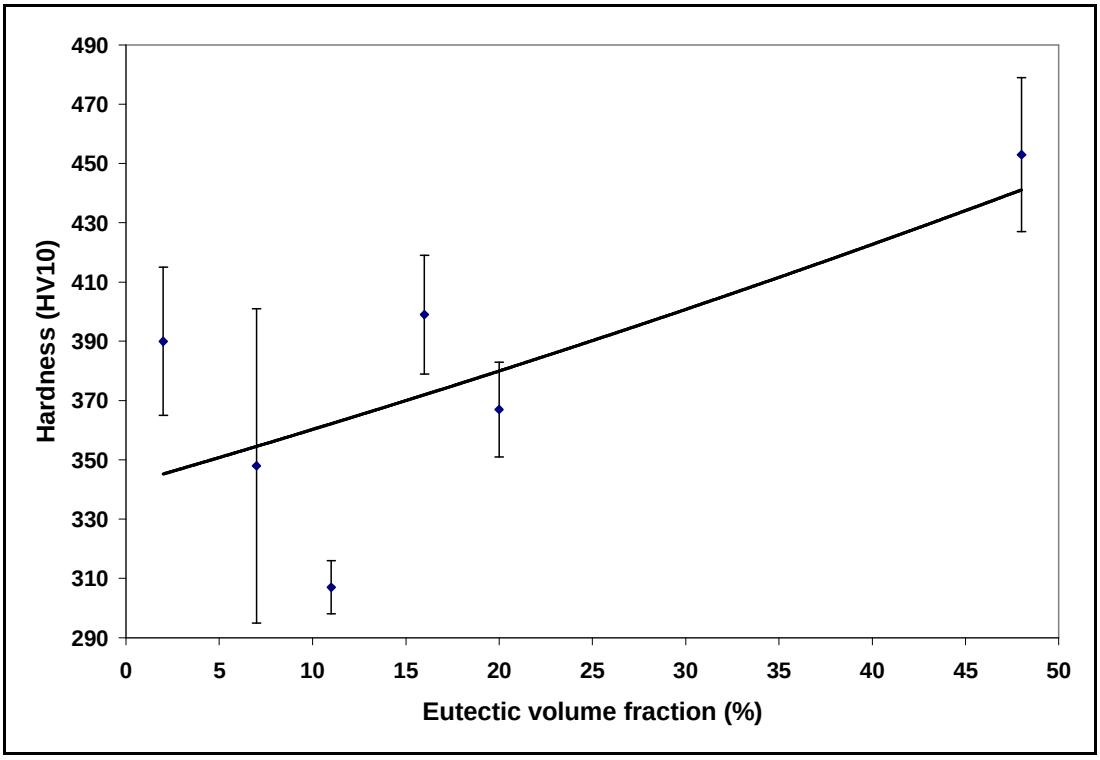

Figure 5.3. Relationship between hardness and eutectic volume fraction (first batch).

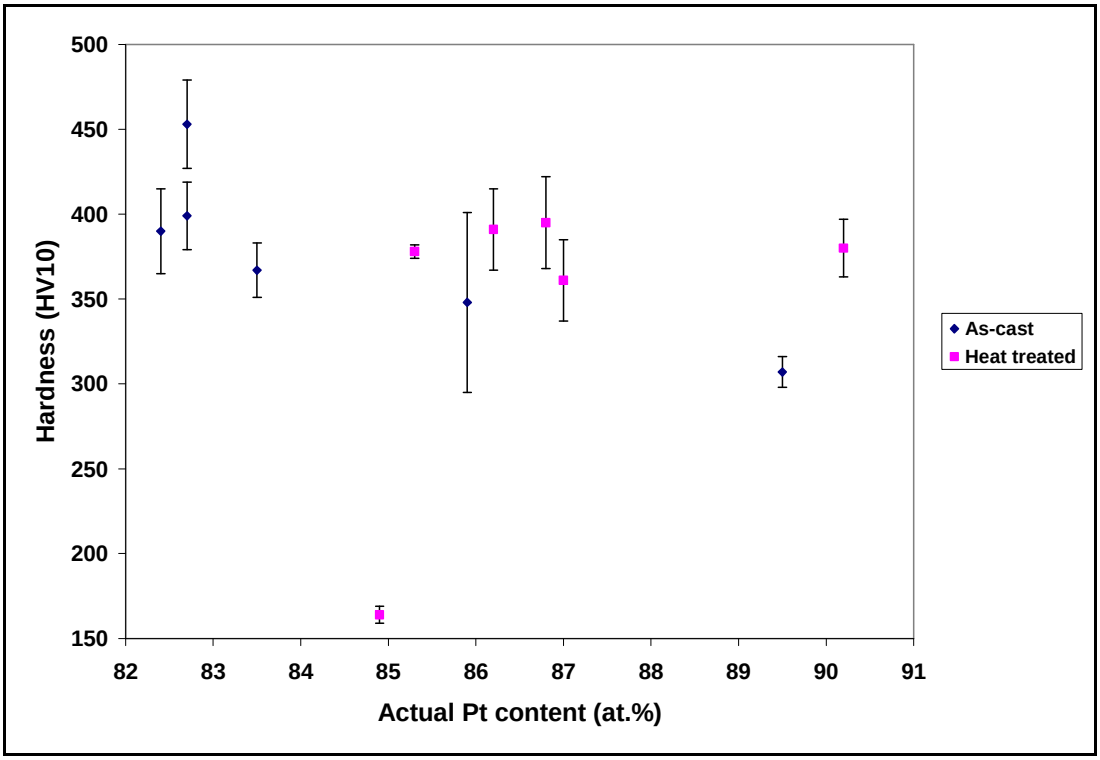

Figure 5.4. Comparison of hardnesses for as-cast and heat treated samples (first batch).

Table 5.2. Summary of microstructure, hardness and slip mode for the first batch of as-cast samples.

Nominal alloy (at.%)	Microstructure	Hardness (HV_{10})	Slip mode
$Pt_{78}:Al_{15.5}:Ru_2:Cr_{4.5}$	(Pt) dendrites with ((Pt) + ~Pt_3Al)	453 ± 26	Wavy slip
$Pt_{80}:Al_{14}:Ru_3:Cr_3$	(Pt) dendrites with ((Pt) + ~Pt_3Al)	390 ± 25	Wavy slip
$Pt_{81}:Al_{11.5}:Ru_{2.5}:Cr_{4.5}$	(Pt) dendrites with ((Pt) + ~Pt_3Al)	399 ± 20	Wavy slip
$Pt_{82}:Al_{12}:Ru_2:Cr_4$	(Pt) dendrites with ((Pt) + ~Pt_3Al)	367 ± 16	Wavy slip
$Pt_{84}:Al_{11}:Ru_2:Cr_3$	(Pt) dendrites with ((Pt) + ~Pt_3Al)	348 ± 53	Wavy slip
$Pt_{85}:Al_7:Ru_3:Cr_5$	(Pt) dendrites with ((Pt) + ~Pt_3Al)	307 ± 9	Planar slip

Table 5.3. Summary of microstructure, hardness and slip mode for the first batch of heat treated samples.

Nominal alloy (at.%)	Microstructure	Hardness (HV_{10})	Slip mode
$Pt_{78}:Al_{15.5}:Ru_2:Cr_{4.5}$	Very fine~Pt_3Al in (Pt) matrix	164 ± 5	Planar slip
$Pt_{80}:Al_{14}:Ru_3:Cr_3$	Very fine ~Pt_3Al in (Pt) matrix	361 ± 24	Wavy slip
$Pt_{81}:Al_{11.5}:Ru_{2.5}:Cr_{4.5}$	Fine ~Pt_3Al in (Pt) matrix	391 ± 24	Wavy slip
$Pt_{82}:Al_{12}:Ru_2:Cr_4$	Fine ~Pt_3Al in (Pt) matrix	378 ± 4	Wavy slip
$Pt_{84}:Al_{11}:Ru_2:Cr_3$	Fine ~Pt_3Al in (Pt) matrix	395 ± 27	Wavy slip
$Pt_{85}:Al_7:Ru_3:Cr_5$	Fine ~Pt_3Al in (Pt) matrix	380 ± 17	Planar slip

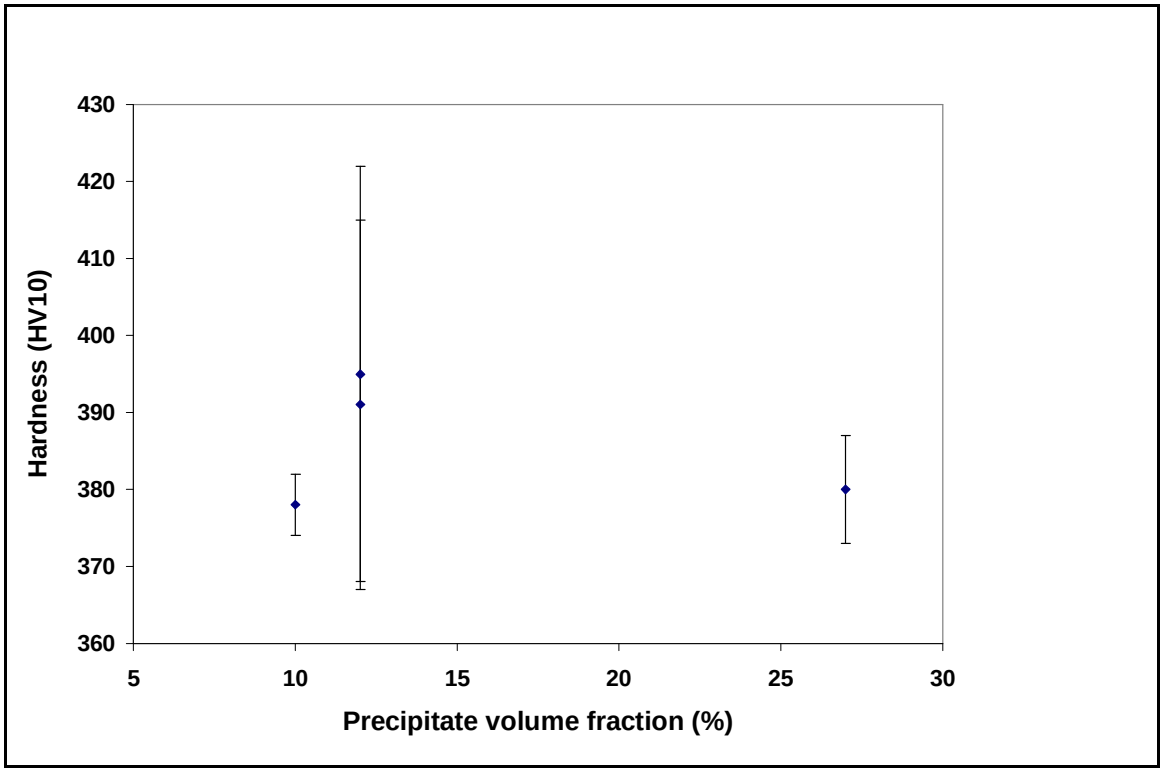

Figure 5.5. Relationship between hardness and precipitate volume fraction (first batch).

5.2 Second Batch of Samples

5.2.1 As-cast samples

The second batch of the as-cast samples was similar to the first batch, although coring was more prevalent, and all samples were homogenous. In all samples, the proportion of the dendrites was higher than the eutectic phase. XRD confirmed the presence of (Pt) and DO'_c - ~Pt_3Al. The XRD spectra of the second batch had low counts and high background. It is known that [URLXRD] low counts and high background in XRD spectra can occur with large grain sizes.

The overall compositions of the as-cast samples varied slightly from the targeted compositions. The partitioning of elements in the dendrites and eutectic was similar to that observed in the first batch of samples. The solubility range of Al was 17 to 19 at.% in the eutectic while it was 3 to 8 at.% Al for the (Pt) dendrites. Ruthenium and Cr had limited solubility in the ((Pt) + ~Pt_3Al) eutectic, and partitioned preferentially to the (Pt). The solubility range of Ru and Cr were 0.2 to 0.3 at.% Ru and 1.0 to 2.5 at.% Cr for the eutectic, while it was between 1.0 to 7.0 at.% Ru and 3.0 to 7.0 at.% Cr for the (Pt) phase. For all

samples, the darker inner part of the dendrites had a high solubility of Ru compared to the lighter outer part, while the solubility of Cr was comparable for both regions.

5.2.2 Heat Treated Samples

The heat treated samples were fairly homogeneous and comprised ~Pt_3Al precipitates in a (Pt) matrix, except Pt_{80}:Al_{11}:Ru_5:Cr_4 where the precipitates were too fine to be clearly seen, and the sample preparation was poor, which made resolution of the precipitates difficult. The Pt_{80}:Al_{11}:Ru_3:Cr_6 and Pt_{80}:Al_{11}:Ru_6:Cr_3 alloys were also fairly difficult to discern compared to the 78 at.% Pt series. XRD confirmed the presence of tetragonal ~Pt_3Al for all samples. Sub-grains were observed, and precipitates formed on both grain boundaries and sub-grain boundaries. The morphology of the majority of the precipitates was rounded, in agreement to the results of Wenderoth *et al.* [2005Wen, 2004Vor], although a few cubic precipitates were observed in some samples. Pt_{80}:Al_{11}:Ru_6:Cr_3 had like Maltese crosses precipitates similar to the findings of Süss *et al.* [2006Süs]. In a study by Somekawa, Singh and Mukai [2007Som] on the effect of precipitate shapes on fracture toughness, spherical shaped precipitates were found to be more effective than a cross network of rod shaped precipitates for improving the fracture toughness in magnesium alloys. Although the study was in a magnesium alloy and with a network of cross shaped rod precipitates, it is thought that cross-like shaped precipitates may reduce the fracture toughness of the Pt-Al-Ru-Cr alloy. The average precipitate size was about 1.2 µm approximatetly two times the precipitate sizes found by Hüller and Wenderoth [2005Hül, 2005Wen].

Comparison of the precipitate volume fractions shows that they increased with decreasing (Pt) content, contrary to the results obtained in the first batch of alloys. The contrary behaviour may be due to the content and ratio of Ru:Cr, since the first batch of alloys had low contents of Ru and Cr. The highest volume fractions were from the higher Cr content alloys, and the 78 at.% series had comparably higher volume fractions than the 80 at.% Pt alloys (Table 5.4). Consequently, 6 at.% Cr is possibly the optimum required to obtain a high volume fraction of precipitates (Figure 5.6 and Table 5.4). A further comparison of these alloys (Pt_{78}:Al_{11}:Ru_5:Cr_6 and Pt_{80}:Al_{11}:Ru_3:Cr_6) shows that a decrease in Pt and an increase in Ru resulted in a higher volume fraction of precipitates (Figure 5.7 and Table 5.4). In the first batch of alloys, Pt_{85}:Al_7:Ru_3:Cr_5 had the highest volume fraction of precipitates and the Cr content is close to 6 at.% Cr. Comparing the three alloys (Pt_{78}:Al_{11}:Ru_5:Cr_6 and

Pt_{80}:Al_{11}:Ru_3:$Cr_6$and Pt_{85}:Al_7:Ru_3:Cr_5) indicates that the optimum Ru content is possibly close to 3 at.%. Similar to the first batch of samples, the proportion of the ~Pt_3Al volume fraction was similar to the results of Huller *et al.* [2005Hül] and those found at Mintek by Cornish *et al.* [2002Cor].

The partitioning behaviour of the elements was similar to the first batch of alloys. The solubility range of Al was 18.9 at.% to 22 at.% Al for the ~Pt_3Al precipitates, and 9 to 10.3 at.% Al for the (Pt) phase. Ru and Cr were found to have solubility ranges of 0.4 to 0.8 at.% Ru and 2.1 to 2.8 at.% Cr for the precipitates, while for the (Pt) phase it was between 1.9 to 2.9 at.% Ru and 4.1 to 6.0 at.% Cr. It was observed for both sets of alloys (80 at.% and 78 at.% Pt) that the solubility of Al in ~Pt_3Al was the highest at 5 at.% Ru. Similar to the first batch of samples, the solubility of Al in ~Pt_3Al decreased with Ru and Cr additions (Figures 5.8 and 5.9).

Table 5.4. Summary of overall EDX compositions (at.%) and approximate ~Pt_3Al volume fractions (%) for second batch of heat treated samples.

Nominal alloy (at.%)	Actual compositions (at.%)				Approximate ~Pt_3Al volume fraction (%)
	Pt	Al	Ru	Cr	
Pt_{80}:Al_{11}:Ru_5:Cr_4	84.1	8.9	3.9	3.1	~Pt_3Al indiscernible
Pt_{80}:Al_{11}:Ru_3:Cr_6	83.9	8.5	2.9	4.7	10 ± 5
Pt_{80}:Al_{11}:Ru_6:Cr_3	83.8	7.8	4.8	3.6	6 ± 4
Pt_{78}:Al_{11}:Ru_5:Cr_6	81.4	9.2	3.4	6.0	24 ± 3
Pt_{78}:Al_{11}:Ru_3:Cr_8	82.5	8.0	2.2	7.1	20 ± 3
Pt_{78}:Al_{11}:Ru_8:Cr_3	81.9	8.7	6.6	2.9	10 ± 5

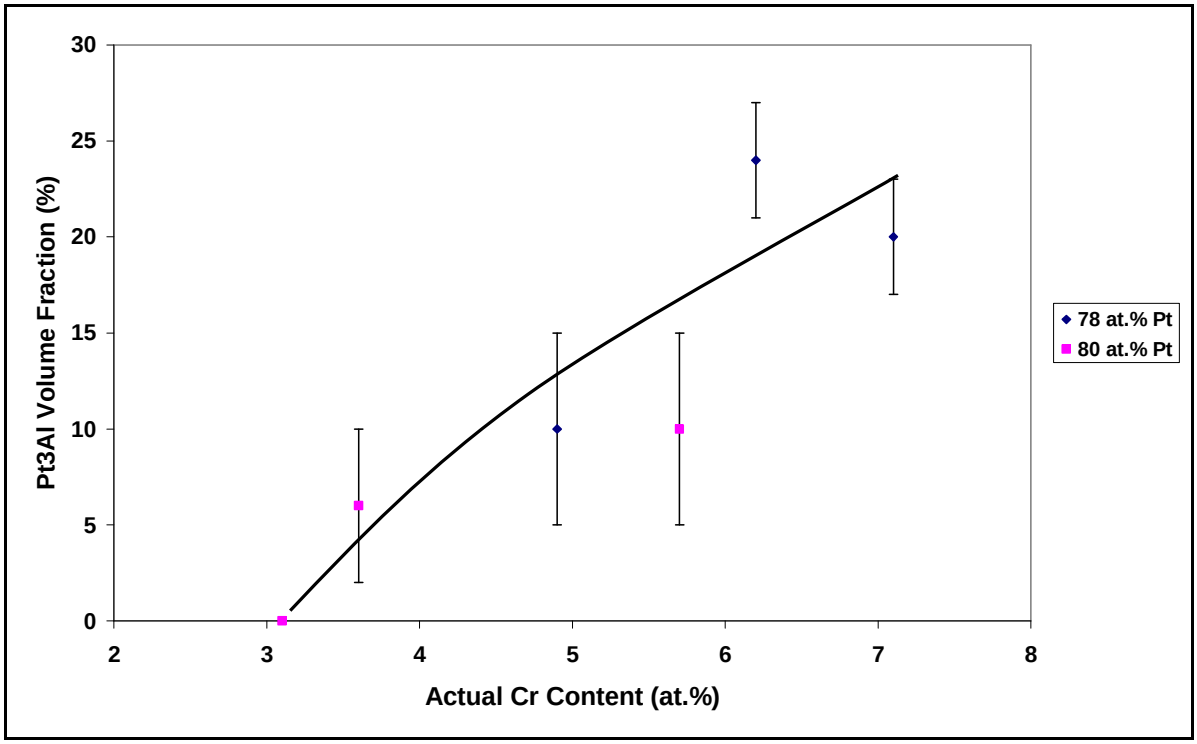

Figure 5.6. Relationship between ~Pt_3Al volume fraction and Cr content (second batch).

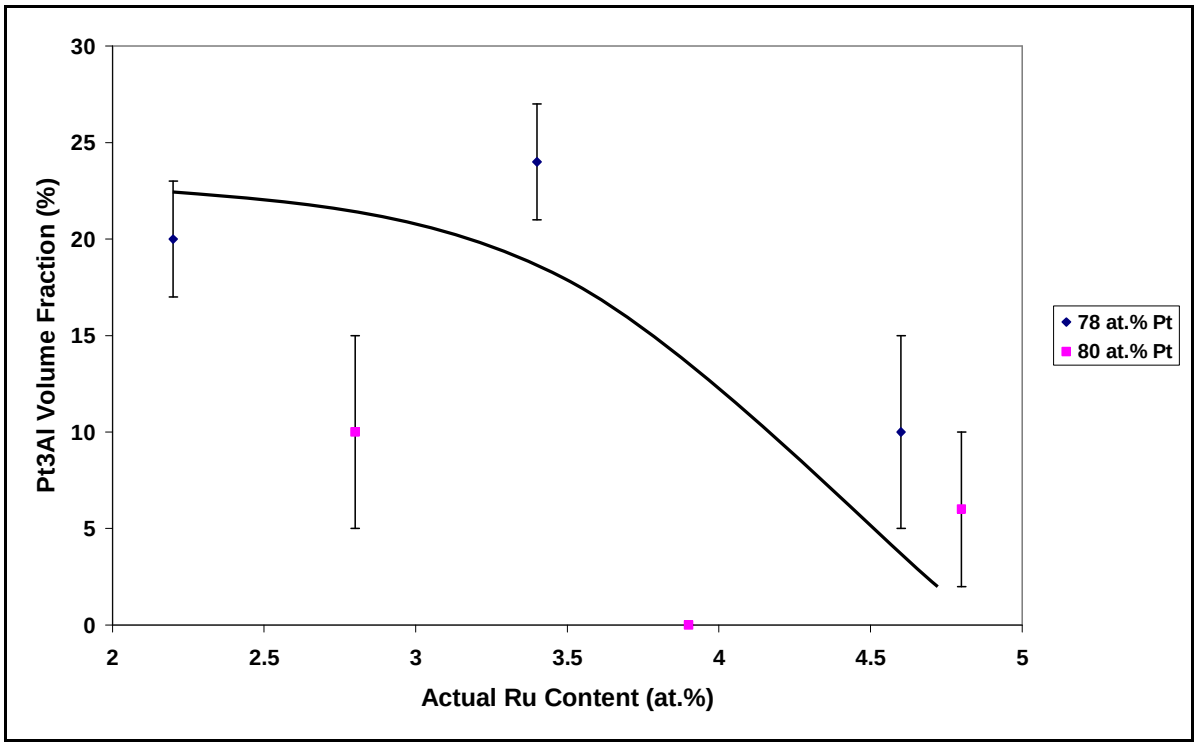

Figure 5.7. Relationship between ~Pt_3Al volume fraction and Ru content (second batch).

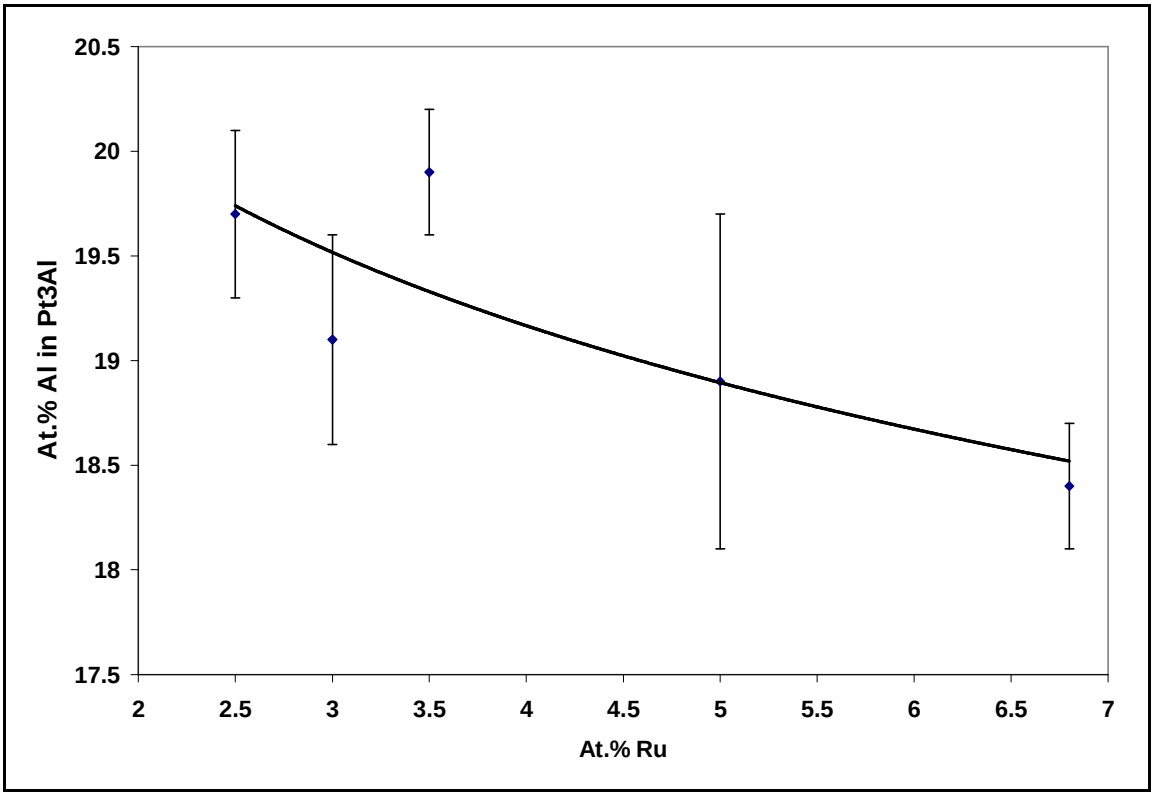

Figure 5.8. Solubility of Al in ~Pt_3Al with Ru additions (second batch).

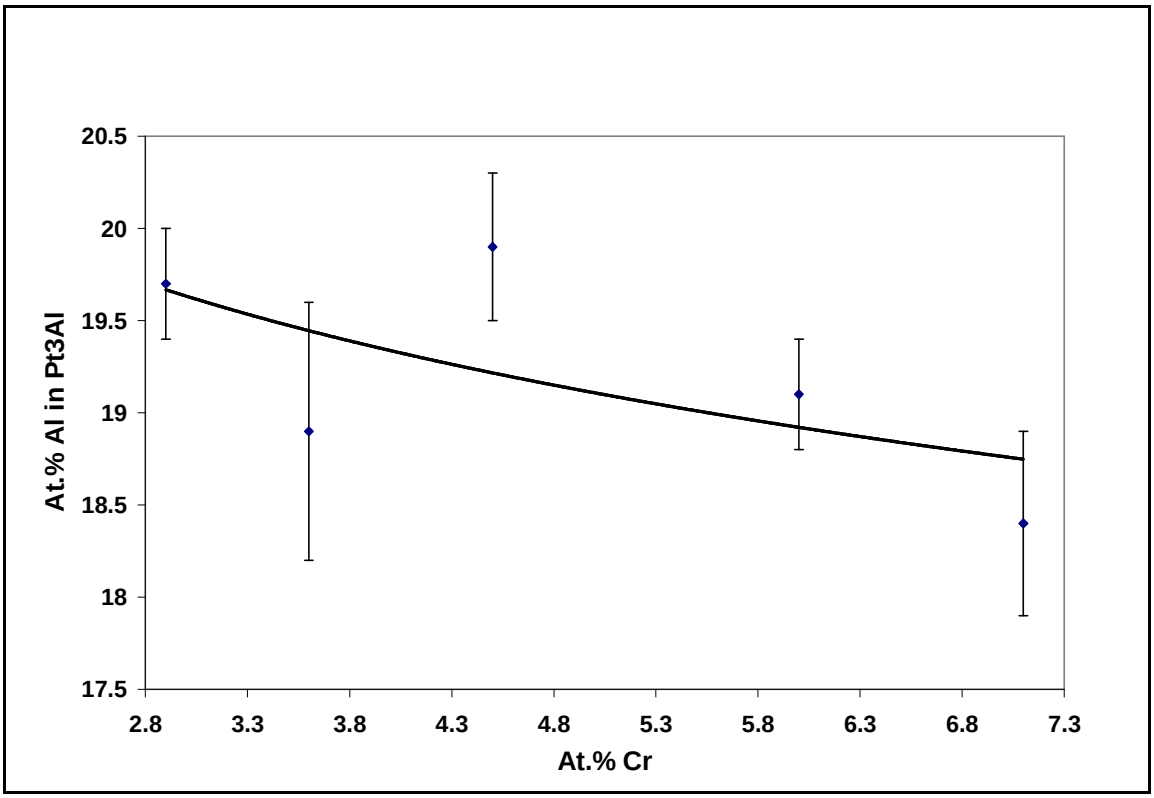

Figure 5.9. Solubility of Al in ~Pt_3Al with Cr additions (second batch).

5.2.3 Mechanical Properties

Pt_{80}:Al_{11}:Ru_3:Cr_6 had the lowest hardness of the as-cast samples (Table 4.52). The hardness increased with increasing eutectic content (Figure 5.10), although there was scatter. There was no clear relationship between the Ru and Cr contents with the hardnesses of the alloys. However, it was noticed for both sets of alloys (80 and 78 at.% Pt) that the highest hardnesses were obtained for the alloys with the lowest Cr contents (Pt_{80}:Al_{11}:Ru_5:Cr_4, Pt_{80}:Al_{11}:Ru_6:Cr_3 and Pt_{78}:Al_{11}:Ru_8:Cr_3).

All alloys in the heat treated condition had lower hardness than the as-cast samples (Table 4.52). Similar to the first batch of samples, the hardness values for all samples were lower than those found by Cornish *et al.* [2002Cor] for the same quartenary, but for slightly different compostions. There was no correlation of hardness with precipitate alignment (one alloy had a high hardness (396 ± 17 HV_{10}), whereas another had a low hardness (226 ± 9 HV_{10}). According to Bhadeshia [2003Bha], the nickel-based superalloys precipitates are aligned, positively affecting the alloys properties in contrast to results of this investigation. Pt_{80}:Al_{11}:Ru_6:Cr_3, where cubic precipitates were observed, gave a relatively low hardness. The 80 at.% Pt samples had lower hardness than the 78 at.% Pt samples (Tables 5.2 and 5.3). However, the difference in hardness of the as-cast and heat treated samples of 80 at.% Pt was less compared to the 78 at.% Pt samples. Figure 5.11 shows that the heat treated samples' hardness decreases with increasing Pt content and showed a peak at about 82 % Pt, while for the as-cast samples no clear relationship could be deduced. The hardness was found to be low at low precipitate volume fraction and gave a maximum at about 11 % ~Pt_3Al and decreased slightly afterwards, and so looked more like a 'shelf' (Figure 5.12). In both conditions, Pt_{78}:Al_{11}:Ru_8:Cr_3 was found to be the alloy with the highest hardness values, as well as the lowest Cr content and highest Ru content. Wavy slip was observed for all as-cast alloys, whereas all heat treated alloys had planar slip. No relationship could be deduced between the slip modes and hardnesses of the alloys. Pt_{78}:Al_{11}:Ru_5:Cr_6 has the highest hardness and precipitate volume fraction. Consequently, Pt_{78}:Al_{11}:Ru_5:Cr_6 is the promising alloy in the second batch of samples.

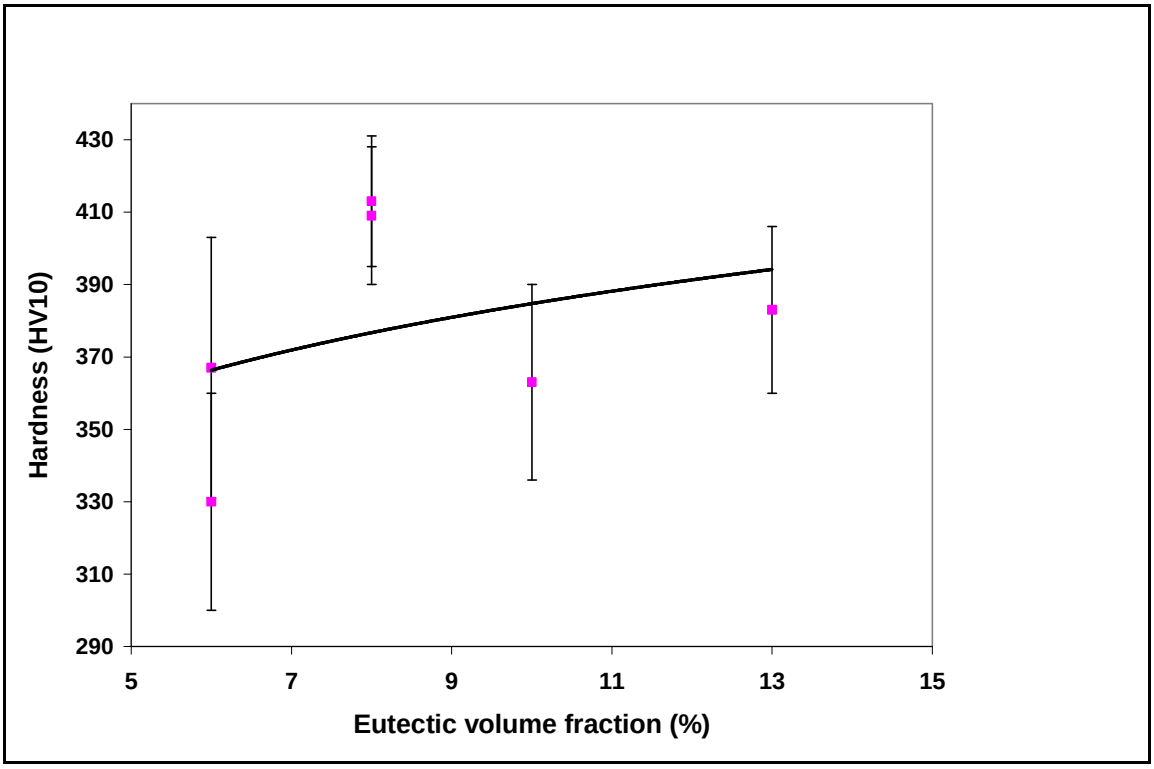

Figure 5.10. Relationship between hardness and eutectic volume fraction (second batch).

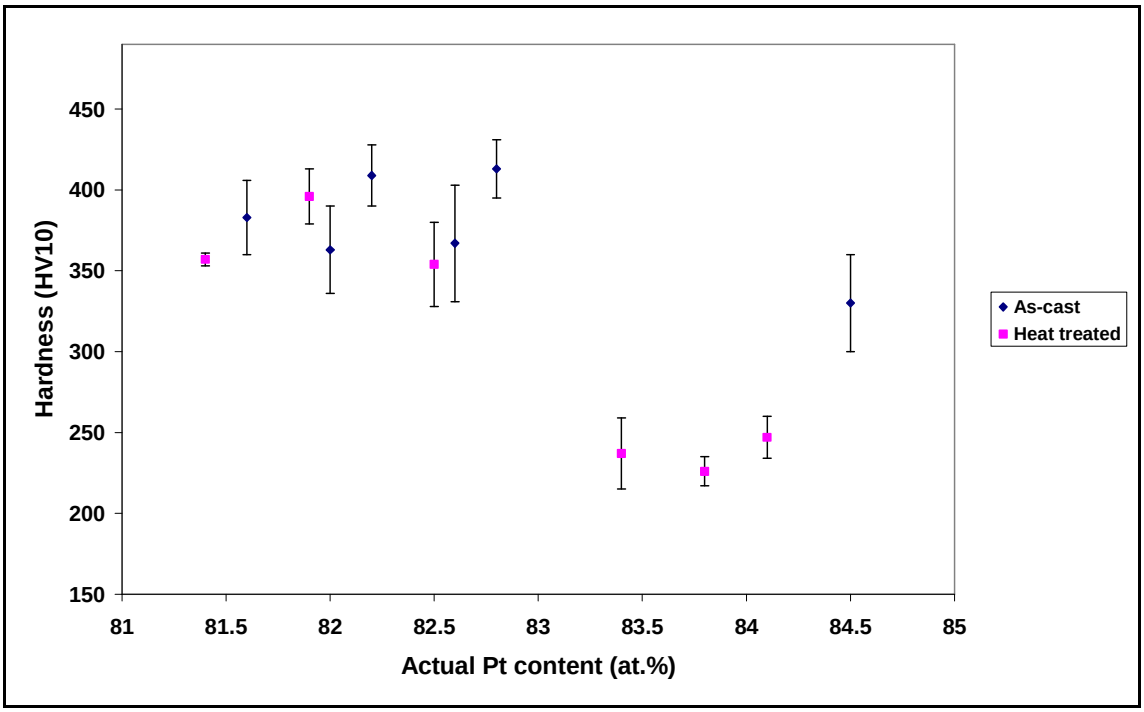

Figure 5.11. Comparison of hardnesses and Pt content for as-cast and heat treated samples (second batch).

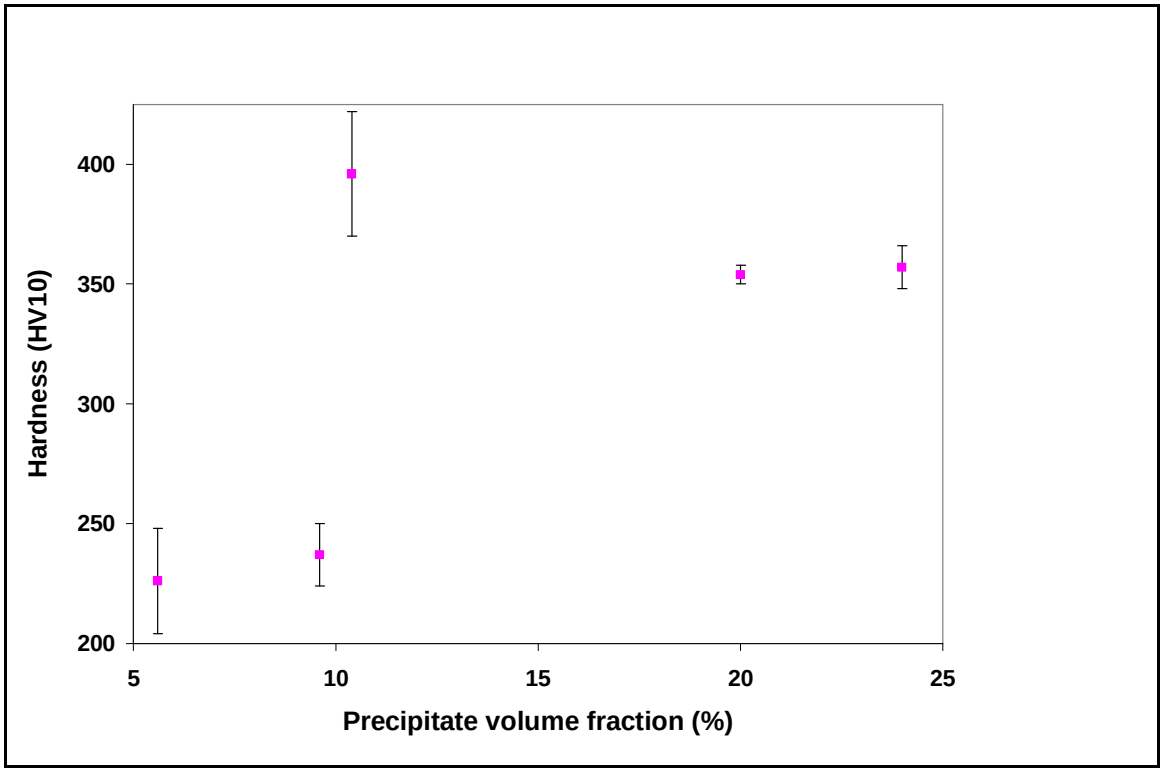

Figure 5.12. Relationship between ~Pt_3Al volume fraction and Ru content (second batch).

5.3 Combined Results for First and Second Batch of Samples

The results for the first and second batch were combined to have more points on the graphs in oder to have better conclusions on the relationships of the different parameters. For all the as-cast samples, the hardness increased with increasing eutectic amount (Figure 5.13), although with much scatter. No relationship between hardness and dendrite arm spacing was observed (Figure 5.14), although an inverse relationship might have been expected. For all of the heat treated samples, the hardness decreased with larger precipitates (Figure 5.15). The samples which had precipitates that were difficult to discern (although precipitates were present according to XRD) had either a very low hardness (164 ± 5 for Pt_{78}:$Al_{15.5}$:Ru_2:$Cr_{4.5}$) or a relatively low hardness (361± 24 for Pt_{80}:Al_{14}:Ru_3:Cr_3). The plots for each batch for hardness against precipitate volume fraction did not give a clear relationship. However, the combined plots for both batches showed that the hardness increased with increasing precipitate volume fraction (Figure 5.16). Aside from one outlier, the solubility of Al in ~Pt_3Al obviously decreased with increasing Ru and Cr additions (Figures 5.17 and 5.18). The hardness showed a slight decrease with increasing platinum content (Figure 5.19). From the first batch of samples Pt_{78}:$Al_{15.5}$:Ru_2:$Cr_{4.5}$ suffered a large reduction in hardness after heat treatment and in

terms of microstructure the decrease is due to fewer precipitates, especially since the Al content had decreased. For the second batch of samples, the 80 at.% Pt specimens had a large reduction in hardness after heat treatment and comparison of their microstructure with the 78 at.% samples shows that the former had very few precipitates. This occurred because Al was lost during heat treatment, and less Al means fewer ~Pt_3Al precipitates. The Cr content also decreased causing an overall increase in the Pt content resulting in more of the (Pt) phase.

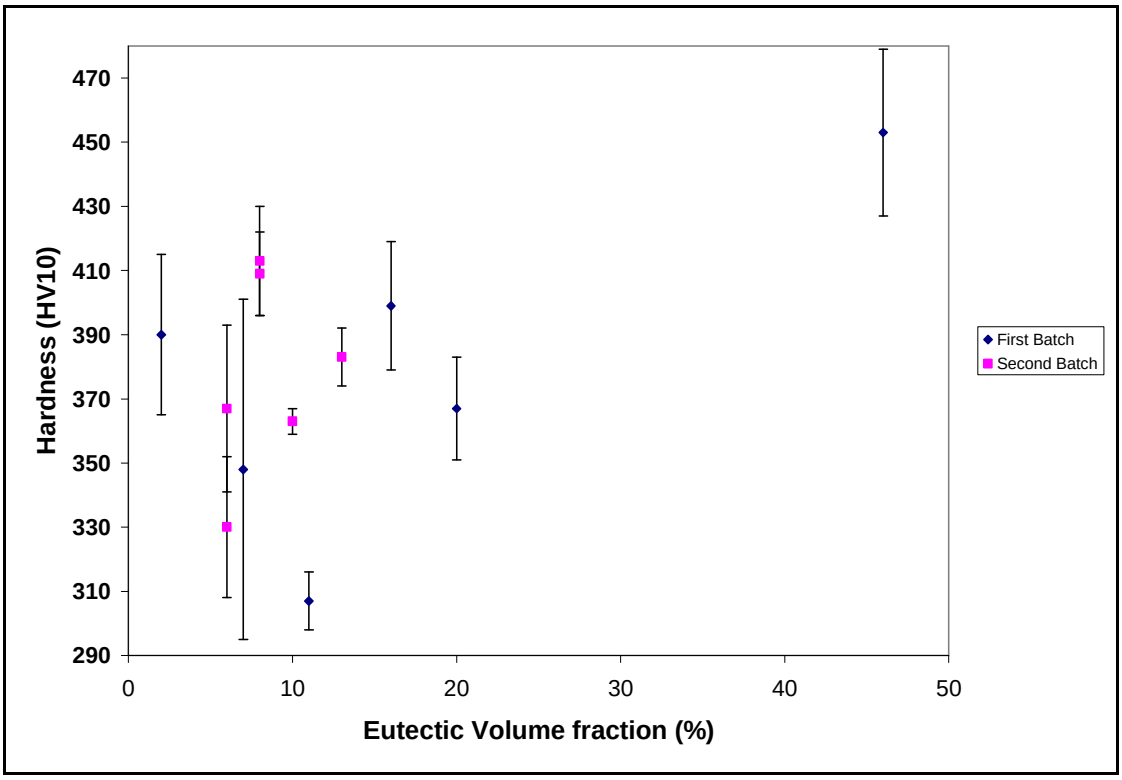

Figure 5.13. Relationship between hardness and eutectic volume fraction for all as-cast samples.

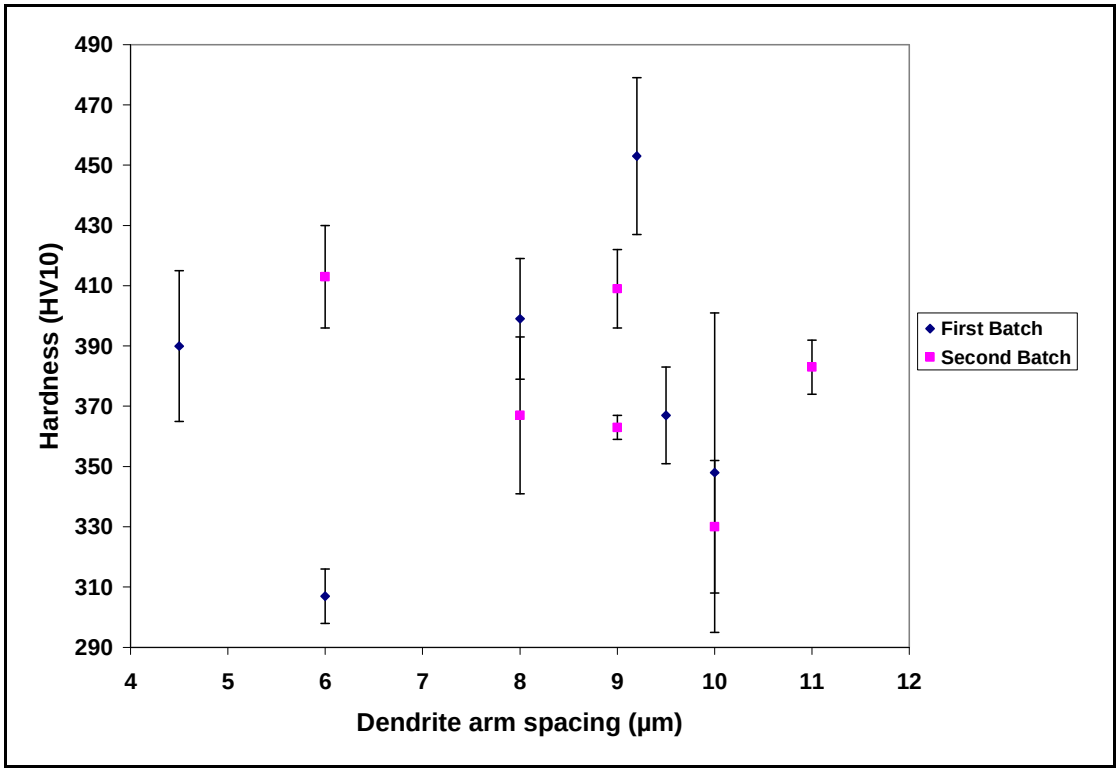

Figure 5.14. Relationship between hardness and dendrite arm spacing for all as-cast samples.

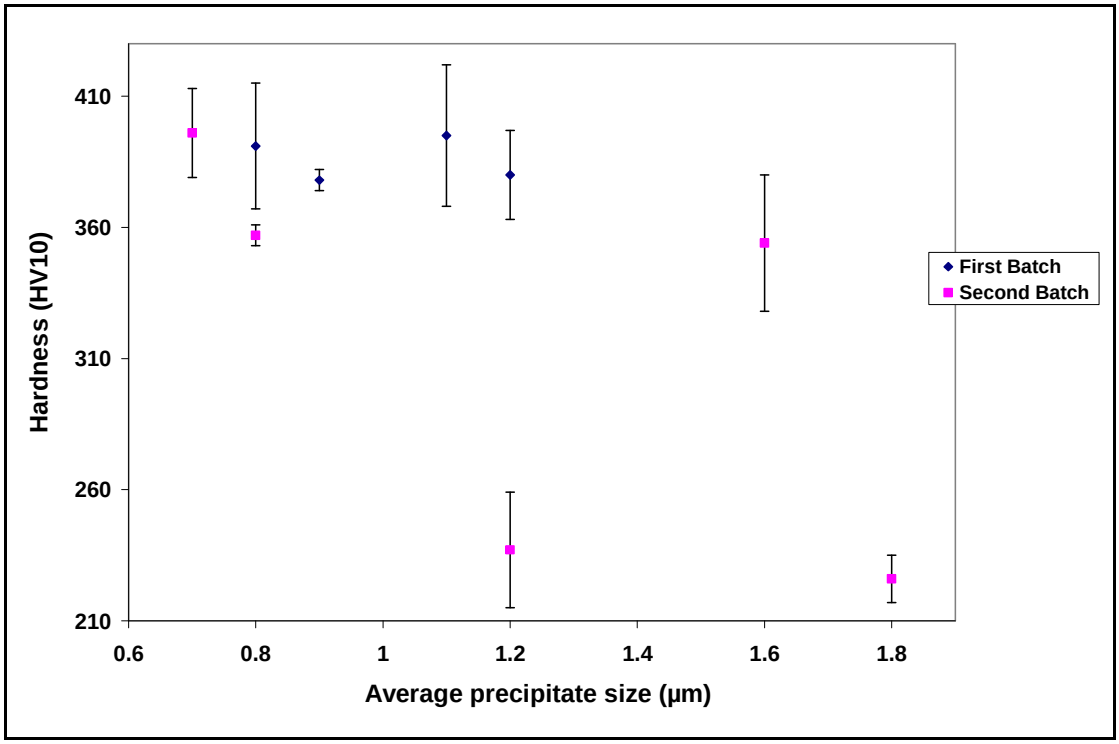

Figure 5.15. Relationship between hardness and precipitate size for all heat treated samples.

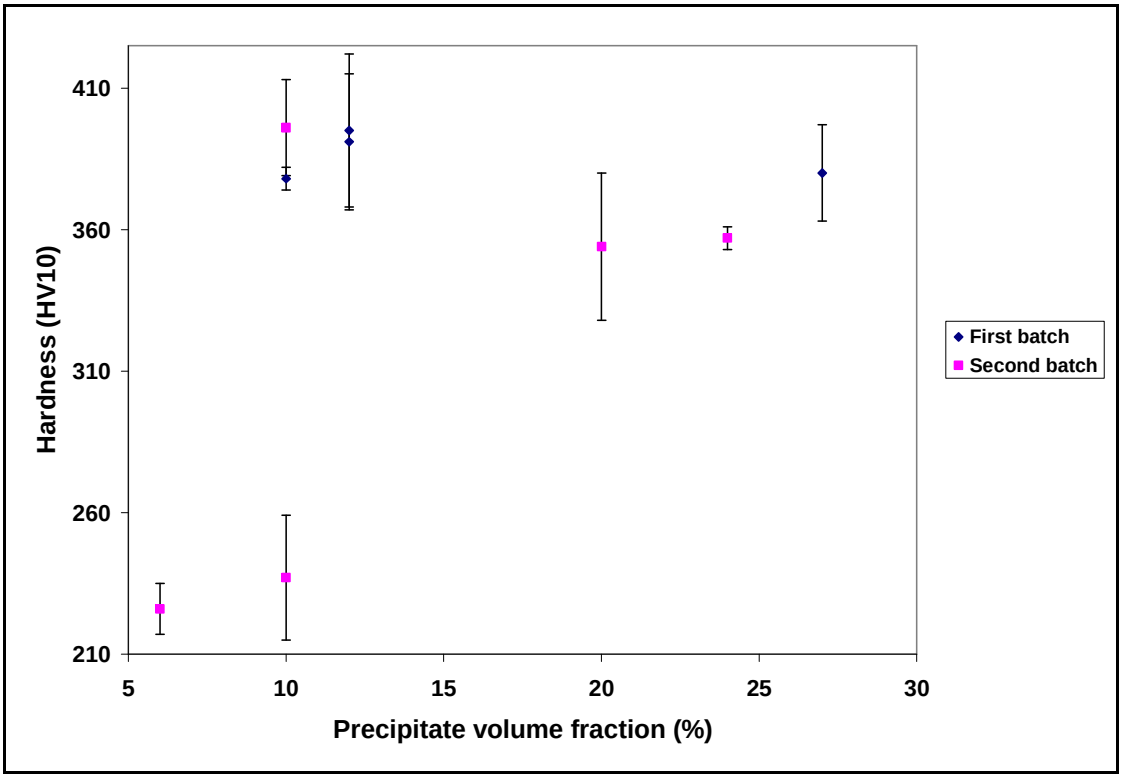

Figure 5.16. Relationship between hardness and precipitate volume fraction for all heat treated samples.

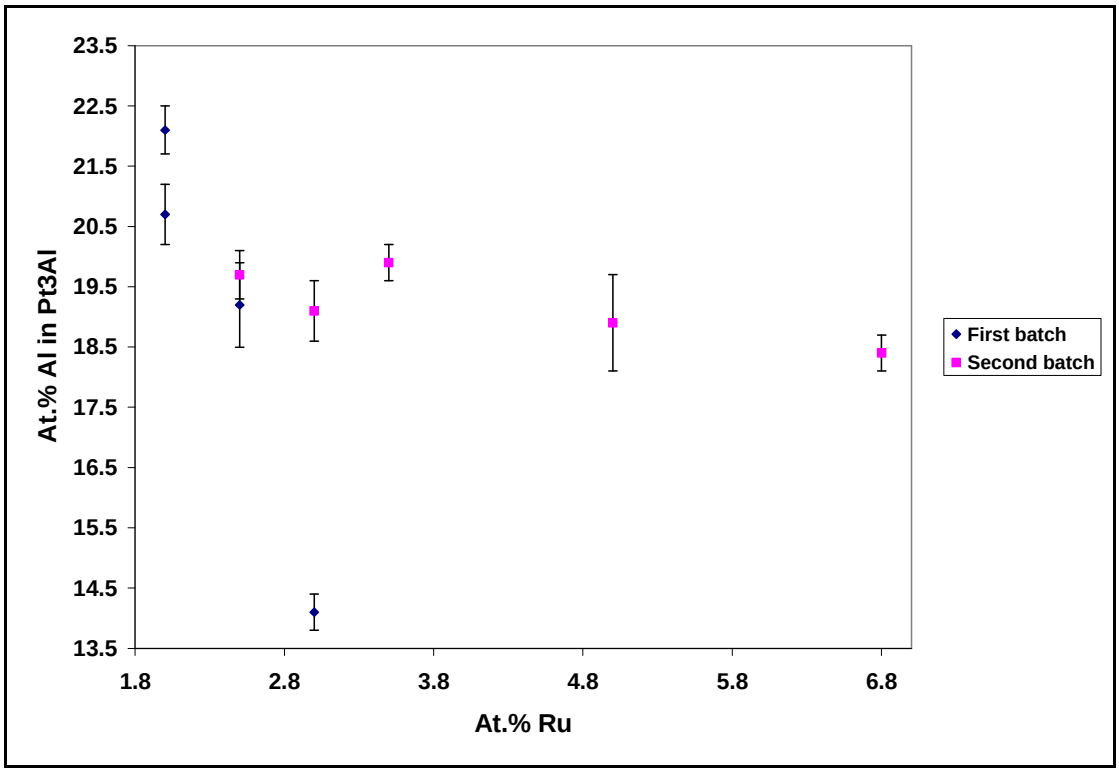

Figure 5.17. Solubility of Al in ~Pt_3Al with Ru additions for all heat treated samples.

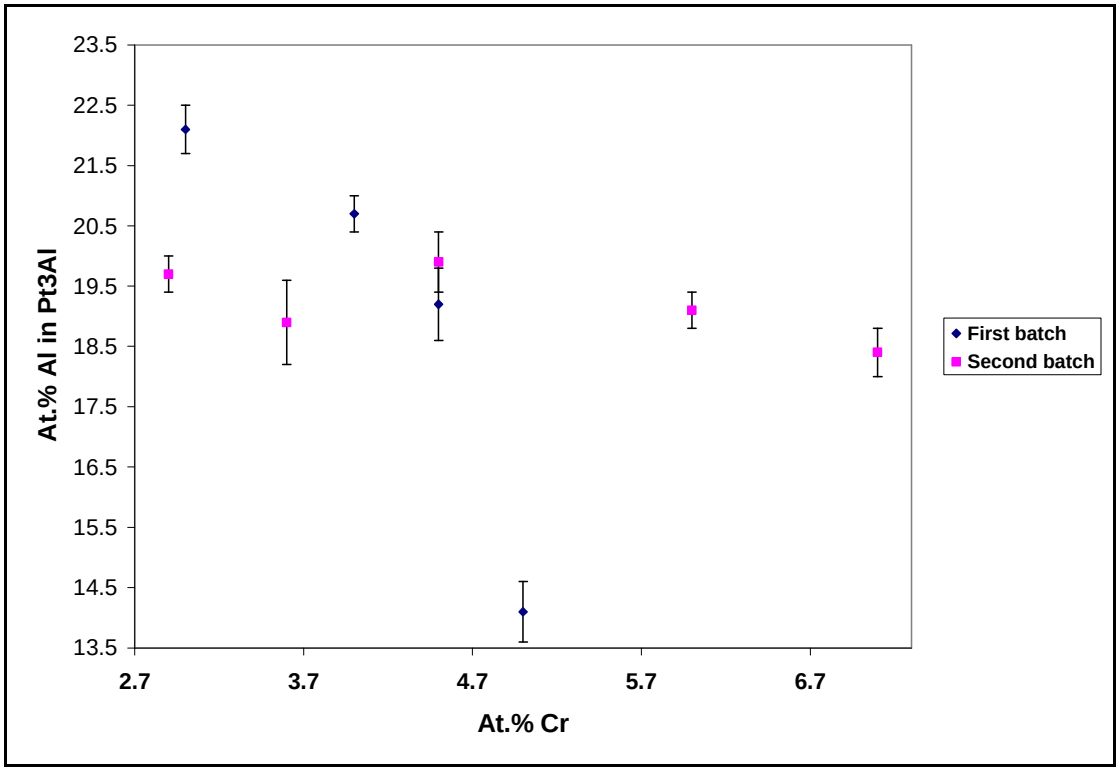

Figure 5.18. Solubility of Al in ~Pt_3Al with Ru additions for all heat treated samples.

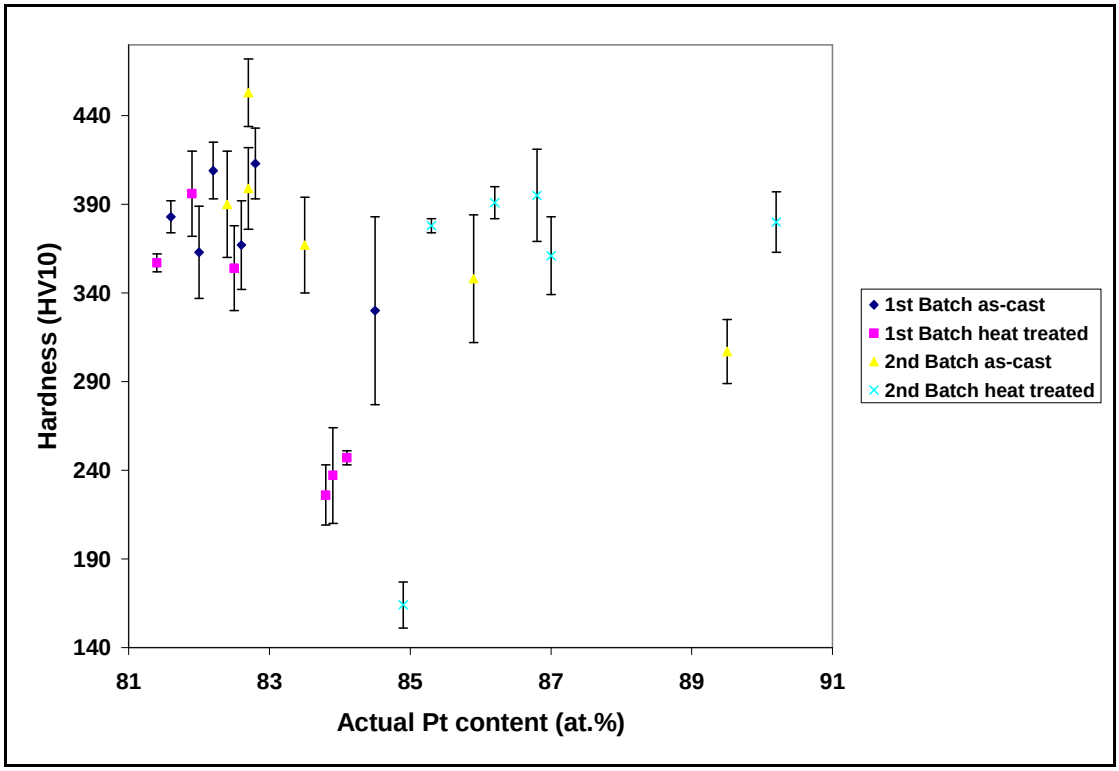

Figure 5.19. Relationship between hardness and actual platinum content for all samples.

5.4 Approximated Yield Strength

The yield strength was approximated using the hardness correlation, given in Equations 2 and 3 and is shown in Table 5.5. The yield strength for the as-cast and heat treated samples was between 700 - 1531 MPa and 582 – 1338 MPa respectively. Comparison of these results with those of Jena and Bayreuth University by Hüller *et al.* [2005Hül] and Wenderoth *et al.* [2005Wen] (Table 5.6) shows that the difference is small for most of the alloys. The errors for the other authors' results were not quoted, and where possible, they were calculated. The heat treated Pt_{78}:Al_{11}:Ru_8:Cr_3 and Pt_{79}:Al_{10}:Cr_3:Ni_8 alloys had similar yield strengths and comparable Pt and Al contents. Although the the maximum precipitate volume fraction in this investigation was still low compared to the 50% of Vorberg *et al.* [2004Vor], the mechanical properties are promising. It should be highlighted that the samples did not undergo the same heat treatment, hence differences in mechanical properties would be expected.

Table 5.5. Approximated yield strength, using hardness correlation.

	As-cast		Heat treated	
Alloy	**Hardness (HV_{10})**	**Yield Strength (MPa)**	**Hardness (HV_{10})**	**Yield Strength (MPa)**
Pt_{78}:$Al_{15.5}$:Ru_2:$Cr_{4.5}$	453 ± 26	1531 ± 92	164 ± 5	582 ± 18
Pt_{80}:Al_{14}:Ru_3:Cr_3	390 ± 25	1318 ± 89	361 ± 24	1220 ±85
$Pt_{81.5}$:$Al_{11.5}$:$Ru_{2.5}$:$Cr_{4.5}$	399 ± 20	1349 ±71	391 ± 24	1322 ± 85
Pt_{82}:Al_{12}:Ru_2:Cr_4	367 ± 16	1240 ± 57	378 ± 4	1278 ± 14
Pt_{84}:Al_{11}:Ru_2:Cr_3	348 ± 53	1176 ±188	395 ± 27	1335 ± 96
Pt_{85}:Al_7:Ru_3:Cr_5	307 ± 9	1038 ± 32	380 ± 17	1284 ± 60
Pt_{80}:Al_{11}:Ru_5:Cr_4	409 ± 19	1382 ± 67	247 ± 13	835 ± 46
Pt_{80}:Al_{11}:Ru_3:Cr_6	330 ± 30	1115 ± 107	237 ± 22	801 ± 78
Pt_{80}:Al_{11}:Ru_6:Cr_3	383 ± 23	1295 ± 82	226 ± 9	764 ± 32
Pt_{78}:Al_{11}:Ru_5:Cr_6	363 ± 27	1227 ± 96	357 ± 4	1207 ± 14
Pt_{78}:Al_{11}:Ru_3:Cr_8	367 ± 36	1240 ± 128	354 ± 26	1197 ± 92
Pt_{78}:Al_{11}:Ru_8:Cr_3	413 ± 18	1396 ± 64	396 ± 17	1338 ± 60

Table 5.6. Available yield strength data from Hüller *et al.* [2005Hül] and Wenderoth *et al.* [2005Wen] for heat treated samples.

Alloy	Yield Strength (MPa)
$Pt_{80}:Al_{11}:Cr_3:Ni_6$	1355
$Pt_{79}:Al_{10}:Cr_3:Ni_8$	1469
$Pt_{77}:Al_{10}:Cr_3:Ni_{10}$	1328
$Pt_{79}:Al_{14}:Cr_4:Ni_4$	1309
$Pt_{79}:Al_{14}:Cr_3:Ni_6$	1410
$Pt_{75}:Al_{14}:Cr_3:Ni_8$	1394

CHAPTER SIX

CONCLUSIONS AND RECOMMENDATIONS

From the first and second batch of samples, Pt_{85}:Al_7:Ru_3:Cr_5 and Pt_{78}:Al_{11}:Ru_5:Cr_6 had the highest volume fraction of ~Pt_3Al precipitates with 27 and 24 % respectively. XRD confirmed the presence of (Pt) and tetragonal ~Pt_3Al. The hardness of Pt_{85}:Al_7:Ru_3:Cr_5 was 380 ± 17 HV_{10} and 357 ± 4 HV_{10} for Pt_{78}:Al_{11}:Ru_5:Cr_6. Pt_{85}:Al_7:Ru_3:Cr_5 appears to be the optimum alloy with a high volume fraction of precipitates and reasonable hardness. However, the differences in hardnesses of Pt_{85}:Al_7:Ru_3:Cr_5 and Pt_{78}:Al_{11}:Ru_5:Cr_6 is 23 HV_{10} together with a very small difference in volume fraction of 3 % and so these alloys have similar properties. Thus, both alloys can be said to be optimum in terms of the volume fraction and hardnesses compared to the rest of the samples. From an economic viewpoint, Pt_{85}:Al_7:Ru_3:Cr_5 is unfavourable since it has a higher Pt content; and this alloy could suffer from oxidation because of low Al content. Thus, Pt_{78}:Al_{11}:Ru_5:Cr_6 is promising from both microstructure and economics. Further investigation will therefore be recommended on compositions close to this alloy.

REFERENCES

[1958Wes] J.H. Westbrook, Precipitation of Ni_3Al from nickel solid solution as ogdoadically diced cubes, *Z. Kristallogr*, (1958), 110, 21-29.

[1962McL] D. McLean, Mechanical Properties of Metals, New York, J.Wiley, 1962.

[1968 Pie] B.J. Piercey, U.S. Patent 3, 5119, 063, (July 18, 1968).

[1970Ver] F.L. Ver Snyder and M.E. Shank, The Development of Columnar Grain and Single Crystal High Temperature materials through directional solidification, *Mat. Sci. Eng*. 6 (1970), 213-247.

[1972Sim] C.T. Sims and W.C. Hagel, in The Superalloys, John Wiley & Sons, Schenectady, New York, Cincinnati, Ohio, (1972).

[1973Joh] Johnson Matthey, GB, Patent Specification 1 340 076, (1973).

[1974Avn] S.H. Avner, Introduction to Physical Metallurgy, McGraw-Hill, Singapore (1974).

[1976Fel] E.J. Felten and F.S. Pettit, Development, Growth, and Adhesion of Al_2O_3 on Platinum-aluminium Alloys, *Oxid. Met*., (1976), 10, 3, 189.

[1980Wee] D.M. Wee, O. Noguchi, Y. Oya and T. Suzuki, *Trans. JIM*, (1980), 21, 237-240.

[1984Gia] A.F. Giamei, D.D. Pearson and D.L. Anton, High-Temperature Ordered Intermetallic Alloys, Boston (1984), 293-300.

[1986Mis] Y. Mishima, Y. Oya and T. Suzuki, Proceedings of the International Conference on Martensitic Transformations, *Japan Institute of Metals*, (1986), 1009–1014.

[1987Sim] C.T. Sims, N.S. Stoloff and W.C Hagel, in Supperalloys II: High temperature Materials for Aerospace and Industrial Power, Wiley Inter-Science, New York, (1987).

[1988Cha] M. Chaudhri and M. Winter, The Load-Bearing Area of a Hardness Indentation *J. Phys., D. Appl. Phys.*, 1988, 21, 370.

[1988Joh] Johnson Matthey, GB, Patent Specification DE 02 342 C2, (1988).

[1988Wha] M.V. Whalen, The Compatibility of Dispersion-Strengthened Platinum with Candidate Propellants, *Plat. Met. Rev*., 32, 1, (1988), 2-10.

[1990Lee] H.T. Lee and S.W. Lee, The Morphology and Formation of Gamma Prime in Nickel-base Superalloy, *J. Mat. Sci. Lett*., 9 (1990), 516-517.

[1990Lup] D. Lupton, *Adv. Mater*., 5, (1990), 29-30.

[1990Mas] T.B. Massalski, Binary Alloy Phase Diagrams, ASM International, (1990), Ohio, USA.

[1990Tho] F.A. Thompson, *Glass, 7,* (1990), 279-280.

[1992Bro] W.F. Brown, Jr. H. Mindin and C.Y. Ho, *Aerospace Structural Metals Handbook*, Cindas/Purdue University, (1992), 4218-4229.

[1993Raj] R. Raj, *J. Am, Ceram. Soc*, 76 (1993) 2147 – 2174.

[1994Gob] M. Gobel, A. Rahmel and M. Schultze, *Oxid. Met*., 41 (1994), 271 – 300.

[1994Nab] F.R.N. Nabarro, The Superiority of Superalloys, *Mater. Sci. Eng.*, (1994), A184, 167-171.

[1995Bel] N.A. Belov, Effect of Eutectic Phases on the Fracture Behaviour of High-Strength Castable Aluminium Alloys, *Metals Science and Heat Treatment, 37, (1995), 5-6, 237-242*.

[1995Eri] G.L. Erikson, *J. Metals*, 47, (1995), 36-39.

[1995Wes] J.H. Westbrook and R.L. Fleisher, Intermetallic Compounds – Principles and Practice, John Wiley and Sons, Chishester, (1995).

[1996Eri] G.L. Erikson, US Patent 6632299 - Nickel-base superalloy for high temperature, high strain application, *Superalloys 1996*, (1996), 35-44.

[1996Nat] National Research Council, Coatings for High-Temperature Structural Materails, National Academy Press, Washington, D.C., (1996).

[1996Yam] Y. Yamabe-Mitarai, Y. Koizumi, H. Murakami, Y. Ro, T. Maruko and H. Harada, Development of Ir-base refractory Superalloys, *Scripta Mater.*, 35, 2 (1996), 211-215.

[1996Wol] I.M Wolff and G. Sauthoff, *Metall. Mater. Trans. A*, (1996), 27A, 2642-2652.

[1997Wil] J.C. Williams, Structural Intermetallics, (1997). Editors M.V. Nathal, R. Darolia, C.T. Liu, P.L. Martin, D.B. Miracle, R. Wagner and M. Yamaguchi, TMS, Seven Springs (1997), 3 – 8.

[1997Yam] Y. Yamabe-Mitarai, Y. Ro, T. Maruko, T. Yokokawa and H. Harada, PGM-Based refractory Superalloys for Ultra-High Temperature Use, Structural Intermetallics (1997), *(Proc. 2nd Int. Symp. On Structural Intermetallics*, Seven Springs, Champion, U.S.A., eds. M.V. Nathal, R.Darolia, C.T. Liu, P.L. Martin, D.B. Miracle, R. Wagner and M. Yamaguchi, Minerals, Metals & Materials Society., 21st-26th Sept., (1997), 805-814.

[1998Gow] G.W. Goward, *5th International Conference on Metallurgical Coatings and Thin Films*, San Diego, 108 – 109 (1998), 73 – 79.

[1998Yam] Y. Yamabe-Mitarai, H. Murakami, Y. Ro, T. Maruko and H. Harada, Ir-base Refractory Superalloys for Ultra-high Temperatures, *Metall. Mater. Trans. A* 29A (1998), 537-549.

[1999Car1] P. Caron and T. Khan, Evolution of Ni-based Superalloys for Single Crystal Gas Turbine Blade Applications, *Aerosp. Sci. Technol*., 3, (1999), 513-523.

[1999Car2] P. Caron and T. Khan, Gas Turbines, *Materials Make the Difference*, Hampshire, 12 (1999), 1-10.

[1999Cle] W.J. Clegg, A. Kelly and J.E. Pitchford, *Key Engineering Materials,* 161-163, (1999), 315-320.

[1999Fai] G.B. Fairbank, C.L. Humphreys, A. Kelly and C.N. Jones, *Conf. Proc. Intermetallics for the Third Millennium, ASM*, Cincinnati, 1st-4th Nov, (1999).

[1999Gu1] Y.F. Gu, Y. Yamabe-Mitarai, Y. Ro, T. Yokokawa and H. Harada, Properties of the $Ir_{85}Nb_{15}$ Two-phase Refractory Superalloys with Nickel Additions, *Metall. Mater. Trans. A*, 30A (1999), 2629-2640.

[1999Gu2] Y.F. Gu, Yamabe-Mitarai, X.H. Yu and H. Harada, Microstructures and Compressive Properties of Ni Alloyed Rh–15 at.% Nb two-phase Refractory Superalloys, *Mater. Lett. A*, 41 (1999), 45-51.

[1999Hil] P.J. Hill, L.A. Cornish and M.J. Witcomb, Constitution of the Al–Ir–Ru System, *J. Alloys Compounds*, 291, (1999), 130-144.

[1999Ngw] K.P. Ngwenya and I.M. Wolff, Precipitation Strengthening in Ferritic Fe-Cr-Al-Ru Alloys, Procedings of the Electron Microscopy Society of Southern Africa, (1999), 29, 19.

[1999Yam] Y. Yamabe-Mitarai, M.H. Hong, Y. Ro and H. Harada, Temperature Dependence of the Flow Stress in Ir_3Nb with the $L1_2$ Structure, *Philos. Mag. Lett*., 79 (9) (1999), 673-682.

[2000Gu] Y.F. Gu, Y. Yamabe-Mitarai and H. Harada, Influence of Ni Addition on Mechanical Properties and Fracture Behaviors of Ir-15Nb two-phase Refractory Superalloys, edited by E.K. Ohriner, R.D. Lanam, P. Panfilov, and H. Harada. *The Minerals, Metals and Materials Society*, Warrendale, PA, (2000), 73-80.

[2000Fai1] G. Fairbank, C. Humphreys, A. Kelly and C.N Jones, Ultra-high Temperature Intermetallics for the Third Millennium, *Intermetallics*, 8 (2000), 1091-1100.

[2000Fai2] G. Fairbank, C. Humphreys, A. Kelly and C.N Jones, New Platinum Alloys for Ultra High Temperature Apllications, presented at *Fifth Charles Parsons Turbine Conference*, Cambridge, UK, 3-7 July (2000).

[2000Hil1] P.J. Hill, P. Ellis, L.A. Cornish, M.J. Witcomb and I.M. Wolff, The Oxidation Behaviour of Pt-Al-X Alloys at Temperatures Between 1200 and 1350°C, *Proc High-Temperature Corrosion and Protection 2000*, Sapora, Japan, 17th-22nd Sept, (2000), 185-190.

[2000Hil2] P.J. Hill, L.A. Cornish and M.J. Witcomb, *Proc. Int. Symp. on High Temperature Corrosion and Protection*, edited by T. Narita, T.Maruyama, and S. Taniguchi (Iron and Steel Institute of Japan, Toyko, (2000), 158-164.

[2000Wol] I.M. Wolff and P.J. Hill, Platinum Metals-Based Intermetallics for High-Temperature Service. *Plat. Met. Rev.*, (2000), 44, (4), p. 158-166.

[2000Völ] R. Völkl, D. Freund, B. Fischer and D. Gohlke, in *Proc. 8th Int. Conf. On Creep and Fracture of Engineering Materilas and Structures. Key Engineering Materials*, Vols. 171-174, edited by T. Sakuma and K. Yagi (Trans Tech Publications, Utilkon-Zürich, Switzerland, (2000), 77-84.

[2000Yu1] X.H. Yu, Y. Yamabe-Mitarai, Y. Ro and H. Harada, Design of Quaternary Ir-Nb-Ni-Al Refractory Superalloys, *Metall. Mater. Trans. A*, (2000), 31A, 173-178.

[2000Yu2] X.H. Yu, Y. Yamabe-Mitarai, Y. Ro and H. Harada, Investigation on Microstructure and Fracture of Quaternary Ir-based Alloys, *Key Engineering Materials*, Vols. 171-174, (2000), 677-684.

[2001Big] T. Biggs, P.J. Hill, L.A Cornish and M.J. Witcomb, An Investigation of the Pt-Al-Ru Diagram to Facilitate Alloy Development, *J. Phase Equilib*. 22 (3) (2001), 214-218.

[2001Fai] G.B. Fairbank, C.J. Humpheys and C.N. Jones, presented at *2nd Int. Symp. On High-Temperature Materials 2001* (Tsukuba, Japan, May 31-June 2, (2001).

[2001Fis1] B. Fischer, D. Freund, J. Merker, R. Völkl and D.F. Lupton, in *Proc. 8th Int. Conf. on Composites Engineering*, edited by D. Hui (University of New Orleans, New Orleans, LA, (2001), 249.

[2001Fis2] B. Fischer, New Platinum Materials for High Temperature Applications, *Adv. Eng. Mater*. 3, 10, (2001), 811-820.

[2001Hil1] P.J. Hill, T. Biggs, P. Ellis, J. Hohls, S. Taylor and I.M. Wolff, An Assessment of Ternary precipitation-strengthened Pt alloys for ultra-high temperature applications, *Mater. Sci. Eng., A* A301, (2001), 167-179.

[2001Hil2] P.J. Hill, L.A. Cornish, P. Ellis and M.J. Witcomb, The Effects of Ti and Cr Additions on the Phase Equilibria and Properties of (Pt)/Pt_3Al Alloys, *J. Alloys Compounds*. 322, (2001), 166-175.

[2001Hil3] P.J. Hill, Y. Yamabe-Mitarai, H. Murakami, L.A. Cornish, M.J. Witcomb, I.M. Wolff and H. Harada, The Precipitate Morphology and Lattice Mismatch of Ternary (Pt)/Pt_3Al Alloys, *3rd International Symposium on Structural Intermetallics*, *TMS*, 527-533. Snow King Resort, Jackson Hole, Wyoming, USA, Sept (2001). Rescheduled for 28th April - 1st May 2002.

[2001Hil4] P.J. Hill, G.B. Fairbank and L.A. Cornish, Platinum Group Metal Overview, New Developments in High-Temperature Platinum Alloys, *JOM*, 53, 10 October (2001), 19-20.

[2001Hil5] P.J. Hill, Y. Yamabe-Matarai and I.M. Wolff, High-Temperature Compression Strengths of Precipitation-Strengthened Ternary Pt-Al-X Alloys, *Scr. Mater*., 44 (1) (2001), 43-48.

[2001Süs] R. Süss, P.J. Hill, P. Ellis and L.A. Cornish, The Oxidation Resistance of Pt-base Superalloy Pt_{80}:Al_{14}:Cr_3:Ru_3 compared to that of Pt_{86}:Al_{10}:Cr_4, *Proc. Microsc. Soc. South. Afr*., 31, 21, Johannesburg, 5th-7th December (2001).

[2001Zha] J.C. Zhao, A Combinatorial Approach for Efficient Mapping of Phase Diagrams and Properties, *J. Mater. Res*., 16, (2001), 1565-1578.

[2002Cor] L.A. Cornish, J. Hohls, P.J. Hill, S. Prins, R. Süss and D. Compton, The Development of Platinum-Based Alloys and their Thermodynamic Database, *J. Mining and Metallurgy*, 38 (3 – 4) (2002), 197 – 204.

[2002Fis] B. Fischer, D. Freund, T. Bromel, R. Völkl, J. Daniel, W. Ross, R. Teschener and C.E. Michelsen. *Proc. 25th Int. Precious Metals Conf.* [CD-ROM] (International Precious Metals Institute, Pensacola, FL, 2002), 99.

[2002Gu] Y.F. Gu, Y. Yamabe-Mitarai, S. Nakazawa, Y. Ro and H. Harada, Microstructures and mechanical properties of $(Ir, Rh)_{75}Nb_{15}$ Ni_{10} alloys *Metall. Mater. Trans. A* 33A, (2002), 1281-1283.

[2002Hil] P.J Hill, N. Adams, T. Biggs, P. Ellis, S. Taylor and I.M. Wolff, Platinum Alloys Based on Pt-Pt_3Al for Ultra-High Temperature Use, *Mater. Sci. Eng.*, A338 (2002), 133-141.

[2003Bha] H.K.D.H. Bhadeshia, Nickel Based Superalloys, University of Cambridge, (2003), http://www.msm.cam.ac.uk/phase-tran/2003/Superalloys.html.

[2003Cho] L.H. Chown and L.A. Cornish, The Influence of Cobalt Additions to Pt-Al and Pt-Al-Ru-Cr Alloy Systems, *African Materials Research Society Conference*, 136-137, University of the Witwatersrand, Johannesburg, 8th - 11th December 2003.

[2003Cor] L.A. Cornish, B. Fischer and R. Völkl, Development of PGM Superalloys for High-Temperature use, *MRS Bulletin*, (2003), 632-638.

[2003Hua] C. Huang, Y. Yamabe-Mitarai, K. Nishida and H. Harada. *Intermetallics*, 11, (2003), 917–926.

[2003Xpe] X´pert Highscore, (PW3209), 1.0d, PANalytical B.V., Almelo, The Netherlands, 31 March, 2003.

[2004Cho] L.H. Chown, L.A. Cornish and B. Joja, "Structure and Properties of Pt-Al-Co Alloys", *Proc. Microsc. Soc. south. Afr.*, Pretoria, 30 November – 3 December, 34, (2004) 11.

[2004Hua1] C. Huang, Y. Yamabe–Mitarai and H. Harada, The Stabilization of Pt_3Al Phase with $L1_2$ Structure in Pt–Al–Ir–Nb and Pt–Al–Nb Alloys, *J. Alloys Compounds*, 366 (2004), 217–221.

[2004Hua2] C. Huang, Y. Yamabe-Mitarai, S. Nakazawa and H. Harada. *Mater. Lett*., 58, (2004), 483–488.

[2004Vor] S. Vorberg, M. Wenderoth, B. Fischer, U. Glatzel and R. Völkl, Pt–Al–Cr–Ni Superalloys: Heat Treatment and Microstructure, *JOM*, 56(9), (2004), 40–43.

[2005Hua] C. Huang, Y. Yamabe-Mitarai, X.H. Yu, S. Nakazawa and H. Harada. *Met. & Mat. Trans*., vol. 36A, (2005), 539–545.

[2005Wen] M. Wenderoth, L.A. Cornish, R. Süss, S. Vorberg, B. Fischer and U. Glatzel, On the Development and Investigation of Quaternary Pt-Based Superalloys with Ni Additions. *Metall. Mat. Trans. A*, 36 A, (2005), 567-575.

[2005Hül] M. Hüller, M. Wenderoth, S. Vorberg, B. Fischer, U. Glatzel and R. Völkl. Optimization of Composition and Heat Treatment of Age-Hardened Pt-Al-Cr-Ni Alloys. *Metall. Mater. Trans. A*, 36A, 3A,(2005), 681-689.

[2005Völ] R. Völkl, Y. Yamabe-Mitarai, C. Huang and H. Harada, Stabilizing the $L1_2$ Structure of $Pt_3Al(r)$ in the Pt-Al-Sc System, *Metallurgical and Materials Transactions A*, 36, (2005), 2881 - 2892.

[2006Dou1] A. Douglas, J.H. Neethling, R. Santamarta, D. Schryvers and L.A. Cornish, Unexpected ordering behaviour of Intermetallic precipitates, *J. Alloys Compounds*, 432, (2007), 96–102.

[2006Dou2] A. Douglas, L.A. Cornish, R. Süss, L. Glaner, L. H. Chown and A. Watson, Experimental and Thermo-Calc™ Work on the Development of Pt-Based

Superalloys, 11th Report, Mintek Confidential Communication C4193M, March 2006.

[2006Mal] N.B. Maledi, J.H. Potgieter, M. Sephton, L.A. Cornish, L. Chown and R. Süss, Hot Corrosion Behavior of Pt-alloys for Application in the Next Generation of Gas Turbines, *Southern African Institute of Mining and Metallurgy Conference 'Platinum Surges Ahead'*, Symposium sries S45, Sun City, 8-12 October 2006. 81-90.

[2006Süs] R. Süss, L.A. Cornish, A. Douglas, A. Mwamba, L. Glaner, L. H. Chown and G. Williams, 4466 Experimental and Thermo-Calc^{TM} Work on the Development of Pt based Superalloys: 13th Report, Mintek, 22 November (2006).

[2007Cor] L.A. Cornish, R. Süss, R. Völkl, M. Wenderoth, S. Vorberg, B. Fischer, U. Glatzel, A. Douglas, L.H. Chown, T. Murakumo, J. Preussner, D. Lupton, L. Glaner, N.B. Maledi, J.H. Potgieter, M. Sephton and G. Williams, Overview of the Development of New Pt-based alloys for High Temperature Application in Aggressive Environments. *J. Southern African Institute of Mining and Metallurgy*, 107 (11) (2007), 697-711.

[2007Mar] M. Marekwa, L.A. Cornish and R. Süss. Unpublished Mintek work (2006).

[2007Som] H. Somekawa, A. Singh and T. Mukai, Effect of Precipitate Shapes on Fracture Toughness in Extruded Mg-Zn-Zr magnesium alloys, *MRS Bulletin*, 22, (2007), 965 – 973.

[2007Wen] M. Wenderoth, R. Völkl, S. Vorberg, Y. Yamabe-Mitarai, H. Harada and U. Glatzel. Microstructure, Oxidation Resistance and High-Temperature Strength of γ′ hardened Pt-base alloys, *Intermetallics*, 15, (2007), 539-549.

[2009Völ] R. Völkl, M. Wenderoth, J. Preussner, S. Vorberg, B. Fischer, Y. Yamabe-Mitarai, H. Harada and U. Glatzel, Development of a Precipitation-Strengthened Pt-base Superalloy, *Mater. Sci. Eng., in press A(2009).*

[URLHar] Hardness correlation URL: http://www.mechanicalproperties.com, links.

[URLXRD] X-ray Diffraction Principles URL:http://www.phys.uen.edu-xrd.

APPENDIX

Appendix A: XRD reference data

Table A.1. XRD reference peak list together with the h, k and l parameters for Pt, 01-087-0636.

h	k	l	d-spacing (Å)	Lattice Parameter (Å)	Position 2θ(°)	Intensity (%)
1	1	1	2.27707	3.9440	39.545	100
2	0	0	1.972	3.9440	45.986	45.7
2	2	0	1.39441	3.9440	67.066	23.2
3	1	1	1.18916	3.9440	80.747	23.6
2	2	2	1.13853	3.9440	85.153	6.5

Table A.2. XRD reference peak list together with the h, k and l parameters for $L1_2$ – Pt_3Al, 00-065-3255.

h	k	l	d-spacing (Å)	Position 2θ(°)	Intensity (%)
1	0	0	3.876	22.926	27.4
1	1	0	2.74075	32.646	20.2
1	1	1	2.23781	40.268	100
2	0	0	1.938	46.84	48.1
2	1	0	1.7334	52.768	9.2
2	1	1	1.58237	58.261	6.7
2	2	0	1.37037	68.404	26.1
2	2	1	1.292	73.198	3.8
3	1	0	1.2257	77.873	2.4
3	1	1	1.16866	82.467	27.5
2	2	2	1.1189	87.014	7.8
3	2	0	1.07501	91.541	1.5
3	2	1	1.0359	96.079	2.7
4	0	0	0.969	105.3	3.8
4	1	0	0.94007	110.051	2.1
4	1	1	0.91358	114.952	1.5
3	3	1	0.88921	120.056	12.9
4	2	0	0.8667	125.439	12.4
4	2	1	0.84581	131.21	1.8
3	3	2	0.82637	137.546	0.9

Table A.3. XRD reference peak list together with the h, k and l parameters for DO'_c – Pt_3Al, 00-048-1815.

h	k	l	d-spacing (Å)	Position 2θ(°)	Intensity (%)
0	0	2	3.907	22.742	3
z1	1	0	3.852	23.071	5
1	1	2	2.743	32.619	11
2	0	0	2.724	32.853	3
2	1	1	2.326	38.68	6
2	0	2	2.235	40.321	100
2	1	2	2.067	43.76	1
0	0	4	1.953	46.459	25
2	2	0	1.926	47.15	36
2	1	3	1.779	51.316	6
1	1	4	1.742	52.488	5
2	2	2	1.728	52.946	3
3	1	0	1.723	53.112	9
2	0	4	1.587	58.075	4
3	1	2	1.576	58.519	5
2	2	4	1.371	68.368	47
4	0	0	1.362	68.883	19
4	0	1	1.342	70.058	1
4	1	0	1.321	71.34	1
2	1	5	1.315	71.716	3
3	2	3	1.307	72.224	2
4	1	1	1.33	72.481	9
0	0	6	1.302	72.545	1
3	1	4	1.292	73.198	12
4	0	2	1.286	73.595	1
3	3	1	1.267	74.886	1
4	1	2	1.252	75.941	1
1	1	6	1.234	77.251	5
3	3	2	1.22	78.306	10
4	2	0	1.218	78.459	1
4	0	3	1.207	79.315	1
4	2	1	1.204	79.551	2
3	2	4	1.195	80.272	1
4	1	3	1.178	81.673	9
2	0	6	1.175	81.926	38
4	2	2	1.163	82.957	33

Table A.3, *Cont.* XRD reference peak list together with the h, k and l parameters for DO'_c – Pt_3Al, 00-048-1815.

h	k	l	d-spacing (Å)	Position 2θ(°)	Intensity (%)
			1.152	83.928	1
2	1	6	1.149	84.197	1
4	0	4	1.117	87.199	30
4	2	6	1.104	88.491	1
4	1	4	1.095	89.412	2
4	3	0	1.09	89.934	1
3	2	5	1.086	90.356	1
4	3	1	1.079	91.107	7
3	3	4	1.073	91.762	1
5	1	0	1.069	92.205	3
5	1	1	1.059	93.335	1
4	3	2	1.05	94.381	2
3	1	6	1.039	95.699	5
4	2	4	1.034	96.313	1
5	1	2	1.031	96.686	12
2	1	7	1.015	98.738	3
4	1	5	1.009	99.535	8
4	3	3	1.005	100.075	6
5	2	1	1.003	100.349	1
3	3	5	0.992	101.885	1
3	2	6	0.986	102.748	1
0	0	8	0.997	104.079	11
2	2	7	0.966	105.767	1

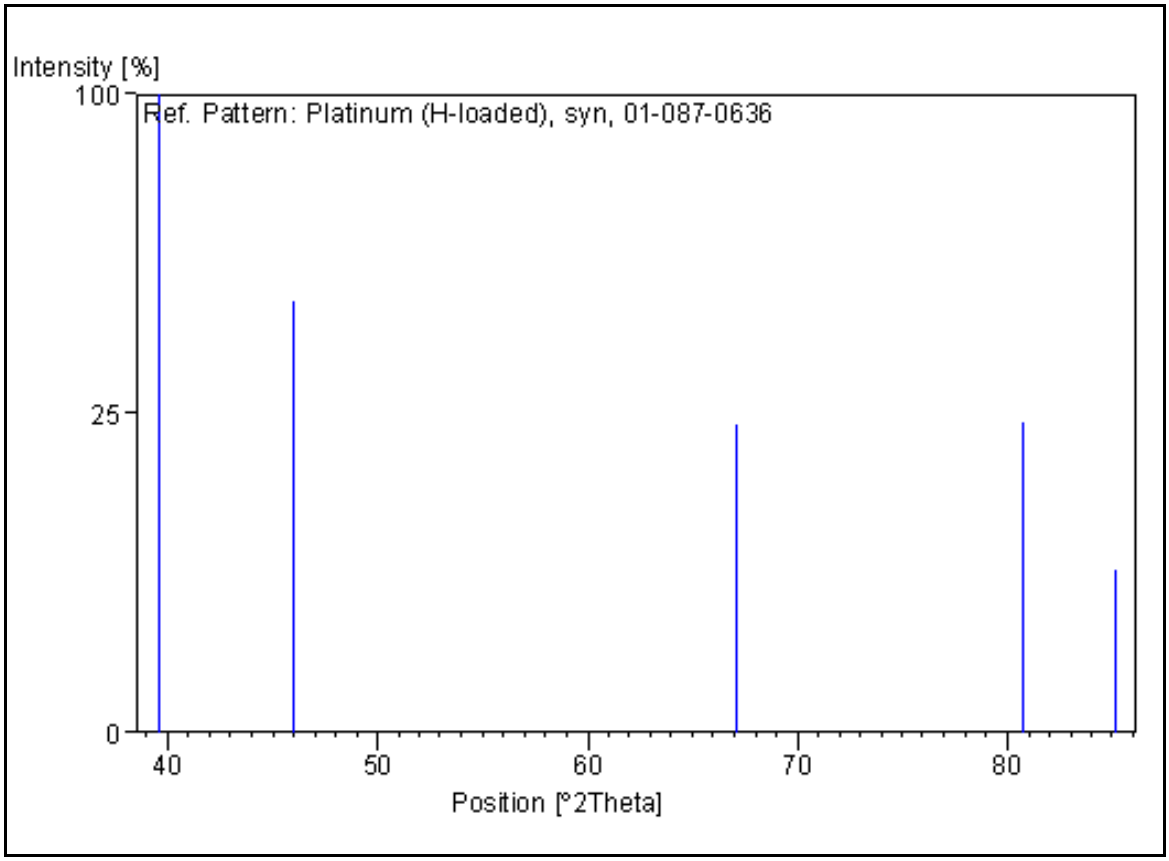

Figure A.1. XRD reference stick pattern for Pt, 01-087-0636.

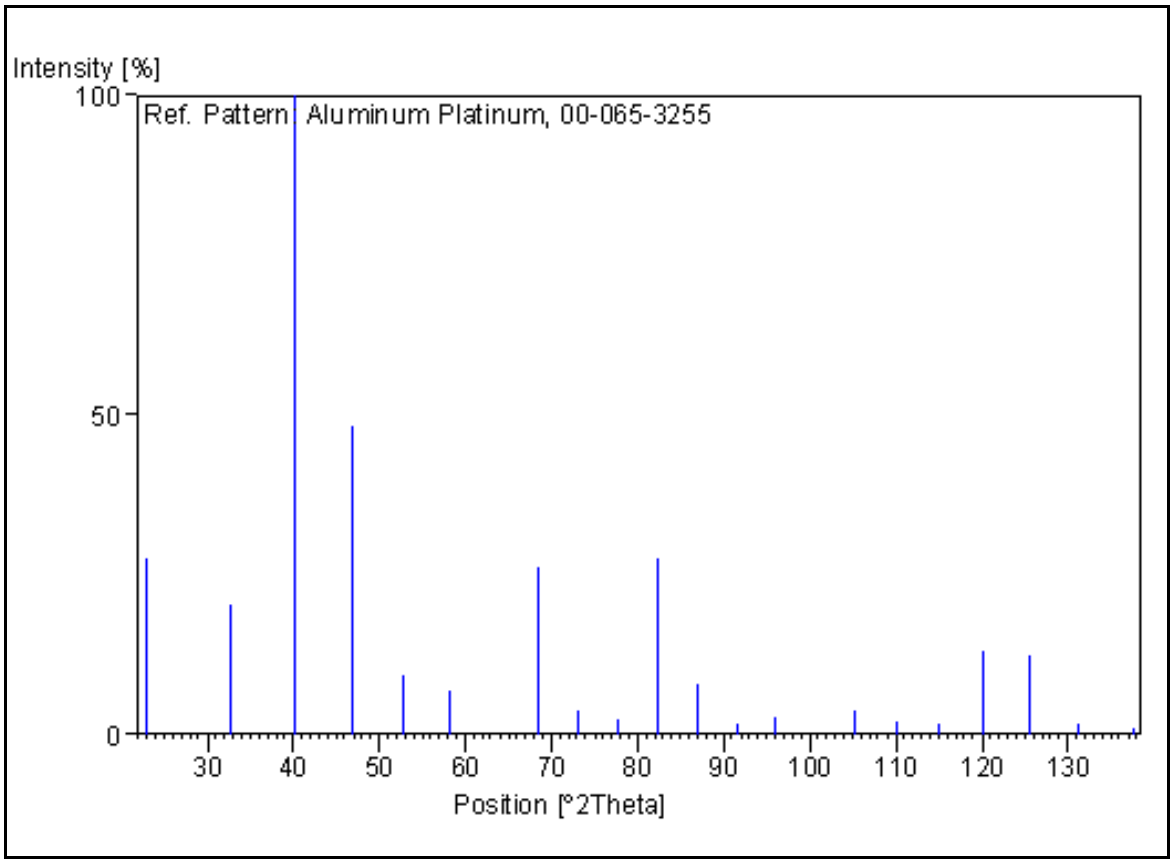

Figure A.2. XRD reference stick pattern for $L1_2$ – Pt_3Al, 00-065-3255.

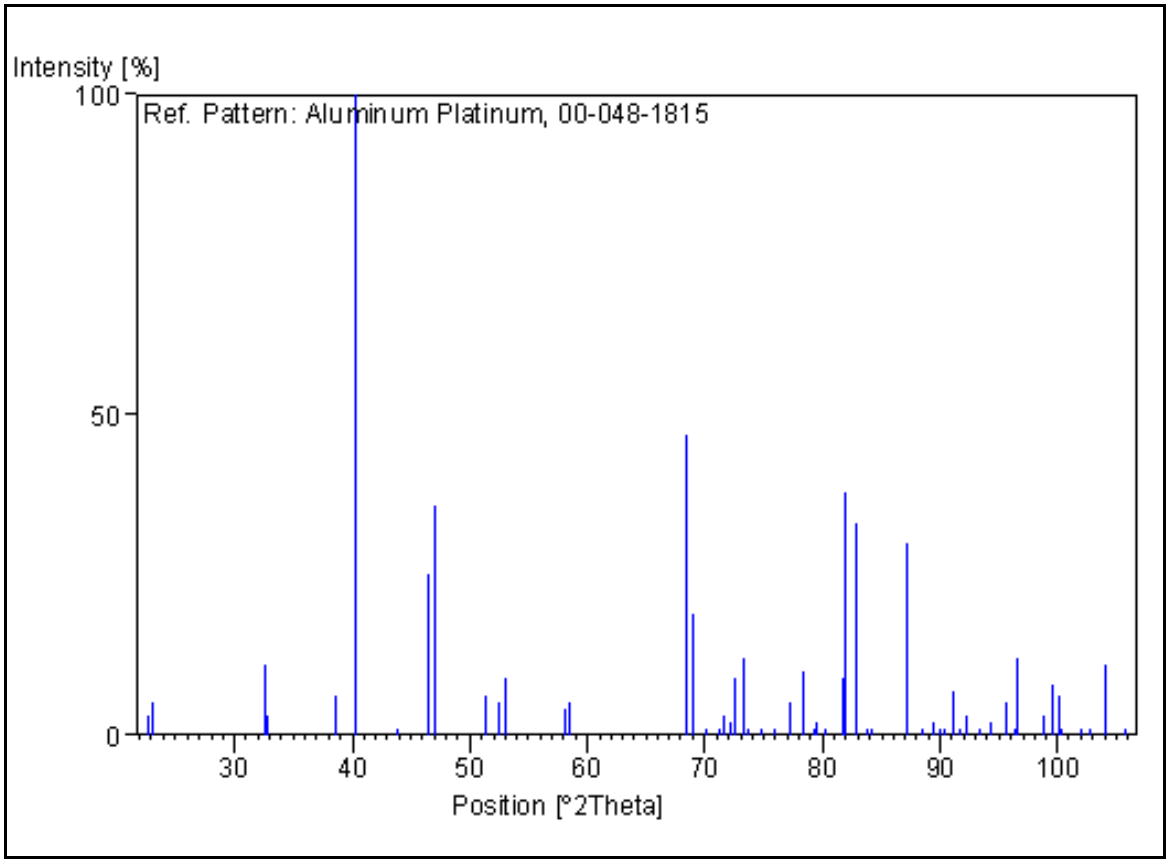

Figure A.3. XRD reference stick pattern for DO′$_c$ - ~Pt_3Al, 00-048-1815.

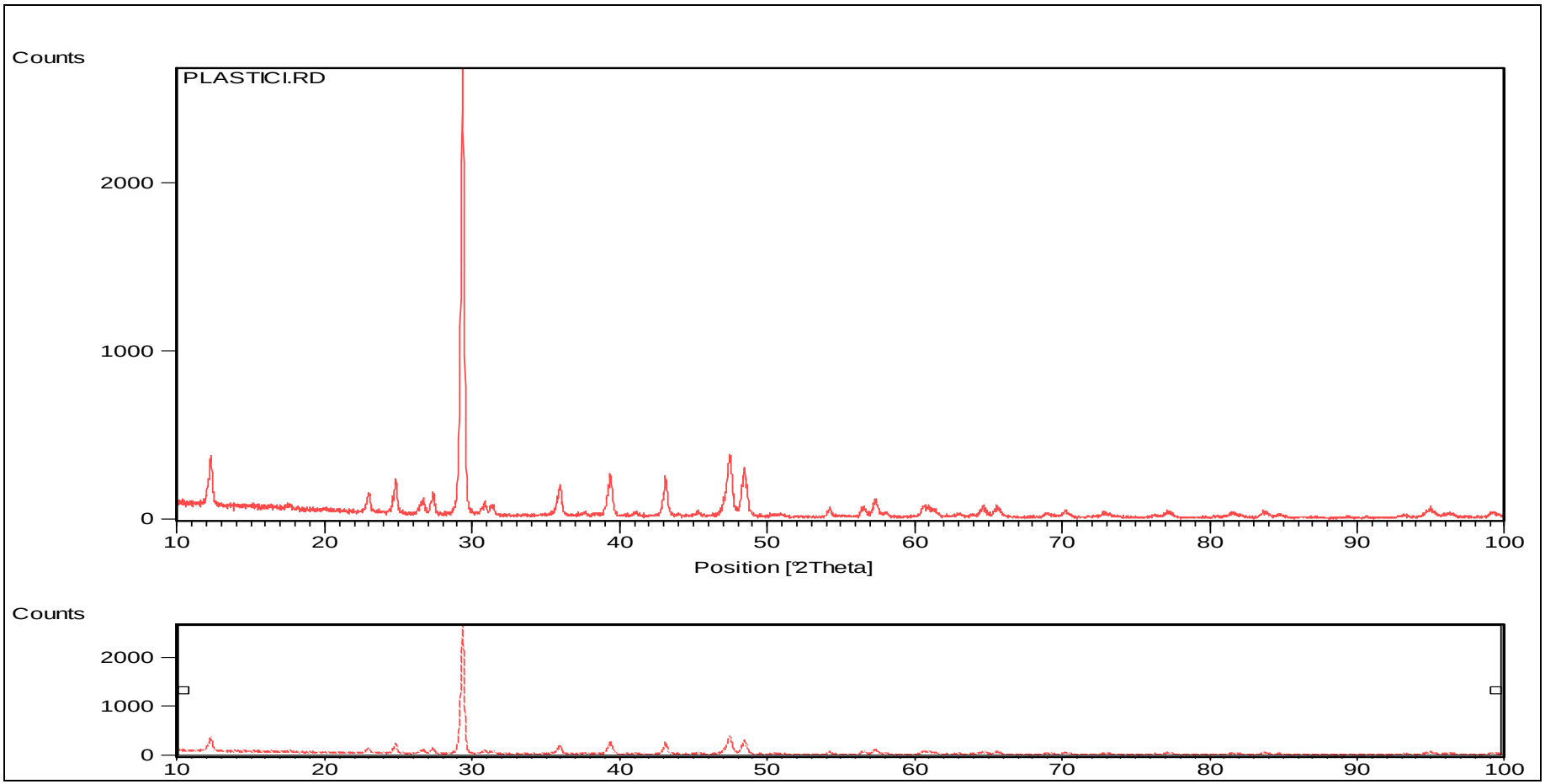

Figure A.4. XRD pattern of plasticine.

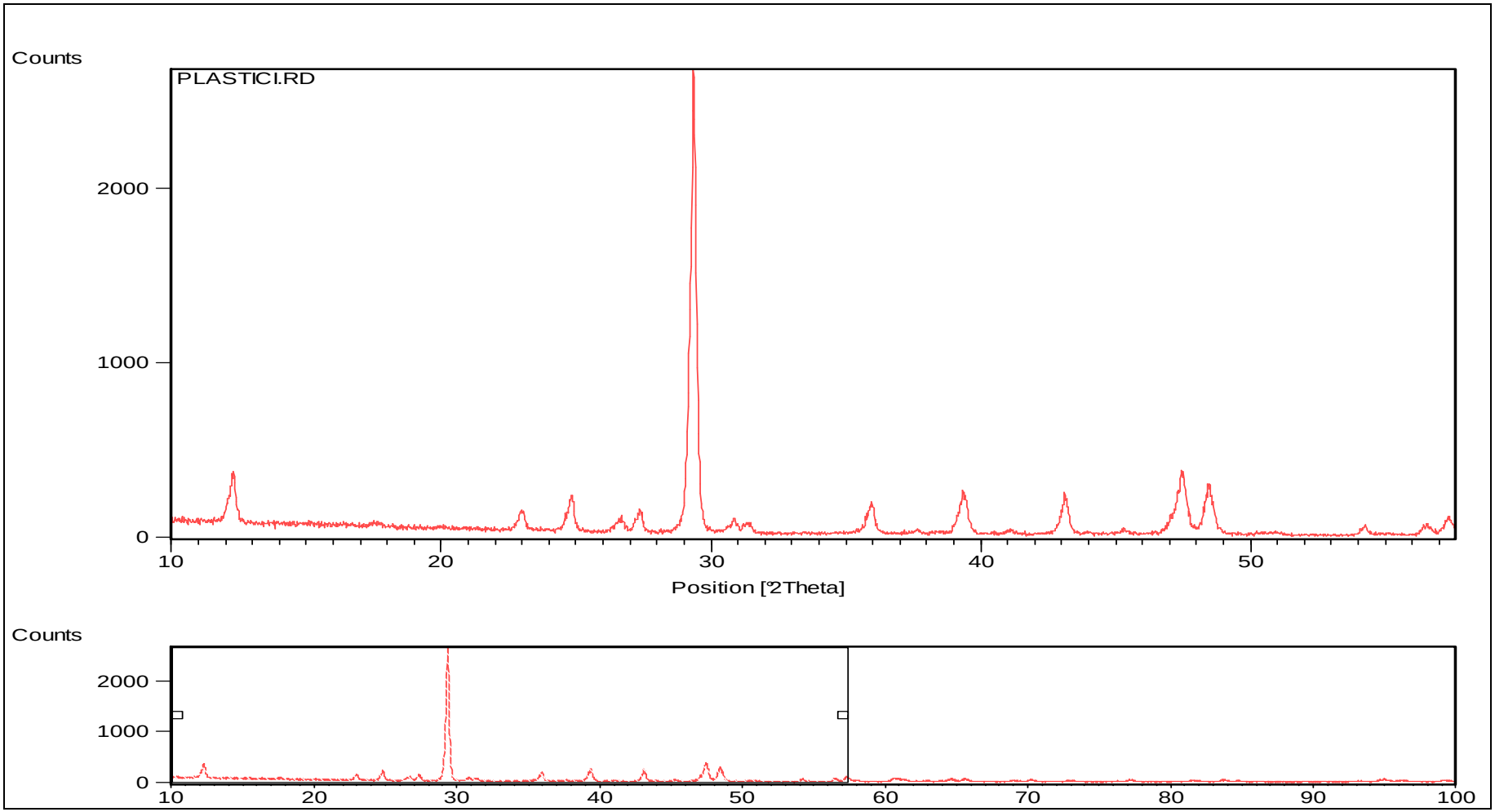

Figure A.5. XRD pattern of plasticine zoomed up to 58 (°2θ) position.

Appendix B: Presentations and papers

Presentations during the course of this investigation:

1. M.B. Shongwe, L.A. Cornish and R. Süss, Optimisation of Compositions and Heat Treatment of Pt-based Superalloys, Materials Physics Research Institute (MPRI) Seminar, University of the Witwatersrand, 25th February 2008.
2. M.B. Shongwe, L.A. Cornish and R. Süss, Optimisation of Compositions and Heat Treatment of Pt-based Superalloys, Centre of Excellence in Strong Materials, Joint Workshop Presentation Seminar, University of the Witwatersrand, 23th April 2008.

Papers during the course of this investigation:

1. M.B. Shongwe, L.A. Cornish and R. Süss, Optimisation of Compositions and Heat Treatment of Pt-based Superalloys, Proceedings of the Microscopy Society of Southern Africa, Volume 38, (2008), p.27.
2. M.B. Shongwe, L.A. Cornish and R. Süss, Improvement of ~Pt_3Al Volume Fraction and Hardness in a Pt-Al-Ru-Cr Superalloy , Advanced Metals Initiative Conference, 18th–19th November 2008.